Author:
Lewis, Simon John

Title:
Influences of load history on the cleavage fracture of steels

University of
BRISTOL

Influences of Load History on the Cleavage Fracture of Steels

Simon John Lewis

October 2009

A dissertation submitted to the University of Bristol in accordance with the requirements of the degree of Doctor of Philosophy in the Faculty of Engineering, Department of Mechanical Engineering.

Number of words: 37984

Abstract

As part of a safety assessment of a component or structure, it is necessary to define in a rigorous manner the limits for its safe use and operation. This requirement leads to a need for accurate descriptions of the conditions for failure.

In determining safe operating limits for failure by fracture, current methods are often overly pessimistic, especially following load history or in the presence of residual stress. Such conservatisms may lead to overdesign and excessive weight or premature removal of infrastructure from service.

A study was conducted, described in this thesis, on the influences of previous load cycles on brittle fracture, primarily in A533B ferritic steel. Potential influences of remnant stresses on measured fracture toughness were explored by extracting test coupons from large scale welded components. Finite element simulations and experimental stress measurement were used to infer the effect on measured toughness.

Re-analysis of previously published experimental data highlighted a range of limitations and practical problems with a number of current fracture criteria. To investigate the issues highlighted in greater depth, a program of fracture testing was conducted covering a wide range of specimen constraint levels and considering specimens with and without prior load history.

The resulting fracture data set was used to study the applicability of numerous local approach methods, as well as crack tip fracture parameters, in terms of their transferability between geometries and ability to predict the effects of load history.

It was shown that the effect of prior loading on fracture behaviour can be extremely significant. It was seen that the local approach, if properly calibrated, is able to predict the influence of load and geometry on fracture to an acceptable accuracy. It was also seen that consideration of fracture, even under brittle conditions, as a stress and strain controlled process improved the quality of the model predictions.

For my parents, Gill and John, and for Lisa.

Acknowledgments

I am greatly indebted to my supervisors Dr. Chris Truman and Prof. David Smith, for their continuing advice and encouragement over the course of this work and the considerable opportunities I have had for travel and international collaboration.

Ian Milnes, Pete Whereat, Guy Pearn, Steve Harding, John Byles and Dave Hooper were all of great help in setting up fracture tests, manufacturing and preparing specimens and overcoming the inevitable unseen issues that go hand in hand with experimental work. I would also like to thank Dr. Adel El-Turki for help with SEM imaging and Dr. Julian Booker for advice on all things statistical.

Dr. Bruce Brown, of Doosan Babcock, kindly fabricated high quality welded specimens at very short notice and David Beardsmore of SERCO TAS provided a great deal of help with use of the JEDI code. Thanks are also due to Dr. Michael Hofmann and Dr. Darren Hughes for their considerable help and patience in making neutron diffraction measurements on the STRESS-SPEC and SALSA instruments. Dr. Ed Oliver and Dr. Anna Paradowska of ENGIN-X were both a huge help in the experimental work on that instrument.

The numerous members of the Solid Mechanics group have been a valued source of advice, motivation and friendship throughout my time as a part of it, you are too numerous to mention you all! In particular however, Dr. Hassan Alizadeh for his help with finite element analyses, Dr. Sayeed Hossain for being a regular at every neutron source in Europe, Chris Aird for his experimental apparatus and Mahmoud Mostafavi for endless technical discussions.

My entire family are also due a huge thank you for constant encouragement. In particular, my sisters and Lisa for never allowing me to take myself too seriously and my parents, whose purchase of a rubber toy hammer (aged 18 months) I credit with putting me on the path to engineering in the first place.

This project was funded by the Engineering and Physical Sciences Research Council (EPSRC), through the provision of a Departmental Training Account (DTA) award.

Acknowledgments

I am greatly indebted to my supervisors Dr. Chris Truman and Prof. David Smith, for their continuing advice and encouragement over the course of this work and the considerable opportunities I have had for travel and international collaboration.

Ian Milnes, Pete Whereat, Guy Pearn, Steve Harding, John Byles and Dave Hooper were all of great help in setting up fracture tests, manufacturing and preparing specimens and overcoming the inevitable unseen issues that go hand in hand with experimental work. I would also like to thank Dr. Adel El-Turki for help with SEM imaging and Dr. Julian Booker for advice on all things statistical.

Dr. Bruce Brown, of Doosan Babcock, kindly fabricated high quality welded specimens at very short notice and David Beardsmore of SERCO TAS provided a great deal of help with use of the JEDI code. Thanks are also due to Dr. Michael Hofmann and Dr. Darren Hughes for their considerable help and patience in making neutron diffraction measurements on the STRESS-SPEC and SALSA instruments. Dr. Ed Oliver and Dr. Anna Paradowska of ENGIN-X were both a huge help in the experimental work on that instrument.

The numerous members of the Solid Mechanics group have been a valued source of advice, motivation and friendship throughout my time as a part of it, you are too numerous to mention you all! In particular however, Dr. Hassan Alizadeh for his help with finite element analyses, Dr. Sayeed Hossain for being a regular at every neutron source in Europe, Chris Aird for his experimental apparatus and Mahmoud Mostafavi for endless technical discussions.

My entire family are also due a huge thank you for constant encouragement. In particular, my sisters and Lisa for never allowing me to take myself too seriously and my parents, whose purchase of a rubber toy hammer (aged 18 months) I credit with putting me on the path to engineering in the first place.

This project was funded by the Engineering and Physical Sciences Research Council (EPSRC), through the provision of a Departmental Training Account (DTA) award.

Author's declaration

I declare that the work in this dissertation was carried out in accordance with the Regulations of the University of Bristol. The work is original, except where indicated by special reference in the text, and no part of the dissertation has been submitted for any other academic award. Any views expressed in the dissertation are those of the author.

SIGNED:  DATE: 10/12/2009

Papers originating from this work

Conference proceedings

"Influence of residual stress in measurement of apparent fracture toughness" S.J Lewis, D.J. Smith, J.D. Booker and C.E. Truman. *9th International Conference of Engineering Structural Integrity Assessment, 2007.*

"A comparison of 2D and 3D fracture assessments in the presence of residual stresses", S.J. Lewis, C.E. Truman and D.J. Smith, *ASME Pressure Vessels and Piping Division Conference 2007.*

"Geometric dependence of fracture criteria in AL2024", S.J. Lewis, M. Mostafavi, M.J. Pavier, D.J. Smith and C.E. Truman, *17th European Conference on Fracture 2008.*

"Prediction of brittle fracture under generalised elastic plastic loading", S.J. Lewis, C.E. Truman and D.J. Smith, *ASME Pressure Vessels and Piping Division Conference 2008.*

"Measurement and modelling of residual stresses in fracture toughness specimens extracted from large components", S.J. Lewis, S. Hossain, M. Hoffmann, C.E. Truman and D.J. Smith, *ASME Pressure Vessels and Piping Division Conference 2008.*

"Characterisation and prediction of brittle fracture in a ferritic steel under general loading conditions", S.J. Lewis, D.J. Smith and C.E. Truman, *12th International Conference on Fracture.*

"Modelling of prestrain effects on fracture using local approach methods", S.J. Lewis, C.E. Truman and D.J. Smith, *ASME Pressure Vessels and Piping Division Conference 2009.*[1]

"Use of local approach methods with non-proportional load histories", S.J. Lewis, C.E. Truman and D.J. Smith, *ASME Pressure Vessels and Piping Division Conference 2009.*

[1] 2nd Prize winner, Student Paper Competition, ASME PVP 2009

Journal publications

"A comparison of 2D and 3D fracture assessments in the presence of residual stresses", S.J. Lewis, C.E. Truman and D.J. Smith, *Journal of Pressure Vessel Technology*, Vol 131, 021408-2 (2009)

"Determination of remnant residual stresses in fracture toughness specimens extracted from large components", S.J. Lewis, S. Hossain, C.E. Truman, D.J. Smith and M. Hofmann, *Strain* (In press)

"Diffraction measurement of plastic strain in A533B ferritic steel - A feasibility study", S.J. Lewis, S. Hossain and C.E. Truman, *Journal of Physics D: Applied Physics* (Under Review)

"Modelling and measurement of residual stresses in autogenously welded stainless steel plates: Part 1 - Fabrication and modelling", S. J. Lewis, H. Alizadeh, C. Gill, A.Vega, H. Murakawa, W. El-Ahmar, P. Gilles, D. J. Smith and C. E. Truman, *International Journal of Pressure Vessels and Piping* (Under Review)

"Modelling and Measurement of Residual Stresses in Autogenously Welded Stainless Steel Plates Part II - Measurements and Comparisons", S. J. Lewis, S. Hossain, H. Alizadeh, C. E. Truman and D. J. Smith, *International Journal of Pressure Vessels and Piping* (Under Review)

"Prediction of brittle fracture in ferritic steels under generalised elastic-plastic loading", S.J. Lewis and C.E. Truman , *Engineering Fracture Mechanics* (Under Review)

Journal publications

"A comparison of 2D and 3D fracture assessments in the presence of residual stresses", S.J. Lewis, C.E. Truman and D.J. Smith, *Journal of Pressure Vessel Technology*, Vol 131, 021408-2 (2009)

"Determination of remnant residual stresses in fracture toughness specimens extracted from large components", S.J. Lewis, S. Hossain, C.E. Truman, D.J. Smith and M. Hofmann, *Strain* (In press)

"Diffraction measurement of plastic strain in A533B ferritic steel - A feasibility study", S.J. Lewis, S. Hossain and C.E. Truman, *Journal of Physics D: Applied Physics* (Under Review)

"Modelling and measurement of residual stresses in autogenously welded stainless steel plates: Part 1 - Fabrication and modelling", S. J. Lewis, H. Alizadeh, C. Gill, A.Vega, H. Murakawa, W. El-Ahmar, P. Gilles, D. J. Smith and C. E. Truman, *International Journal of Pressure Vessels and Piping* (Under Review)

"Modelling and Measurement of Residual Stresses in Autogenously Welded Stainless Steel Plates Part II - Measurements and Comparisons", S. J. Lewis, S. Hossain, H. Alizadeh, C. E. Truman and D. J. Smith, *International Journal of Pressure Vessels and Piping* (Under Review)

"Prediction of brittle fracture in ferritic steels under generalised elastic-plastic loading", S.J. Lewis and C.E. Truman , *Engineering Fracture Mechanics* (Under Review)

Nomenclature and abbreviations

ϵ_{ij}	Tensorial strain component
ϵ_{ij}^{el}	Elastic strain component
ϵ_{ij}^{pl}	Plastic strain component
ϵ_{ij}^{th}	Thermal strain component
ϵ_A	Diffraction anisotropy strain
ϵ_e^p	Equivalent plastic strain
ϵ_Y	Yield strain
$\Delta\sigma$	Change in diffraction peak width
σ_{ij}	Tensorial stress component
σ_{th}	Local threshold stress
σ_0	Normalising Weibull stress
σ_1	Maximum principal stress
σ_f	Local fracture stress
σ_h	Hydrostatic stress
σ_w	Weibull stress
σ_Y	Yield stress

AR	As-received
BCC	Body centred cubic lattice
CT	Compact tension specimen
CUCF	Compress-unload-cool-fracture
DBT	Ductile-brittle transition
EDM	Electro Discharge machining
FAD	Failure assessment diagram
FCC	Face centred cubic lattice
FEA	Finite element analysis
HCP	Close packed hexagonal lattice
LUCF	Load-unload-cool-fracture
NCT	Notched compact tension specimen
PUCF	Punch-unload-cool-fracture
RNB	Round notched bar specimen
SEB	Single edge bend specimen
SENB	Single edge notched bend specimen
SEM	Scanning electron microscopy
SIF	Stress intensity factor
WPS	Warm prestress

E	Young's modulus
F_k	Force on elastic singularities
J	Value of the J integral
J_m	Modified J integral value
K_{IC}	Plane strain fracture toughness
K_{res}	K due to residual stress only
K_I	Mode I stress intensity factor
K_I^{el}	K_I from elastic analytical analyses
K_I^p	K due to primary stresses
K_I^s	K due to secondary stresses
K_J	K determined from J
K_r	R6 Normalised toughness
L_r	R6 Normalised applied load
m	Weibull modulus
Pf	Probability of fracture
Pf_r	Pf estimated ranking equation
R^2	Coefficient of determination
R^2_{Pf}	R^2 Between model Pf and Pf_r
W	Strain energy density

Contents

List of Figures

List of Tables

Chapter 1

Introduction and objectives

Failure of engineering components or structures is deemed to occur when the component is no longer able to carry out the function for which it was designed. One mechanism for failure is excessive yielding, where the geometry is altered so as to make the structure unfit for use. A second mode of failure is fracture such that separation of the structure into two or more parts has occurred or stiffness has been excessively degraded. In practice, a component that has not yet 'failed' but is showing signs of yield or cracking is generally removed from service in anticipation of eventual failure.

Yielding of engineering materials has been shown to be well characterised by laws based on resolved shear stress or the second invariant of deviatoric stress, such as those due to Tresca and von-Mises [1]. As such, yielding of structures under complex three dimensional loads can be accurately predicted and avoided by competent design.

Understanding of fracture in engineering materials is still far from complete. Although fracture is by no means a recent phenomenon, research into the area has only gathered pace in the last 60 years. At the current time, proven design guidelines and integrity assessment methods are available. However, they tend to employ high levels of conservatism, leading to overdesign or unnecessary removal of structures from service. This is especially true in areas where knowledge is limited such as the prediction of the effects of load history or prediction of failure under complex multi-axial loads.

As is often the case, research into the area was driven by in-service failures that could not be explained using the methods of the time. Such situations have often arisen as a result of introducing new technology. One of the best known examples is the failures of the Liberty ships, built during the 1940s.

These cargo vessels were revolutionary in that, as the first all welded ships, production was considerably faster and cheaper than for previous riveted designs. Unfortunately a large number of catastrophic failures of these vessels, including a number which broke completely in two, highlighted several unforeseen issues. Chiefly, it was found that inferior welding resulted in many flaws which served as nucleation points for subsequent cracking [2]. Cracks were also seen to originate from areas where the design of the vessels had resulted in stress concentrations and, in addition, the steel from which the ships were constructed was found to have a low toughness.

Another often cited failure is that of the de Havilland Comet, the world's first commercial jet airliner. Early models suffered cracking to the fuselage, resulting in a number of fatal accidents. This was later found to be caused by fatigue mechanisms, with cracks often emanating from the corners of the square windows [3], highlighting the need to consider stress concentrators in design.

Current drivers for fracture research tend to be proactive, rather than reactive, an indicator perhaps of the increase in understanding in the area. It has been said that

Failure is the opportunity to begin again, more intelligently [1]

however there are many cases when failure would be regarded as a catastrophe, rather than an opportunity. It is therefore unsurprising that the current trend, to safely reduce conservatism in design and assessment methodologies, is driven largely by the needs of the aerospace and power generation sectors where the consequences of failure can be severe.

In aerospace there is a constant desire to reduce overall weight and thereby improve fuel efficiency. In such cases, excessive conservatism in failure assessment methods may lead to unnecessary over design. In the power generation sector, in the U.K. particularly, there is an increasing need to prolong the life of an ageing plant infrastructure beyond the original design life. This requires that continuing safe operation can be demonstrated to regulatory authorities, often requiring that integrity assessment methods be updated in order to reduce the high levels of conservatism employed for the original designs.

This work presents the results of a project aimed at investigating the effects of load history on observed cleavage fracture properties. Previous loadings,

[1] Henry Ford

whether due to proof testing or operational service, are known to have potentially significant influences on subsequent structural behaviour due to ductile damage, generation of residual stress and work hardening.

When assessing the risk of fracture, the stress intensity at a crack tip in a component is commonly compared with a material fracture toughness. It is generally assumed that this toughness value is a material property, however observed experimental values may be strongly influenced by residual stresses, load history and geometry. Therefore, a differentiation is necessary between the 'apparent' or measured toughness and the true resistance of the material to fracture. Predictions throughout this thesis are of apparent toughness, i.e. that which would be measured during testing, as this is a measure of the change in failure load following strain history. The aims at the outset of the work described in this thesis were as follows:

1. Determine whether residual stresses in fracture specimens could have a significant influence on measured material fracture properties.

2. Quantify the potential influence of prior loading on measured fracture toughness in the cleavage regime and determine the significance of any effects relative to the inherent experimental scatter.

3. Determine the ability of current fracture criteria to predict the effects of residual stress and load history in general and provide guidance for improving the accuracy of failure assessments under such conditions.

Chapter 2 presents a review of the current state of research into the mechanisms leading to brittle fracture as well as a range of methods used to model and predict the phenomenon. A concern at the inception of this work was that when attempting to measure the change in material properties during operation, stresses remaining in extracted test coupons may influence and distort results. A case study into the potential influence of this effect was undertaken and is described in chapter 3.

Experimental testing can be a time consuming and expensive process. It was, therefore, important to have clear aims when designing experiments. To aid this, an investigation of previously published data was undertaken. The aim was to determine the scope and applicability of a number of the methods described in chapter 2, to determine areas for further research. The results of this work are presented in chapter 4.

From the findings of chapter 4, a program of fracture testing was devised. The experimental methods and specimen details are presented, along with results in chapter 5. The variation of stress and strain in the experimental specimens were then analysed using finite element analyses. In addition, trends in the raw fracture data were analysed using statistical methods. Both analyses are presented in chapter 6.

One of the most promising approaches for modelling of fracture in complex situations is the so-called local approach. Although highly flexible, the framework relies on model parameters, with physical meanings, to be determined by calibration to experimental data. The potential for error in such methods has previously been commented on:

> *A theory may be so rich in descriptive possibilities that it can be made to fit any data* [2]

Determining between a model fitting a given data set and a model which is an accurate representation of the fracture process is the subject of chapter 7. The models resulting from the fitting in chapter 7 as well a number of other predictive methods are applied to the facture tests of chapter 5 in chapter 8. Finally, chapters 9 and 10 discuss the findings of this work and draw conclusions as to their implications.

[2] Phillip Johnson-Laird, 'The Computer and the Mind'

Chapter 2

Literature review

A great deal of research effort has been devoted to the study of fracture of engineering alloys. This chapter presents a brief overview of current published material on the subject, covering the micromechanical processes leading to failure and current models used to describe and predict fracture behaviour.

2.1 Brittle fracture mechanisms

Brittle fracture is the subject of considerable current research as it is a common cause of sudden and unforeseen failure [4, 5]. Furthermore, it is often linked to catastrophic failure with severe consequences. Brittle fracture is also associated with relatively low energy failure mechanisms with little or no permanent deformation prior to failure (although this is not always the case). The two primary modes of brittle failure are intergranular fracture, where crack propagation occurs along material grain boundaries, and transgranular cleavage, where the crack path runs through material grains.

Cleavage fracture is the term used to describe rapid crack propagation along specific crystallographic planes. In general, the crack path follows the atomic planes with lowest separation energy, usually those with lowest atomic packing density and the greatest interplanar spacing. In the case of BCC (body centre cubic) crystal structures, such as ferritic steels, cleavage occurs predominantly on the [100] plane [6].

The stress required to overcome atomic cohesive forces in steels is generally an order of magnitude higher than that required to cause macroscopic yielding. Specific conditions are therefore required to permit stresses high enough to promote cleavage fracture. Firstly, plastic deformation must usually be

constrained to allow local stresses, at a granular scale, to become sufficiently large. As a result, cleavage fracture is commonly seen in materials with BCC and HCP crystal structures where there are limited slip systems available, but less commonly in FCC structures where the [111] plane provides many slip directions.

Secondly, local stress concentrations are necessary to increase the stress at an intragranular scale. These are commonly assumed to be microcracks, nucleated at cracked second phase particles such as carbides [7, 8, 9] or MnS inclusions [10]. It has also been suggested that deformation twins may act as nucleation points for microcracks [11, 12].

The assumption that fractured carbides act as microcrack nucleators was recently called in to question by Coates and co-workers [13] who investigated a large number of fracture surfaces in A533B ferritic steel and found no evidence of carbide cracking. It was suggested that cracks are nucleated from regions of microvoids [14]. Microvoid clusters were also reported in cleavage fracture by a number of others [15, 16]. The overall process for failure by cleavage fracture is generally accepted to be [17]:

1. Microcracks are nucleated by slip mechanisms.

2. Stresses immediate to the nucleated crack cause it to propagate, resulting in a grain sized crack.

3. If stresses in the neighbouring regions are high enough, the crack is able to cross the grain boundary and advance into neighbouring grains.

4. Once a crack has grown to the size of multiple grains, it is generally assumed to propagate to overall failure.

This process is illustrated in figure 2.1. It has been suggested by Chen [18] that at different temperatures, there are different 'critical' events which lead to global failure. At very low temperatures (-196°C), it was stated that cleavage fracture is primarily controlled by nucleation of microcracks, i.e. stresses are high but plastic strain must increase sufficiently before fracture occurs. At slightly warmer temperatures (-100°C), fracture was deemed to require a combination of strain to nucleate microcracks, stress triaxiality to prevent blunting of microcracks and local stress to propagate the microcrack into the surrounding matrix and over grain boundaries.

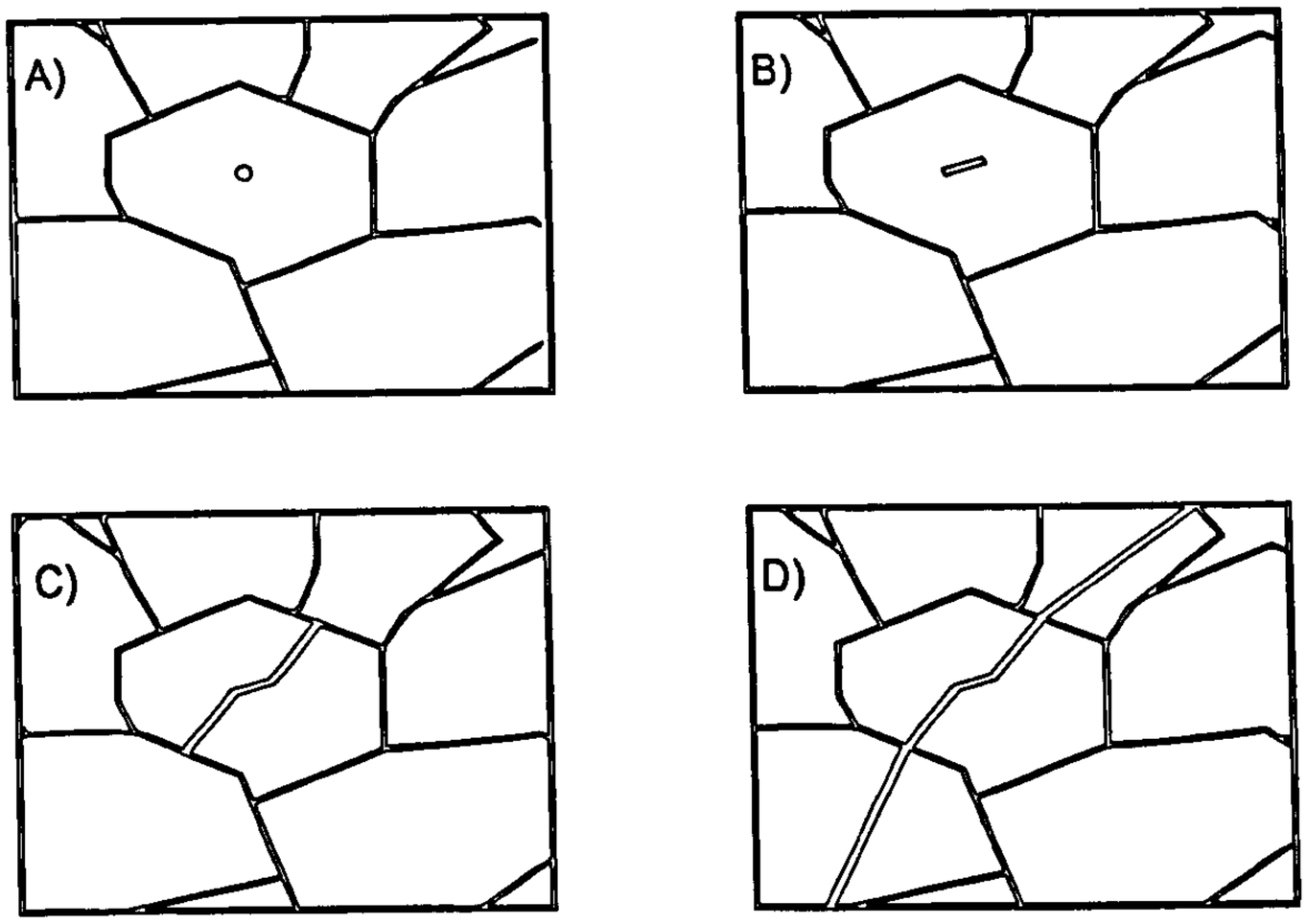

Figure 2.1: A) Material grain containing a defect nucleator B) Strain induced nucleation of a microcrack C) Propagation of microcrack through the material lattice D) Crack propagation over grain boundary into neighbouring grains.

This interpretation of very low temperature failure is called into question by the recent work of Chapuliot and Le Corré [19] where fatigue cracks were seen to propagate by cleavage at -253°C. The fact that stable cleavage crack growth was possible at this temperature suggests that micocrack nucleation is not the critical event for failure, even at very low temperatures. It is therefore likely that global failure is dependent on propagation of microcracks over grain boundaries.

2.2 Linear Elastic Fracture Mechanics (LEFM)

The starting point for the majority of modern fracture mechanics was the work of Inglis [20] and Griffith [21]. Inglis analysed the stress concentration at elliptical flaws and showed that the stress at the tip of such a flaw, σ_a, could be expressed in terms of the applied stress σ,

$$\sigma_a = 2\sigma\sqrt{\frac{a}{\rho}} \tag{2.1}$$

where a and ρ are the major dimension and minimum radius of curvature of the flaw, as shown in figure 2.2. This leads to an expression for the fracture

stress [22],

$$\sigma_f = \left(\frac{E\gamma_s}{4a}\right)^{1/2} \tag{2.2}$$

where E is Young's modulus, γ_s the energy required for creation of free surfaces and a, previously the major dimension of an elliptical flaw, can be interpreted as the length of a sharp crack-like defect.

Following this work, Griffith sought to rectify the difference between the empirical strength of materials and their theoretical strength, based on the attractive forces between atomic bonds. By assuming the presence of defects within materials, he showed that flaws produced stress concentrations which, in turn, lowered the effective macroscopic strength of the material. By balancing the strain energy surrounding the flaw with the energy needed to create new surfaces, and thus propagate the crack, the fracture stress becomes,

$$\sigma_f = \left(\frac{2E\gamma_s}{\pi a}\right)^{1/2} \tag{2.3}$$

assuming no dissipation of energy. The definition of equation 2.3 is only strictly suitable for pure brittle fracture, where a crack may propagate once energy is available to overcome the atomic bonds. In most materials, such as metals, some permanent deformation is likely to occur prior to this. Therefore, energy of dislocation movement should be included into the surface energy term such that $\gamma = \gamma_s + \gamma_p$, where the plastic term γ_p is generally dominant. Based on these models, which are in turn based on atomic bond strength, fracture can be seen to be a stress driven process.

Further work to better account for the dissipative effects of plastic deformation on fracture was undertaken by Irwin [23, 24], Orowan [25] and others, but will not be discussed here. A more detailed overview of such work may be found elsewhere [22].

2.3 Crack tip fracture parameters

Practical application of the concepts introduced by the early work into fracture mechanics required the formulation of a useful failure criterion that was applicable during the component design process. The most commonly used approaches tend to be based on the crack tip parameters K and J, often referred to as crack tip or 'global' fracture parameters as they serve to relate

external load to the stress field at the crack tip.

2.3.1 Stress intensity factor, K

The stress intensity factor originates from analytical solutions for the stress field around a sharp crack [26]. Using a series expansion, it can be shown that the stresses immediate to the crack tip are dominated by a $1/\sqrt{r}$ singularity such that as $r \to 0$, for an isotropic linear-elastic material,

$$\sigma_{ij}^{I} = \frac{K_I}{\sqrt{2\pi r}} f_{ij}^{I}(\theta) \tag{2.4}$$

$$\sigma_{ij}^{II} = \frac{K_{II}}{\sqrt{2\pi r}} f_{ij}^{II}(\theta) \tag{2.5}$$

$$\sigma_{ij}^{III} = \frac{K_{III}}{\sqrt{2\pi r}} f_{ij}^{III}(\theta) \tag{2.6}$$

where r and θ are crack tip coordinates, defined in figure 2.2 B. The superscripts I, II and III correspond to opening tensile, in-plane shear and out of plane shear loadings. Assuming that failure is driven by local stresses and that local stresses are controlled by a single parameter K, failure is deemed to occur (in mode I loading) when $K_I = K_{IC}$, where K_{IC} is the material fracture toughness. It should be noted that in general $K_{IC} \neq K_{IIC} \neq K_{IIIC}$ and K_{IC} is usually the lowest of the three as tensile failure tends to be the lowest energy failure mode. Experimental values of K_{IC} are commonly obtained using thick specimens to approximate plane strain conditions [27], with the intention of obtaining lower bound values. Under such conditions, local stresses are assumed to be given by

$$\sigma_{11} = \frac{K_I}{\sqrt{2\pi r}} \cos\frac{\theta}{2}\left(1 - \sin\frac{\theta}{2}\sin\frac{3\theta}{2}\right) \tag{2.7}$$

$$\sigma_{22} = \frac{K_I}{\sqrt{2\pi r}} \cos\frac{\theta}{2}\left(1 + \sin\frac{\theta}{2}\sin\frac{3\theta}{2}\right) \tag{2.8}$$

$$\sigma_{12} = \frac{K_I}{\sqrt{2\pi r}} \cos\frac{\theta}{2}\sin\frac{\theta}{2}\cos\frac{3\theta}{2} \tag{2.9}$$

2.3.2 The J integral

The J integral as suggested by Rice [28] and independently derived by Eshelby [29] can be obtained by evaluating the rate of change in potential energy, within

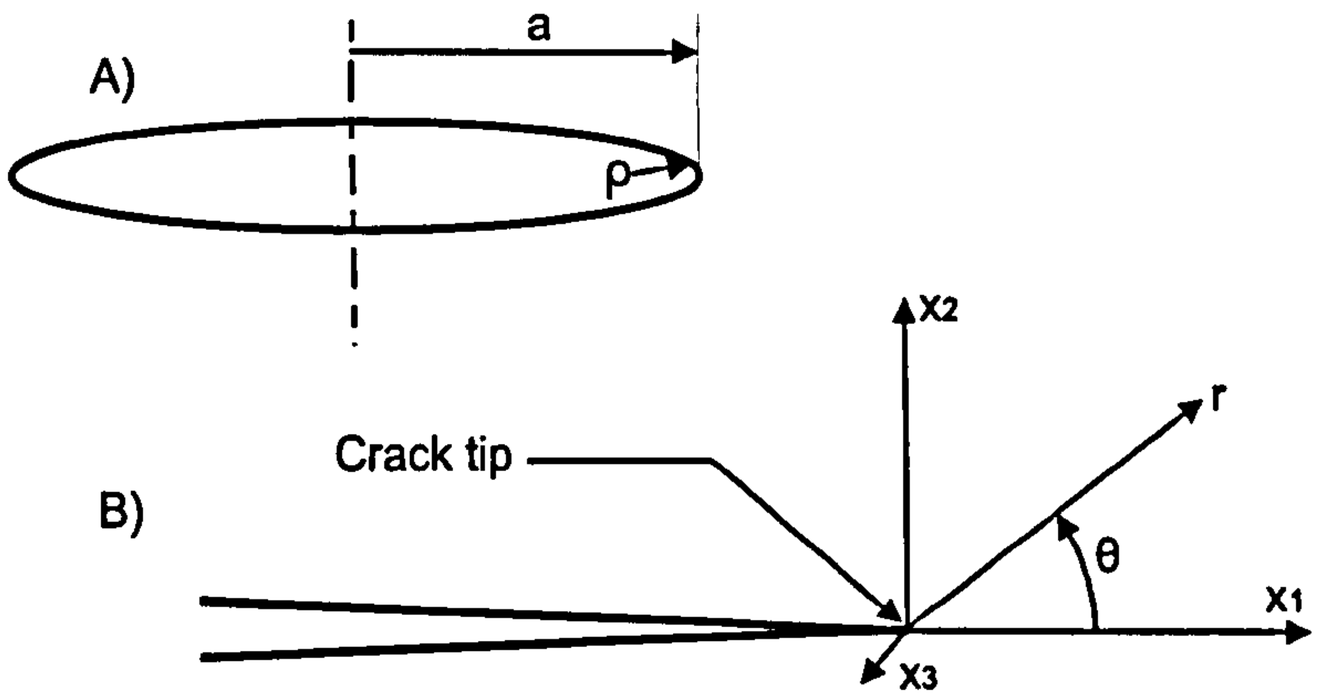

Figure 2.2: Nomenclature used for geometry of A) elliptical defect and B) region near a sharp crack

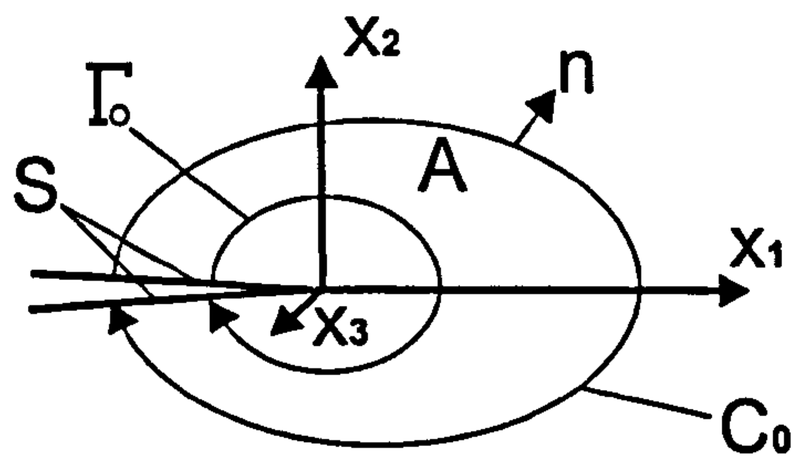

Figure 2.3: Notation for 2D contour integral

a region of material containing a singularity, during an infinitesimal change in the singularity's position. In the case of crack tip movement, this energy is assumed to be that needed for the creation of free surfaces. Ignoring kinetic energy and body forces, J is expressed as follows,

$$J = \lim_{\Gamma_0 \to 0} \int_{\Gamma_0} \left(W\delta_{kj} - \sigma_{ij} \frac{\partial u_i}{\partial x_k} \right) \eta_k n_j ds \tag{2.10}$$

$$W = \int^{\epsilon_{ij}} \sigma_{ij} d\epsilon_{ij} \tag{2.11}$$

where Γ_0 is a contour around the crack tip, indicated in figure 2.3, and W is strain energy density. This formulation relates to the extension of a sharp crack (i.e. movement of a stress/strain singularity) in the generalised x_k direction.

The term η_k is the component of assumed crack extension in the x_k direction, u_i is displacement in the x_i direction and δ_{kj} is Kronecker's delta. In the above integral dS represents integration about a contour, the outward normal of which is n. Using the divergence theorem, equation 2.10 can be expressed around a general contour C_0. Assuming the crack faces (S in figure 2.3) are traction free,

$$J = \int_{C_0} \left(W\delta_{kj} - \sigma_{ij}\frac{\partial u_i}{\partial x_k} \right) \eta_k n_j ds - \int\int_A \left(\frac{\partial W}{\partial x_k} - \sigma_{ij}\frac{\partial \epsilon_{ij}}{\partial x_k} \right) \eta_k dA \qquad (2.12)$$

where dA represents integration over the area enclosed by the contour C_0. If W is a single valued function of ϵ_{ij}, such as in elastic materials, and assuming W has no explicit dependence on x_k,

$$\frac{\partial W}{\partial x_k} = \frac{\partial W}{\partial \epsilon_{ij}}\frac{\partial \epsilon_{ij}}{\partial x_k} = \sigma_{ij}\frac{\partial \epsilon_{ij}}{\partial x_k} \qquad (2.13)$$

hence the area integral of equation 2.12 is zero and J can be evaluated as

$$J = \int_{C_0} \left(W\delta_{kj} - \sigma_{ij}\frac{\partial u_i}{\partial x_k} \right) \eta_k n_j ds \qquad (2.14)$$

with C_0 being any path starting and ending on opposite faces of the crack.

The path independence of J is crucial as it provides a single unambiguous value. It was shown by Begley and Landes [30, 31] that the values of J at onset of crack propagation are approximately constant under high constraint (i.e. plain strain) conditions and can therefore be used to predict fracture in such cases.

Unfortunately, equation 2.14 becomes path dependent for elastic-plastic materials. In addition, due to plastic dissipation, J can no longer be interpreted as the energy release rate of crack extension. Material behaviour may be expressed with the Ramberg-Osgood (RO) strain hardening law,

$$\frac{\epsilon}{\epsilon_Y} = \frac{\sigma}{\sigma_Y} + \alpha\left(\frac{\sigma}{\sigma_Y}\right)^n \qquad (2.15)$$

where σ_Y and ϵ_Y are the yield stress and strain and α and n are constants. For materials characterised by equation 2.15, it has been shown [32, 33] that J is the dominant characterising factor for the near-tip stress field in the same manner as K for a linear elastic material. The near tip stresses are then

approximated by,

$$\sigma_{ij} = \sigma_Y \left(\frac{EJ}{\alpha \sigma_Y^2 I_n r} \right)^{\frac{1}{n+1}} \tilde{\sigma}_{ij}(n, \theta) \tag{2.16}$$

commonly known as the HRR stress field. In equation 2.16, I_n is an integration constant and the function $\tilde{\sigma}_{ij}$ is the dimensionless variation of stress with angle.

Although the dependence of stress magnitude on J was derived for a non linear elastic material, the relationship holds for elastic-plastic materials as long as monotonic loading conditions are satisfied. If unloading occurs following plastic deformation, J no longer fully characterises the stress field in its standard form as W cannot be determined from the current strain state.

Domain formulation

The J integral is commonly evaluated from stress and strain fields determined using finite element analyses and as such a discrete form of the integral in equation 2.14 must be implemented. In such cases, numerical evaluation of a path integral can be prone to inaccuracies. It is therefore common to implement a domain integral, thereby reducing the effect of errors at any single gauss point or node on the calculation. Following Li et al [34], equation 2.14 around a closed contour C, where $C = C_0 + S + \Gamma_0$, can be expressed as an area integral via the divergence theorem.

$$J = \int \int_A \left[\left(\sigma_{ij} \frac{\partial \epsilon_{ij}}{\partial x_k} - \frac{\partial W}{\partial x_k} \right) q_k + \left(\sigma_{ij} \frac{\partial u_i}{\partial x_k} - W \delta_{kj} \right) \frac{\partial q_k}{\partial x_j} \right] dA \tag{2.17}$$

In this case, η_k is replaced by a smooth function q_k where $q_k = \eta_k$ on Γ_0 and $q_k = 0$ on the contour C_0. Multiplication by q_k makes the path integral around C equal to that around Γ_0. Where the surfaces S are traction free, this allows convenient conversion to an area integral. In the limiting case where $\Gamma_0 \to 0$, A is the area enclosed by the outer contour C and $q_k = \eta_k$ at the crack tip only. For proportional loading conditions, J can then be expressed.

$$J = \int \int_A \left[\left(\sigma_{ij} \frac{\partial u_i}{\partial x_k} - W \delta_{kj} \right) \frac{\partial q_k}{\partial x_j} \right] dA. \tag{2.18}$$

Calculation in the presence of incompatible strains

Incompatible strain is used here to describe any strains which do not conform to the current stress state, according to the material stress/strain response. This term encompasses plastic stains from prior material deformation, as well as thermal strains. Such incompatible strains are also commonly referred to as eigenstrains. The presence of an initial strain field causes the integral of equation 2.14 about a closed contour to be nonzero, hence removing path independence.

Many authors have proposed methods to account for thermal strain fields [35, 36, 37] and residual stresses [38, 39, 40, 41]. Decomposing the strain into mechanical (ϵ_{ij}^m) and initial (ϵ_{ij}^*) strains gives,

$$\epsilon_{ij} = \epsilon_{ij}^m + \epsilon_{ij}^* \tag{2.19}$$

Mechanical strain is the sum of the elastic and plastic strains and incompatible strains represent any 'non-mechanical' strains, such as thermal or initial state plastic strains. In general these two components can be defined as,

$$\epsilon_{ij}^m = \epsilon_{ij}^{el} + \epsilon_{ij}^{pl} - \epsilon_{ij}^{pl0} - \epsilon_{ij}^{th} \tag{2.20}$$

$$\epsilon_{ij}^* = \left(\epsilon_{ij} - \epsilon_{ij}^{el}\right)^0 + \epsilon_{ij}^{th} = \epsilon_{ij}^{pl0} + \epsilon_{ij}^{th} \tag{2.21}$$

$$W^m = \int^{\epsilon_{ij}^m} \sigma_{ij} d\epsilon_{ij}^m \tag{2.22}$$

where ϵ_{ij}^0 represents strain in the initial state and ϵ_{ij}^{th} refers to thermal strains. In general, the 'initial' material state should be taken as that of the body with pre-existing strains before the introduction of a crack [42]. It is worth noting that the initial state elastic strains are included in the modified work energy density term as elastic strain energy is recoverable and compatible with the current stress field. The definition of the initial state as that before crack introduction, rather than after introduction but before external loading, is chosen as it avoids difficulties in determining between plastic strains and work due to the initial strain state and the stress concentration at the crack tip.

Substituting these modified strain and work terms into equation 2.12 re-

sults in equation 2.23.

$$J = \int_{C_0} \left(W^m \delta_{kj} - \sigma_{ij} \frac{\partial u_i}{\partial x_k} \right) \eta_k n_j ds - \int \int_A \left(\frac{\partial W^m}{\partial x_k} - \sigma_{ij} \frac{\partial \left(\epsilon_{ij}^m + \epsilon_{ij}^* \right)}{\partial x_k} \right) \eta_k dA \tag{2.23}$$

For application in FE code, an equivalent domain integral is used. Following the same methodology as for equation 2.18,

$$J = \int \int_A \left[\left(\sigma_{ij} \frac{\partial u_i}{\partial x_k} - W^m \delta_{kj} \right) \frac{\partial q_k}{\partial x_j} + \left(\sigma_{ij} \frac{\partial \left(\epsilon_{ij}^m + \epsilon_{ij}^* \right)}{\partial x_k} - \frac{\partial W^m}{\partial x_k} \right) q_k \right] dA \tag{2.24}$$

It can be seen that if proportional loading is satisfied then equations 2.23 and 2.24 reduce to,

$$J = \int \int_A \left[\left(\sigma_{ij} \frac{\partial u_i}{\partial x_k} - W^m \delta_{kj} \right) \frac{\partial q_k}{\partial x_j} + \sigma_{ij} \frac{\partial \epsilon_{ij}^*}{\partial x_k} q_k \right] dA \tag{2.25}$$

which has been shown to be path independent for cases involving initial residual stresses [38, 43, 44] and thermal stress fields [36]. For cases involving non proportional loading, Lei [42] showed that equation 2.23 should be used. Equations 2.24 and 2.25 are equivalent for proportional loading. Therefore, if any doubt exists as to the nature of the loading, the most general version should be applied.

It should be noted that equation 2.10 can be applied in all cases, provided that it can be evaluated about a vanishingly small contour. In practice, the need to use finite element analyses to calculate J in complex structures means this is not feasible as the non-continuum deformation zone around the crack tip cannot be accurately modelled.

Physical meaning of contour integrals

The J integral can be interpreted as potential energy release rate per unit crack advance under elastic loading conditions. An alternative definition is provided by Eshelby [29, 45] who showed that using only elastic strains, the J integral represents the force on any inhomogenities or defects enclosed by the contour. The method of [29] is based only on elastic strains, giving the force

on elastic singularities as,

$$F_k = \int_{\Gamma_0} (W\delta_{kj} - \sigma_{ij}\beta_{ik})\,\eta_k n_j ds \tag{2.26}$$

where β_{ik} is the elastic distortion tensor such that the elastic displacements are given as $\delta u_i^e = \beta_{ik}\delta x_k$. This formulation was used as a basis for the prediction of the warm prestress effect by Chell [46, 47].

For a power law hardening elastic material, the value of J is often considered to provide a single valued characterising parameter for the crack tip stress fields [32, 33]. Provided local monotonic loading conditions are satisfied (W is a single valued function of strain), this definition holds for proportionally loaded elastic-plastic hardening materials.

Modified J values for use in generalised elastic-plastic conditions no longer have any clear physical meaning. Some studies [42] suggest that the use of the path independent form of J still holds as a characterising parameter, as in equation 2.16. However, elastic-plastic RO material properties were used in this analysis and equation 2.24 was unable to account for variations in constraint, therefore the validity of J as a characterising parameter for the stress field is not clear.

2.3.3 Two parameter models

In order for any model of fracture to be of use in avoiding failure, it is vital that results obtained from laboratory samples may be applied to in-service components, often referred to as 'similitude'. In practice, it is known that measured values of K and J at failure are strongly dependent on specimen geometry and load type [48, 49]. Such effects are generally grouped together under the term 'constraint' which is associated with the stress triaxiality in the fracture process region.

Constraint corrections to the stress intensity factor have evolved from the work of Williams [26] who suggested a series expansion for near tip stress fields. The first term of this expansion is characterised by K, however inclusion of the second term T has been shown to have a significant influence on the crack tip stress field and plastic region [50, 51]. For mode I loading the resultant plane strain stress field is

$$\sigma_{ij} = \frac{K_I}{\sqrt{2\pi r}} f_{ij}(\theta) + \delta_{i1}\delta_{1j}T + \delta_{i3}\delta_{3j}\upsilon T \tag{2.27}$$

where the 'T-stress' is the magnitude of the second term. It should be noted that equation 2.27 and the T parameter in general are the product of elastic analyses.

A similar approach for elastic-plastic stress fields was suggested by O'Dowd and Shih [52] who noted that the difference between the true stress state and a reference stress state was generally constant with angular position and distance from the crack tip for $-\pi/2 < \theta < \pi/2$. Furthermore, they noted that the difference for σ_{11} and σ_{22} was much greater than that for the shear stress σ_{12}. The approximate local stress field could then be determined with the addition of a constant hydrostatic shift, Q.

$$\sigma_{ij} \approx \sigma_{ref} + Q\sigma_Y\delta_{ij} \tag{2.28}$$

Where σ_{ref} is generally taken as that for which $T = 0$ or the HRR field solution of equation 2.16 and σ_Y is the yield stress. In practice, Q is usually defined as in equation 2.29.

$$Q = \frac{\sigma_{22} - (\sigma_{22,ref})_{T=0,r=2J/\sigma_Y,\theta=0}}{\sigma_Y} \tag{2.29}$$

Toughness values are commonly observed to follow either a $K-T$ or $J-Q$ locus [53]. However such two parameter methods, while providing useful information about changes to the near tip stresses, do not in themselves provide predictions for changes in measured fracture toughness. They may however be used in conjunction with micro-mechanical approaches to predict failure, for example determining Weibull stress in terms of J or K as in [54].

Measured plane strain fracture toughness K_{IC} is assumed to correspond to $T = 0$ and $Q = 0$ and cracks in a real component to $T < 0$. It is also assumed that K_{IC} is a minimum and will not decrease further with $T > 0$ [55], therefore using K_{IC} should produce conservative estimates of failure.

2.3.4 Strain energy density methods

Strain energy density was proposed by Sih and Macdonald as a fracture criterion [56]. Failure was deemed to occur when the value of strain energy per unit volume reached a critical value on a contour r_o about a crack tip. In this case r_o was defined as the contour surrounding the non-continuum region in the immediate vicinity to the crack tip (figure 2.4).

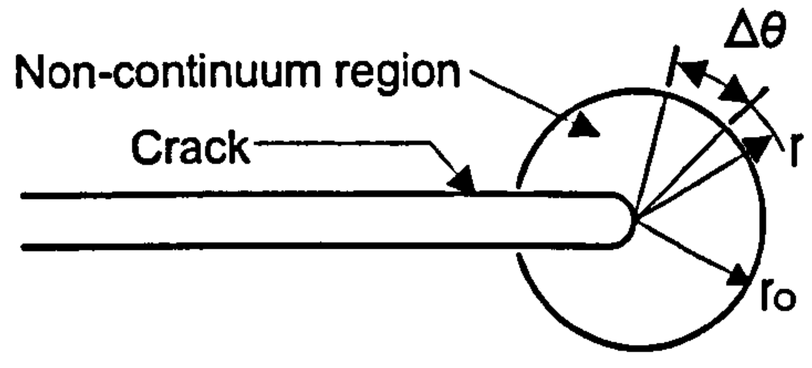

Figure 2.4: Nomenclature used for strain energy density criterion.

This method provides a prediction of crack propagation when S, the strain energy density (equivalent to W in equation 2.11), on r_o is equal to a critical value S_c. The direction of propagation was assumed to be that where $\delta S/\delta\theta = 0$. It was also stated in [56] that the strain energy density could be split into components, due to material volume change (S_v) and material distortion (S_d),

$$S = S_v + S_d \tag{2.30}$$

and that in general the region where $S_v > S_d$, i.e. where volume change was dominant over distortion, corresponded with the plane of crack propagation. The criterion has been applied to fracture under gross yielding conditions [57], assuming that the location of fracture was determined by the minimum value of S within the yielding region. The critical value of S, required for failure, was seen to be different for plastic and elastic material. This is unsurprising considering the dissipative nature of plastic deformation.

A similar method was applied by Chow and Xu [58] to predict mixed mode ductile fracture. It was suggested that the location of crack initiation was given by the location of maximum dilatational energy density, S_v^{max}. This approach was altered somewhat to include the influence of stress multiaxiality by Labeas and Kermanidis [59]. They defined a stress multiaxiality factor q as,

$$q = \frac{\sigma_e}{\sigma_h} \tag{2.31}$$

where σ_e is the effective or von-Mises stress and σ_h the hydrostatic stress. It is assumed in [59] that crack propagation occurs in the direction where q is a minimum (i.e. where $dq/d\theta = 0$). The core radius r_0 was defined as the distance from the tip to the point where q was a minimum (i.e. where hydrostatic stresses dominate over deviatoric components) and crack propagation was deemed to occur when $S = S_c$ at this point. This method was shown

to provide reasonable prediction of propagation load and direction as well as variation of crack extension with load.

The use of strain energy has been shown to have some potential as a fracture parameter under a range of conditions. There are some practical difficulties with definition of the core radius r_0 and the proper treatment of energy dissipated by plastic deformation. The use of volumetric strain energy does, however, suggest a link between hydrostatic stress and fracture initiation.

Influence of hydrostatic stress

The suggestion of maximum dilatational energy as a fracture criterion is generally in keeping with observed experimental trends. Measured fracture toughness is often higher for low constraint specimens. This can be explained in terms of a critical value for S_v as a greater fraction of the input work is dissipated by plastic flow rather than inducing volumetric change. Failure in cracked or notched specimens is seen to occur at the location of the crack tip or notch root and in the case of round notched bars it has been noted that fracture nucleates from the centre of the minimum cross section [60]. In all cases, failure is noted to occur where the stress state is highly triaxial; i.e. where the hydrostatic stress σ_h and therefore S_v ($S_v \propto \sigma_h^2$) is highest.

Specimens with shallow and deep cracks were studied by Matsoukas [61]. Crack opening displacement at failure was observed to decrease as σ_h at the crack tip rose. Analyses of Bridgeman type tensile specimens [60, 62] showed a clear reduction in failure strain with increasing hydrostatic stress.

Kao and co-workers showed [63] that the ductility of 1045 stainless steel tensile test specimens increased significantly with ambient hydrostatic pressure. It was proposed that under varying levels of ambient pressure, the failure mechanism may also change. Similar results were shown in 7075 aluminium alloy by Auger and Francois [64].

In terms of the Beremin type local approach (section 2.4.1) it has been reported [65, 66, 67, 68] that, using maximum principal stress σ_1 to control local crack propagation, the method is insensitive to biaxial loading. Use of local hydrostatic stress σ_h resulted in correct prediction of the reduction in failure load under biaxial conditions. Defining the constraint parameter Q based on deviations in hydrostatic stress, rather than crack opening stress as in equation 2.29, has been shown to improve prediction of constraint change and multiaxial loading [67, 68].

It appears that material failure by fracture may be strongly linked to levels of hydrostatic stress and therefore local volume change. Physically, levels of volumetric strain and hydrostatic stress have a strong influence on void growth [69] and differing hydrostatic stress fields have been proposed as a cause for differing apparent fracture toughness under differing loading regimes [70].

2.4 Local approach models

2.4.1 The Beremin model

Perhaps the best known and most widely used of the local approach methods is that proposed by Beremin [71]. The model is based on the assumption that fracture is nucleated at carbides or other similar inclusions which fail according to equation 2.3. The variation of inclusion sizes is assumed to be given by a power law distribution with constants ξ and β,

$$p(l) = \xi l^{-\beta}, \quad \beta > 1 \tag{2.32}$$

where $p(l)$ is the probability density function (PDF) for existance of an inclusion of size l in a given volume V_0. The probability of an inclusion of some critical size l_c occurring is then given by

$$P(l \geq l_c) = \int_{l_c}^{\infty} p(l)dl = \frac{\xi}{\beta - 1} l_c^{1-\beta} \tag{2.33}$$

Using equation 2.3, critical tensile stress for fracture is inversely proportional to the square root of defect size. Substituting this relationship into the above equation gives the probability of inclusion failure Pf, in a given volume δV,

$$Pf_{\delta V} = \frac{\sigma_1^{2(\beta-1)}}{k(\beta - 1)} \frac{\delta V}{V_0} \tag{2.34}$$

where σ_1 is the maximum principal stress and k the constant of proportionality between σ_1 and $1/\sqrt{l_c}$. Assuming a weakest link theory of failure, such that component failure occurs when microcrack propagation at any carbide occurs, allows the overall failure probability to be written as

$$Pf = \prod_i^N \left(1 - \left(\frac{\sigma_1}{\sigma_0}\right)^m \frac{\delta V}{Vo}\right) \tag{2.35}$$

where $m = 2(\beta - 1)$ and σ_0 is a normalising constant given by $\sqrt[m]{k(\beta - 1)}$. In the product notation, i is a given element of volume and N is the total number of volume elements. Provided that $Pf_{\delta V}$ (the probability of fracture in any single volume element) is small, the overall fracture probability may be approximated to

$$Pf = 1 - \exp\left(-\left(\frac{\sigma_w}{\sigma_0}\right)^m\right) \tag{2.36}$$

where σ_w, often termed the 'Weibull stress' is given by

$$\sigma_w = \left(\frac{1}{V_0}\int_V \sigma_1^m dV\right)^{1/m} \tag{2.37}$$

It is also assumed that plastic strain is necessary for nucleation of microcracks, such that the integration volume in equation 2.37 is taken to be all material regions where plastic strain is non-zero. However, some authors have proposed that if microcracks are not propagated upon nucleation then blunting occurs such that they will not propagate under subsequent loading. It is therefore suggested that the integration volume V should include only regions where yielding is currently occurring. The active volume V_a can then be defined as all regions where the equivalent plastic strain is an increasing function of time (or a time-like variable, i.e. load).

$$\frac{d\epsilon_e^{pl}}{dt} > 0 \tag{2.38}$$

This has been shown to improve the accuracy of predictions of the Beremin model under conditions where non-proportional loading occurs, such as in warm prestressing [72, 73] or where residual stress due to prior loading must be considered [74].

Introduction of thresholds to the Beremin approach

A number of authors have proposed modifications to equations 2.36 and 2.37 to improve the accuracy and applicability of the Beremin model. One of the most widely used variants is that proposed by Gao and co-workers [75] who suggested that prediction of fracture could be improved by the addition of a threshold into the Weibull distribution of equation 2.36. This addition originates from another statistical model, based on stress intensity factor K,

as proposed by Wallin [76] and produces the following probability distribution.

$$Pf = 1 - \exp\left(-\left(\frac{\sigma_w - \sigma_{w,min}}{\sigma_0 - \sigma_{w,min}}\right)^m\right) \tag{2.39}$$

In [75] it is acknowledged that the addition of the threshold Weibull stress, $\sigma_{w,min}$, does not have a rigorous physical justification. However it can be interpreted as a parameter acknowledging the need for high stresses, in an volume covering multiple material grains, to propagate cracks over grain boundaries. A similar model, proposed by Bakker and Koers [77] to account for fracture behaviour in the ductile-brittle transition (DBT) region alters the definition of Weibull stress to

$$\sigma_w = \sigma_{w,min} + \left(\frac{1}{V_0}\int_V (\sigma_1 - \sigma_{w,min})^m \, dV\right)^{1/m} \tag{2.40}$$

with the probability function remaining as in equation 2.39. The inclusion of the threshold in the calculation of σ_w suggests a threshold stress for initial propagation of micro defects, rather than propagation of microcracks over grain boundaries.

A similar formulation is proposed by Xia and Shih [78] such that the Weibull stress is determined by

$$\sigma_w = \left(\frac{1}{V_0}\int_V (\sigma_1 - \sigma_{th})^m \, dV\right)^{1/m} \tag{2.41}$$

The formulation of equation 2.41 is not a strictly rigorous threshold in terms of the original probabilistic model. A maximum size may be assumed to exist for local defects or inclusions. This may be due to a maximum occurring defect size or an assumption that large defects will fail when the surrounding matrix stress is too low for resulting microcracks to propagate over grain boundaries. Introducing a maximum defect size, l_{th}, into the integral of equation 2.32 results in,

$$P(l \geq l_c) = \int_{l_c}^{l_{th}} \xi l_0^{-\beta} dl_0 = \frac{\xi}{\beta - 1}\left(l_c^{1-\beta} - l_{th}^{1-\beta}\right) \tag{2.42}$$

which leads to.

$$\sigma_w = \left(\frac{1}{V_0}\int_V (\sigma_1^m - \sigma_{th}^m)\, dV\right)^{1/m} \tag{2.43}$$

Equation 2.43 allows justifiable incorporation of a 'local' threshold stress, σ_{th}, corresponding to the minimum local stress required to propagate microcracks

from a defect. Practically, when evaluated from finite element results, $\sigma_1^m - \sigma_{th}^m$ is an averaged value over an element volume and so may be equally be interpreted as a threshold stress for propagation over grain boundaries.

Although physically easier to justify, the threshold formulation of equation 2.43 raises difficulties in the calibration of the value of σ_{th}, hence equation 2.39 has been more commonly used. The use of equation 2.43 may be justified in cases where

$$\begin{aligned} \left(\int_{V_{th}} (\sigma_1^m - \sigma_{th}^m)\, dV\right)^{1/m} &\approx \left(\int_V \sigma_1^m dV\right)^{1/m} - \sigma_{w,min} \\ \rightarrow \sigma_{th}^m V_{th} &\approx \sigma_{w,min}^m \end{aligned} \tag{2.44}$$

with V_{th} representing the active volume where $\sigma_1 > \sigma_{th}$. Physically, the use of a threshold Weibull stress may be justified in cases where the volume active in the fracture process remains approximately constant.

Multiple defect distributions

An alternative interpretation of the Beremin-type local approach, conceived to deal with intergranular brittle fracture, was proposed by Yahya *et al* [79] who noted that a bi-modal distribution was sometimes observed in failure data, and postulated that this could be attributed to failure originating from two competing defect populations. They reasoned that failure at coarse defects, such as MnS inclusions in ferritic steels, could occur at low loads in regions where global yielding had not yet occurred. In addition, it was assumed that failure at smaller inclusions occurred only at higher stresses in regions where a degree of plasticity was required to nucleate local micro-cracks. This leads to a global failure probability of the form

$$Pf = 1 - \exp\left(-\int_V \left(\frac{\sigma_1}{\sigma_{01}}\right)^{m_1} \frac{dV}{V_0} - \int_{V_{pl}} \left(\frac{\sigma_1}{\sigma_{02}}\right)^{m_2} \frac{dV}{V_0}\right) \tag{2.45}$$

where m_1 and σ_{01} correspond to failure at coarse inclusions, assumed to be possible any point in the sample volume V, and m_2 and σ_{02} relate to failure at smaller inclusions, occurring only in the plastically deformed volume V_{pl}.

2.4.2 Strain controlled models

A number of authors have suggested alternative models for fracture, based on local strains as well as stresses, thereby moving away from a criterion based solely on Griffith type fracture. Such a modification was suggested by Beremin [71] who noted that the apparent strength of A508 ferritic steel, according to equation 2.37, increased with plastic strain. Based on experimental observations, a modified definition of σ_w was proposed,

$$\sigma_w = \left[\frac{1}{V_0}\int_V \left(\sigma_1 \exp\left(-\frac{\epsilon_1}{2}\right)\right)^m dV\right]^{1/m} \tag{2.46}$$

where ϵ_1 is the local strain in the direction of the maximum principal stress (not necessarily equal to the maximum principal strain following plastic deformation). The same formulation was employed by Kantidis [80, 81] for intergranular fracture of A533B ferritic steel. The increase in local fracture stress was interpreted in [71] as a result of an increased density of barriers to microcrack propagation. Increasing dislocation density with plastic strain is assumed to cause a reduction in the 'effective' grain size, i.e. the distance a newly propagated microcrack can advance before encountering a barrier.

Kroon and Faleskog [82, 83] assumed that plastic strain served to increase the number of defects in a given volume by increasing the number of nucleated microcracks. The local failure probability is then a function of the local stress and number of local defects, which is a function of local strain,

$$Pf_{\delta V} = h\left(\sigma_1, \epsilon\right)\frac{\delta V}{V_0} = h_1(\epsilon)h_2(\sigma_1)\frac{\delta V}{V_0} \tag{2.47}$$

In [82] it was assumed that the PDF for size of the local defect population followed an exponential law such that,

$$p(l) = \frac{1}{\alpha}\exp\left(-\frac{l_0}{\alpha}\right) \tag{2.48}$$

where α is a normalising constant. Following the same method used to obtain equation 2.36 and introducing a threshold maximum defect size, as in equation 2.42, leads to

$$h_2(\sigma_1) = \left(\exp\left(\frac{\sigma_0}{\sigma_1}\right)^2 - \exp\left(\frac{\sigma_0}{\sigma_{th}}\right)^2\right) \tag{2.49}$$

It was assumed that the number of nucleated microcracks was a linear function

of equivalent plastic strain. Global fracture probability then becomes

$$Pf = 1 - \exp\left(-\int_V C\epsilon_e^p \left[\exp\left(\frac{\sigma_0}{\sigma_1}\right)^2 - \exp\left(\frac{\sigma_0}{\sigma_{th}}\right)^2\right] \frac{dV}{V_0}\right) \tag{2.50}$$

where ϵ_e^p is the equivalent or von-Mises plastic strain and C is a constant relating nucleation of defects to ϵ_e^p.

In [82] it was also proposed that σ_1 should be replaced with an averaged value over some local volume. This suggests that the average stress, over some distance from the microcrack in question, must be sufficiently high in order for it to propagate past local boundaries to failure. This is similar to the inclusion of a critical distance r_0 in RKR fracture theory [84]. Therefore, in addition to the parameters C, σ_{th} and σ_0, an averaging length scale L must also be determined.

A similar argument for defect nucleation was employed by Gao and co-workers [85], assuming a power law distribution of microcracks as in equation 2.36, resulting in an alternative definition of Weibull stress.

$$\sigma_w = \left(\frac{1}{V_0}\int_V \epsilon_e^p \sigma_1^m dV\right)^{1/m} \tag{2.51}$$

A thorough experimental investigation of the local stress and strain field at the initiation point of brittle fracture was undertaken by Hohe [16, 86]. Using finite element analysis and SEM inspection of fracture surfaces, it was noted that fracture initiated at points were local stress was unchanging with time. It was therefore suggested that strain criteria must also be accounted for when predicting local fracture probabilities. Based on these results, a criterion for microdefect nucleation was suggested as

$$\ln \epsilon_{pl} \leq \left(a\frac{\sigma_h}{\sigma_e} + b\right) \tag{2.52}$$

with a and b being constants. Equation 2.52 states that in the presence of plastic deformation, triaxiality must be sufficiently high for critical defects to nucleate without blunting due to the plastic deformation. It was also shown in [86], as well as in [85] that inclusion of strain to control defect nucleation improved model agreement with experimental data.

2.4.3 Incremental formulations

Considering loading to failure as an incremental process allows the contribution of each volume element to the change in overall fracture probability to be interpreted as shown in figure 2.5

An alternative definition for the function $h(\sigma_1, \epsilon)$, as in equation 2.47, has been proposed by Bordet and co-workers [87] who explicitly considered the probability of microcrack nucleation and ensuing propagation. The probability of nucleation over the strain increment $\delta\epsilon_e^p$ was given as

$$P_{nucl} \propto \frac{\sigma_Y}{\sigma_{Y0}} \exp\left(-\frac{\sigma_Y}{\sigma_{Y0}} \frac{\epsilon_e^p}{\epsilon_{e,0}^p}\right) \delta\epsilon_e^p \tag{2.53}$$

where σ_Y is the yield stress, dependent on temperature and strain rate, σ_{Y0} is the yield stress at a temperature T_0 and $\epsilon_{e,0}^p$ is a reference equivalent plastic strain. Using the local threshold formulation as given in equation 2.43, the probability that a microcrack is nucleated and propagated is given by

$$P_{cleav} = \int_0^{\epsilon_e^p} C \frac{\sigma_Y}{\sigma_{Y0}} \exp\left(-\frac{\sigma_Y}{\sigma_{Y0}} \frac{\epsilon_e^p}{\epsilon_{e,0}^p}\right) (\sigma_1^m - \sigma_{th}^m)\, d\epsilon_e^p \tag{2.54}$$

with the necessary calibration constants being $C, \sigma_{Y0}, \epsilon_e^p, \sigma_{th}$ and m. The global fracture probability is expressed by

$$Pf = 1 - \exp\left(-\int_V \int_0^{\epsilon_e^p} C \frac{\sigma_Y}{\sigma_{Y0}} \exp\left(-\frac{\sigma_Y}{\sigma_{Y0}} \frac{\epsilon_e^p}{\epsilon_{e,0}^p}\right) (\sigma_1^m - \sigma_{th}^m)\, d\epsilon_e^p dV\right) \tag{2.55}$$

An alternative method, also based on variations across an increment of strain, has been suggested by Stőckl *et al* [88]. They described the change in failure probability across a load increment as,

$$\Delta Pf = 1 - \exp\left(\int_V \frac{\Delta\epsilon_e^p}{\Delta\epsilon_{e,0}} \exp\left(-\frac{\epsilon_e^p}{\epsilon_{e1}}\right) \left(\frac{\bar{\sigma_1}}{\sigma_0}\right)^m \frac{dV}{V_0}\right) \tag{2.56}$$

where $\epsilon_{e1}, \Delta\epsilon_{e,0}, m$ and σ_0 are material constants. The exponential term within the integral, as in equation 2.55, represents the decreasing number of unbroken carbides as strain increases with the linear dependence on ϵ_e^p describing the increasing number of nucleated microcracks. The stress term $\bar{\sigma_1}$ is the mean value of σ_1 over the load increment and the global failure probability at load increment n is given by $Pf_n = Pf_{n-1} + \Delta Pf(1 - Pf_{n-1})$.

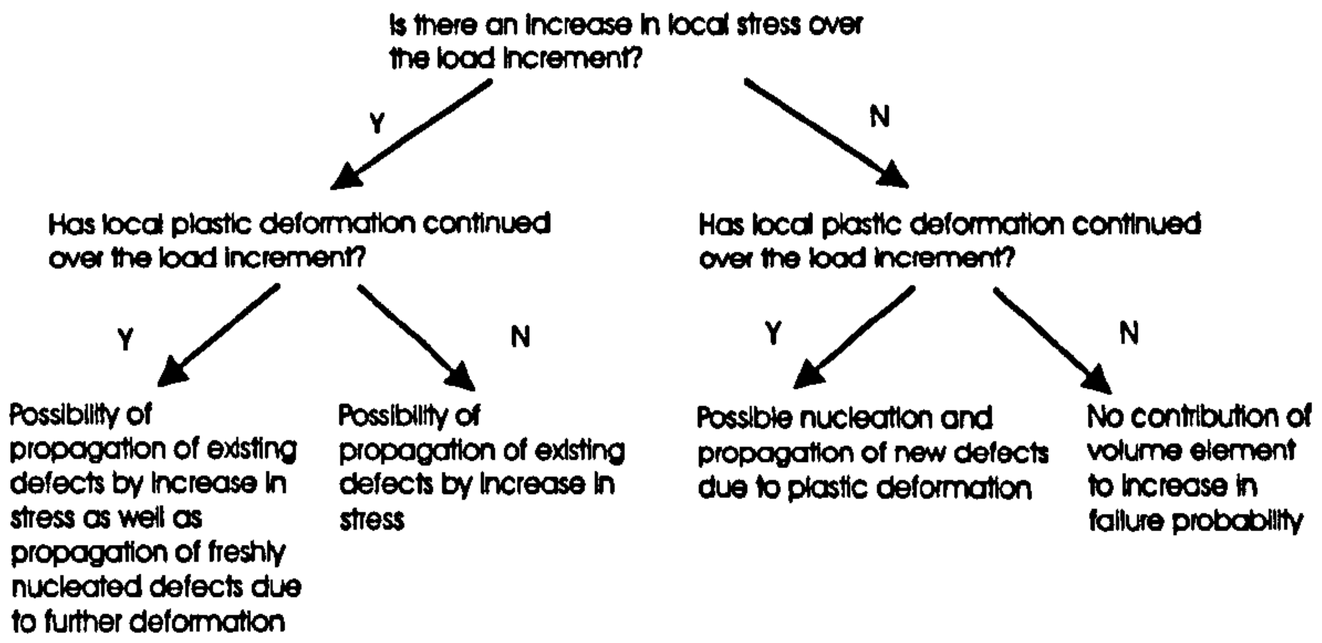

Figure 2.5: Effects of local incremental stress and strain changes on incremental failure probability

2.5 Influence of strain on fracture

The effects of plastic strain on material behaviour are numerous. In general, material yield stress is increased with plastic strain in engineering materials. For components under load, the result will be to inhibit yielding and thereby increase peak stresses. A review of the effect of load history on fracture by Smith [89] concluded that there was no clear trend in experimental results for the effect of prestrain on brittle fracture.

In terms of fracture behaviour, the effect of cold work is dependent on the failure mechanism and specimen type. The effect on experimental fracture parameters can be strongly affected by the method of determination and measured effects are not always aligned with the change in strength at a micromechanical scale.

2.5.1 Effect on J, K and COD at failure

A number of authors have investigated the effect of room temperature prestrain on fracture behaviour at room temperature and low temperatures. In general, increasing cold work results in a reduction in measured values of crack tip opening displacement δ_C (CTOD), K_{IC} and J_{IC} at failure. Such findings have been reported in steels [90, 91, 92, 93, 94] and aluminium [95].

Other authors [96, 97, 98] have noted varying increasing and decreasing K_{IC} and J_{IC} with increasing levels of prior strain. A decrease in CTOD at failure with strain was noted by Clayton [99] however K at failure, calculated

via $K = (2\delta_C \sigma_Y E)^{0.5}$, was seen to rise then fall with increasing prestrain.

When comparing findings from various authors, it is difficult to draw firm conclusions based on K and J values. Experimental methods used to determine values may produce apparent variations in strength with strain levels that are not manifested at a micromechanical scale. For example, work hardening increases yield stress and thus reduces plastic deformation near the crack tip, thereby reducing δ_C. This may result in a critical fracture stress being reached at a lower applied load, manifested as a lower K_{IC}. This would suggest a reduced material fracture resistance when the local fracture stress is in fact unchanged. Predictions of varying K_{IC} based on local fracture stress [95] suggest that this may be the case.

The apparent increase and decrease in fracture toughness seen by many authors was suggested to be related to the number of mobile dislocations [96]. It was suggested that where mobile dislocation density increases, crack tip blunting may occur more readily, thus increasing fracture load. This is in part supported by results for materials showing yield point elongation [97, 90] where prestrain in the discontinuous yielding region results in increasing measured toughness. When work hardening begins to occur, i.e. where dislocation movement becomes limited, the measured J_{IC} values begin to decrease. An investigation into the variation of dislocation structure with prestrain [100] drew similar conclusions.

2.5.2 Effect on fracture stress

While variations in J_{IC} and K_{IC} with prestrain have corresponded to fracture at room temperature, i.e. ductile modes of failure, the effects on fracture stress and local approach predictions have generally been investigated for low temperature brittle fracture.

Groom and Knott [101] tested notched bend specimens with varying degrees of cold work and found that increasing prior strain increased the fracture stress σ_f for cleavage failure, as well as an increase in the apparent effective surface energy for fracture. Sandstrom and co-workers [102] also noted an increase in σ_f, based on similar notched bend tests. The effective surface energy was found in [102] to be near-independent of the level of strain. The dependence noted in [101] was attributed to an incorrect assumption for the effective shear stress acting on dislocations.

Tests by Margolin and co-workers [103] also showed an increase in cleavage

fracture stress for monotonic prestrain but no clear relationship between σ_f and accumulated strain during cyclic preloading. Similar rises in σ_f with strain were also reported by Beremin [104] and Groom [101]. A notable exception is the work of Reed and Knott [105] which suggested decreasing cleavage fracture stress with increasing prior strain.

For interganular brittle fracture in notched tensile specimens, Kantidis et al [80] found that prestrain increased σ_f, determined from finite element analyses. Yahaya et al. [79] submitted smooth specimens to cyclic prestrain and found the fracture stress to be near independent of the cumulative prestrain.

2.6 Conclusions

Although two parameter approaches and the expansion of J to non proportional loading regimes may improve the scope of applicability of crack tip fracture parameters, there are inherent limitations that cannot be escaped.

The usual justification for both J and K as fracture parameters is that fracture is stress controlled and the stress field in the region contributing to failure is characterised by these parameters. However both are essentially two dimensional parameters, generalised to three dimensions by assuming plane stress or plane strain, and as such offer no interpretation of the effects of out of plane stresses apart from their indirect influence on stresses in the $x1 - x2$ plane. The assumed structure of the stress fields due to series expansions may also be violated by multiaxial loading, local variations in yield stress due to work hardening and any pre-existing residual stress fields.

Local approach methods appear to offer a framework for accounting for such effects as no prior assumptions are necessary about the nature of the local stress field. This means that two specimens with greatly differing global stress fields may have the same value of σ_w and therefore probability of failure. Local approaches also offer the ability to directly predict the effect of constraint change on fracture [68].

The formulation of an appropriate local approach parameter for general, non proportional elastic-plastic loading is still unclear and appropriate calibration of model parameters is an open issue. Correct calibration is essential for transferability of Weibull stress type values [106], therefore reliable and repeatable calibration methods are an absolute necessity.

Global parameters such as J are still useful from a practical point of view as K_{IC} may be reasonably determined from a smaller number of tests than needed for reliable Weibull parameter calibration. Many common SI assessment codes are also formulated with K_{IC} values in mind [107] and, as such, assessments are inherently conservative [108]. Coupled with the availability of many analytical solutions for K, there is often no need for the additional complication of local approach methods.

Nonetheless, the current need to reduce conservatism to prolong life, and future need to reduce over design, especially in transport applications, point to the use of the local approach to fracture for more accurate transference of laboratory specimen results to complex in-service situations. Furthermore, there also appears to be an increasing body of evidence for accounting for hydrostatic stress and local strain effects in local approach methods to improve their predictive capabilities for multiaxial and non-proportional loadings.

Chapter 3

Effects of specimen extraction on measured fracture toughness

3.1 Introduction

As K_{IC} is often used as a critical measure of material fracture resistance, it is important that the value of K_{IC} (or more properly the distribution of values) for the material in question is well known.

Even for well characterised materials, it is well documented that physical properties may change during service. Repeated thermal and mechanical load cycles, irradiation, hydrogen embrittlement and corrosion are known to contribute to such changes. To obtain current K_{IC} values for material exposed to such load histories, samples may be extracted from ex-service components or specimens exposed to similar conditions in a laboratory environment.

When these altered material samples are tested, it is often assumed that the fracture specimens are small enough to be stress free, regardless of the residual stress state in the original 'parent' component. If this is not the case, the measured K_{IC} (and indeed any other mechanical property) may be adversely affected.

In a fracture assessment, residual and applied stresses may be accounted for using, for example, a modified J integral [74]. If the material K_{IC} or J_{IC} used for comparison is also affected by residual stresses, the resulting assessment is in danger of 'double accounting' - including the effects of residual

stress as an increased crack driving force K and a reduced toughness K_{IC}. This may lead to overly pessimistic estimates of a safe operating load. To investigate the potential severity of such a situation, experimental specimens were fabricated to investigate the relaxation of stresses in extracted fracture toughness specimens. Further to the possibility of unrelaxed stresses, there is an increasing body of evidence highlighting the effect of plastic strain history on ensuing fracture behaviour, as discussed in chapter 2.

Methods of stress measurement by material removal and measurement of resultant strain relaxation are almost exclusively based in elastic superposition and therefore offer no insight into plastic strain levels. To investigate levels of plastic deformation it is necessary to use methods based on smaller scale phenomena such as diffraction techniques. Plastic strain history has been investigated using a number of methods including X-ray diffraction [109] and electron back scatter diffraction [110]. From an engineering perspective, neutron diffraction is the most attractive prospect due to the superior penetration of neutrons in many common structural alloys. The feasibility of using neutron diffraction data to measure plastic deformation was investigated in this work using prestrained samples fabricated from an A533B ferritic steel, as used in the fracture tests detailed in chapter 5.

3.2 Specimen fabrication

To obtain accurate estimates of the residual stresses remaining after specimen extraction from industrial components, the choice of 'parent' component for extraction of test specimens was carefully considered. Welding processes often prompt fracture assessments on in-service components as welding is commonly employed to repair cracked components which are not easily replaced. Examples may be found in power generation or petro-chemical applications where large structural components must be repaired to prolong the life of existing infrastructure. A typical repair weld process is shown in figure 3.1.

Welding produces highly complex three dimensional residual stress states, in addition to affecting material properties in the near weld region through significant heating. Determination of weld material fracture behaviour is a common motivator for extraction of fracture specimens. Large scale welded components were therefore selected from which to extract small samples for measurement. Two variants were chosen in this case - one to represent a

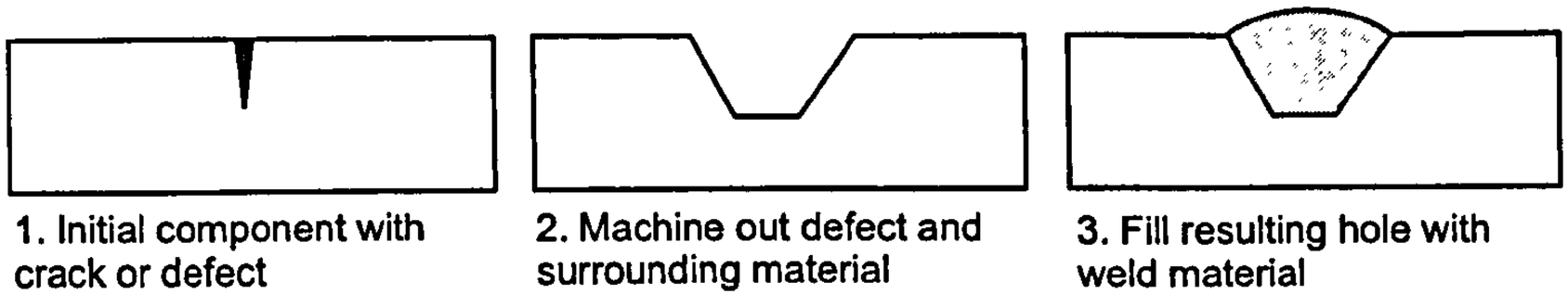

Figure 3.1: Example of a typical repair welding process

situation where one would expect to see significant stresses remaining and one where the remaining stresses were expected to be minimal.

3.2.1 Parent specimens

The first component chosen was a large repair welded plate, manufactured from P275 ferritic steel. This plate was previously examined by Brown and co-workers [111], where fabrication details may be found. The 'letterbox' repair weld in the plate was of considerable size, as shown in figure 3.2. This component was chosen as it would permit extraction of specimens of standard CT specimen size (62.5×60×25mm) consisting almost entirely of weld material. Previous measurements suggested the membrane component of the stress field was dominant in this region. Considering the relatively small size of the extracted sample, in comparison to the original plate, it was hoped the extraction process would relax the majority of the internal stresses.

The second parent component was selected to maximise the residual stress field remaining in the extracted samples, thus approximating a 'worst case scenario' for extraction from a real component. In this case an autogenously welded plate, manufactured from 316L austenitic stainless steel, was chosen such that specimens could be extracted containing the entire weld cross section.

An autogenous weld was selected in order to minimise the complexity of numerical modelling of the welding process by removing the need to simulate the deposition of weld filler material. An austenitic steel was selected for the plate material to further simplify matters by removing the effects of any material phase change such as would be expected in a ferritic steel. Using a reduced weld size in the autogenous weld specimens, the aim was to ensure that as much of the initial residual stress field as possible remained self-balancing across the extracted region. The intention was to minimise the relaxation of

stress during the extraction process.

The specimen dimensions, illustrated in figure 3.3, were chosen to allow comparison with previously reported work on welded austenitic steel plates [112]. All specimens were cut from a larger 20mm thick plate before heat treatment (in air for one hour at 1050°C and then furnace cooled). This was intended to ensure even material properties throughout the samples as well as relieving any residual stress built up in the plates prior to welding.

To confirm the stress/strain curves used for the FE modelling, tensile test specimens were cut from one of the plates in the post-annealed state. Tensile tests were carried out according to ASTM standards [113]. A plot of the assumed material stress strain behaviour, taken from [114], and the measured stress/strain behaviour is presented in figure 3.4.

Two specimen types were manufactured; with welds running the full length of the plate as well as with a weld of length 60mm at the plate centre, as illustrated in figure 3.3. In all cases, Argon shrouded TIG welding was employed with no filler material used. During welding, the plates were placed on top of a polymer foam material to minimise heat loss by conduction. No additional restraint or clamping was employed during the welding, allowing the specimens to deform freely during welding and cooling.

A total of four partially welded specimens and four fully welded specimens were manufactured. One specimen of each type was instrumented with a number of thermocouples and a strain gauge in order to record temperature and strain variations during the welding process. Positions of the thermocouples and strain gauges, in the coordinate system of figure 3.3, are given in table 3.1. The velocity of the weld arc was kept constant throughout the welding process with the arc being sparked and shut off at the designated weld start and stop positions. As such, the dwell of the arc at either end was assumed to be negligible. In the case of the fully welded specimens, run-out plates were attached at either end of the weld so that the arc could be initiated and shut off in this scrap material, ensuring consistent heating across the length of the final specimens. Weld parameters are displayed in table 3.2.

3.2.2 Extracted specimens

The extracted samples were selected such that they would be 'blanks' of suitable size to be machined to standard CT fracture specimen geometries as detailed in chapter 5. In the case of the 316L plate, two specimens were ex-

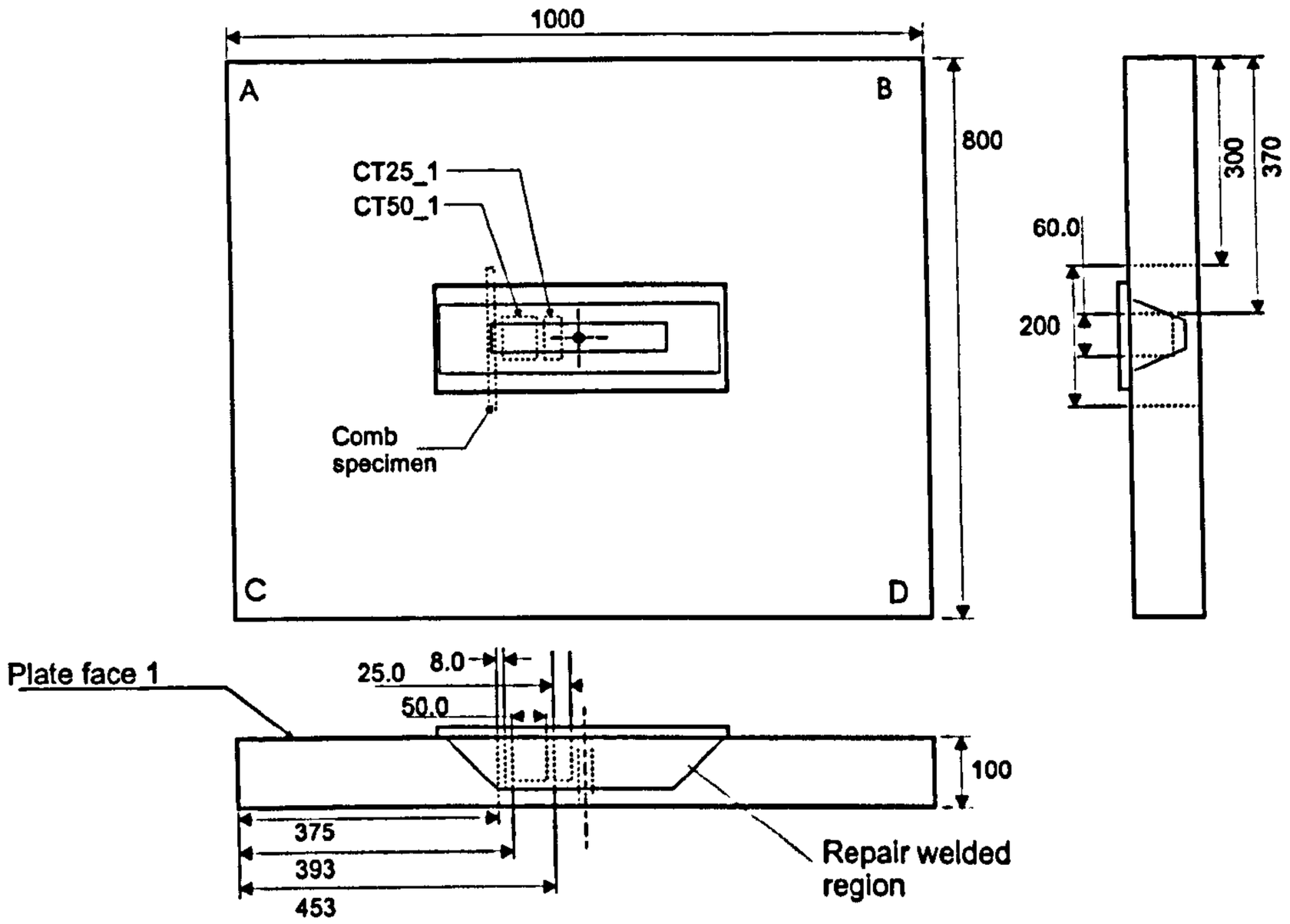

Figure 3.2: Geometry and extracted specimen locations for letterbox repair welded P275 ferritic steel plate. Dimensions in mm.

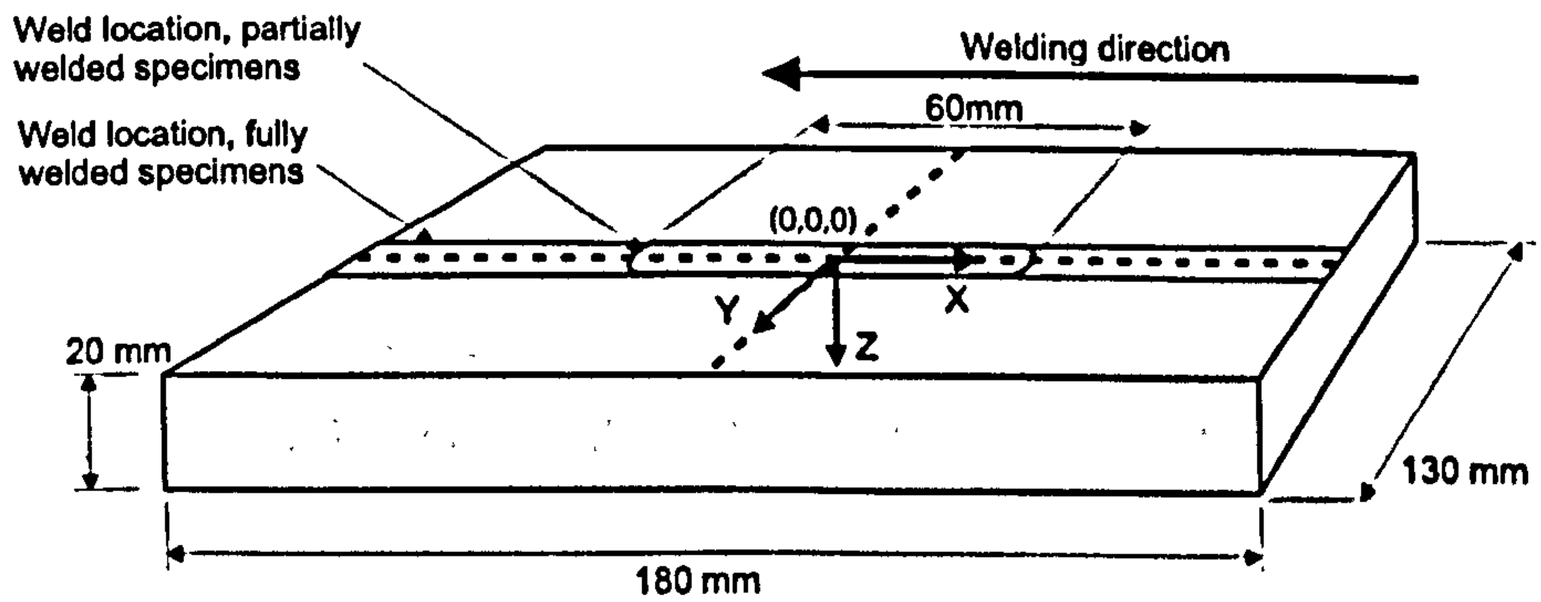

Figure 3.3: Autogenously welded 316L plates, dimensions and weld location.

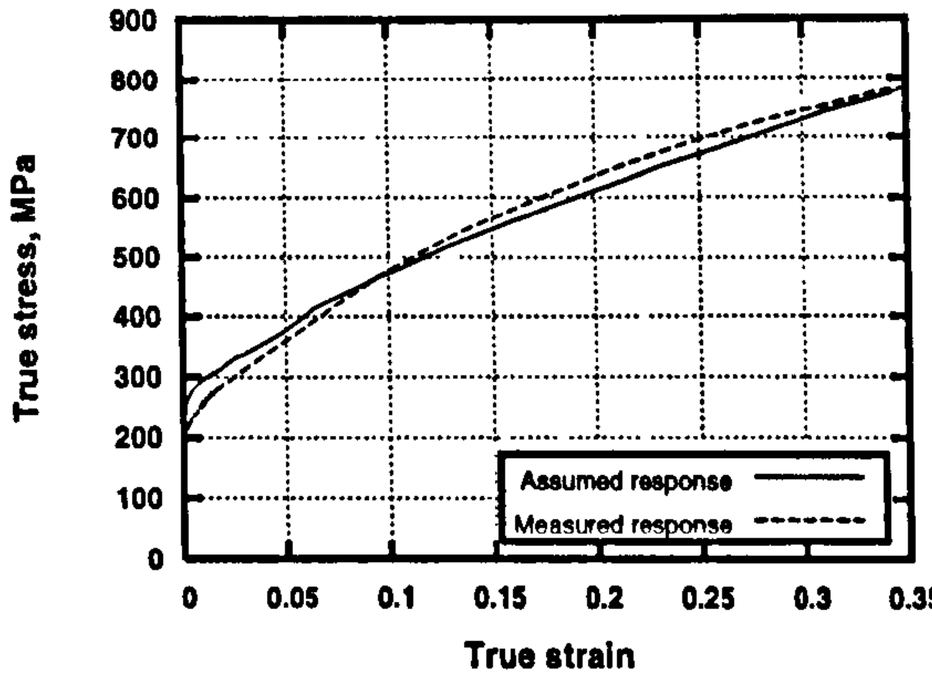

Figure 3.4: Material stress/strain response at 20°C assumed from previous investigations and measured in this work.

tracted. These were orientated such that one would have the eventual crack location along the weld line and the other would have the crack running perpendicular to the weld.

In this work, the limited time available for neutron diffraction measurements meant that only the sample aligned along the weld could be measured. As a result only this sample is illustrated in figure 3.5. In addition a 'comb' type specimen was extracted from one of the partially welded plates, as shown in figure 3.6. The comb was designed to allow an examination of any variation in the stress free lattice spacing, via neutron diffraction, in regions adjacent to and far from the weld. The geometry was intended, by the creation of free surfaces, to relax any macro-scale stresses. Measurements made from this specimen were therefore assumed to correspond to the stress free state.

In the case of the P275 plate, specimens were extracted with the short transverse direction orientated along the welding direction of the parent plate, as labelled 'CT25_1' and 'CT50_1' in figure 3.2. Two specimens were extracted of dimension 62.5×60×25mm and 62.5×60×50mm, with the intention of investigating the effect of specimen thickness on stress relaxation. In addition, a comb specimen was extracted such that the length of the comb ran transverse to the weld, as labelled 'Comb specimen' in figure 3.2. All three extracted geometries are detailed in figure 3.7. As before, the comb specimen was intended to provide a benchmark from which stress free lattice spacings could be determined.

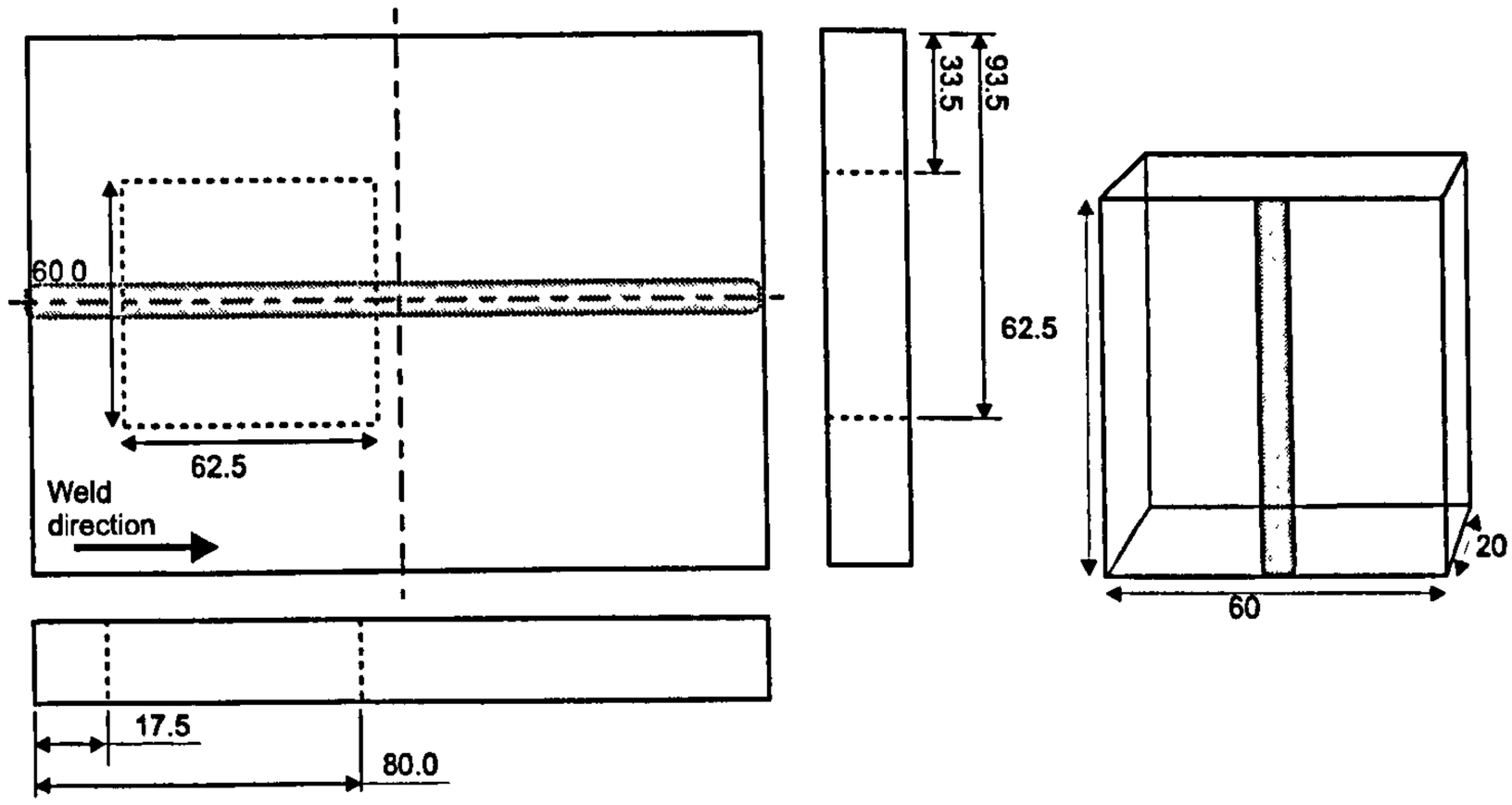

Figure 3.5: Geometry and extracted specimen locations for autogenously welded 316L austenitic steel plate. Dimensions in mm.

In all cases, specimens were cut out using a wire EDM (electro-discharge machining) process in order to minimise machining stresses in the extracted samples.

3.2.3 Specimens for plastic strain measurement

To investigate the effectiveness of the neutron diffraction methods for plastic strain measurement it was necessary to manufacture suitable test specimens containing well defined plastic strain fields. Tensile test specimens were chosen as reference samples to 'benchmark' the diffractive techniques. In addition, a number of pre-strained 'blanks' for compact tension CT type fracture specimens were fabricated in order to compare with the data obtained from the tensile test samples. All samples were manufactured from A533B ferritic steel as used in the fracture tests detailed in chapter 5, where subsequent fracture testing of the prestrained samples is also detailed.

A number of tensile tests were undertaken, according to the ASTM E8 standard [113], and consistent stress/strain behaviour was recorded in all tests. Stress/strain data are displayed in table 3.4. The tensile test specimens were cylindrical, with diameter 8mm and gauge length 80mm. To prestrain the CT blanks, such that a uniform strain field was created with minimal residual stress, a number of large tensile-type specimens were manufactured. These

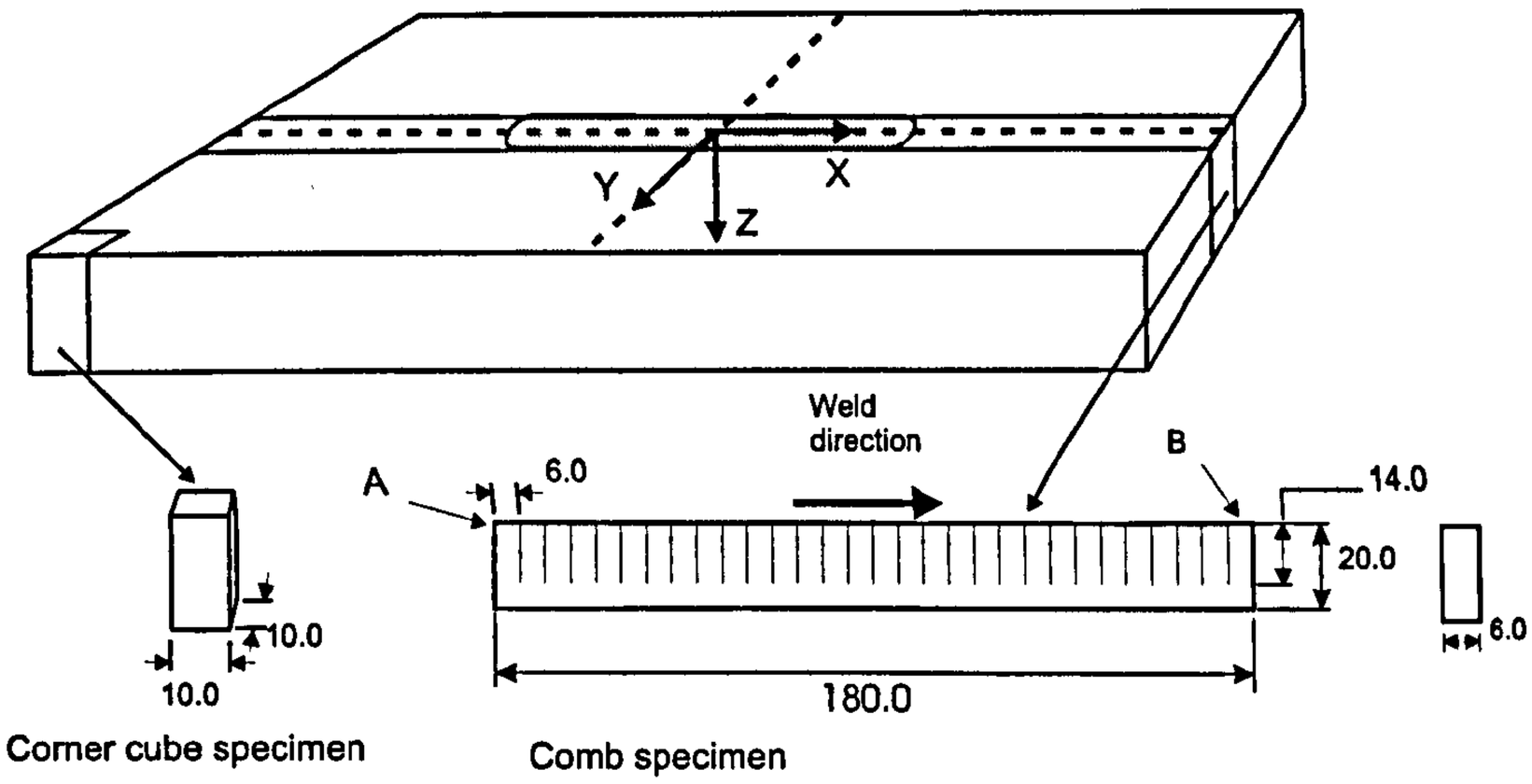

Figure 3.6: Geometry for extracted comb specimen taken from one of the partially welded 316L austenitic steel plates. Dimensions in mm.

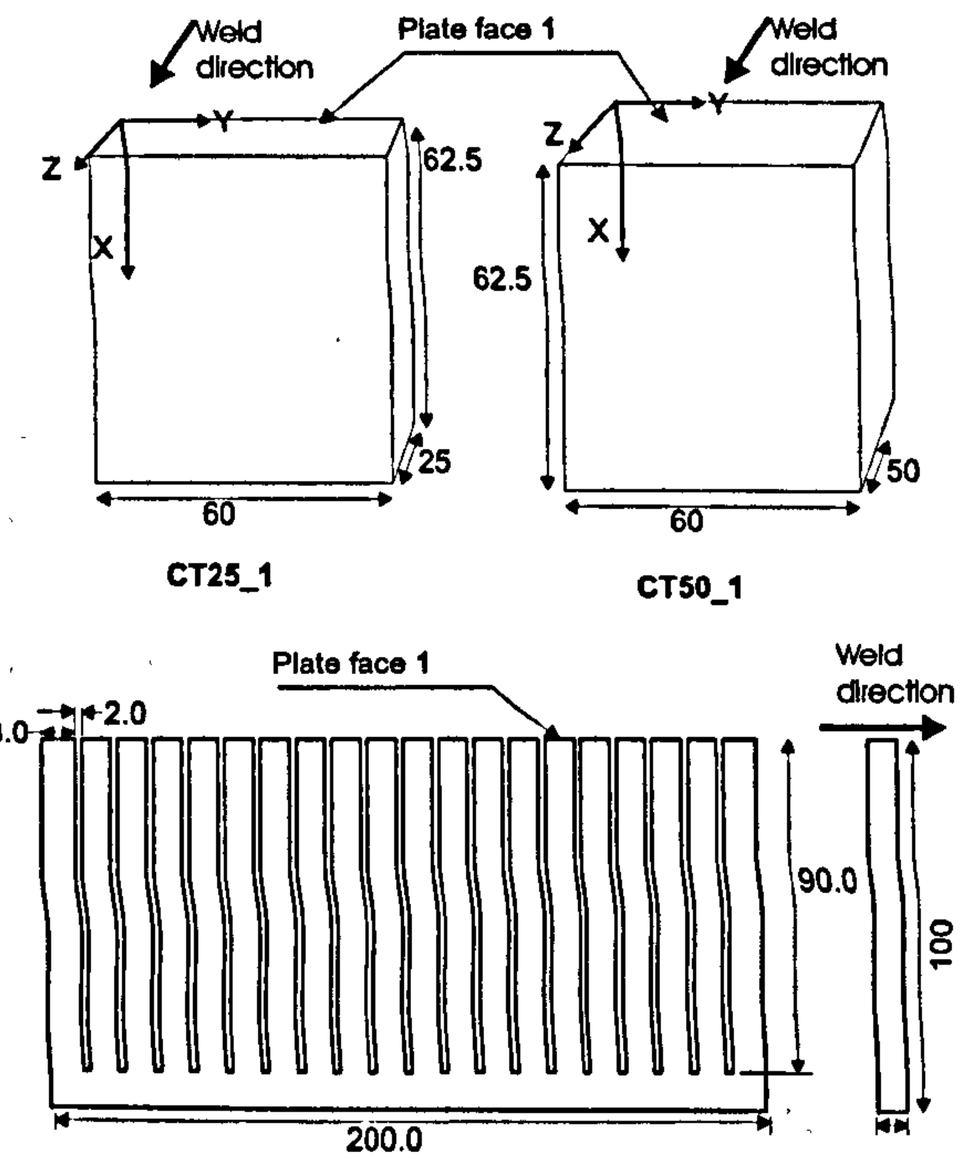

Figure 3.7: Geometry for extracted comb and CT blank specimens taken from the large repair welded plate of figure 3.2. Dimensions in mm.

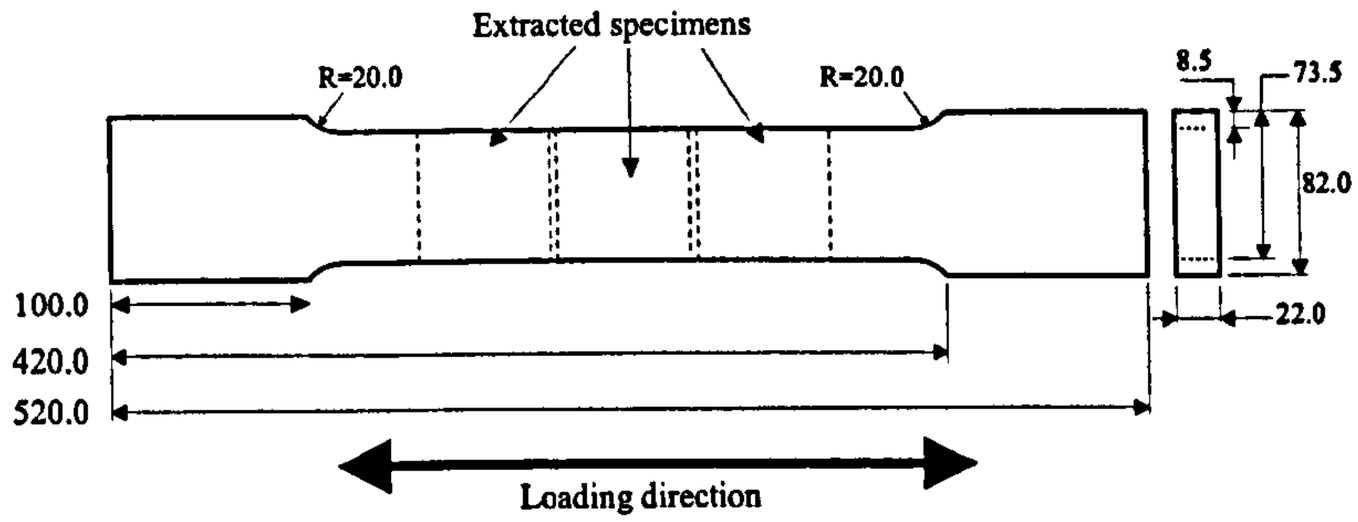

Figure 3.8: Large tensile specimens, used to generate uniform plastic strain in extracted 'blanks'. Dimensions in mm.

were preloaded to the desired level of uni-axial plastic strain (1%, 3% and 5%), determined according to clip gauges fixed to the centre of the specimens, before being cut into sections as illustrated in figure 3.8.

The specimens used were designed to provide the simplest possible, uni-axial plastic strain field to minimise the number of complicating factors when attempting to determine the level of deformation.

3.3 Numerical stress predictions

3.3.1 Autogenously welded plates

In addition to experimental measurements, finite element predictions were made for the stresses within the specimens extracted from the autogenously welded plates. Predictions for the welded plates, published in [115, 116], were conducted by H. Alizadeh using the ABAQUS finite element code. Uncoupled thermal and mechanical analyses were employed, with thermal analyses being tuned to match the thermocouple data collected during manufacture. The mechanical analysis was then conducted using a non-linear isotropic hardening model. Detailed information on the modelling of the weld process may be found in [116].

A new mesh was then created, also using the ABAQUS code, to allow extraction of specimens. Stress and strain fields from the previous weld analysis of [116] were then mapped onto the new mesh for this work, including the plastic strain history (i.e. the current state of material hardening). As some interpolation was needed, due to the differing mesh structures, an equilibrium step was included in the analysis immediately after mapping. The relaxation

in this step was found to be negligible, indicating that the effect of mapping process on the stress and strain fields could be ignored.

The extraction process was approximated by removal of elements in the area surrounding the specimens in order to simulate the creation of free surfaces by the cutting process. Extraction was simulated by removal of material instantaneously along each side of the specimen as well as incrementally to better simulate the cutting process. It was found that away from the newly created surface, where neutron diffraction measurements were taken, the effect on the relaxed stress field was minimal. Contour plots of the stress longitudinal to the welding direction in the plate before and after the extraction process are presented in figure 3.9.

3.3.2 Repair welded plate

Finite element predictions were made as part of an earlier paper [111] for the P275 plates but analyses were conducted under 2D plane strain conditions and therefore could not be used as a basis for extraction modelling. However, as part of the work conducted in [111], deep hole drilling measurements were made through the thickness of the plate at the centre of the weld. This measurement provided stress data in the directions longitudinal to and transverse to the repair weld, corresponding respectively to the Z and Y directions in the extracted specimen (figure 3.7). To obtain a crude estimate of likely stresses in the extracted P275 specimens, the DHD results across the extracted region were decomposed into components due to membrane loading (uniform stress), pure bend loading (linear variation) and a self balancing component. As an initial estimate, it was assumed that the extraction process would reduce the bending and membrane components to zero but would not affect the self balancing component.

As a somewhat more refined estimate, the stress field throughout the specimen prior to extraction was assumed to be described by the values from the DHD measurement in [111]. The resultant stresses in the Y and Z directions were imposed on the specimen as an initial condition, with all faces restrained to simulate the conditions in the parent plate. The constraints were then removed to simulate the extraction process, such that the stresses were allowed to relax. Although far from exact, this analysis does account for the effects of yielding and plastic deformation due to the initial stress field and the coupling between the relaxation of orthogonal components.

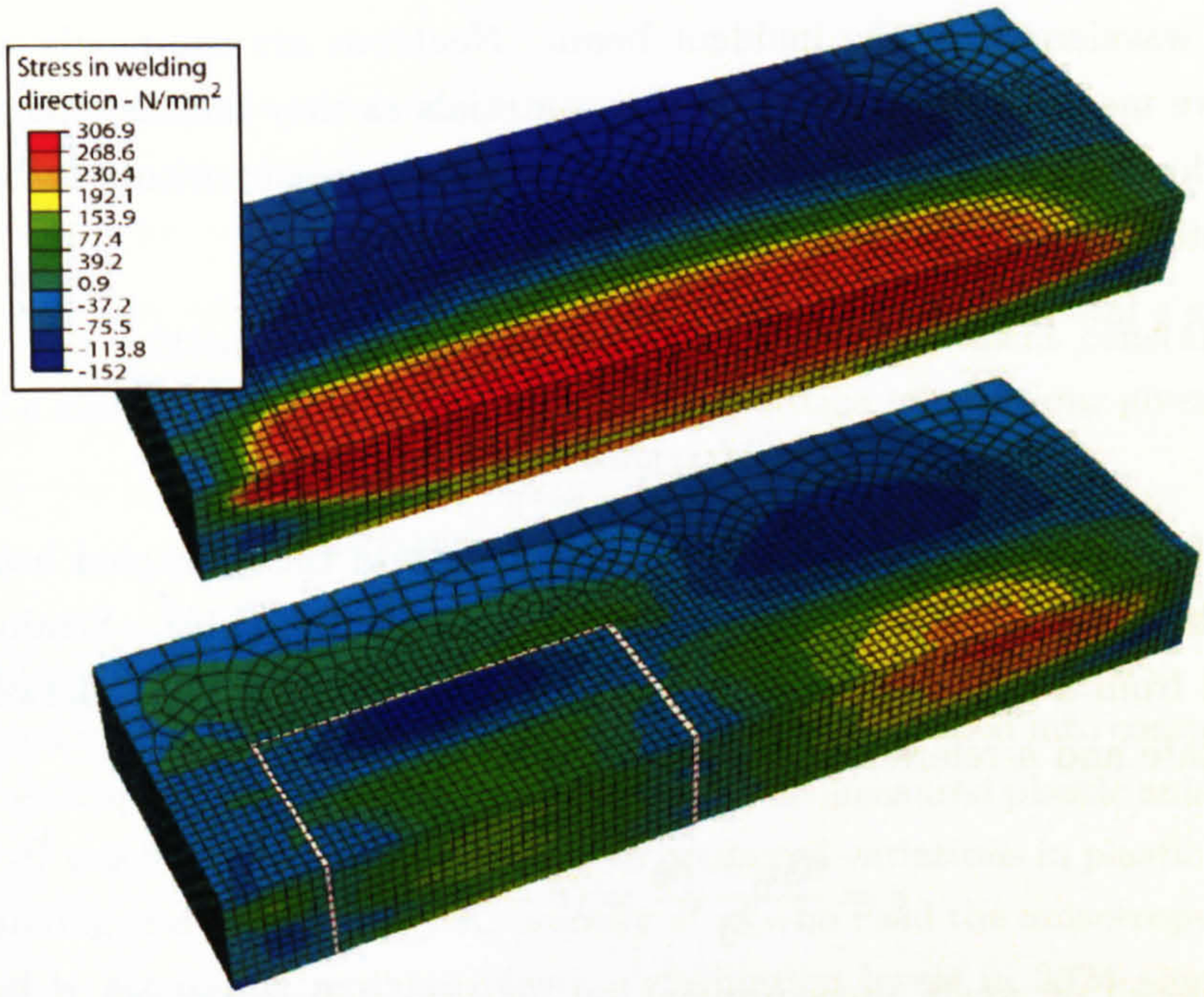

Figure 3.9: Contour plot of stresses longitudinal to welding direction in fully welded austenitic steel plate before and after simulated specimen extraction.

3.4 Stress and strain measurements

To obtain residual stress data for the welded plates, without damaging them such that subsequent specimen removal was not possible, the disturbance of the stress field by the measurement method needed to be minimised. For this reason the decision was made not to use any of the range of stress measurement methods based on strain relaxation such as hole drilling, layer removal or slotting. As an alternative it was decided to use non-destructive diffraction based methods, in this case neutron diffraction. Neutrons have good penetration in most engineering materials ($\approx$ 40mm in steels) and strain measurement by neutron diffraction has been shown to produce accurate, high resolution stress and strain data, e.g. [117].

3.4.1 Strain measurement with neutron diffraction

The measurement of elastic stress and strain by diffraction methods makes use of Bragg's law which states that diffraction through materials occurs preferentially at certain crystallographic planes, determined by the interplanar spacing

and the wavelength of the incident beam. Neutrons are commonly used for diffractive measurement in engineering materials as they have a typical penetration depth of the order of several cm, allowing measurements to be made in the interior of specimens.

Bragg's law is generally written as

$$2d_{hkl}\sin\theta = n\lambda \tag{3.1}$$

where θ is the diffraction angle, λ the wavelength of the diffracted beam and d_{hkl} is the spacing between the planes of Miller index {hkl}. Strain is determined from a change in spacing of Miller index planes, d_{hkl}, between the loaded state and a reference stress free state.

$$\epsilon = \frac{d_{hkl} - d_0}{d_0} = (\theta - \theta_0)\cot\theta \tag{3.2}$$

Further detail of strain measurement by neutron diffraction can found in a number of other published works, e.g. [118, 119] and so will not be entered into here.

Anisotropy strain

The anisotropy strain method for plastic strain determination is based on measuring the deviation of diffraction peaks from specific crystal planes from their theoretical positions. In a cubic crystal structure the spacing of a given plane, d_{hkl}, is a function of the lattice unit cell size a

$$d_{hkl} = \frac{a}{\sqrt{h^2 + k^2 + l^2}} \tag{3.3}$$

If the material lattice parameter a is known, equations 3.1 and 3.3 can be used to predict the locations of the diffraction peaks for each {hkl} plane.

It has however been noted, for example by Ezelio [120] when measuring a Nickel super-alloy and Rogge in stainless steel [121], that strains measured from differing diffraction peaks begin to diverge with increasing deformation. This anisotropy in peak response was further investigated by Daymond and co-workers [122] who modified the standard Rietveld refinement method [123] for diffraction spectra such that the lattice parameter tracks a single peak of Miller index {h00}. The strain from any other peak, ϵ_{hkl}, is then assumed to

deviate according to

$$\epsilon_{hkl} = \epsilon_{h00} - \frac{\gamma A_{hkl}}{C} = \epsilon_{h00} - \epsilon_A A_{hkl} \tag{3.4}$$

Where γ is a fitted anisotropy parameter, C is an instrument constant and A_{hkl} is a measure of the stiffness of individual lattice orientations given by

$$A_{hkl} = \frac{h^2k^2 + k^2l^2 + h^2l^2}{(h^2 + k^2 + l^2)^2} \tag{3.5}$$

This allows an 'anisotropy strain' ϵ_A to be defined, where $\epsilon_A = \gamma/C$. It was suggested in [122] that γ and therefore ϵ_A could be partitioned into components due to elastic and plastic strain anisotropy and the measured plastic anisotropy strain ϵ_A^{pl} was found to correlate well with predicted variations in plastic strain. This finding was confirmed by Korsunsky *et al* who used the anisotropy strain method to accurately measure plastic deformation levels in 2024 aluminium [124].

Diffraction peak broadening

In a perfectly ordered atomic lattice, under uniform strain, one would expect very sharp diffraction peaks approximating a delta function. In reality, due to inhomogenities inside a typical measurement volume and individual diffraction instrument characteristics, experimental peaks are similar to a Gaussian distribution.

Due to variations in lattice stiffness with orientation, load is not carried evenly by neighbouring material grains. After plastic deformation, this results in the build up of intragranular residual stresses, meaning two neighbouring grains in the same macroscopic strain field will be experiencing differing levels of local strain. As a result, the diffraction behaviour of each grain will differ slightly, resulting in a broadening of the measured diffraction peak which generally samples multiple material grains. The presence of dislocations may also result in peak broadening, even for measurements based on a single grain, as local regions of tension and compression are created in the surrounding lattice [125].

Increasing diffraction peak width was suggested as a method for plastic strain measurement on a welded aluminium bar by Smith [126], although in such cases it is difficult to separate the broadening effects of plastic deformation

from those due to local material variations from the welding process. The peak broadening approach was later used [127] to qualitatively estimate equivalent plastic strain levels in the aluminium sample of [126] as well as in a cracked ferritic steel beam. It was suggested, based on a fit to experimental data, that the relationship between the change in diffraction peak width at half height, $\delta\theta_w$, and the prior plastic strain ϵ^p was given by

$$\delta\theta_w = 0.162\left[1 - \exp\left(-0.3\left|\epsilon^p\right|\right)\right] \tag{3.6}$$

It was also noted that the peak broadening was insensitive to the diffraction vector direction, suggesting it is a suitable measure of equivalent plastic strain ϵ_e^p, rather than an approach for determining plastic strain levels in specific directions.

3.4.2 Measurements in parent plates

Strain measurements on the welded 316L plates were made using the SALSA strain diffraction instrument at the Institute Laue-Langevin (ILL), Grenoble, France. Data were recorded in the X, Y, and Z directions as shown in figure 3.3. Measurements were made as scans along lines of interest as detailed in table 3.3 in specimens referred to as PW1 (partial weld) and FW3 (full weld). In addition, a further line scan was made along the DHD1 line in an additional partially welded specimen, henceforth referred to as PW3, in order to check the repeatability of the stress field created by the welding process. In all cases a measurement volume of 2mm×2mm×2mm was used and all measurements were made using the diffraction peak corresponding to the {311} lattice plane, as this has been shown to exhibit a minimum sensitivity to plastic and elastic strain anisotropy [122].

Measurement of the stress free reference spacing and peak position, d^0_{hkl} and θ^0_{hkl}, were made based on a 10mm×10mm×20mm specimen cut from the corner of one of the partially welded specimens (see figure 3.6). All cuts were made using wire EDM to ensure no machining stresses were induced by the cutting. .

To compensate for the variation in grain structure, a further 'comb' reference specimen was extracted from one of the partially welded specimens, as shown in figure 3.6. Additional measurements were made on the comb specimen on the STRESS-SPEC instrument at the FRM-II facility, Munich, based on the {311} peak as before. To allow comparison with the SALSA

data, the STRESS-SPEC results were first adjusted, according to equation 3.1, to account for the slightly differing wavelengths used at each instrument ($\lambda = 1.65\text{m}^{-10}$ for SALSA and 1.67m^{-10} for STRESS-SPEC).

To allow for small constant shifts in the measured values, due to the individual characteristics of each instrument, it was assumed that the mean measured d_0 spacing in each case should be identical. To achieve this, the STRESS-SPEC results were scaled slightly so that the mean of the results from the two end teeth of the comb (labelled A and B in figure 3.6) was identical to the mean of the values obtained at SALSA from the cuboid sample. The two data sets prior to this adjustment are displayed in figure 3.10(a), the eventual correction applied to the STRESS-SPEC values corresponded to a reduction in the stress free lattice spacing of 0.06%.

A scan along the weld direction in the comb specimen, corresponding to line L in table 3.3, showed a slight increase in the stress free lattice spacing in the region under the weld with an accompanying decrease in the value of θ_0, as illustrated in figure 3.10(b). This was equivalent to a strain change of approximately $100\mu\epsilon$. This is in keeping with previous works where a variation in stress free lattice spacing has been observed in the heat affected zone of welded components, e.g. [128].

To account for this variation, separate averaged values of d_0 were used for the calculation of strain under the weld and in the regions away from the weld. It is apparent in figure 3.10(b) that there is a slight anisotropy in the d-spacing in the near weld region and as such, separate values of θ_0 were used in the longitudinal and transverse direction, although the difference between the two was not considered to be large. As detailed information regarding the stress free lattice spacing in the normal direction (Z in figure 3.3) was not measured, an average of the longitudinal and transverse values was used.

Based on the determined strain values, stresses were calculated in the measured directions using generalised Hooke's law. It was assumed that the X, Y and Z directions corresponded to the axes of principal stress in the plate. While this cannot be known for certain without strain data in other directions, it has been shown that incorrect assumption of principal axes does not result in error in the calculated stresses in the directions of measurement [129].

For points along the lines L, L2, T and T2, plane stress assumptions were used when calculating stresses. As these lines lie 2mm from the plate surface

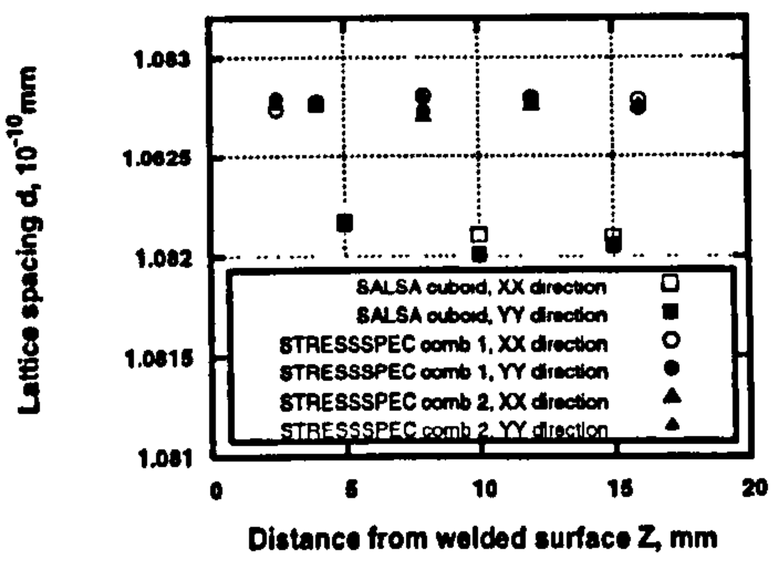

(a) Comparisons of 316L plate lattice spacings from the SALSA and STRESS-SPEC instruments.

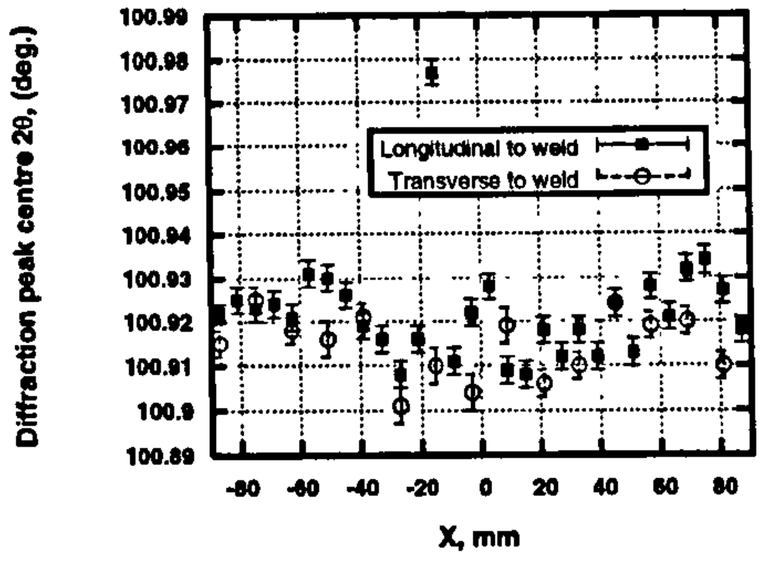

(b) Variation of the diffraction peak position, 2θ, along the length of the extracted comb specimen. Weld extent from X=30 to X=-30.

Figure 3.10: Stress free lattice diffraction measurements on 316L austenitic stainless steel.

it was felt that the stress in the Z direction could be assumed negligible.

3.4.3 Measurements in extracted specimens

Residual stress measurements on all extracted specimens were made via neutron diffraction (ND) using the STRESS-SPEC diffraction instrument at the FRM-II facility in Munich, Germany. Measurements were made by scanning along lines within the extracted specimens. Line locations are illustrated in figure 3.11.

A gauge volume of 2mm×2mm×2mm was used in all cases with strain calculated from the movement of a single diffraction peak. Measurements were made using the diffraction peak corresponding to the {311} lattice plane for the 316L steel and the {310} plane in the P275 steel. The differing peaks were necessary due to the differing material crystal structures as the {311} orientation does not produce a valid diffraction peak in a BCC (i.e. ferritic steel) crystal structure. An incident neutron wavelength of $1.67\text{x}10^{-10}$m was used in both cases.

Additional measurements were made using a 5mm×5mm×5mm gauge volume in the 50mm thick specimens extracted from the P275 plate, labelled 'CT50_1' in figure 3.7. The increased gauge volume was used in an attempt to increase the maximum diffraction path length along which measurements could be made. The ratio of the diffraction peak height to the background

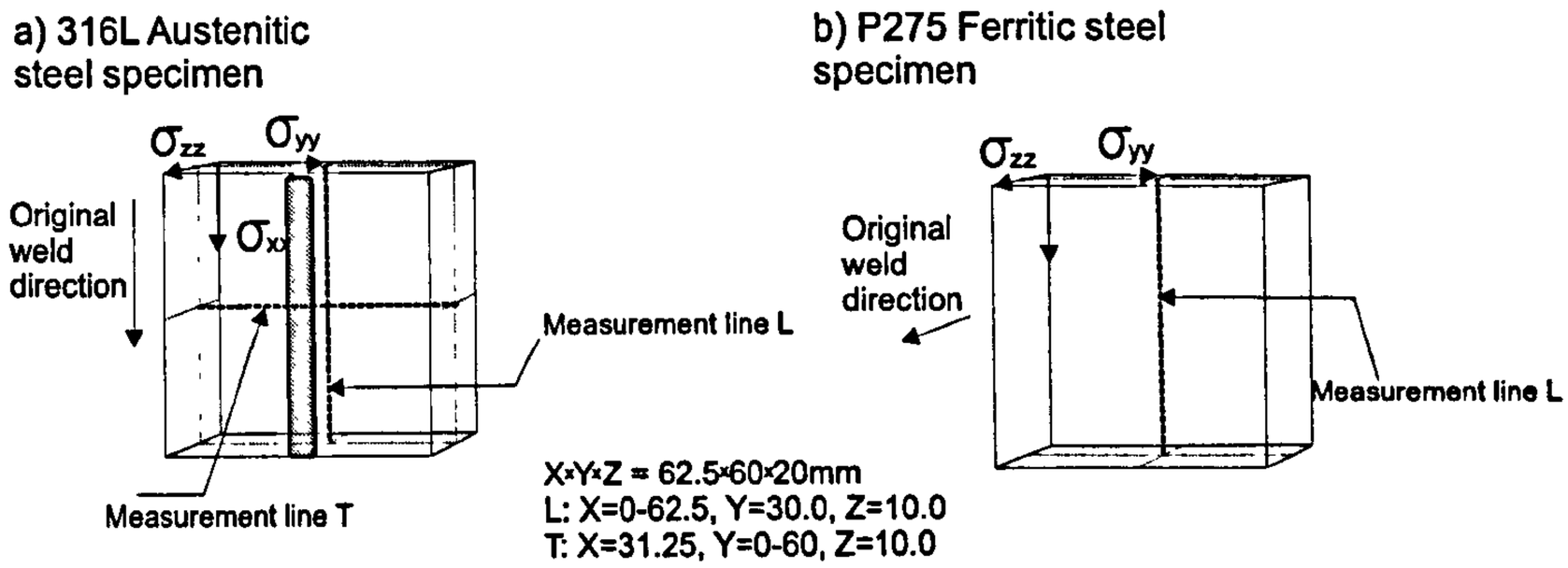

Figure 3.11: Positions of measurement lines in extracted specimens from a) 316L steel plate b) P275 steel plate.

noise level, measured at the detector in the 50mm specimens, was less than 20% of that recorded in the 25mm specimens. As a result it was felt that strains could not be determined from the diffraction peak position with any confidence and as such, results for this specimen are not displayed.

For the P275 steel, stress free diffraction peak positions, $2\theta_0$, were made along a number of 'teeth' on the extracted comb specimens. In this case the variation in θ_0 across the centre of the weld, where specimens were removed, was found to be small and a single mean value was used for strain calculation.

In the 316L material, measurements of $2\theta_0$ were made along the length of the comb 2mm below the weld surface, as well as along the length of a number of the 'teeth' (i.e. through the thickness of the original plate). As discussed in section 3.4.2, the values of $2\theta_0$ under the weld itself were found to differ appreciably from those measured at the ends of the comb specimen where the heating effect of the weld was negligible.

As such, an average from the comb HAZ under the weld was used for strain calculation near the weld (i.e. line L in figure 3.11 (a)) and an average from the end teeth used for points away from the weld (i.e. line T in figure 3.11 (a)).

Strain components were measured along the three mutually orthogonal directions of the specimens, denoted X, Y and Z in figure 3.11. Stresses were calculated from the measured strains using the standard Hooke's law equations, $\sigma_{ij} = C_{ijkl}\epsilon_{kl}$, where C is the stiffness tensor. As in section 3.4.2, it was assumed that the X, Y, and Z directions corresponded to the principal axes.

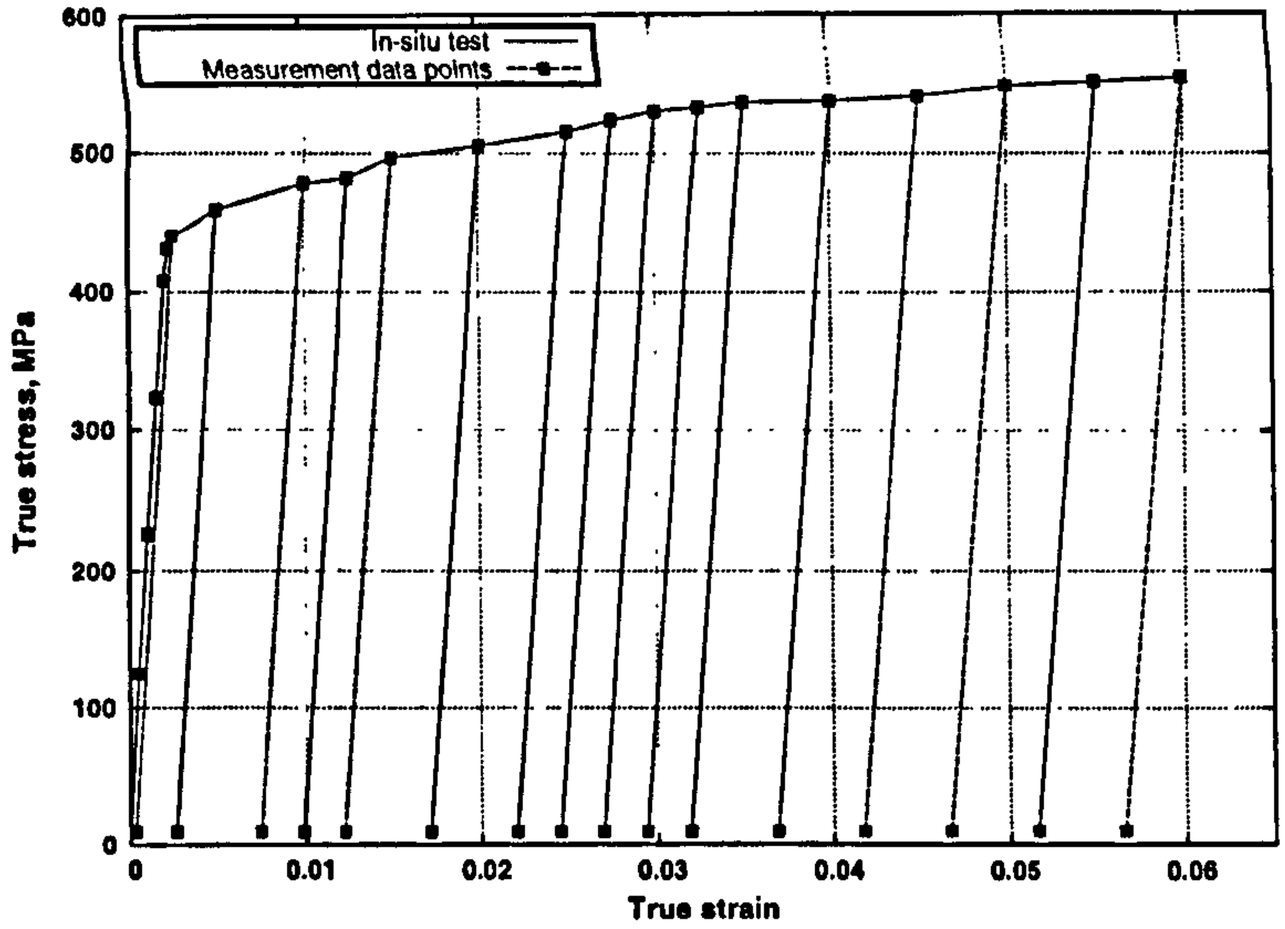

Figure 3.12: Material stress/strain response from in-situ tensile testing showing points where calibration diffraction measurements were undertaken.

3.4.4 Measurements of plastic strain

Neutron diffraction measurements were made using the ENGIN-X instrument on the ISIS neutron source at Rutherford Appleton laboratories, U.K. In order to maximise the quality of the diffraction spectra in the thicker prestrained blanks, while retaining reasonable count times, a measurement gauge volume of 4mm×4mm×4mm was used throughout. A time of flight (TOF) instrument such as ENGIN-X, allowing collection of data from multiple diffraction peaks, was necessary in order to determine the anisotropy strain parameter ϵ_A.

An 'in-situ' tensile test was undertaken on the ENGIN-X instrument in order to record neutron diffraction spectra under varying applied loads. Measurements were taken at increasing levels of plastic strain, with and without applied load in order to separate the elastic and plastic components of peak broadening and anisotropy strain. The results of the in-situ tensile test, along with the data points where diffraction spectra were recorded, are presented in figure 3.12.

3.5 Results

3.5.1 Stress measurement in autogenously welded 316L specimens

Results of neutron diffraction measurements in the plates after autogenous welding along lines LT and DHD1 (as described in table 3.3) are shown for fully welded specimens in figures 3.13 and 3.14 and partially welded specimens in figures 3.15 and 3.16. It can be seen that there is good agreement between the finite element model predictions and the measured neutron diffraction results. It should be noted that plane stress conditions were assumed when calculating stresses from strains.

Use of the measured ϵ_{zz} component when calculating σ_{xx} and σ_{yy} was found to significantly increase scatter. Agreement between measured and predicted strains was significantly better than for stresses, when calculated with all three measured components. It was therefore apparent that the increase in scatter was due to error propagation when combining measured strains to calculate stresses, effectively increasing the 'noise' in the calculated stress data.

Ideally a greater number of strain components than the minimum of 3 would have been measured but experimental time constraints were such that this was not possible. The resulting set of over-specified simultaneous equations for the stress tensor could then have been solved using a least squares method, such as Moore-Penrose pseudo inversion, resulting in reduced error sensitivity. Nonetheless, as the centre of the measurement volume was situated 2mm from the plate surface for line LT, the assumption that $\sigma_{zz} = 0$ was felt to be reasonable and was supported by the finite element results, even for line DHD1 where points up to 10mm from the surface were measured. The assumption of plane stress conditions was not observed to significantly alter the magnitudes or overall distribution, compared to the use of 3 strain components, suggesting that is was a reasonable approximation of the specimen stress state.

Measurements were also made along the other lines described in table 3.3 but are not displayed for brevity as the comparisons in figures 3.13 to 3.16 serve to illustrate that the finite element simulation of [116] provides a good approximation of the stress field in the 'parent' welded plates and, from figure 3.16, the repeatability of the stresses arising from welding process can be seen in the two nominally identical (PW1 and PW3) partially welded specimens

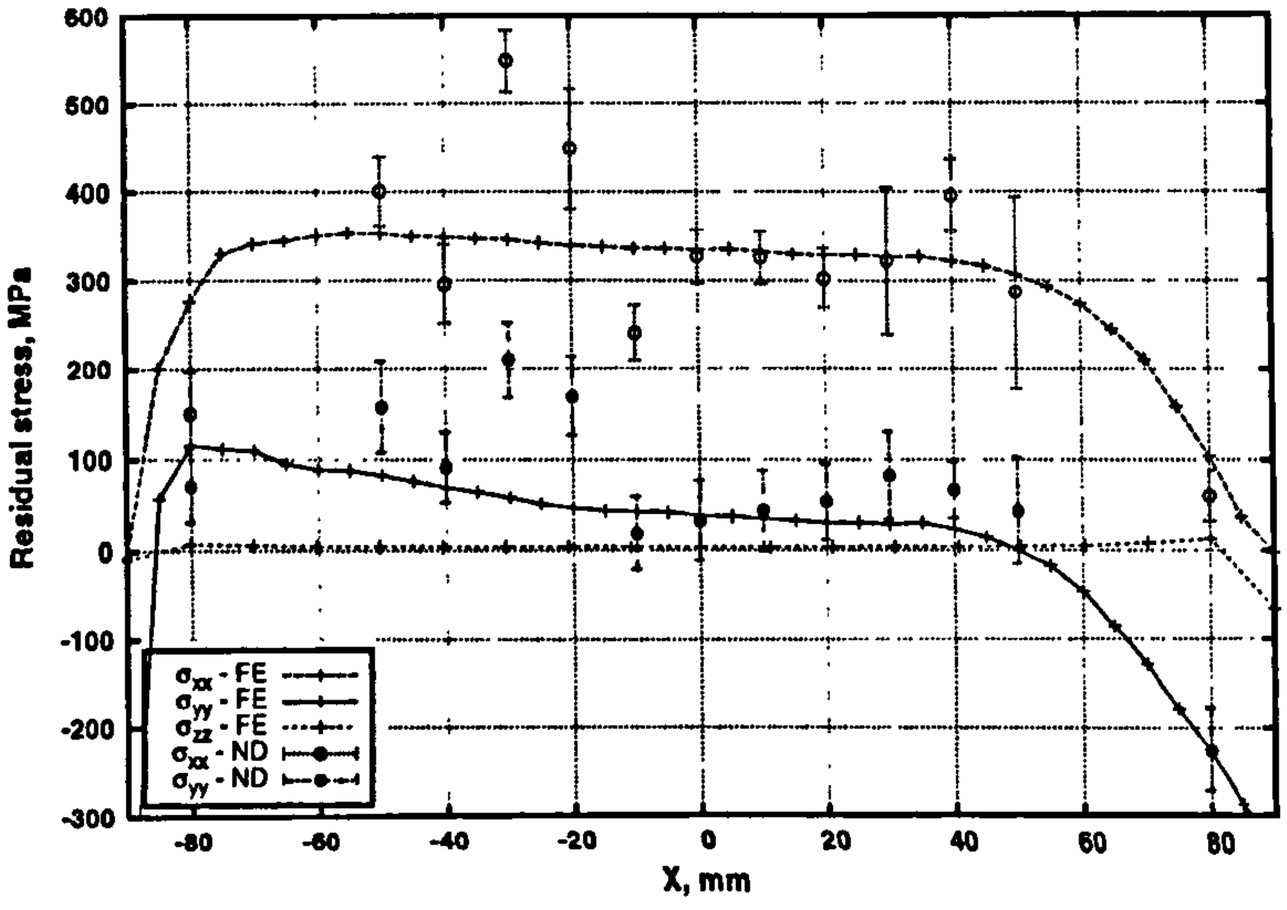

Figure 3.13: Finite element predictions and neutron diffraction measurements along line LT, described in table 3.3, in the fully welded 316L plates. X and Y directions as detailed in figure 3.3.

measured.

Measured stresses in the specimen extracted from the autogenously welded plate are displayed in figures 3.17 and 3.18. In both cases it appears that the modelling of the extraction process provides a reasonable estimate of the stress relaxation effect, although the results from the finite element analyses are consistently slightly higher than the measured values. This is typical of many similar comparisons between FEA and measurement results and is largely attributable to the simple isotropic hardening model used.

3.5.2 Stress measurement in P275 ferritic steel specimens

The through-thickness stress measurements in the original repair welded plate, as made in [111], are displayed over the region of the extracted specimen in figure 3.19. It can be seen that there is a considerable 'membrane' (i.e. constant) component to the stress field in both the Y and Z directions (longitudinal and transverse to the original weld) as in figure 3.7.

Simplistic estimates of the relaxed stresses, by removing the membrane and bending stress components from the DHD measurement, maintains the same field structure but reduces the overall mean value to zero, as would be

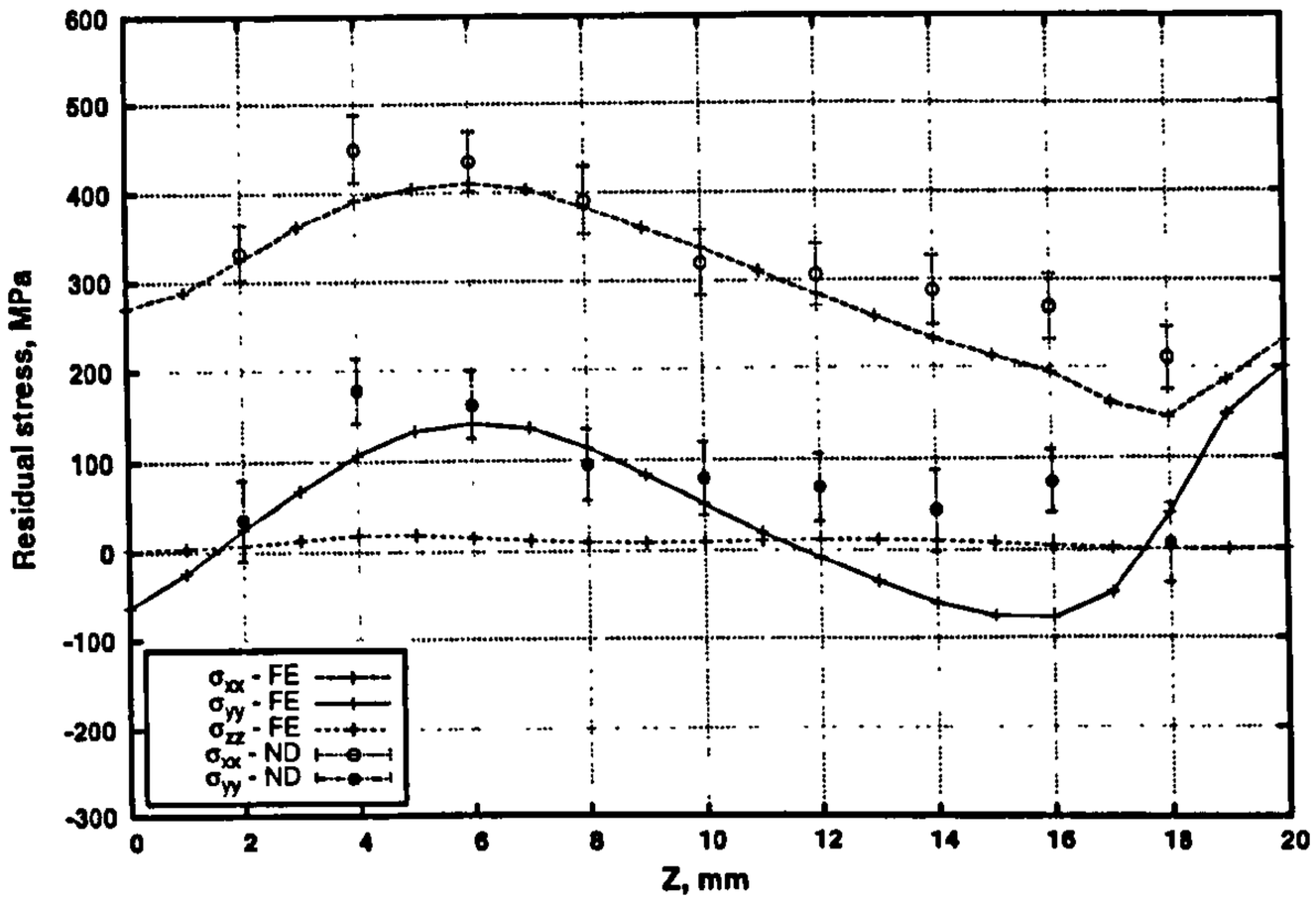

Figure 3.14: Finite element predictions and neutron diffraction measurements along line DHD1, described in table 3.3, in the fully welded 316L plates. X and Y directions as detailed in figure 3.3.

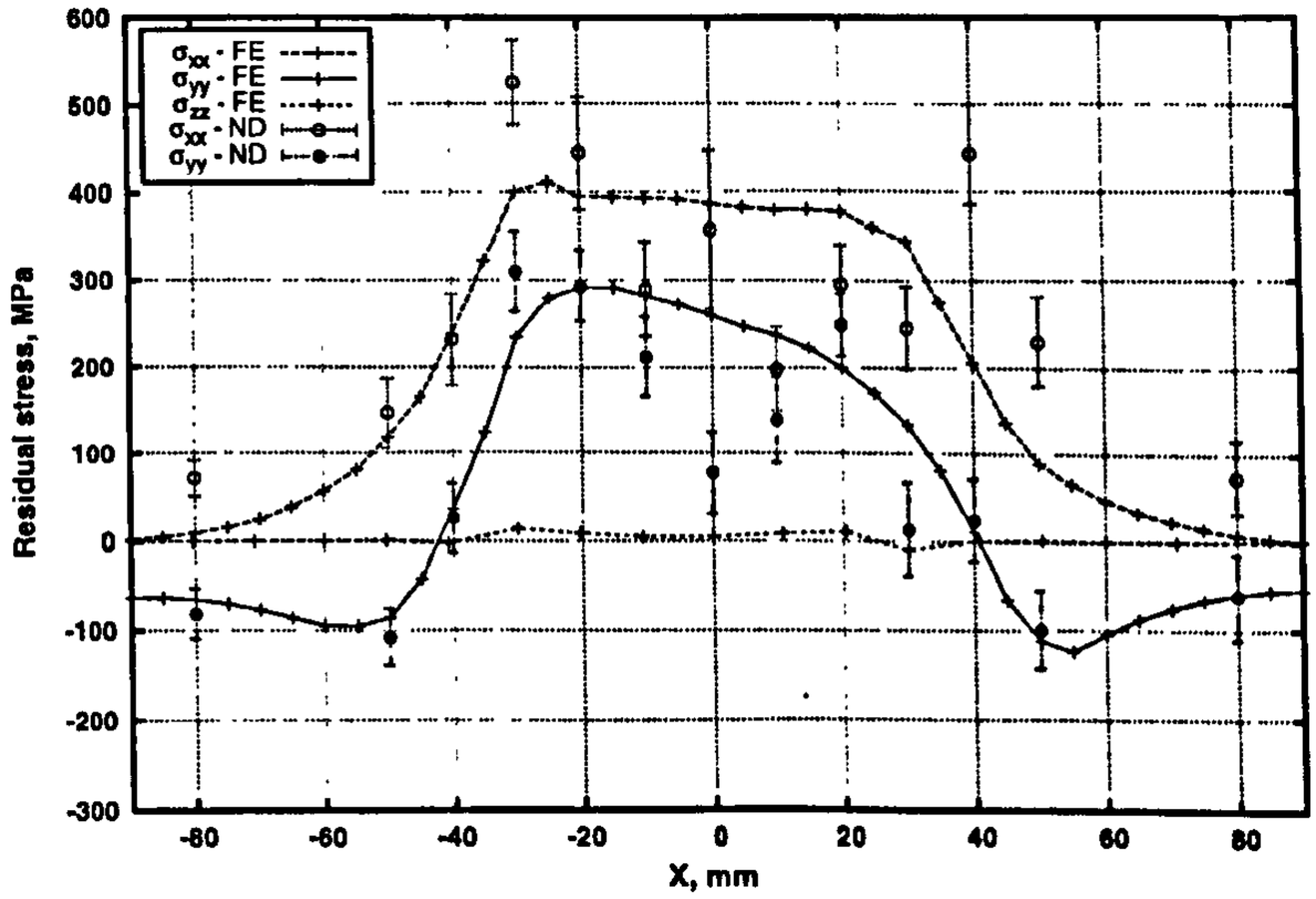

Figure 3.15: Finite element predictions and neutron diffraction measurements along line LT, described in table 3.3, in the partially welded 316L plates. X and Y directions as detailed in figure 3.3.

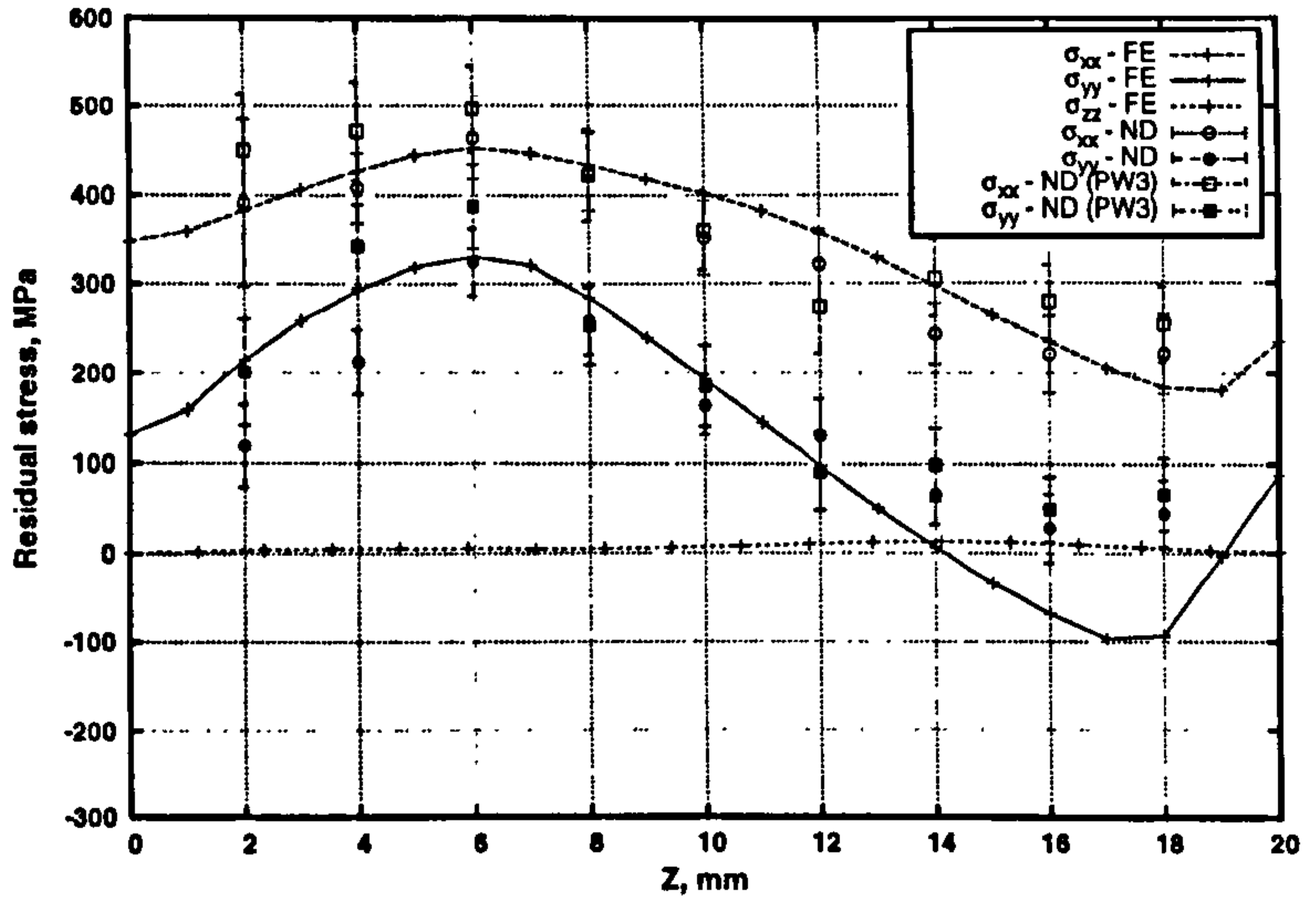

Figure 3.16: Finite element predictions and neutron diffraction measurements along line DHD1, described in table 3.3, in the partially welded 316L plates. X and Y directions as detailed in figure 3.3.

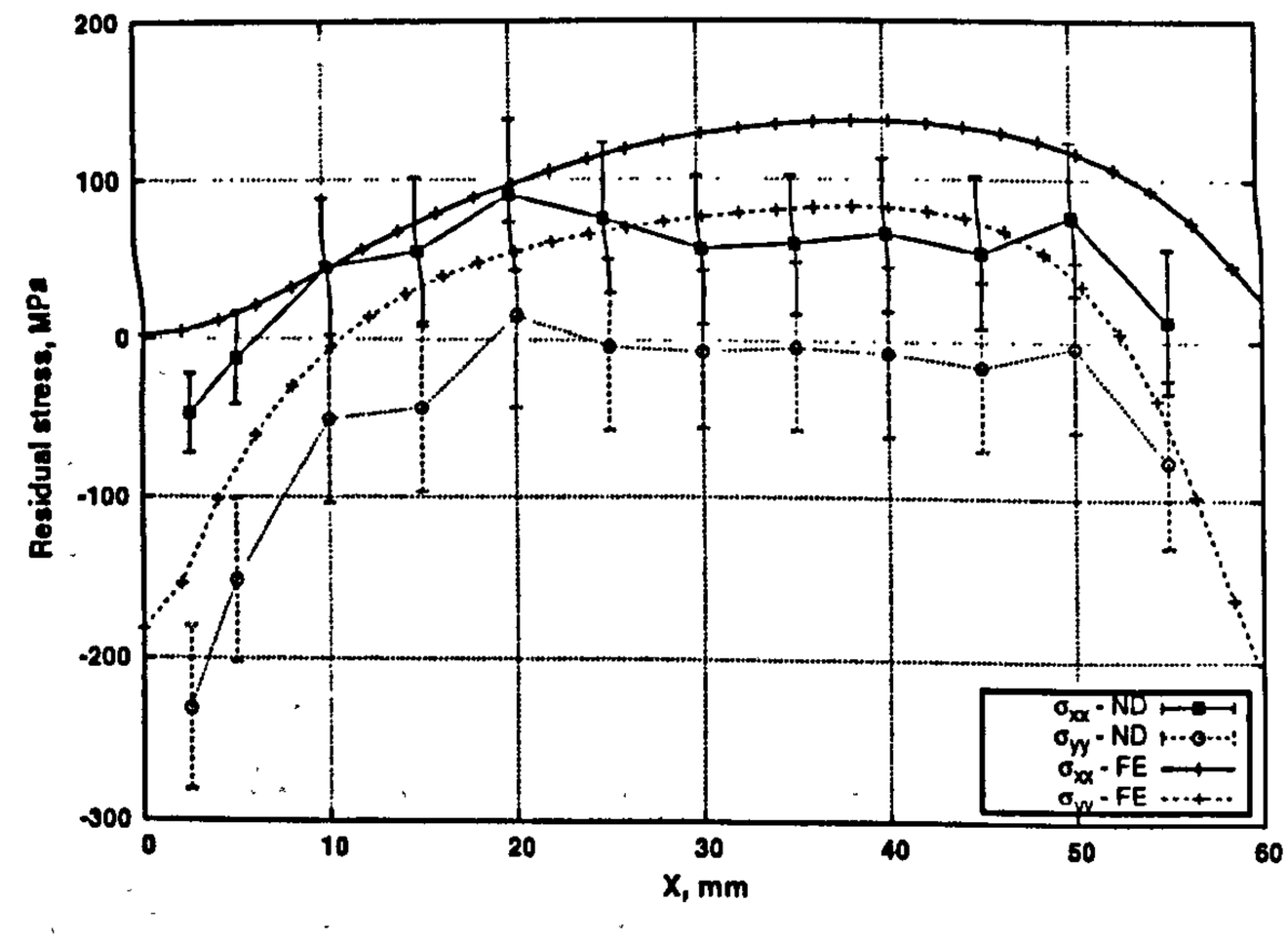

Figure 3.17: Neutron diffraction measurements and finite element stresses, along line L as illustrated in figure 3.11, in specimens extracted from autogenously welded 316L plate.

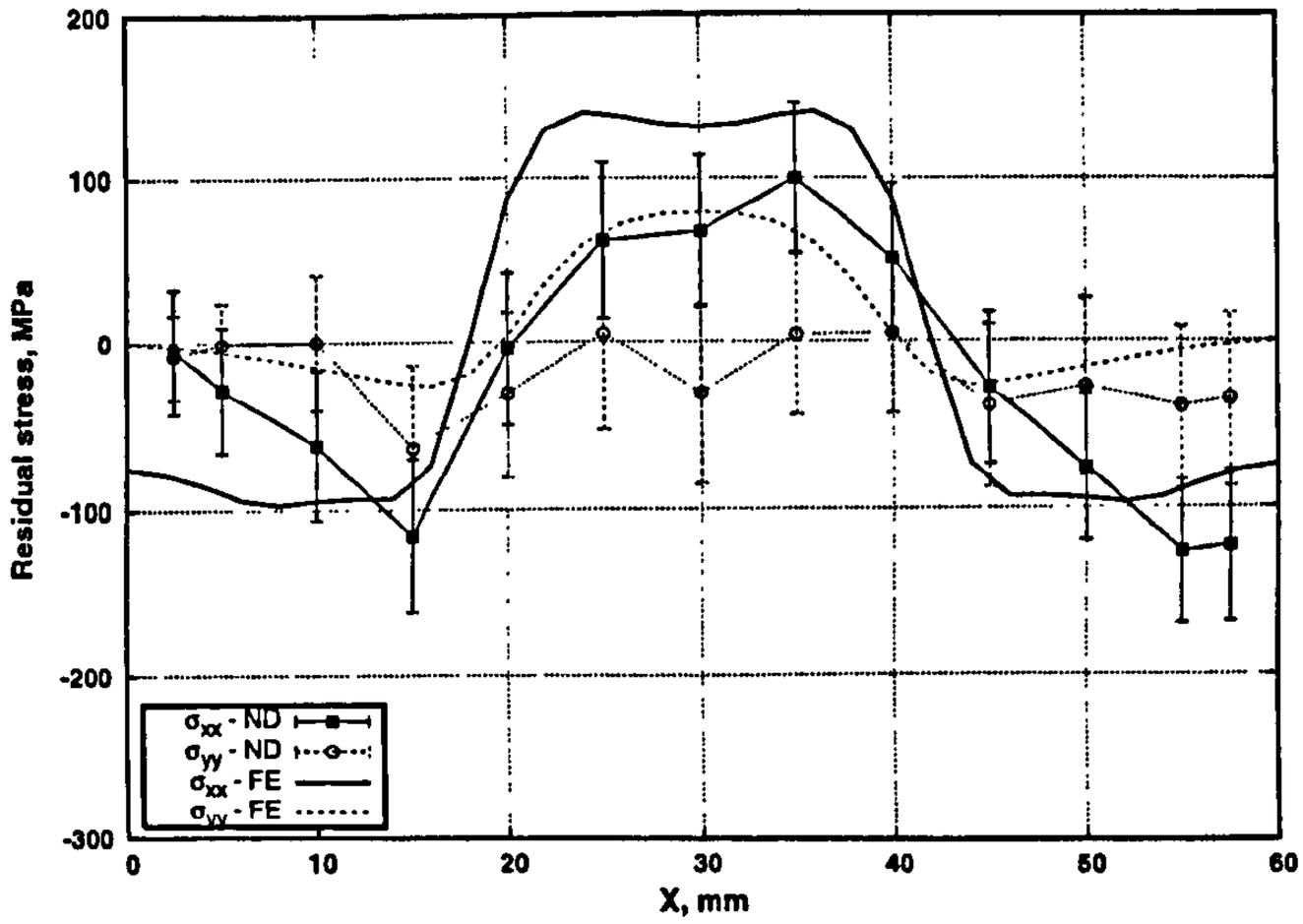

Figure 3.18: Neutron diffraction measurements and finite element stresses, along line T as illustrated in figure 3.11, in specimens extracted from autogenously welded 316L plate.

expected. The finite element relaxation simulation, which allowed for yielding caused by the relaxation, produced relaxed fields of similar overall magnitude but with a reduction in the peak value of σ_{yy} and, perhaps more significantly, an inversion of the overall profile of σ_{zz}.

The neutron diffraction measurements made in this specimen confirm the magnitudes of the predicted stresses. A clear correlation with the trends cannot be determined, although this is to be expected given the low magnitudes of the stresses measured which are of the same order of magnitude as the error in the measurements.

3.5.3 Plastic strain measurement in A533B ferritic steel

The stress/strain response from the tensile test was examined based on the strains recorded from a number of single diffraction peaks in addition to that obtained from Pawley refinement of the entire diffraction spectra. The results are displayed, in comparison to the predicted response from the macroscopic Young's modulus (determined via a strain gauge fixed to the specimen), in figure 3.20. It should be noted here that applied stress was obtained from the applied load and strain gauge reading in the usual way and strain for each

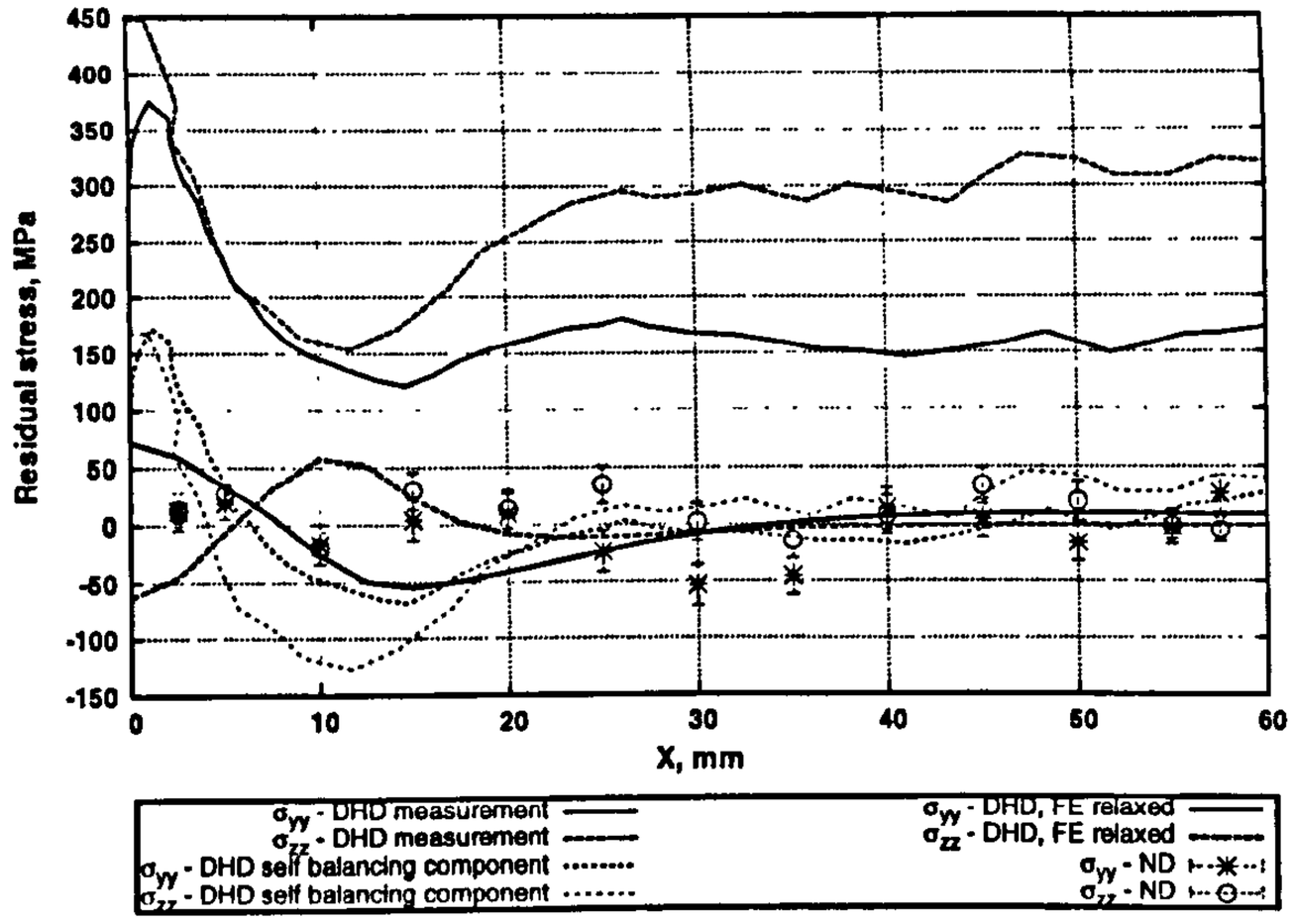

Figure 3.19: Stresses from neutron diffraction measurements, along line L as illustrated in figure 3.11, in specimens extracted from the repair welded P275 plate.

peak from equation 3.2. This avoids the need for peak-specific stiffness values to determine valid macroscopic stresses from single peak strains.

It can be seen that there exists a significant anisotropy in the response of differing peaks, even in the elastic region. The {200} peak displayed strains greater than those predicted from the macroscopic behaviour, as would be expected as it has the lowest stiffness according to equation 3.5. The strains from each peak then reduce with increasing A_{hkl} with the stiffest response exhibited by the {222} peak with a limiting value of $A_{hkl} = 1/3$.

It can be seen that the Pawley refinement overestimates the macroscopic stiffness which is best represented by the {310} peak response. This is in keeping with the findings of [122] where the {311} peak was found to provide the best match with the macroscopic response in an austenitic steel. The slight difference in Miller index can be attributed to the fact that the {311} plane does not produce a diffraction peak in a FCC cubic structure such as that in the ferritic steel tested here.

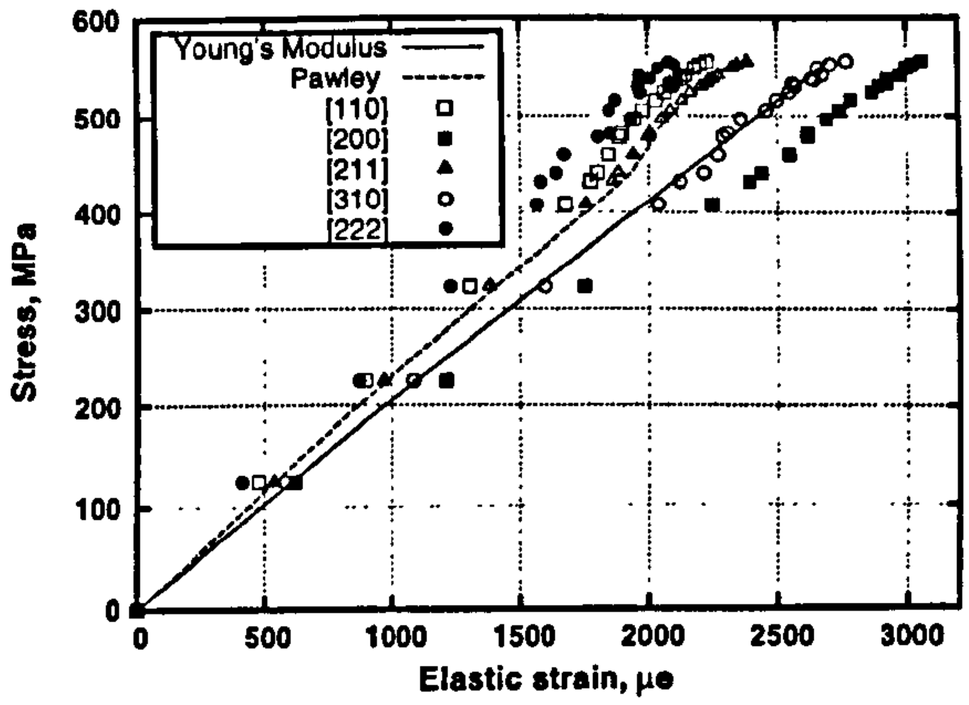

Figure 3.20: Strain measurements from in-situ tensile test based on Pawley refinement of the full diffraction spectra and analysis of individual peaks.

Anisotropy method results

On examination of the diffraction spectra obtained from both the tensile test (TT) and prestrained blank (CT) specimens it was decided to limit the data range used to determine anisotropy strains to the three best defined diffraction peaks. In this case these corresponded to the {100}, {200} and {211} lattice planes as displayed in figure 3.21.

The anisotropy strain, ϵ_A, as defined in equation 3.4 was partitioned into elastic and plastic components, following [122], with the elastic component assumed to vary linearly with the elastic strain in the direction of measurement. The variation of the anisotropy strain under elastic load, ϵ_A^{el}, with the {200} peak strain was found to be well approximated by a linear relationship, as plotted in figure 3.22. The {200} peak strain was selected as it represents the reference peak, corresponding to $A_{hkl} = 0$, used in determination of ϵ_A. Measurements longitudinal and transverse to the loading directions, where elastic strains were tensile and compressive respectively, exhibited ϵ_A values of opposite sign.

Measurements taken at each unloaded step in the tensile test showed increasing build up of residual elastic strain with increasing plastic deformation, as highlighted in figure 3.23. It is apparent that in both measured directions, the highest magnitude residual strains are present on the {200} peak with the {310} peak showing the lowest overall level of residual strain in both directions, again suggesting that results based on the {310} plane may be most

appropriate for comparison with macroscopic strain predictions such as those from finite element analyses. In both directions the Pawley refinement strain provides a lower bound to the single peak values.

The plastic component of the anisotropy strain, ϵ_A^{pl} was obtained by subtracting the elastic component, as determined by the linear fit to the {200} peak strain, from the total anisotropy strain. The variation in ϵ_A^{pl} with macroscopic plastic strain, shown in figure 3.24, shows clear separation between the values obtained in the loaded and unloaded states, suggesting that the plastic anisotropy is not so simply decoupled. It is also apparent, from a comparison between figures 3.22 and 3.24, that the 'elastic' component is of much greater magnitude than the 'plastic' component, making accurate determination of ϵ_A^{pl} more difficult. Nonetheless, there is a clear increasing trend between ϵ_A^{pl} and the level of plastic strain, independent of measurement direction, suggesting that plastic anisotropy may be a reasonable measure of the overall level of plastic deformation.

The results from the prestrained blanks are plotted in figure 3.25, as with the tensile test data, the {200} peak strain was used to estimate and remove the 'elastic' component of the anisotropy strain. The results show a similar trend to those made on the TT specimen, although there is a noticeable separation between the values of ϵ_A^{pl} measured in the directions longitudinal and transverse to the prestrain direction and considerable scatter in the measured value of ϵ_A^{pl} for differing points having experienced the same level of macroscopic plastic strain. In addition, it is apparent that the magnitude of ϵ_A^{pl} in these specimens is considerably higher than that measured in the TT specimen. This may suggest a geometric component affecting the anisotropy factor, for example measurement path length, or a more complex three dimensional stress/strain state at a granular scale which must be accounted for.

Peak broadening method results

Traditionally, peak broadening is quantified using the measured peak full width half maximum (FWHM) as this can be easily defined, regardless of the details of the peak's shape. The peaks recorded in this work were fitted using a combination of Gaussian, Lorentzian and exponential components to account for peak asymmetry due to the experimental apparatus. The width of a single peak fit is affected only by the Gaussian component, the width of which is in turn a function of the Gaussian parameter σ. As σ is a linear function of the

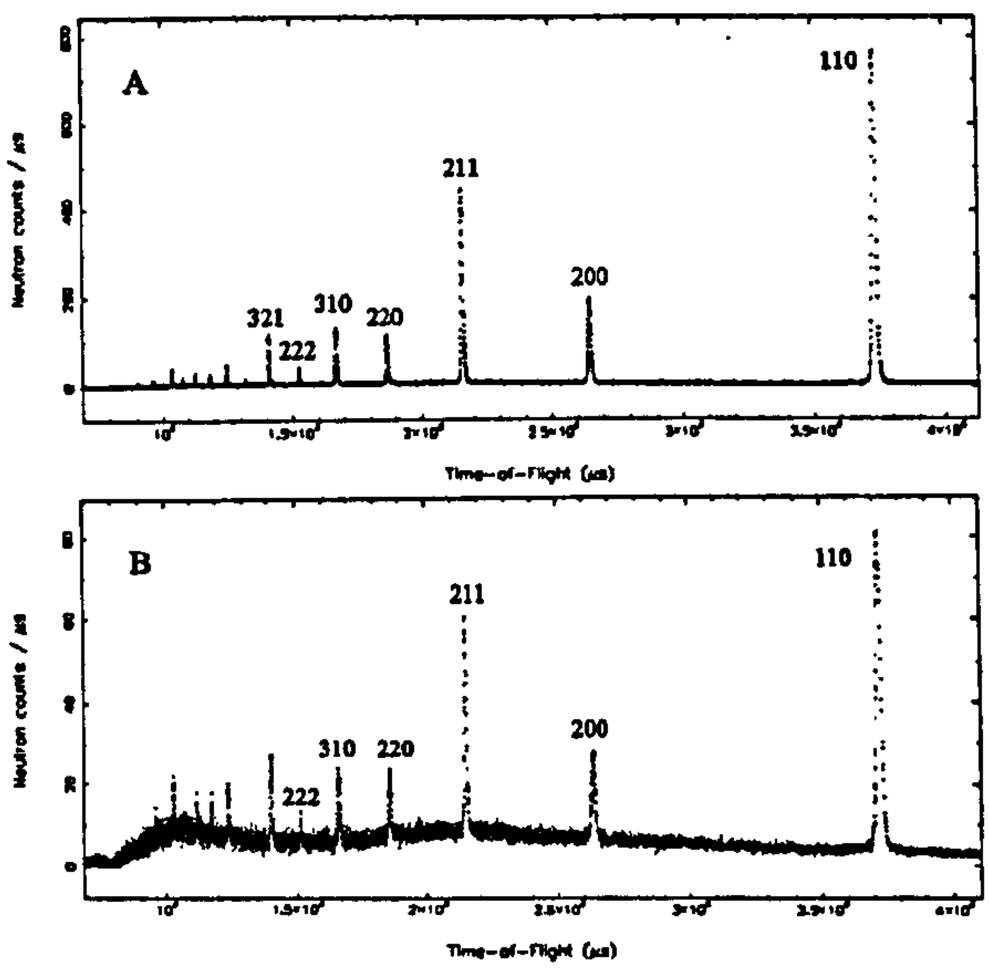

Figure 3.21: Diffraction spectra recorded from A) Tensile test specimens and B) extracted prestrained blanks.

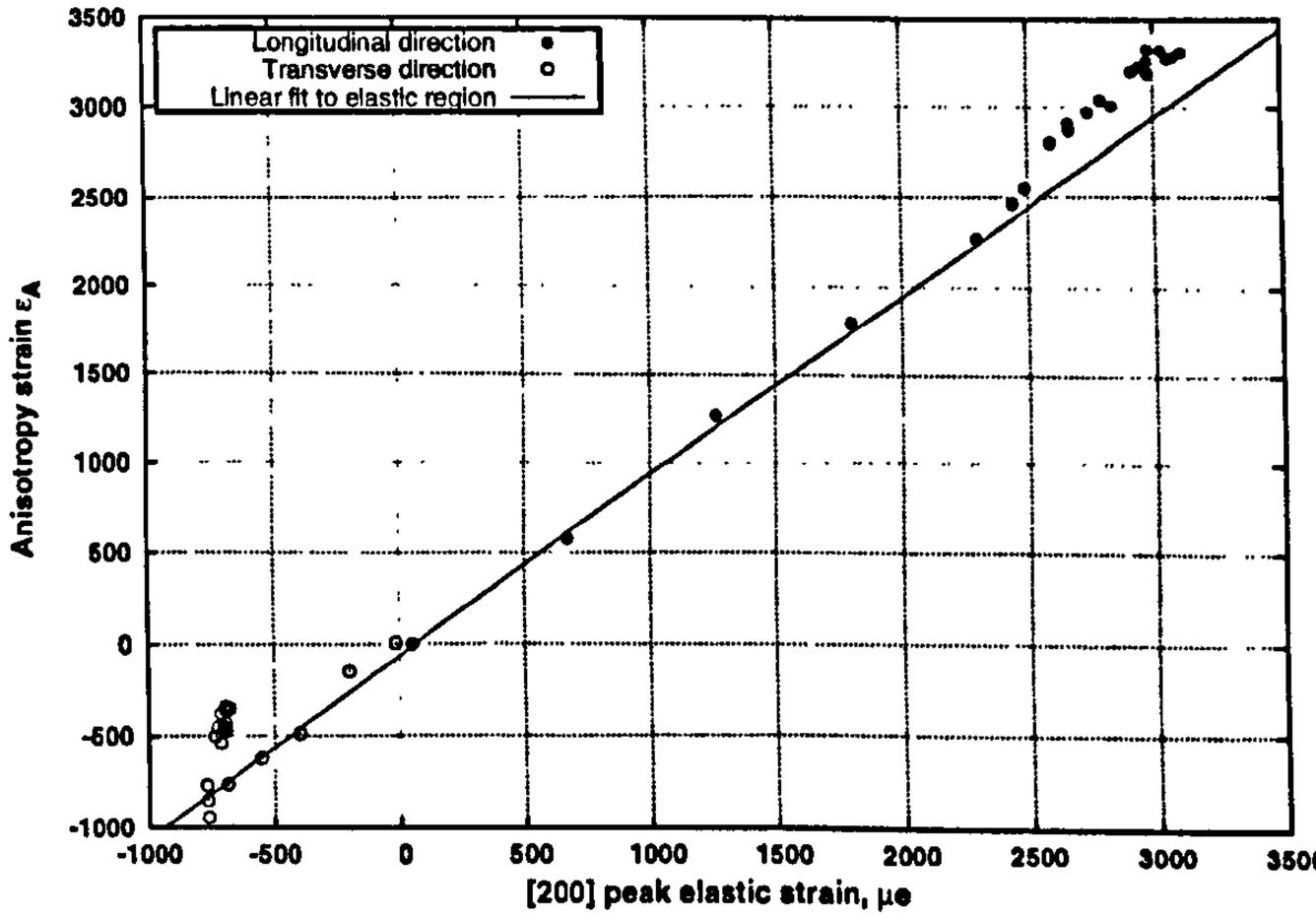

Figure 3.22: Evolution of the anisotropy strain, ϵ_A, measured in the tensile test specimen in directions longitudinal and transverse to the loading axis.

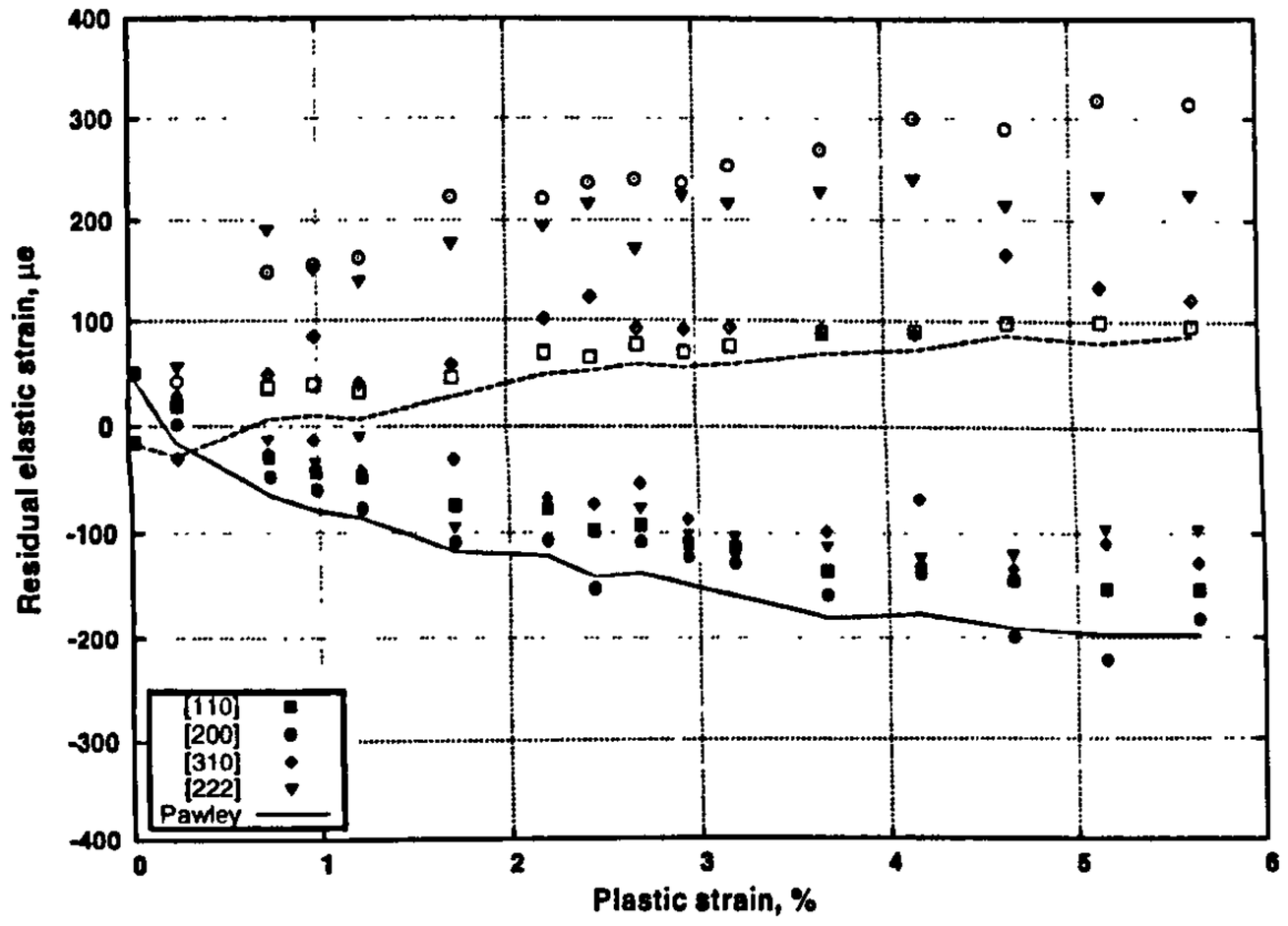

Figure 3.23: Residual strains, based on single diffraction peaks and Pawley refinement, measured in the tensile test specimen upon unloading to 10MPa. Filled symbols denote longitudinal strains, open symbols correspond to transverse strains.

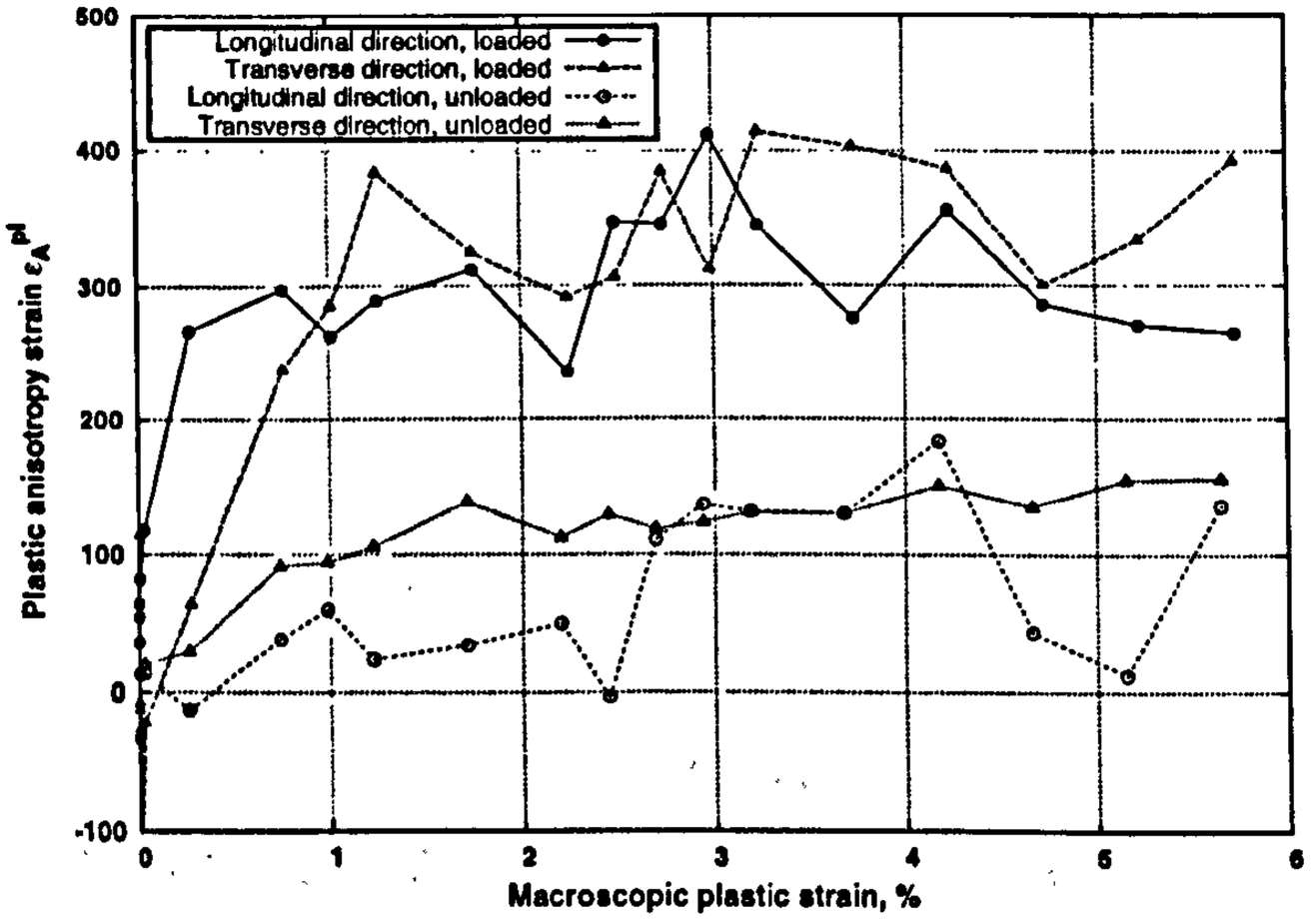

Figure 3.24: Plastic anisotropy strain, ϵ_A^{pl}, measured in the tensile test specimen in loaded and unloaded states, in directions longitudinal and transverse to the loading axis.

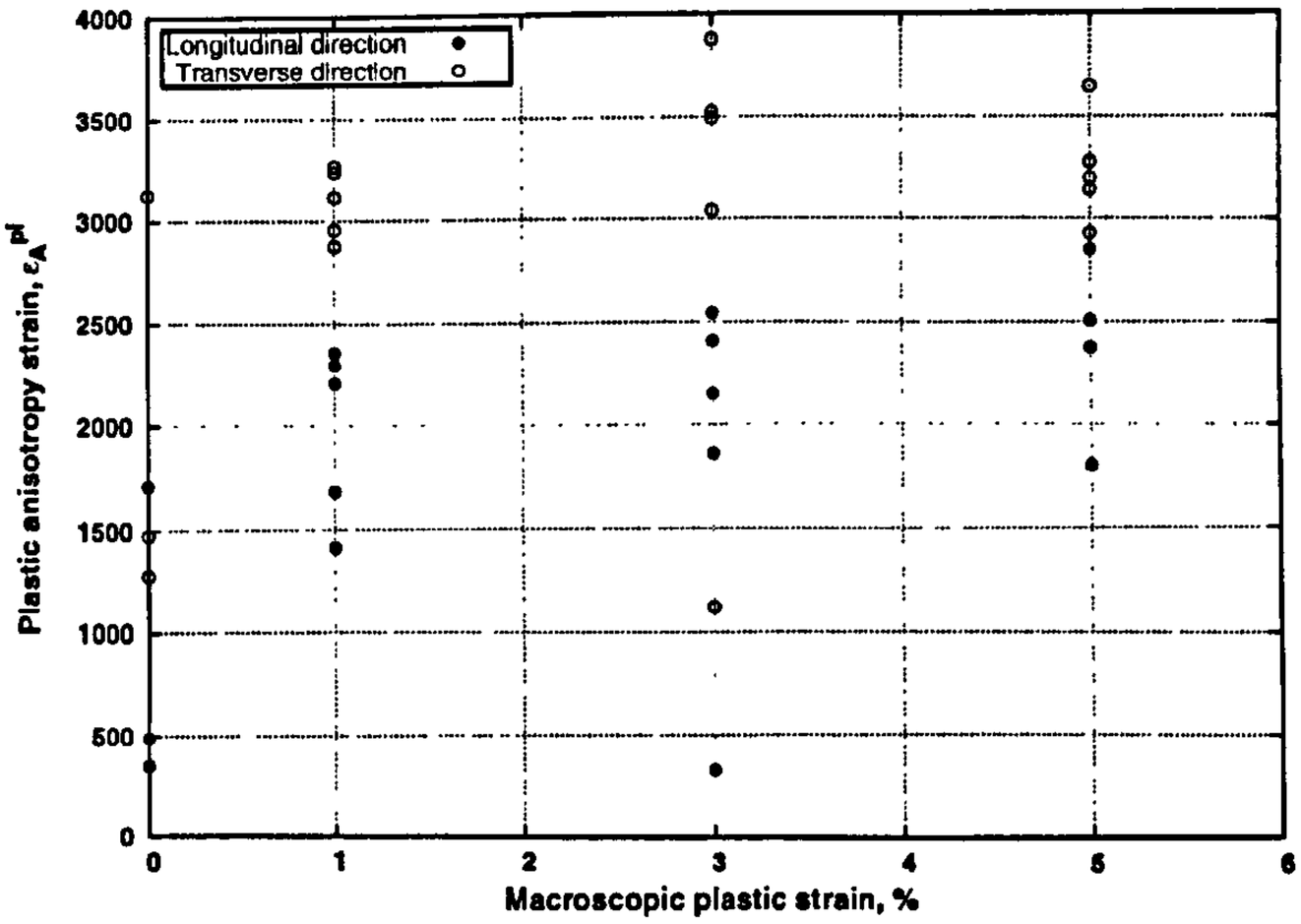

Figure 3.25: Plastic anisotropy strain, ϵ_A^{pl}, measured in the extracted CT blanks, in directions longitudinal and transverse to the loading axis.

Gaussian peak width and is obtainable directly from the fitting process, it was chosen as an appropriate peak width parameter for this work.

Variation of peak σ, recorded during the tensile test, shows a clear link between the onset of yielding and a dramatic increase in peak width (figure 3.26). There is also a weak dependency on elastic strain levels. There is no clear trend in the case of the {310}, {222} or {110} peaks but for the {200} and {211} there appears to be a linear dependence between the change in peak width, $\Delta\sigma$, and the level of strain in the elastic region.

It was found that a linear fit between the absolute magnitude of elastic strain in the direction of measurement and the change in σ was able to well represent the measured data in the elastic region. Fit was best for the {200} and {211} peaks and, as such, σ values from these two peaks were chosen as representative measures of plastic deformation.

Assuming a linear correlation with the level of elastic strain allowed for a separation of the elastic and plastic contributions to the peak broadening. Values with and without correction for elastic strain are plotted in figures 3.27 and 3.28, it can be seen that removal of the elastic component brings the loaded and unloaded measurements considerably closer together. Following the work of [127], an exponential fit was used to estimate the variation of $\Delta\sigma$

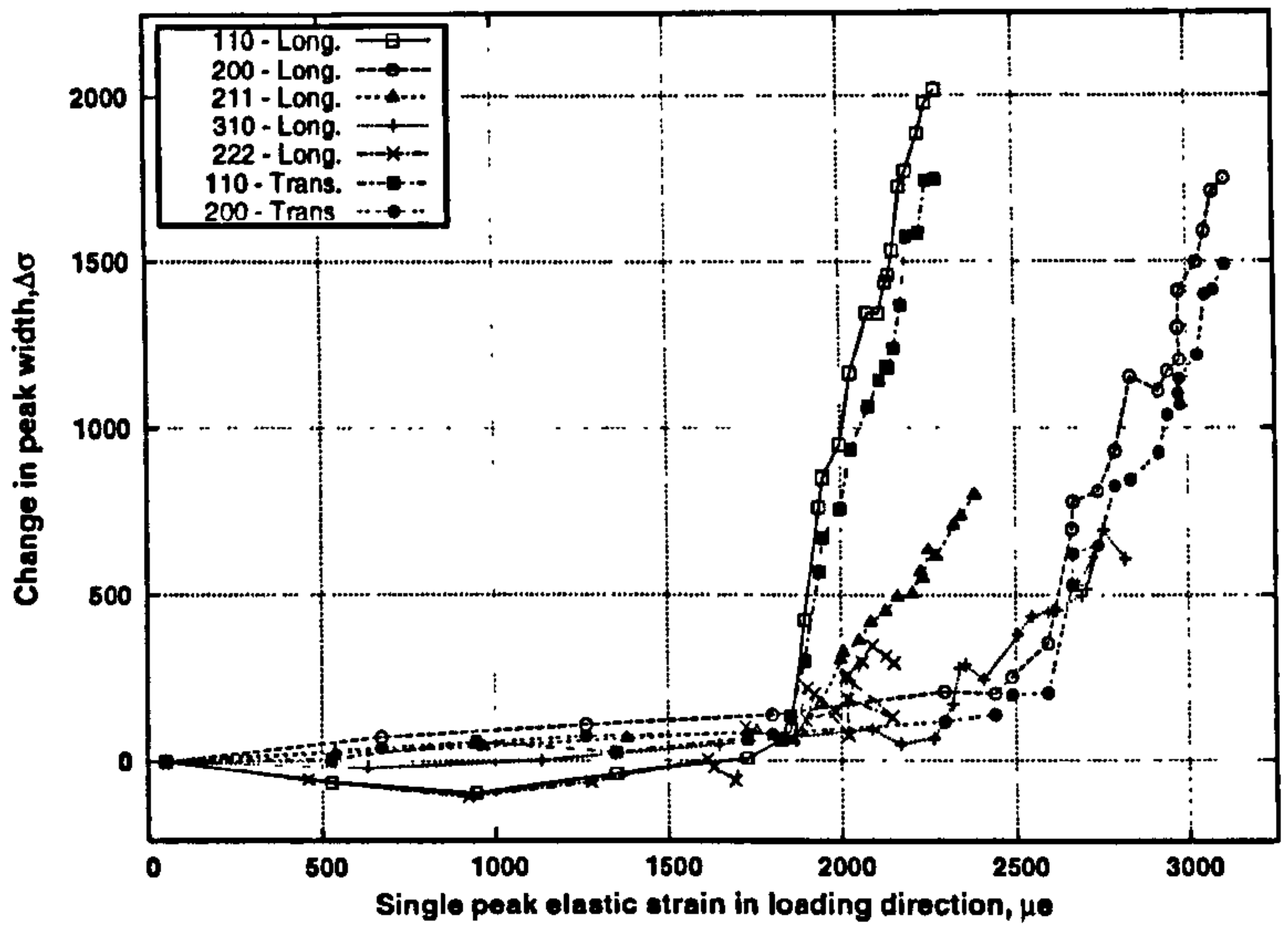

Figure 3.26: Variation in peak σ component as a function of peak strain, as recorded during the in-situ tensile test.

with plastic strain, the best fit equations are included in figures 3.27 and 3.28.

Results from the prestrained blanks showed similar variation between $\Delta\sigma$ and the level of equivalent plastic strain, indicated in figures 3.29 and 3.30. The overall magnitudes of the peak width increase are significantly larger in the 'blank' specimens than those suggested by the fit to the tensile test data. There is also significant scatter between measurements made in samples with the same level of macroscopic plastic strain.

3.6 Discussion

3.6.1 Effect of remnant residual stress

One of the aims at the outset of this section of work was to produce repeatable test specimens with residual stresses and thermal histories similar to those seen in real components, whether due to fabrication, repair processes or service history. The autogenous welding process used on the 316L plates can be seen to produce repeatable stress fields as shown in figure 3.16. Furthermore, the neutron diffraction measurements made on the plates suggest that finite element methods are able to produce acceptable predictions of the stress fields in such components.

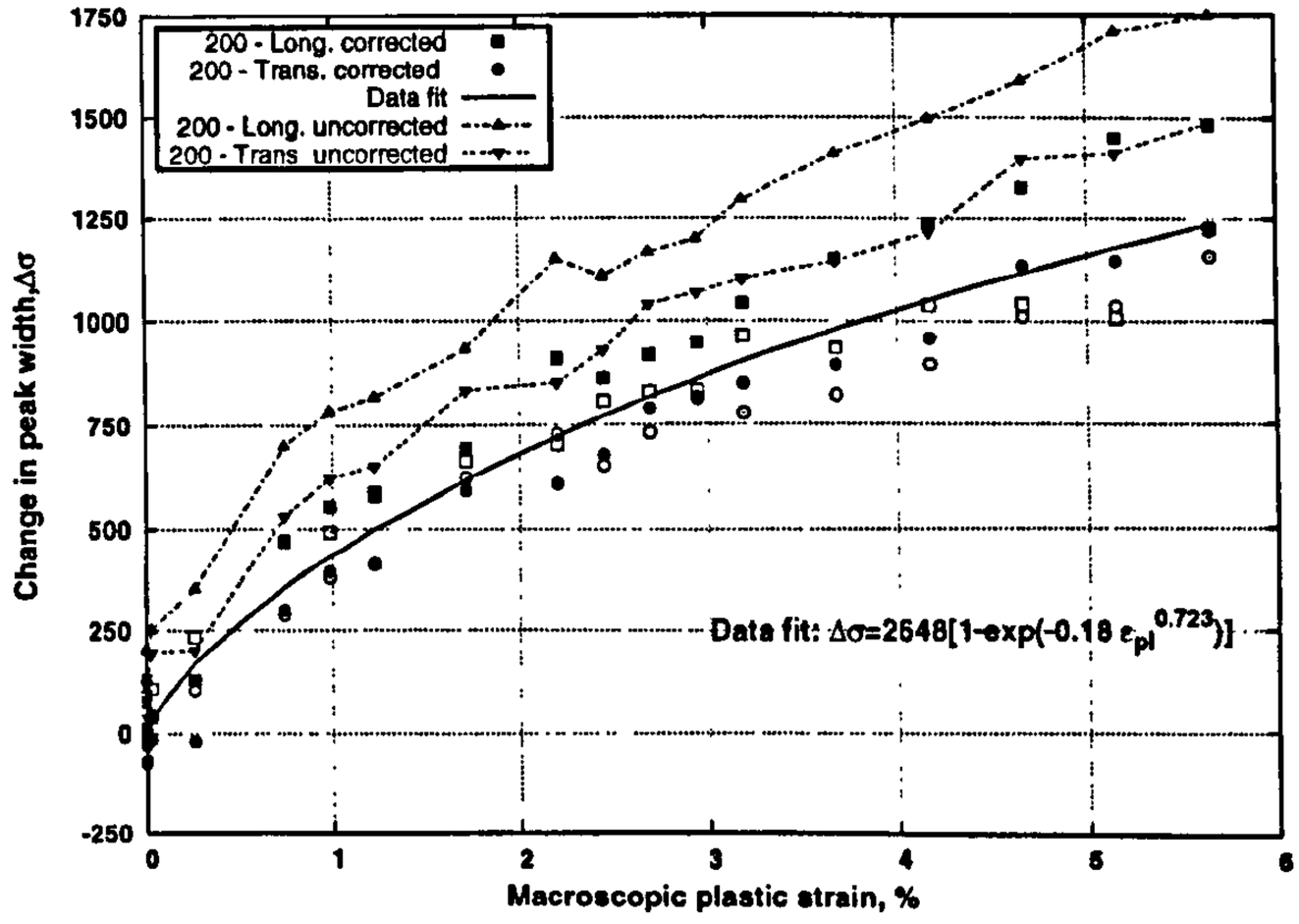

Figure 3.27: Variation in {200} peak σ component as a function of macroscopic plastic strain, as recorded during the in-situ tensile test. Open and closed symbols represent the loaded and unloaded states for each plastic strain level.

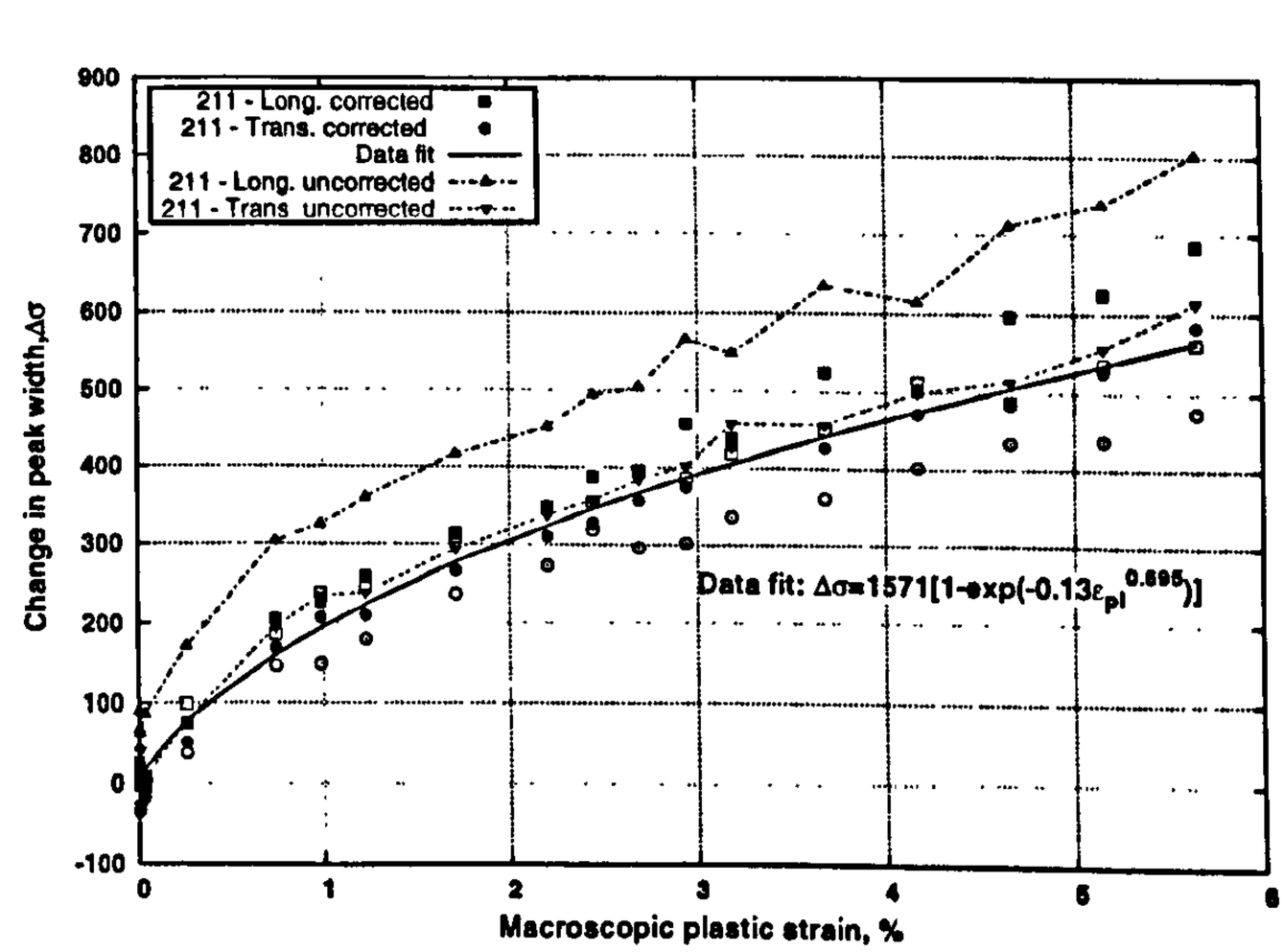

Figure 3.28: Variation in {211} peak σ component as a function of macroscopic plastic strain, as recorded during the in-situ tensile test. Open and closed symbols represent the loaded and unloaded states for each plastic strain level.

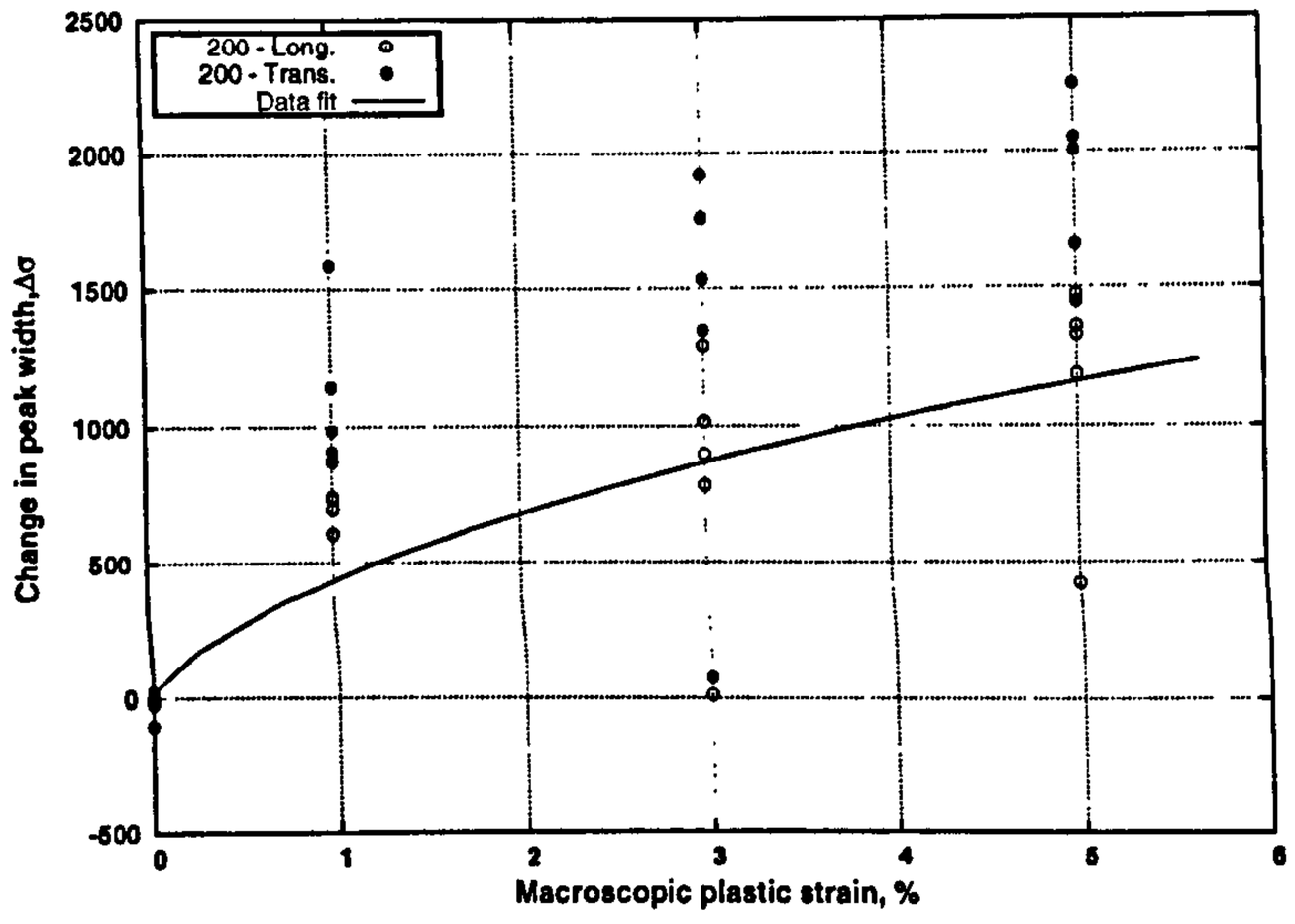

Figure 3.29: Variation in {200} peak σ component as a function of macroscopic plastic strain, as recorded in extracted prestrained blanks, compared with analytical broadening function as fitted to tensile test data.

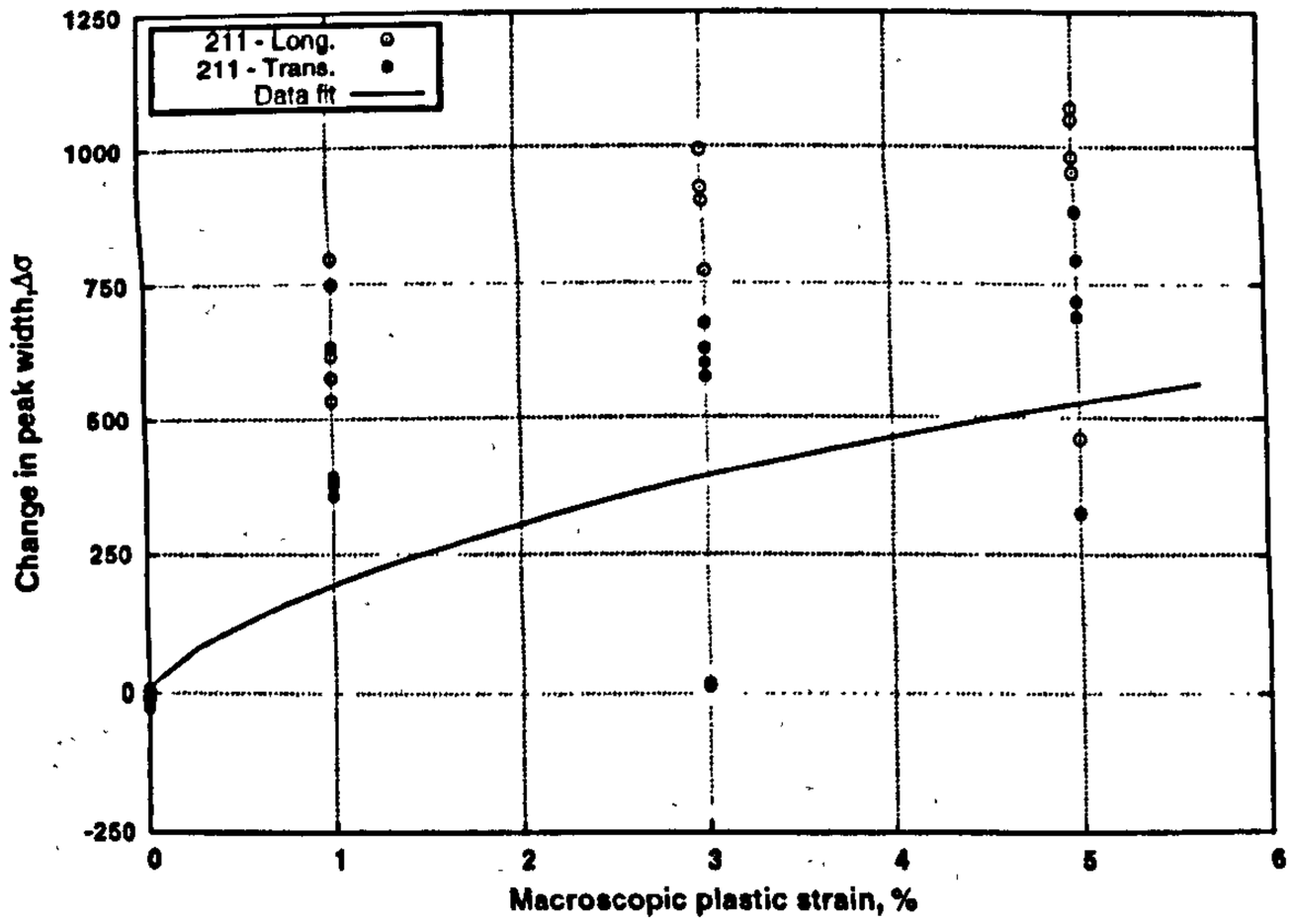

Figure 3.30: Variation in {211} peak σ component as a function of macroscopic plastic strain, as recorded in extracted prestrained blanks, compared with analytical broadening function as fitted to tensile test data.

It can be seen from the results produced that, depending on the stress field existing in the initial component, considerable stresses may remain in specimens extracted for fracture testing. The current analysis also shows that acceptable predictions of these remaining stresses can be made and, therefore, it may be possible to account for such remaining stresses when calculating fracture toughness. This has been successfully achieved in previous work [44].

Using a modified J integral, as in equation 2.24, based on the FE predictions of stresses remaining in the extracted 316L specimens, a value of K_{res} - the stress intensity factor due to residual stress only - of 12.9 MPa.m$^{0.5}$ was obtained. This value was calculated assuming plane strain conditions and room temperature material properties. Values of K_{IC} for a similar steel (316H) at 20°C were found to be of the order of 100 MPa.m$^{0.5}$ [74]. Therefore, although the value of K_{res} is significant, it is unlikely that the remaining stresses will have a significant effect on measured values. This is especially true if testing is carried out at room temperature as appreciable plasticity upon re-loading to failure may 'wash out' the majority of the initial residual stress field [108]. It should also be mentioned that the FE stresses, used to calculate the above value of 12.9 MPa.m$^{0.5}$, were higher than those measured, and therefore this value is likely to represent an over estimate of K_{res}.

Results from the P275 plate indicate that in cases where the parent component residual stress field is 'long range', i.e. where the distance across which the stress field is self-balancing is appreciably larger than the extracted specimen dimensions, remaining stresses can effectively be ignored.

The results do however indicate the importance of having accurate knowledge of the stress field in a prospective parent component in order to make informed assumptions about the likely impact of any remaining residual stress on measured toughness. There are also a number of other factors which should be considered when assessing likely impact on apparent K_{IC}, for example the expected ratio of K_{IC} to the material yield stress σ_Y. This will have an important impact on the size of the plastic region when loading the fracture specimen to failure and therefore the impact of the remaining residual stress. Furthermore, the specimen geometry will affect not only the level of plasticity (through varying constraint) but also the magnitude of the un-relaxed stresses.

In reality, the level of plastic strain in a material is also known to affect measured K_{IC} values, as discussed in chapter 2, and as such strain effects should also be considered.

3.6.2 Feasibility of plastic strain determination

It is apparent that both plastic anisotropy strain and diffraction peak broadening are strongly related to levels of macroscopic deformation. It would also appear that there are other influencing factors affecting the variation of these parameters with macroscopic plastic strain which inhibit accurate calibration and transference of relationships between specimens.

Variation of the anisotropy strain was found to be dominated by the elastic strains in the measurement volume. This is in contrast to the results presented in [122] where the values of ϵ_A^{pl} were of similar magnitude to those obtained for ϵ_A^{el}. Due to the dominance of the elastic anisotropy in this work, separation of the relatively small plastic component was difficult.

It is noticeable that, using a simple linear relationship between elastic strain on the {200} peak and ϵ_A^{el}, there is a consistent difference between the values of ϵ_A^{pl} measured with and without external loading (figure 3.24). This represents a significant problem in terms of using ϵ_A^{pl} to measure plastic deformation as a dependence on elastic lattice strain is still apparent.

In the works of [124] and [122], ϵ_A^{pl} was seen to vary in a near-linear fashion with plastic strain and was shown to be transferable between geometries. The primary difference between these trends and those here may be related to the differing crystal structure of the tested materials. Both previous works used FCC materials (austenitic steel and aluminium), in contrast to the BCC ferritic steel used in the current work.

It can be shown that the FCC structure possesses close packed slip planes of Miller index {111}, in the case of a BCC structure there are no close packed planes, resulting in a greater inter-atomic spacing in the slip plane, generally corresponding to {110}. The result is that the Burger's vector $|b|$ for a BCC structure is greater than for the FCC case, equal to $a\sqrt{3}/2$ compared to $a/\sqrt{2}$. As the slip system in the FCC structure has far greater symmetry than that in a BCC lattice, slip is able to occur in a more uniform manner throughout the material, rather than at a limited number of preferentially aligned grains.

Therefore, since ϵ_A is essentially a measure of disorder in the lattice structure and likely to be related to dislocation movement, it may well be that deformation in FCC materials is more easily characterised by this method. Nonetheless this does not explain the considerable increase in ϵ_A^{pl} measured in the extracted blanks compared with the tensile test data. It may be that the deformation at a granular scale in the thicker samples is more disordered

than that in the tensile test samples, possibly due to higher constraint levels generating stresses transverse to the load direction.

The increase in peak broadening shows only negligible dependence on elastic strain, often within the margin of experimental error which was of the order of $\sigma \pm 100$. Despite showing good independence from both elastic strain and measurement direction, the calibrated $\Delta\sigma$-ϵ_{pl} relationship still underestimated the measured response from the thicker 'blank' samples. This may be a result of the increasing disorientation in the thicker samples or simply the increased path length reducing the accuracy of the measurements.

The agreement is however significantly better than for the anisotropy method and the tensile test fit provides a reasonable lower bound to the recorded changes in σ in the CT samples. It may be that repeat measurements on a fixed wavelength diffraction instrument, providing more detailed measurements of the shape of a single diffraction peak, may yield better results with this approach than time of flight instruments such as ENGIN-X.

It is also worth noting that plastic strain, in an engineering sense, has questionable relevance at the small scales of interest for diffraction measurements. The two methods used here are based on measurement of increasing inhomogenity of strain within the measurement volume. It may well be that this cannot be simplistically related to the levels of macroscopic deformation without a more rigorous consideration of the deformation at a micromechanical scale.

An example may be the existence of Lűder's strains which would produce considerable variation in local stresses and strains across local deformation bands. The A533B steel tested was seen to exhibit discontinuous yielding in figure 5.6, up to around 1% plastic strain. It is notable that the sharpest rise in both ϵ_A^{pl} and $\Delta\sigma$ occurred between 0% and 1% plastic strain in the prestrained blanks so it may be possible that the presence of regions of discontinuous deformation may have contributed to the increase in the scatter and value of both parameters.

It is also important to consider the role of dislocation movement and nucleation during plastic deformation, which may be influenced by a number of microstructural considerations for example grain size, current dislocation population and the presence of dislocation nucleators such as impurity atoms in the lattice.

3.7 Conclusions

A series of neutron diffraction measurements were used to investigate the relaxation of stresses in samples of sizes typical of CT fracture specimens, extracted from large welded 'parent' plates. Stresses were measured in the parent plates after welding and in the extracted samples. The potential influence of the remnant stresses on subsequent measured fracture toughness was also considered.

An investigation was also conducted into the ability of diffraction peak broadening ($\Delta\sigma$) and anisotropy of strain (ϵ_A^{pl}) determined from differing diffraction peaks to characterise plastic deformation. Variation of $\Delta\sigma$ and ϵ_A^{pl} with strain in A533B ferritic steel was calibrated from tensile test specimens. The determined relationships between the anisotropy strain or change in peak width with plastic strain were then used to attempt to measure plastic strain in prestrained blanks for CT fracture specimens.

The results of this work have produced the following conclusions:

1. Neutron diffraction measurements, made on a 'blank' for a CT fracture specimen extracted from an autogenously welded plate, have shown that considerable residual stresses may remain in fracture specimens removed from large scale components.

2. From comparison with neutron diffraction data, finite element methods were shown to produce good estimates of the stresses remaining in specimens after removal from larger components.

3. Based on the limited data available, remaining stress magnitudes were seen to depend on the nature of the initial stress field. Where the residual stress field was self balancing over a short distance considerable stresses remained. Where the stresses were self balancing over a scale much larger than the extracted component, the stresses in the extracted specimen were near zero.

4. The stress intensity factor, resulting from residual stress in the 'worst case scenario' specimens taken from an autogenously welded plate, was found to be 12.9 MPa.m$^{0.5}$, compared to a fracture toughness of approximately 100 MPa.m$^{0.5}$.

5. The {310} diffraction peak exhibited a minimal effect of elastic or plastic

anisotropy in the ferritic steel tested and also provided the closest approximation to the macroscopic stress/strain response. As such it would appear that the {310} peak is an appropriate choice for the determination of macroscopic stresses in such materials.

6. Both the plastic anisotropy strain ϵ_A^{pl} and the peak width broadening parameter $\Delta\sigma$ were found to be correlated with levels of macroscopic strain, although the quantitative variation was found to vary considerably between the sample geometries used in this work.

7. The elastic contribution of the anisotropy strain was found to dominate the overall strain anisotropy response. This is in contrast to previous work on FCC materials (austenitic steels and aluminium) where the elastic and plastic components were of similar magnitude.

8. Plastic strain levels were found to be well correlated with levels of peak broadening, although considerably larger increases in peak width were noted in thicker specimens. It is likely that use of single wavelength diffractometer instruments may reduce the overall scatter in measurements in such samples by allowing more detailed determination of a single appropriate diffraction peak.

9. It was noted that many of the problems in plastic strain measurement encountered in this work were not noted in other published works. It is believed that this may be due to the BCC atomic structure of the ferritic steel used in this case, compared to the FCC aluminium and austenitic steels used in other works.

Chapter 4

Re-analysis of existing experimental data

4.1 Introduction

In order to study the capabilities of the models of fracture discussed in chapter 2 it was elected to re-analyse a range of previously published experimental data. The aim of this exercise was to attempt to determine the range of validity and limitations of a number of models for brittle fracture. At the outset, the intention was to provide guidance for the design of future experiments, modifications to existing models of fracture or formulation of new approaches.

4.2 Fracture data considered

In order to consider a wide range of specimen geometries, a range of previously reported cleavage fracture data were re-analysed. All data sets corresponded to low temperature cleavage fracture of ferritic steels.

4.2.1 A508 CT specimens

Fracture data were obtained by Mahmoudi [130] for A508 steel compact tension (CT) specimens, and have been reported in [131]. All specimens were loaded to failure at $-170°C$.

In all cases, 'cracks' were inserted by means of EDM wire machining, producing notches with nominal end diameters of 0.1mm. Three specimen variants were tested, corresponding to the as-received (AR) case as well as

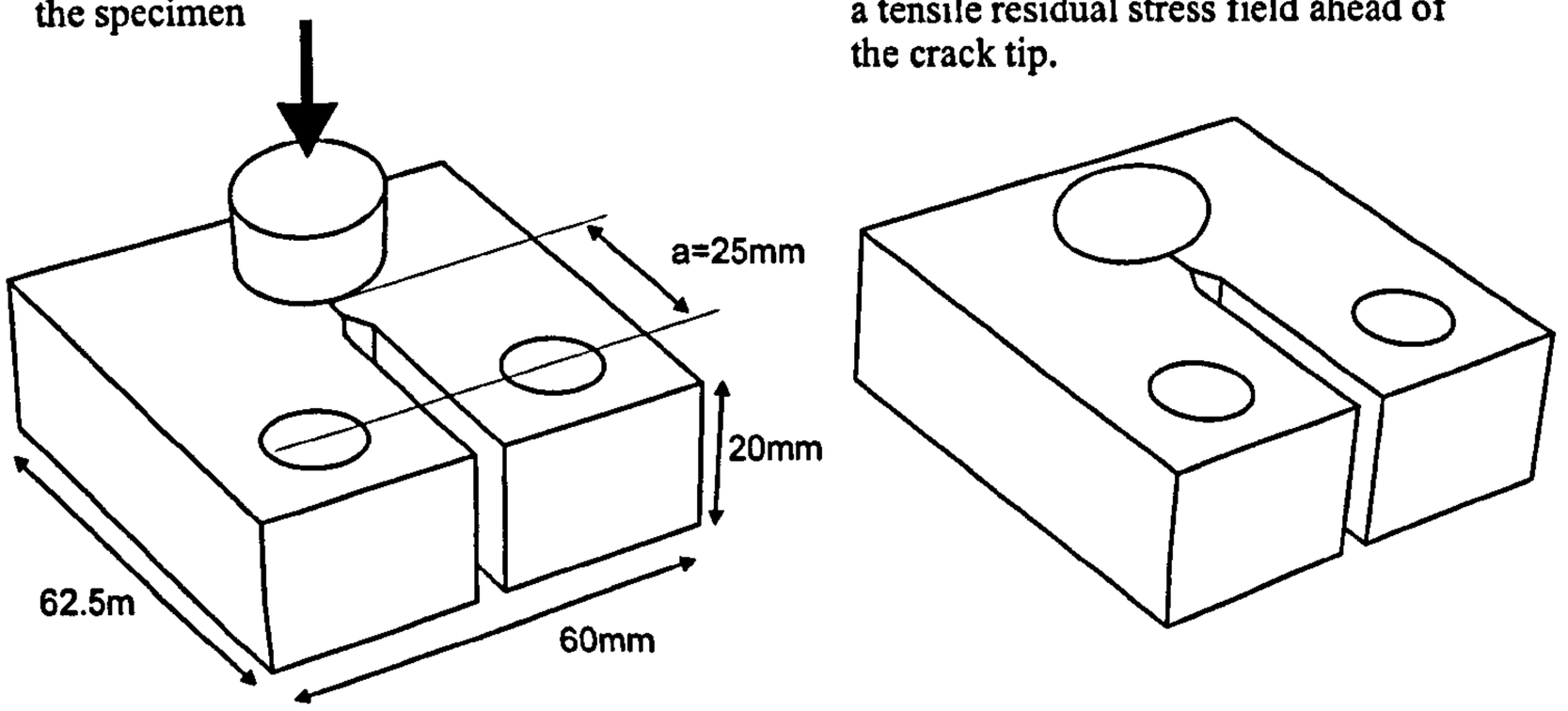

Figure 4.1: Schematic diagram of punching process used in CT specimens subjected to the PUCF load cycle.

following preloading at room temperature (load-unload-cool-fracture, LUCF) and side punching at room temperature (punch-unload-cool-fracture, PUCF).

The LUCF cycle consisted of applying a 62.5kN tensile preload to the CT specimen at 20°C before cooling and loading to fracture. The specimen geometry and side punching process used in the PUCF cycle is illustrated in figure 4.1, further detail can be found in [132]. Preloading was applied to all samples after creation of the EDM notch.

4.2.2 A533B SEB/SENB specimens

A number of single edge-cracked bend (SEB) specimens, fabricated from A533B ferritic steel, were tested to failure in 3-point bending by Mirzaee-Sisan [74]. The geometry for these specimens is displayed in figure 4.2. All specimens were fractured at −150°C by 3 point bend loading.

A total of 8 single edge-notched bend specimens (hence referred to as SENB), with EDM wire cut notches of diameter 0.1mm, were fractured in the AR state and a further 5 were fractured following a cycle of in-plane compression (compression-unload-cool-fracture, CUCF). These have since been re-analysed in [44].

The compression tools and specimen geometry are illustrated in figure 4.2 (A). Specimens undergoing the CUCF cycle were subjected to compression (at

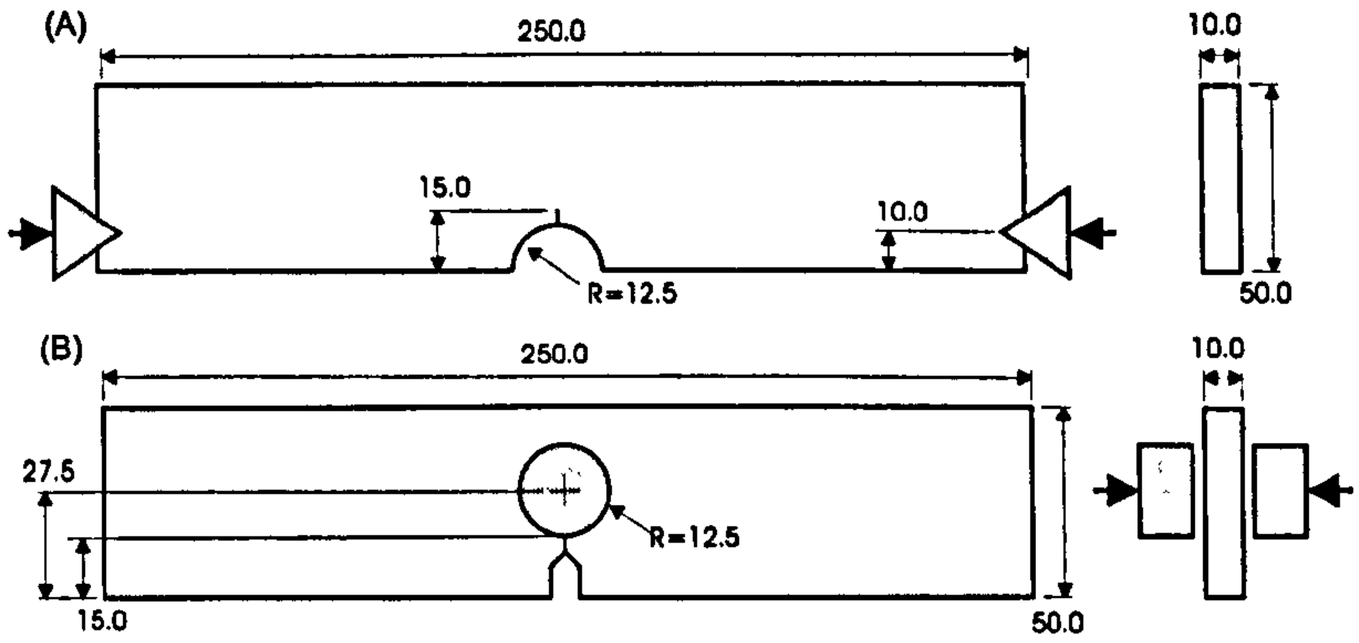

Figure 4.2: Geometry of A) SENB and B) SEB specimens showing preloading by in-plane compression and side punching. Dimensions in mm.

20°C) and unloaded to create a tensile residual stress field at the notch root, before introducing a sharp notch by EDM wire machining. Samples were then cooled and loaded to failure. Further detail as to the preload and manufacture may be found in [74].

A further 20 SEB specimens, of dimensions as in figure 4.2 (B), were also tested in [74]. The total crack length was 15mm, such that a/w was comparable with the SENB specimens. All specimens of this geometry were subjected to fatigue pre-cracking at room temperature, rather than creating notches with EDM cutting. A total of 10 of the SEB specimens were subjected to side punching at room temperature (following pre-cracking) as illustrated in 4.2 (B), before cooling and loading to failure.

4.2.3 A508 RNB specimens

Round notch bar (RNB) specimens, manufactured from A508 steel, were also tested by Mirzaee Sisan [74]. Loading to fracture was undertaken at -150°C.

Three RNB specimen types were tested, and reported previously in [72]. Specimen geometries are illustrated in figure 4.3, with minimum diameters of 7.7mm, 8mm and 15mm (henceforth referred to as RNB7.7, RNB8 and RNB15 respectively). A total of 27 specimens (9 of each geometry type) were fractured in the AR state. In addition, 8 RNB7.7 and 8 RNB8 specimens were fractured with a LUCF load cycle, using room temperature preload such that the net tensile stress at the minimum cross section was 995 MPa.

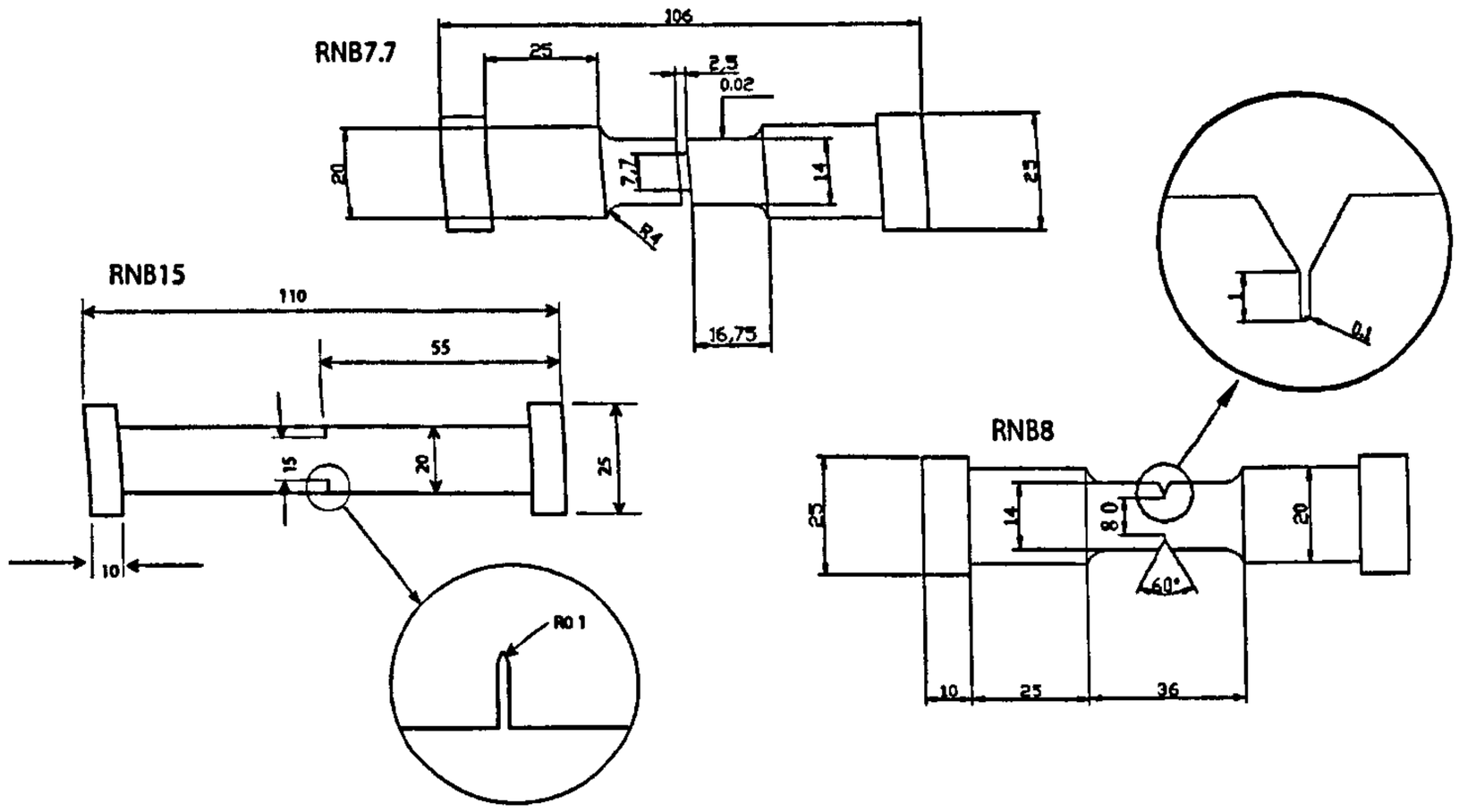

Figure 4.3: Geometry of round notched bar specimens, diagram adapted from [74]. Dimensions in mm.

4.3 Finite element simulations

To apply many of the fracture models discussed in chapter 2, detailed stress and strain field data were needed. To obtain estimates of the stresses and strains at failure, finite element simulations of the fracture tests were performed. All modelling was carried out using the ABAQUS finite element package, versions 6.6 and 6.71 [133] .

4.3.1 A508 Steel CT specimens

Making use of the two planes of symmetry in the CT specimens, 1/4 of the total geometry was modelled with appropriate symmetry boundary conditions. The mesh used, including the refined structure around the EDM notch, is shown in figure 4.4. Minimum element dimensions in the region immediate to the notch tip were approximately 20μm. The mesh was constructed with approximately 22000 second order brick type elements, ABAQUS element type C3D20R, with 20 nodes and 8 Gauss points per element.

The code used to calculate values of F_k (as in equation 2.26 and discussed further in section 4.4.1) was only valid for two dimensional geometries. Therefore, two dimensional plane strain models were also constructed for the LUCF and AR cases. Values of F_k were not calculated for the PUCF specimens as

the load cycle could not be adequately simulated in two dimensions.

Loading of the specimens was modelled by applying a distributed load to the inside of the loading pin holes in the specimens. In the case of the LUCF load cycle, discrete steps were included for the preload, subsequent unload, cooling and final reloading to fracture. Material properties at 20°C and -170°C were taken from [130] assuming isotropic hardening.

4.3.2 A533B Steel SEB/SENB specimens

One quarter models of the SEB and SENB specimens were also constructed, making use of the symmetry of the geometry as before. In the case of the fatigue pre-cracked SEB specimens, the crack was modelled by removing the symmetry boundary condition along the crack surface. The near crack mesh structure is illustrated in figure 4.5 (A). Meshes were constructed of approximately 16000 second order brick elements, ABAQUS element type C3D20R.

For the SENB specimens, where EDM notches were used to initiate fracture, the wire cutting process was simulated by removing elements along the cutting path. The notch tip mesh in this case is illustrated in figure 4.5 (B). To allow redistribution of stresses during the cutting process, elements were removed in 4 increments to simulate the build up of a plastic wake behind the moving crack tip [134]. As for the A508 CT tests, two dimensional models were also constructed to allow calculation of the Eshelby force F_k.

Loading in three point bending was applied experimentally using rollers. This was approximated in the modelling by constraining a small region on the specimen, where the roller would have been in contact, to move as a rigid body. Material constitutive properties at 20°C and -150°C were assumed to match those found by Smith [135], also reproduced in [74], using an isotropic hardening model.

4.3.3 A508 Steel RNB specimens

Due to the rotational and axial symmetry of the RNB geometries, axisymmetric half models were used in all cases. Meshing was carried out with second order axisymmetric elements with 8 nodes and 4 integration points per element, ABAQUS element type CAX8R with approximately 2000 elements per model. Material response at 20°C was taken from [136] and behaviour at -150°C was assumed from [137] as in [74].

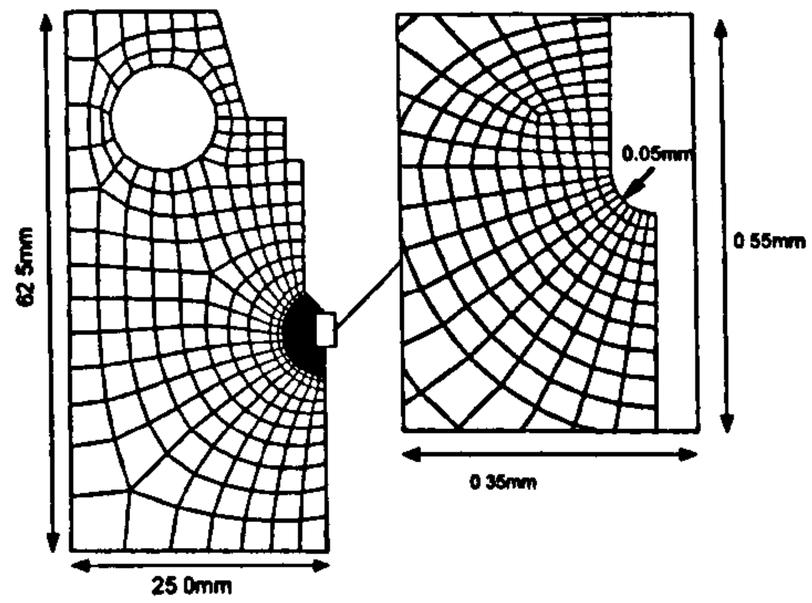

Figure 4.4: Mesh structure for finite element modelling of A508 CT specimens.

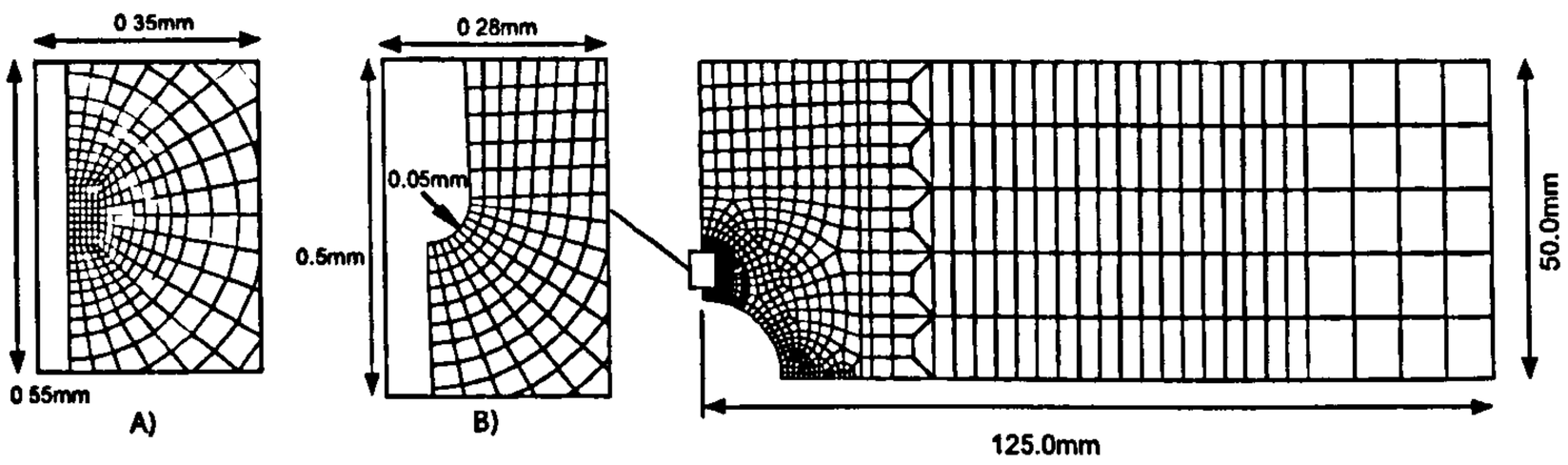

Figure 4.5: Mesh structure for finite element modelling of A533B SEB and SENB specimens.

For specimens subjected to the LUCF load cycle, discrete steps were used to model the initial load, subsequent unload, cooling to -150°C and final load to failure.

4.4 Fracture models considered

4.4.1 Crack tip parameters

J integral

Values of the J integral may be calculated according to equation 2.18 using an inbuilt routine in the ABAQUS finite element code. However, as the PUCF, LUCF and CUCF load cycles result in strongly non-proportional loadings, modified, path independent J values were also calculated according to equation

2.24 using the JEDI (J by equivalent domain integral) postprocessor[1]. The modified J formulation of equation 2.24 is henceforth referred to as J_m.

Eshelby force on singularities

The Eshelby force was calculated, based on finite element results, with a code developed by the author using the MATLAB software package. To do so, equation 2.26 was converted to an area integral

$$F_k = \int_{A_{fpz}} \left(\frac{dW}{dx_k} - \sigma_{ij} \frac{d\epsilon_{ij}}{dx_k} \right) dA \tag{4.1}$$

which was then evaluated in discrete form according to

$$F_k = \sum_{I=1}^{N} \left[\left(\frac{dW}{dx_k} \right)^I - \sigma_{ij}^I \left(\frac{d\epsilon_{ij}}{dx_k} \right)^I \right] v^I \tag{4.2}$$

where the superscript I indicates values at an integration point and v^I is a weighting value, equivalent to the volume associated with the integration point. The integration area A_{fpz} was taken to be the crack tip plastic zone, as obtained from the FEA results using the von Mises yield criterion. During an infinitesimal crack advance, the crack tip plastic region is assumed to move with the crack tip.

Probabilistic models

A number of authors have suggested methods of using crack tip parameters in probabilistic models of failure to describe the scatter in fracture data e.g. [76]. A commonly used model, based on the stress intensity factor K is

$$Pf = 1 - \exp\left(- \left[\frac{K_I - K_m}{K_0 - K_m} \right]^M \right) \tag{4.3}$$

and a similar form is proposed here for F_k,

$$Pf(F_k) = 1 - \exp\left[- \left(\frac{F_k}{\alpha} \right)^\beta \right] \tag{4.4}$$

where K_0, K_m, m, α and β are fitted parameters. When crack tip stresses are controlled by K, it was demonstrated in [76] that for equation 4.3 $M = 4$ and

[1]The author wishes to thank SERCO TAS for making the JEDI code available.

a threshold of $K_m = 20$ MPa.m$^{0.5}$ was sugested.

4.4.2 Local approach models

Stress based models

A number of local approach models, based on the Beremin formulation, were used to predict fracture after prior loading. Weibull stresses according to equations 2.37 and 2.43 were calculated from finite element results, using MATLAB code to evaluate the discrete formula

$$\sigma_w = \left[\sum_{i=1}^{I}\left((\sigma_1^i)^m - (\sigma_{th}^i)^m\right)v^i\right]^{1/m} \tag{4.5}$$

with $v^i = 0$ when $\sigma_1^i < \sigma_{th}^i$. Equation 4.5 was evaluated over the currently yielding material volume, i.e. that where plastic strain is increasing. This was determined from the ABAQUS output variable *YIELD*, which determines whether or not local effective plastic strain has increased over the last load increment. For the standard Beremin model of equation 2.37, the threshold σ_{th} was set to zero.

Stress and strain based models

The simplest strain modified local approach formula used was based on the formulation of Gao [85]. Using equivalent plastic strain to characterise defect nucleation and including a local threshold stress, Weibull stress was defined as

$$\sigma_w = \left(\frac{1}{V_0}\int_V \epsilon_e^p\,(\sigma_1^m - \sigma_{th}^m)\,dV\right)^{1/m} \tag{4.6}$$

which is evaluated using the discretised equation.

$$\sigma_w = \left[\sum_{i=1}^{I}(\epsilon_e^p)^i\left((\sigma_1^i)^m - (\sigma_{th}^i)^m\right)v^i\right]^{1/m} \tag{4.7}$$

Equation 4.6 assumes that nucleated defects remain active, as such the active microcrack population is an increasing function of strain. If it is assumed that defects, not propagated by local stresses, are blunted by further plastic deformation, a modified Weibull stress can be defined.

$$\sigma_w = \int_{Va} \left[\int (\sigma_1^m - \sigma_{th}^m)\, d\epsilon_e^p \right] dV \tag{4.8}$$

which is evaluated incrementally over a load step. Between load steps $k-1$ and k, the increase in σ_w is

$$\Delta\sigma_w^m = \sum_{i=1}^{I} \left((\bar{\sigma}_1^{i,k})^m - \sigma_{th}^m \right) (\Delta\epsilon_e^p)^{i,k} v^i \tag{4.9}$$

where $(\Delta\epsilon_e^p)^{i,k}$ is the increment of equivalent plastic strain at integration point i between steps $k-1$ and k. The stress term $\bar{\sigma}_1^m$ is the mean value of σ_1^m over the load increment given by

$$\bar{\sigma}^m = \frac{1}{(\sigma^k - \sigma^{k-1})} \int_{\sigma^{k-1}}^{\sigma^k} \sigma^m d\sigma = \frac{(\sigma^k)^{m+1} - (\sigma^{k-1})^{m+1}}{(\sigma^k - \sigma^{k-1})(m+1)} \tag{4.10}$$

The current Weibull stress is then $(\sum \Delta\sigma_w^m)^{1/m}$. A more complete derivation is presented in appendix C.

4.5 Calibration of local approach parameters

In order to usefully employ any of the local approach criteria so far discussed, it is necessary to determine reliable values for the relevant modelling constants. Traditionally this is achieved by selecting values which maximise agreement between the model in question and experimental sets of failure data. The choice of parameter to represent goodness of fit and the algorithm used for the fitting process can have a considerable effect on the determined model parameters and therefore any predictions of future failure.

4.5.1 Matching Weibull slope, m

Equation 2.36 is perhaps the most commonly used and constants can be obtained using linear rectification and the method of least-squares fitting (LSF). Using logarithms, equation 2.36 can be arranged into a linear function of $\ln(\sigma_w)$, m and $\ln(\sigma_0)$.

$$\ln(-\ln(1-Pf)) = m\ln(\sigma_w) - m\ln(\sigma_0) \tag{4.11}$$

Failure data are arranged, for example by fracture load, and assigned estimated failure probabilities using a ranking equation such as [138]

$$Pf_r^i = \frac{i - 0.5}{N} \tag{4.12}$$

where i is the position of a given test in the ranked data set and N is the total number of tests. Failure data are then plotted on axes of $\ln(\sigma_w)$ against $\ln(-\ln(1 - Pf_r))$. A linear fit is then performed with the slope and intercept providing the values of m and $-m\ln(\sigma_0)$.

As a value of m must be assumed in order to calculate values of σ_w, the best fit value for m is found when the assumed value is equal to the value found from the linearisation. A searching algorithm for this method was suggested by [139].

1. Assume an initial value for m, hence referred to as $m*$.

2. Calculate Weibull stresses at fracture loads.

3. Plot $\ln(-\ln(1 - Pf_r))$ against $\ln(\sigma_w^i)$.

4. Perform linear fitting to estimate values of m and σ_0, m^{fit} and σ_0^{fit}.

5. If $m^{fit} = m*$, then $m = m^{fit}$ and $\sigma_0 = \sigma_0^{fit}$. If $m^{fit} \neq m*$, set $m* = m^{fit}$ and repeat steps 2-5 until the value of m converges.

4.5.2 Maximising coefficient of determination R^2

For the linear equation $y = Ax + B$, the parameters A and B are easily determined by linear regression. The correlation between the model obtained from this fit and the data used to calculate the fit can be characterised by the coefficient of determination, R^2.

$$R_{xy}^2 = \left[\frac{\sum (x^i - \bar{x})(y^i - \bar{y})}{(N-1)S_x S_y}\right]^2 \tag{4.13}$$

where $\bar{x}$ and S_x are the mean and standard deviations for the values of x.

Equation 2.36 may be linearised with respect to σ_w as follows

$$[-\ln(1 - Pf)]^{1/m} = \frac{\sigma_w}{\sigma_0} \tag{4.14}$$

where for a given m, σ_w is calculated at failure loads and then linear regression of equation 4.14 may be performed to obtain the value of σ_0. The value of R^2 may then be calculated for the fit, taking $x^i = \sigma_w^i$ and $y^i = [-\ln(1-Pf_r^i)]^{1/m}$, hence referred to as R_f^2. Alternatively the correlation between Pf as predicted from the model and estimated from equation 4.12 may be calculated by setting $x^i = Pf_r^i$ and $y^i = Pf(\sigma_w^i, m, \sigma_0)$, hence referred to as R_{Pf}^2. This may be more appropriate as a measure of goodness of fit as the linearisation method may unduly weight the fitting process. This in turn may mean that the 'best' fit to the linearised data does not necessarily produce the best agreement with the estimated failure probabilities.

Determining m by maximising R^2 requires a 'grid search' approach. Values of σ_w are calculated for a range of m, a corresponding σ_0 is found from the linearisation of equation 4.14 and R^2 for the fit is determined. The variation of R^2 with m can then be examined to find the value of m which maximises R^2. Care should be taken, however, to ensure that a large enough range of m values is examined such that an overall, rather than local, maximum of R^2 is found. Typically, a range of m from 1 to 40 was investigated in this work.

4.5.3 Obtaining valid model constants

The variation in Weibull parameters m and σ_0 obtained by fitting can be strongly affected by both the algorithm used to determine 'best' values and the data used for calibration. The validity of a calibrated model can be tested by its ability to predict failure in other geometries or load cases. If additional data are not available, it is important that best practices for calibration are determined to maximise confidence in the calibrated values.

The issue of Weibull parameter calibration has been studied by many authors both in terms of the accuracy of fitting algorithms [138, 140, 141, 142, 143, 144] and the influence of data used [139, 106, 15, 75, 145]. It has been shown by a number of authors [141, 144, 143] that the method of section 4.5.1 tends to systematically over estimate m . There may, therefore, be an argument for applying a correction to remove bias on fitted values before applying them to predictive methods.

It was noted by Gao [75] that many pairs of m and σ_0 values provide equally good correlation with high constraint fracture data, arising from self-similarity of near crack stress fields at increasing load under small scale yielding conditions. It is therefore difficult to select values valid for other, untested

geometries. As a result, it was suggested that calibration should be carried out based on high and low constraint fracture data.

Following work discussed in chapter 2, investigating the relative influences of principal and hydrostatic stress on fracture, the local approach models so far discussed were calculated using σ_1 and σ_h for comparative purposes.

4.6 Results

4.6.1 Parameter calibration

Determination of the parameters m and σ_0 was carried out using the method described in section 4.5.1. For the A533B SEB/SENB and A508 RNB specimens fracture data was available for multiple geometries in the AR state. In these cases, all the available data were used for fitting model parameters. The ranking formula of equation 4.12 was applied to individual geometries separately, ranking by fracture load, rather than ranking the entire material data set by, for example, σ_w.

Where calibration via the method of section 4.5.1 proved unsuccessful, i.e. where the best fit value did not converge to that used to calculate σ_w, values were determined by maximising R^2_{Pf} between the predicted failure probabilities from the model and those found from ranking the experimental data. Confidence limits on the Weibull modulus m are only displayed where converged m values were found. As the R^2 maximisation approach relies on a specified value of m, for which an optimum value of σ_0 is calculated, the method provides confidence limits on σ_0 but not on m.

Inclusion of a threshold stress σ_{th} introduces an additional level of complexity to the calibration process. Incorporating an additional degree of freedom into the process in section 4.5.1 raises the possibility of finding multiple valid m and σ_0 values with varying σ_{th}.

Optimum values of m, σ_0 and σ_{th} may be found by maximising R^2. However, there is then some ambiguity as to whether any improved fit is a result of a better physical model or simply the addition of another degree of freedom. To avoid such issues, threshold stresses were estimated as follows:

1. Following [76] is was assumed that fracture of cracked specimens would not occur when $K_I < 20$ MPa.m$^{0.5}$

2. From FE analyses, the maximum values of σ_1 and σ_h at an external load

corresponding to $K_I = 20$ MPa.m$^{0.5}$ were determined.

3. Maximum stresses were rounded down to ensure conservatism. The threshold stresses σ_{th} were then assumed to be equal to the rounded maximum values.

For the A508 CT data, the maximum stresses at 20 MPa.m$^{0.5}$ were $\sigma_1 =$ 1503 MPa and $\sigma_h = 999$ MPa. These values were rounded down to 1450 MPa and 950 MPa. For the A533B SEB specimens, maximum values of $\sigma_1 = 1345$ MPa and $\sigma_h = 1010$ MPa were found and $\sigma_1 = 1221$ MPa and $\sigma_h = 802$ MPa for the EDM notched SENB samples. As the 20 MPa.m$^{0.5}$ threshold is applicable to plane strain toughness data, and there is a well known increase in K_I at fracture in lower constraint specimens, it was decided that threshold stresses of $\sigma_1 = 1220$ MPa and $\sigma_h = 800$ MPa could reasonably be used.

In the case of the RNB geometries, maximum stresses at the minimum cross section were determined at the lowest failure load for each specimen type. Maximum values were found for the RNB15 geometry with $\sigma_1^{min} = 1555$ MPa and $\sigma_h^{min} = 1116$ MPa. The lowest values, from the RNB7.7 samples, were $\sigma_1^{min} = 1125$ MPa and $\sigma_h^{min} = 755$ MPa. As the lowest experimental failure load cannot be reliably equated to the minimum load for failure, these values were rounded down to threshold values of $\sigma_1 = 1000$ MPa and $\sigma_h = 650$ MPa to ensure conservatism.

Calibrated values for m and σ_0 are displayed in tables 4.1 to 4.6. Converged values of m were found for all models fitted to the A508 CT data, with or without a threshold stress (tables 4.1 and 4.2) as displayed in figure 4.6(a). For the SENB data, figure 4.6(b) shows that only the Beremin model produced converged m values. For the RNB data, converged m values were not found for any of the models considered (figure 4.6(c)). It can be seen that the confidence limits for the fitted parameters are large in all cases. This is especially true for the normalising parameter σ_0 where upper and lower limits may differ by an order of magnitude. This may be a result of the relatively small amount of experimental data available or a characteristic of the fitting process.

Variation of R^2 with m for all three data sets is plotted in figure 4.7. Figure 4.7(a) shows that no reliable peak exists for the high constraint CT data. More defined peak values were found for the SEB/SENB data (figure 4.7(b)) and weakly defined peaks were found for the RNB data (figure 4.7(c)). This would suggest that a sizeable degree of uncertainty may be associated with the fit values for the RNB data. In addition, the high m values suggested

by the fitting will result in greatly increased sensitivity to any inaccuracies in the finite element analyses upon which predictions are based.

As very high m values were produced by maximising R^2_{Pf} for all three RNB geometries, a fitting to each RNB geometry separately was also undertaken. The results are shown in figure 4.8. Variation in best fit values of σ_0 with m (determined using R^2_{Pf}) can be used to graphically estimate optimum values by examining the location where the $m - \sigma_0$ lines intersect. In the case of the Beremin model figure 4.8(a) shows that, when σ_h is used to describe failure, the optimum value of m lies between 25 and 30. This is supported by the value of 26.5 found by fitting to all three geometries (table 4.5). For other model variants, figures 4.8(a) and 4.8(b) show three distinct intersection points, leaving some ambiguity as to the 'true' value.

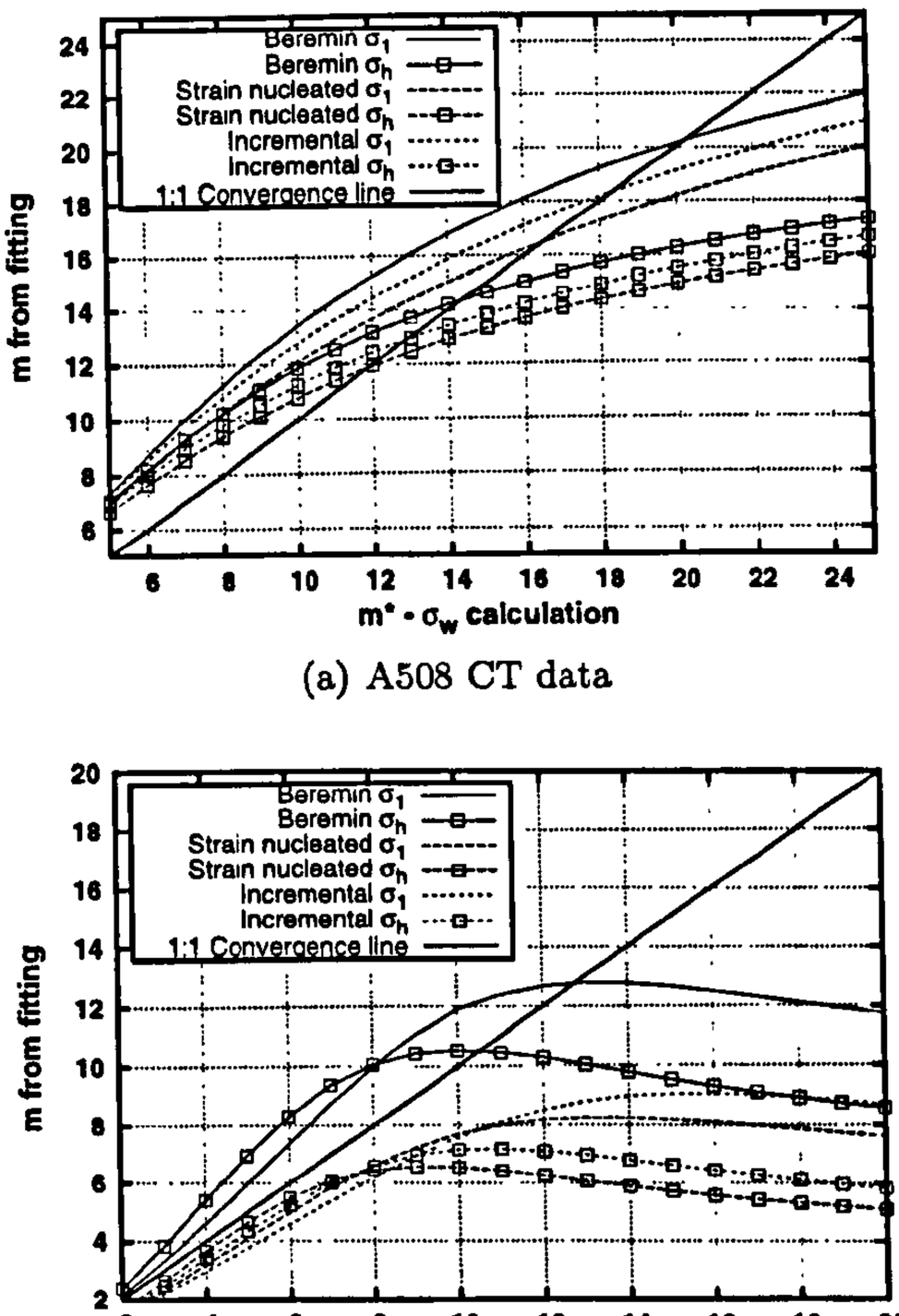

(a) A508 CT data

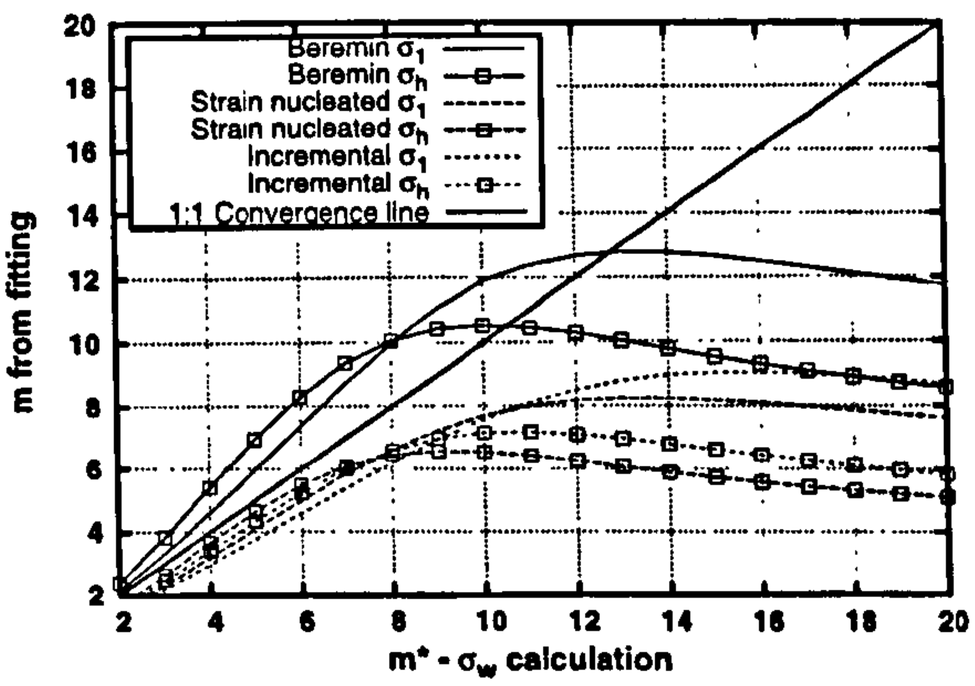

(b) A533B SENB data

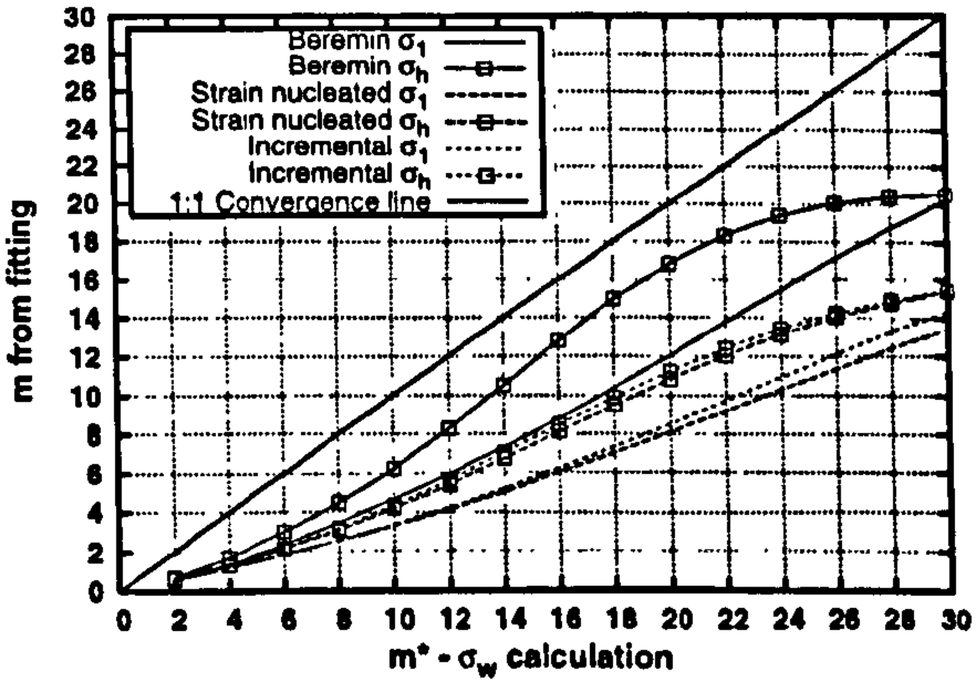

(c) A508 RNB data

Figure 4.6: Weibull slope m from best fit plotted against $m*$ used to calculate Weibull stress σ_w.

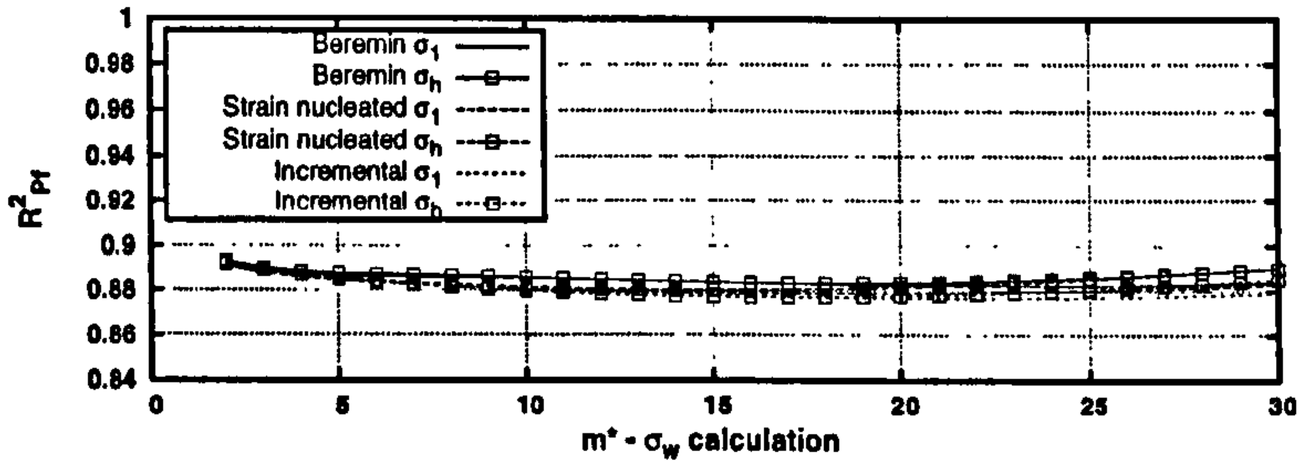

(a) A508 CT data

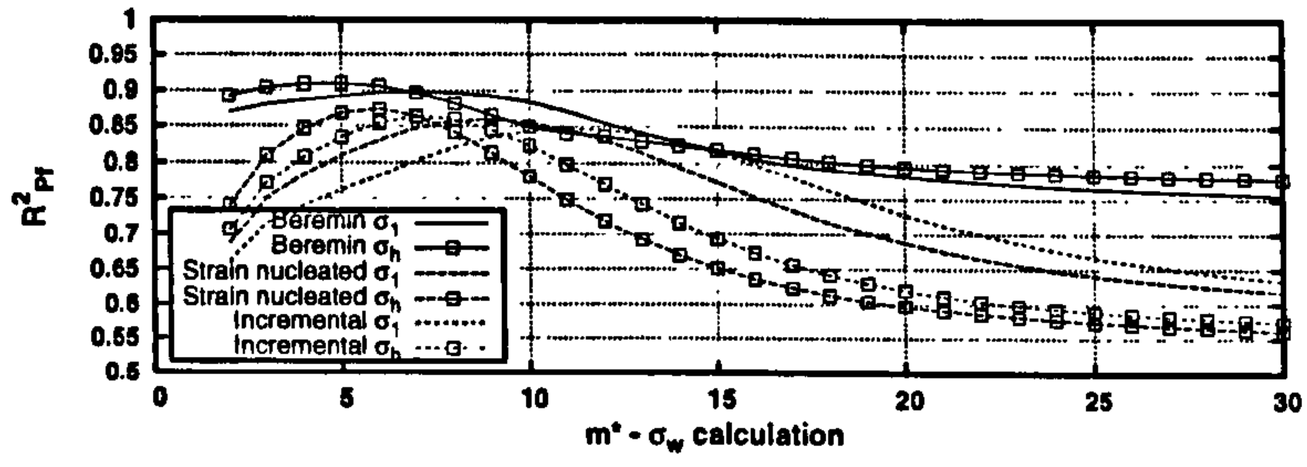

(b) A533B SENB data

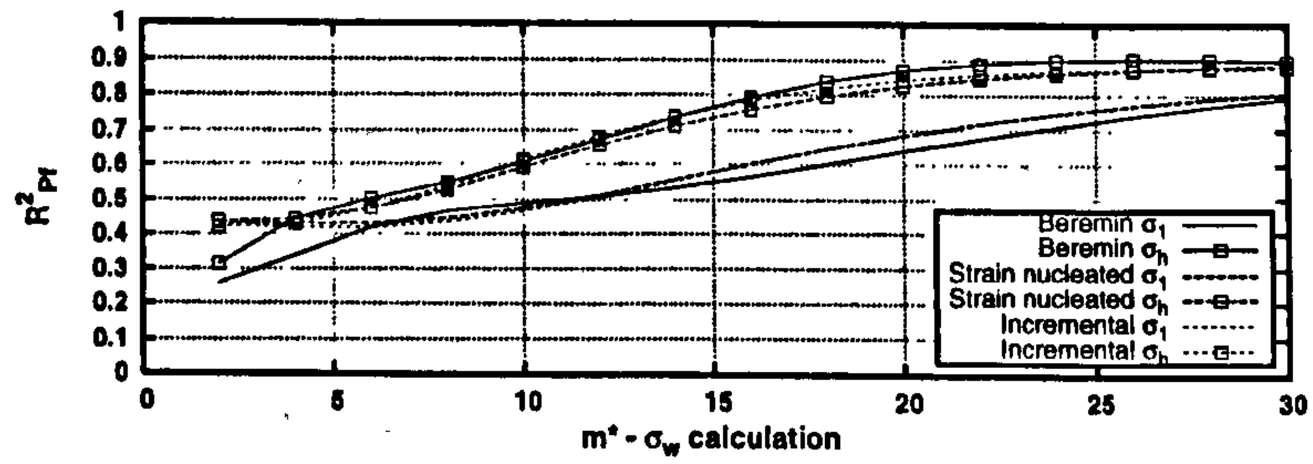

(c) A508 RNB data

Figure 4.7: Variation of fit correlation $R^2_{P_f}$ with m for CT, SENB and RNB data sets.

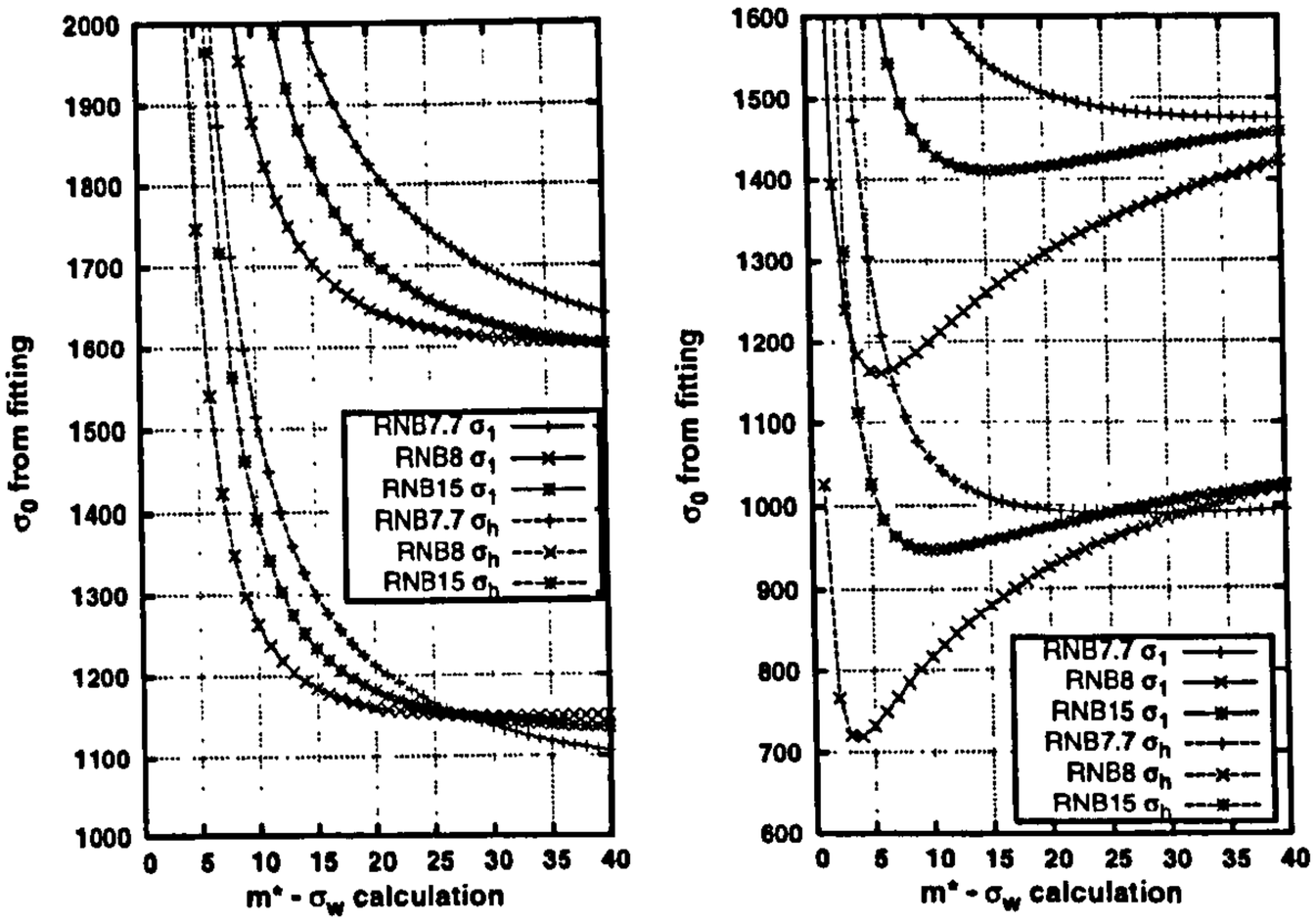

(a) Beremin model (b) Incremental strain model

Figure 4.8: Variation of fitted σ_0 with m for individual RNB geometries.

4.6.2 Prediction of load history effects

A508 CT data

The modified J integral J_m was able to produce path independent values for contours of increasing size about the crack tip. This is illustrated for representative applied loads by figure 4.9(a) where contour 1 is the first ring of elements surrounding the crack tip, contour 2 the first two rings of elements and so on. The inconsistency in values about the first contour, immediate to the crack tip, can be attributed to the problems of accurately modelling the stress and strain field in the near tip region using finite element analyses. The resulting variation of J_m with applied load for the three load cycles applied is plotted in figure 4.9(b). Of particular note is the variation of J_m for the LUCF cycle, where it can be seen that under no applied load the value of J_m is negative. Although not entirely unsurprising as the tensile preload produces compressive crack tip stresses, the negative value raises questions with regards to physical interpretation of the J_m parameter. The lines labelled 'init' in figure 4.9(b) correspond to calculations where the initial state for J_m was defined as the cracked structure, following preload. For the other results plotted, no initial state was defined.

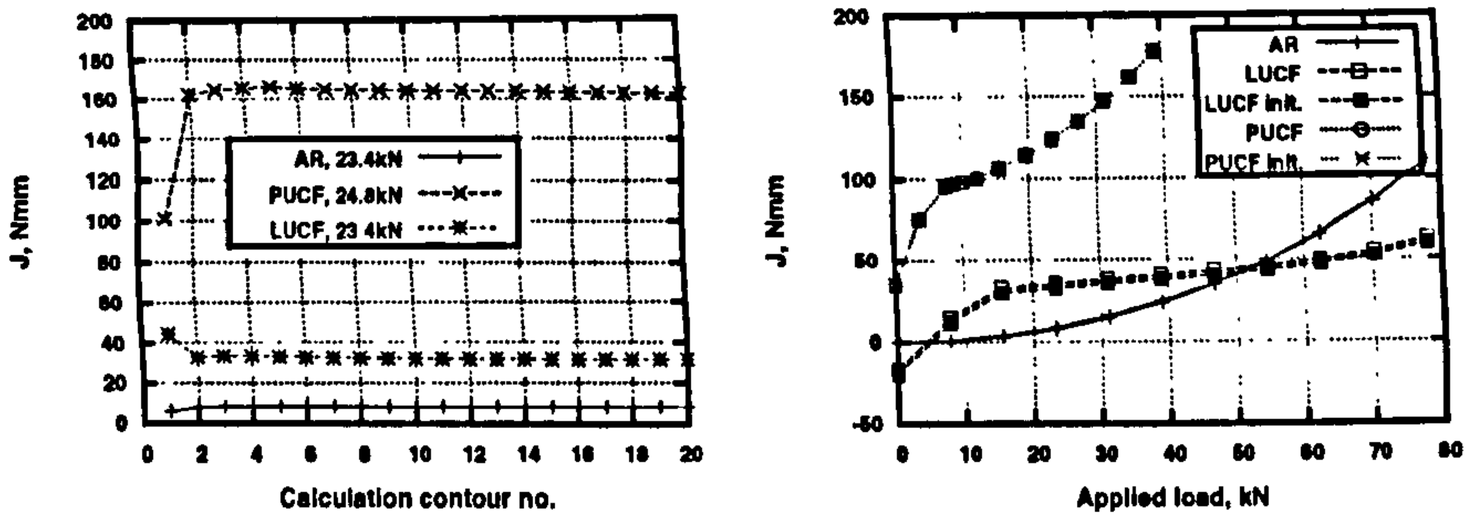

(a) Variation of J_m with domain (b) Variation of J_m with load

Figure 4.9: Variation of modified J integral with calculation domain and applied load for CT specimens.

Predictions of PUCF and LUCF failure, using F_k and J_m are displayed in figure 4.10 along with fitted parameters in equation 4.3 and 4.4. Values of K were calculated from J_m using equation 4.15.

$$K_J = \sqrt{\frac{EJ}{1-\nu^2}} \tag{4.15}$$

Predictions of failure using local approach methods, based on hydrostatic and principal stress, can be seen in figures 4.11 and 4.12. Introduction of a threshold stress, while introducing a slight change in the fitted m and σ_0 values, was not found to significantly alter the predictions for failure compared with figures 4.11 and 4.12.

A533B SENB data

As for the CT data, the modified J integral was found to produce path independent values beyond the contour immediate to the crack tip. Variation of J_m with load for the SENB specimen variants is shown in figure 4.13 and the resulting predictions of PUCF and CUCF failure are shown, along with those based on F_k, in figure 4.14. As equation 4.3 was calibrated to the SENB and SEB data, two lines are plotted in figure 4.14 labelled 'Fit to AR data - J_m', these correspond to the SEB and SENB AR data.

Agreement of the calibrated local approach models with the AR data used for calibration can be seen in figure 4.15 and the predictions of failure after prior loading in figures 4.16 and 4.17. As for the A508 CT specimens, the

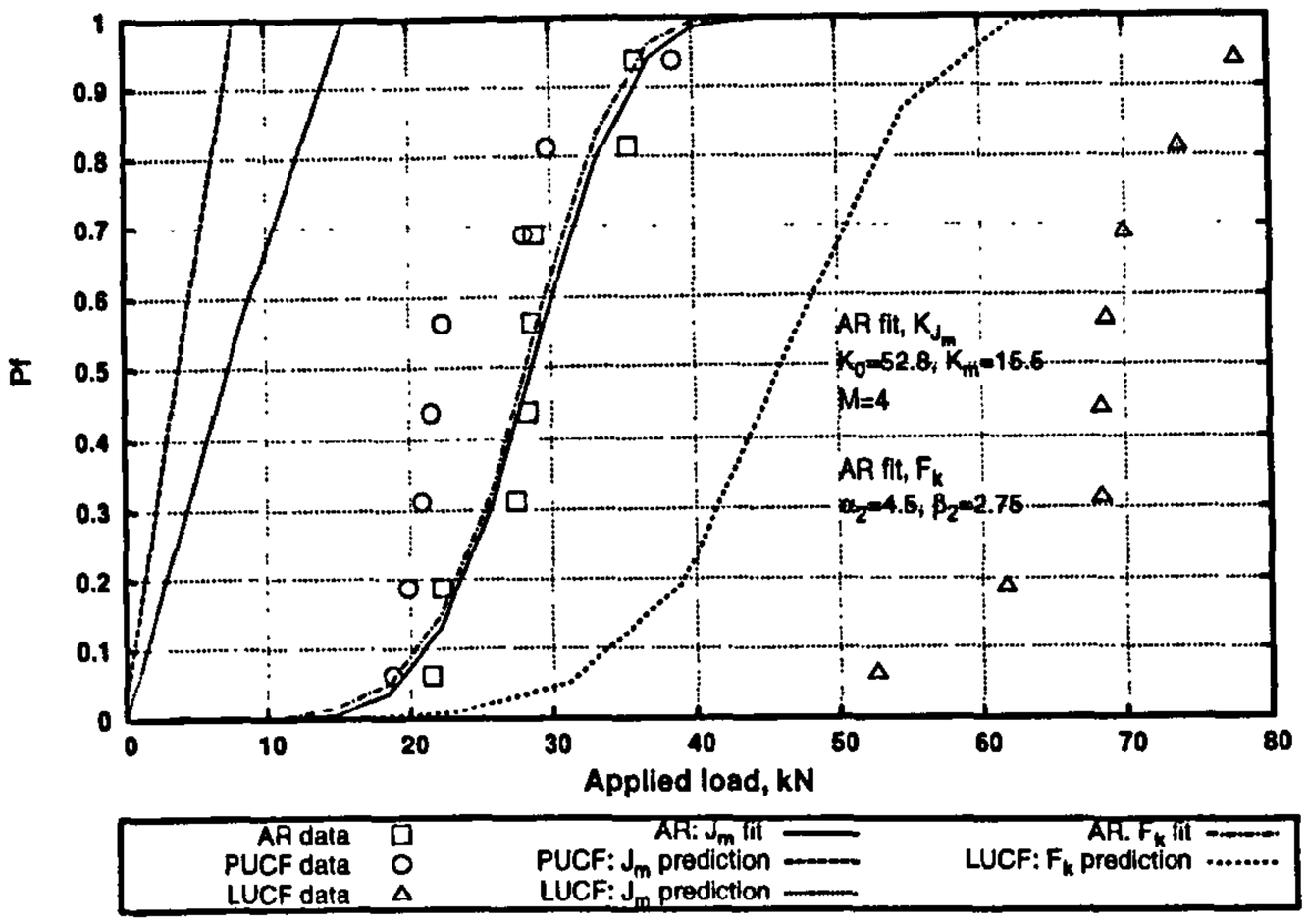

Figure 4.10: Prediction of CT specimen failure probability for PUCF and LUCF load cycles, based on modified J integral and Eshelby force on the crack tip plastic zone.

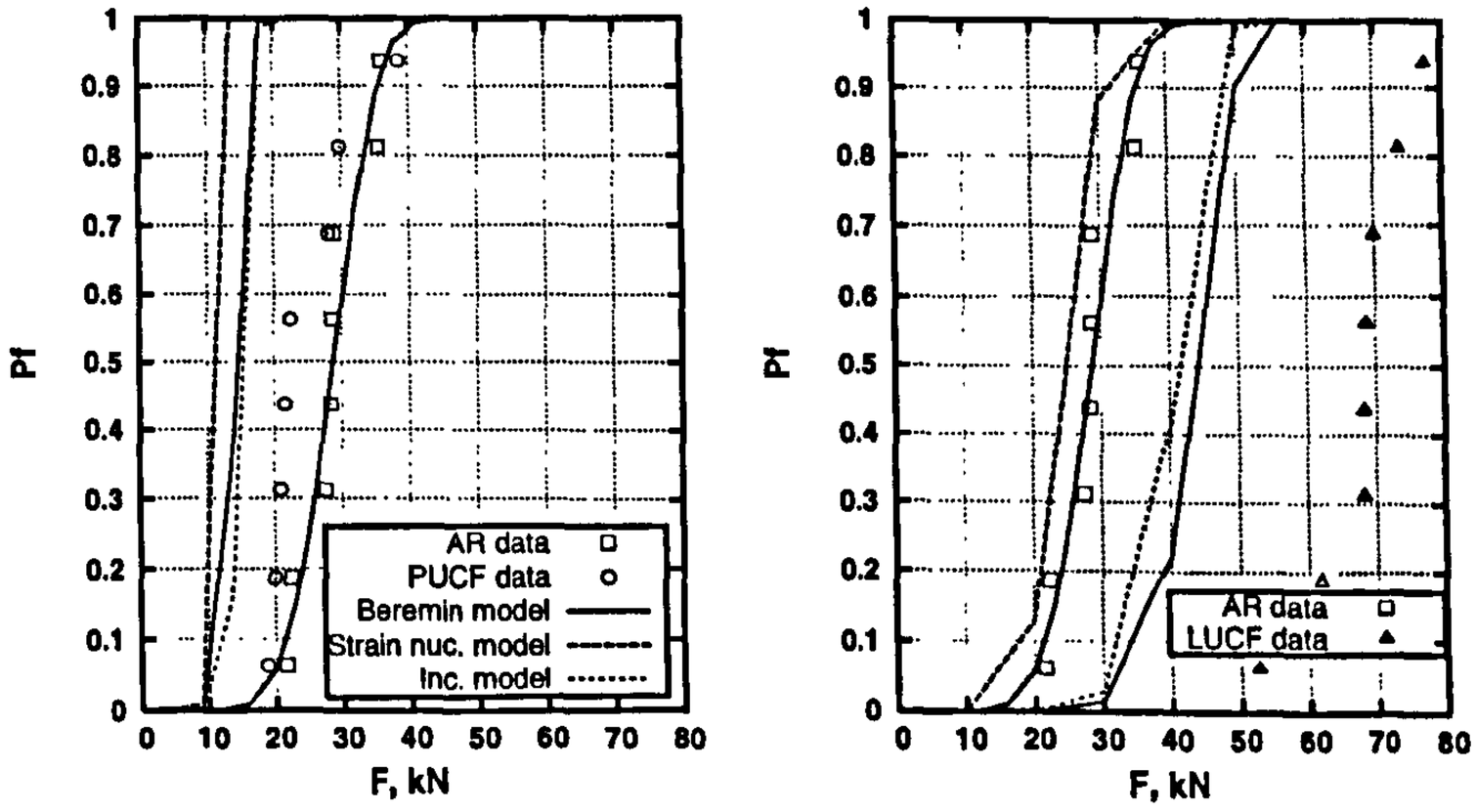

(a) PUCF failure prediction

(b) LUCF failure prediction

Figure 4.11: Prediction of CT failure probability with load history using local approach methods based on σ_1. Lines in b) correspond to local approach models as described by the key in a). Beremin = equation 2.37, Strain nucl. = equation 4.6, Inc. = equation 4.8.

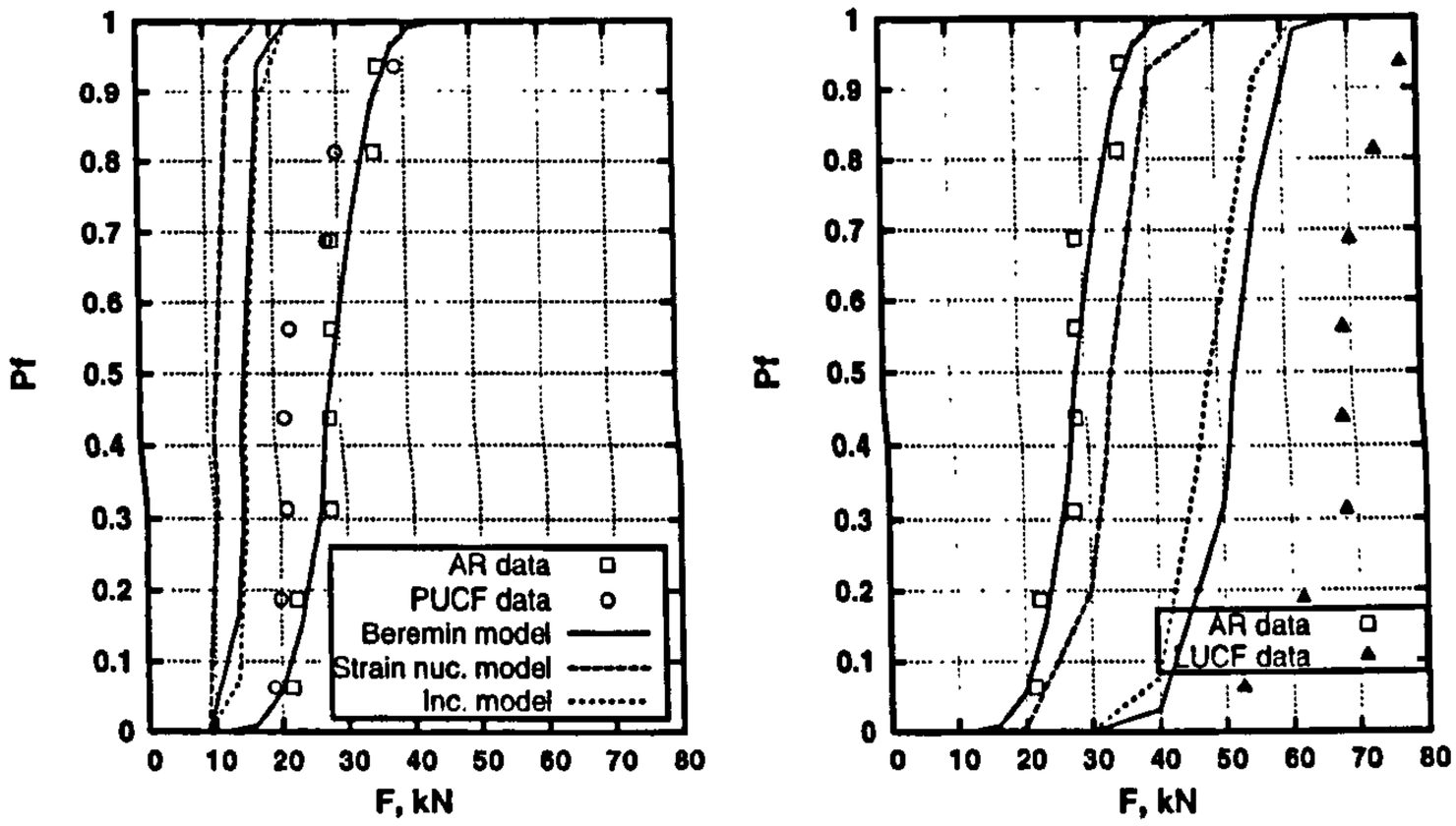

(a) PUCF failure prediction

(b) LUCF failure prediction

Figure 4.12: Prediction of CT failure with load history using local approach methods based on σ_h. Lines in b) correspond to local approach models as described by the key in a). Beremin = equation 2.37, Strain nucl. = equation 4.6, Inc. = equation 4.8.

effect of introducing a threshold stress on prediction of fracture after prior loading is small. Almost no effect was noted for the PUCF load cycle but some effect on the CUCF predictions was noted. Predictions for failure after the CUCF load cycle, for models including a threshold stress, are displayed in figure 4.18.

A508 RNB data

Local approach model predictions of failure, for the calibration AR data, are shown for models based on σ_1 in figure 4.19 and σ_h in figure 4.20. Again, little effect was noted from the introduction of a local threshold, as can be seen by comparing figures 4.19 and 4.21.

Predictions of failure following warm prestressing, based on the local approach fits to the AR data, are shown in figure 4.22. As for the AR data, introduction of a threshold stress was seen to have little effect and so plots are only presented for models without a local threshold.

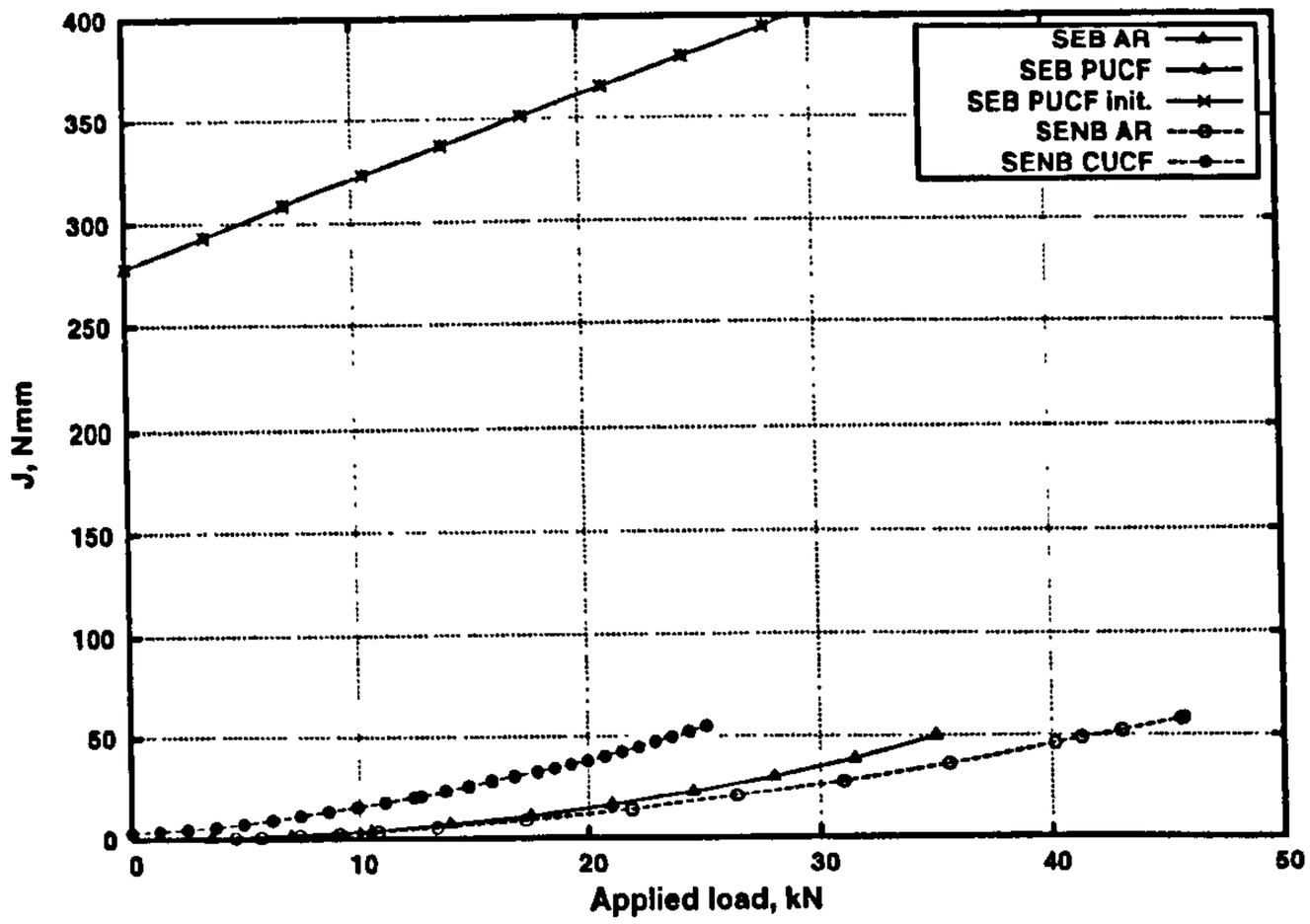

Figure 4.13: Variation of J_m with applied load for SEB and SENB specimens.

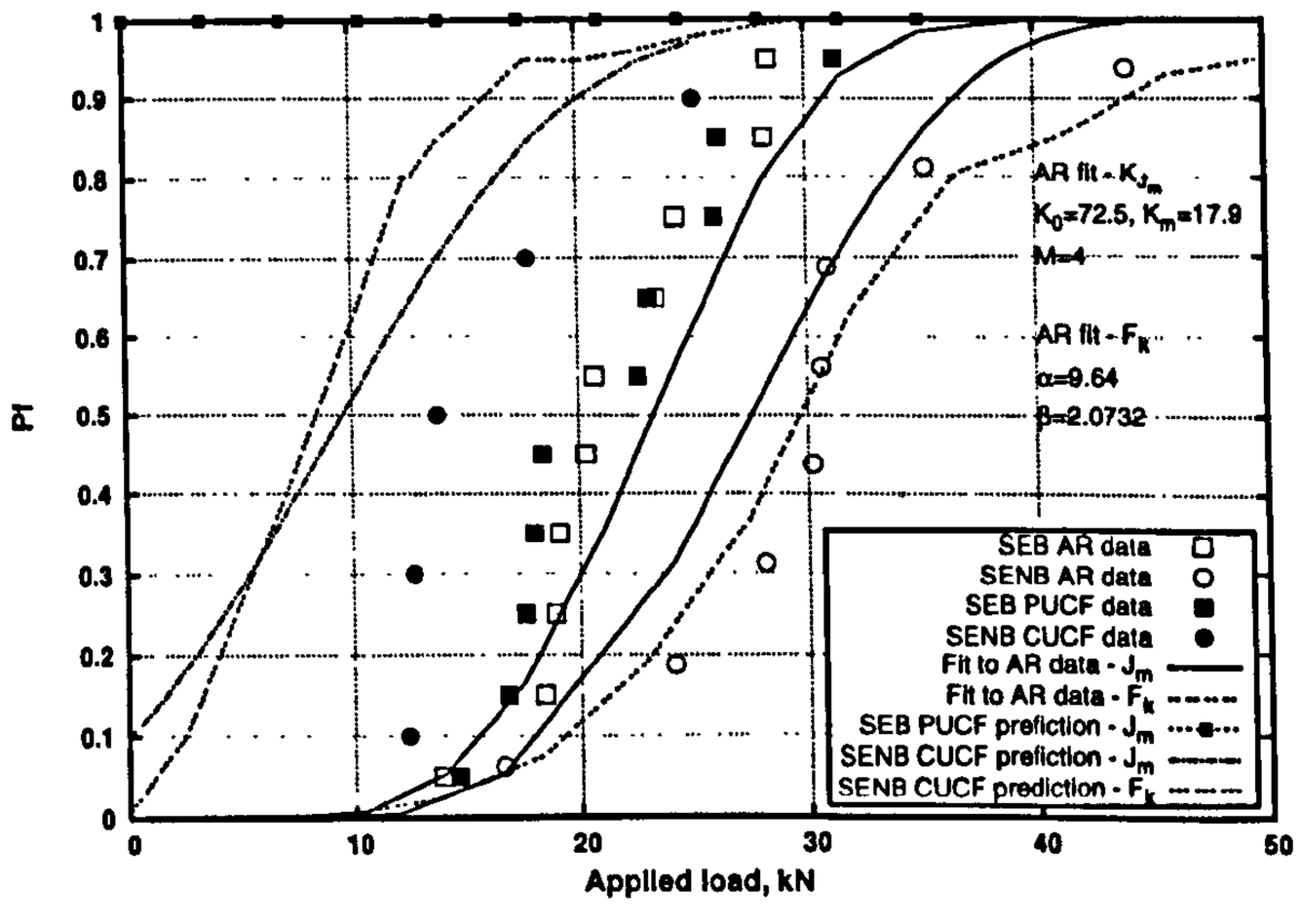

Figure 4.14: Prediction of effect of CUCF and PUCF cycles for SEB and SENB specimens, based on modified J integral and Eshelby force on the crack tip plastic zone.

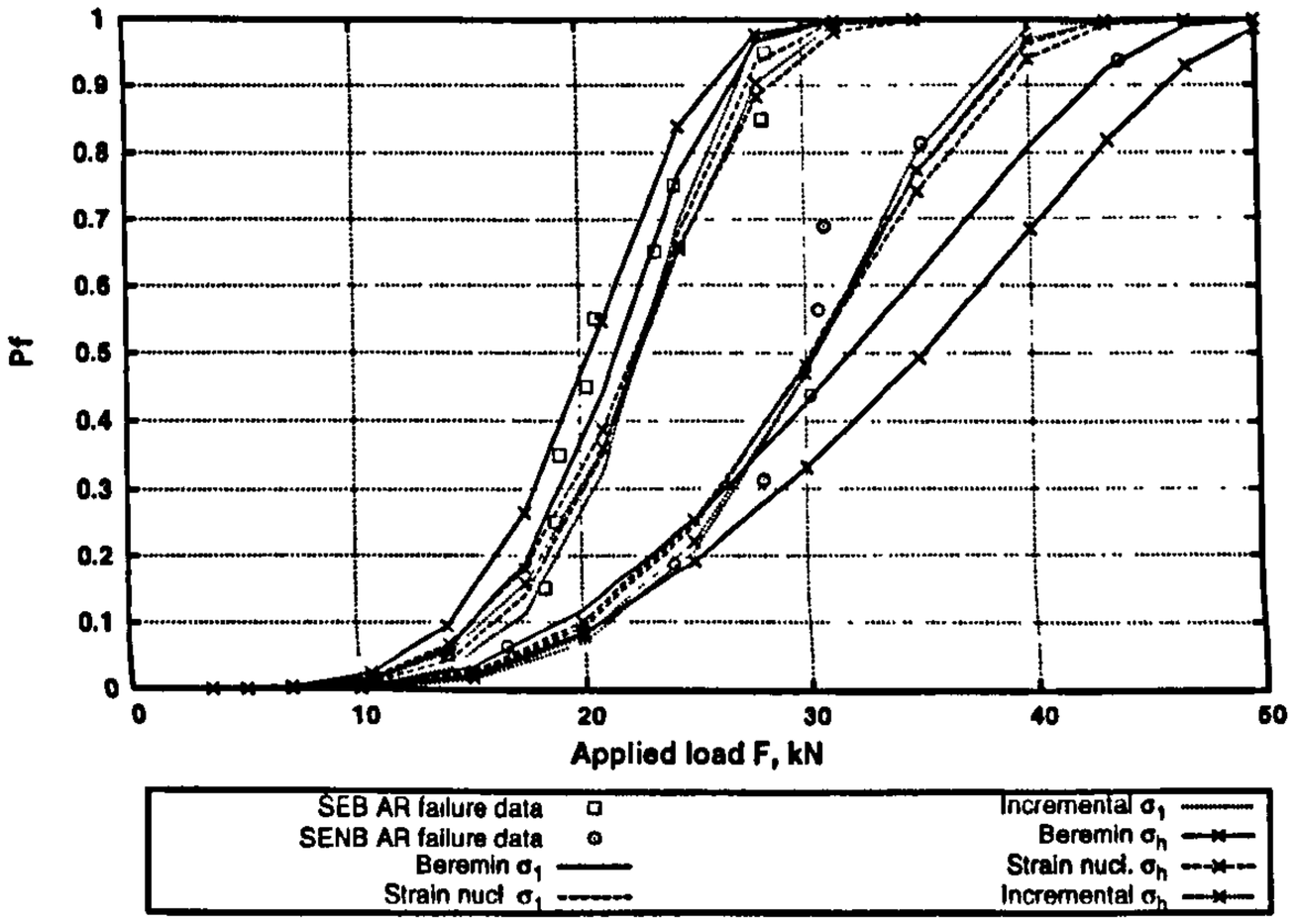

Figure 4.15: Agreement of local approach model fits with AR failure data for SEB and SENB specimens. Beremin = equation 2.37, Strain nucl. = equation 4.6, Inc. = equation 4.8.

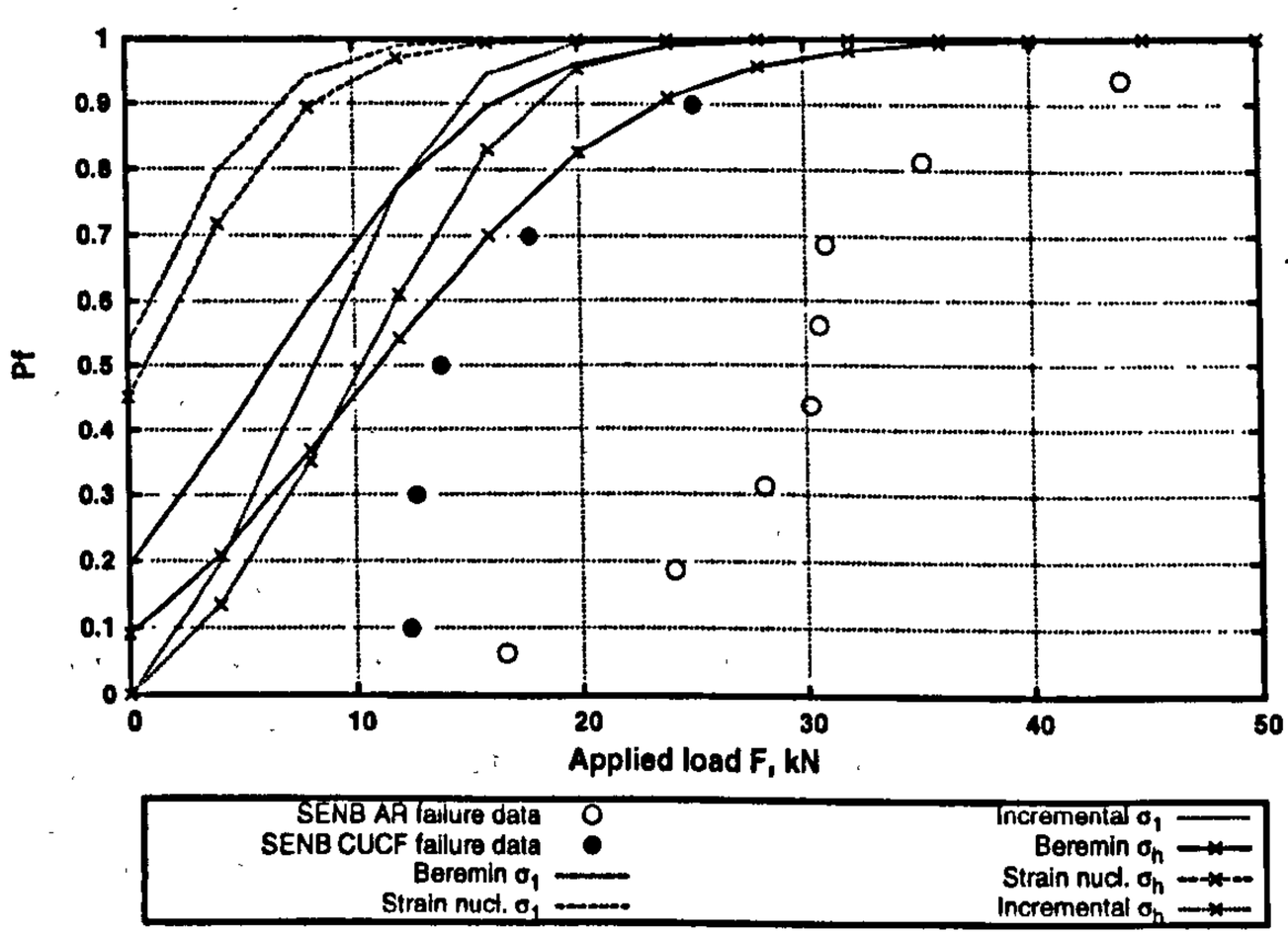

Figure 4.16: Prediction of SENB specimen failure after CUCF load cycle, based on local approach models. Beremin = equation 2.37, Strain nucl. = equation 4.6, Inc. = equation 4.8.

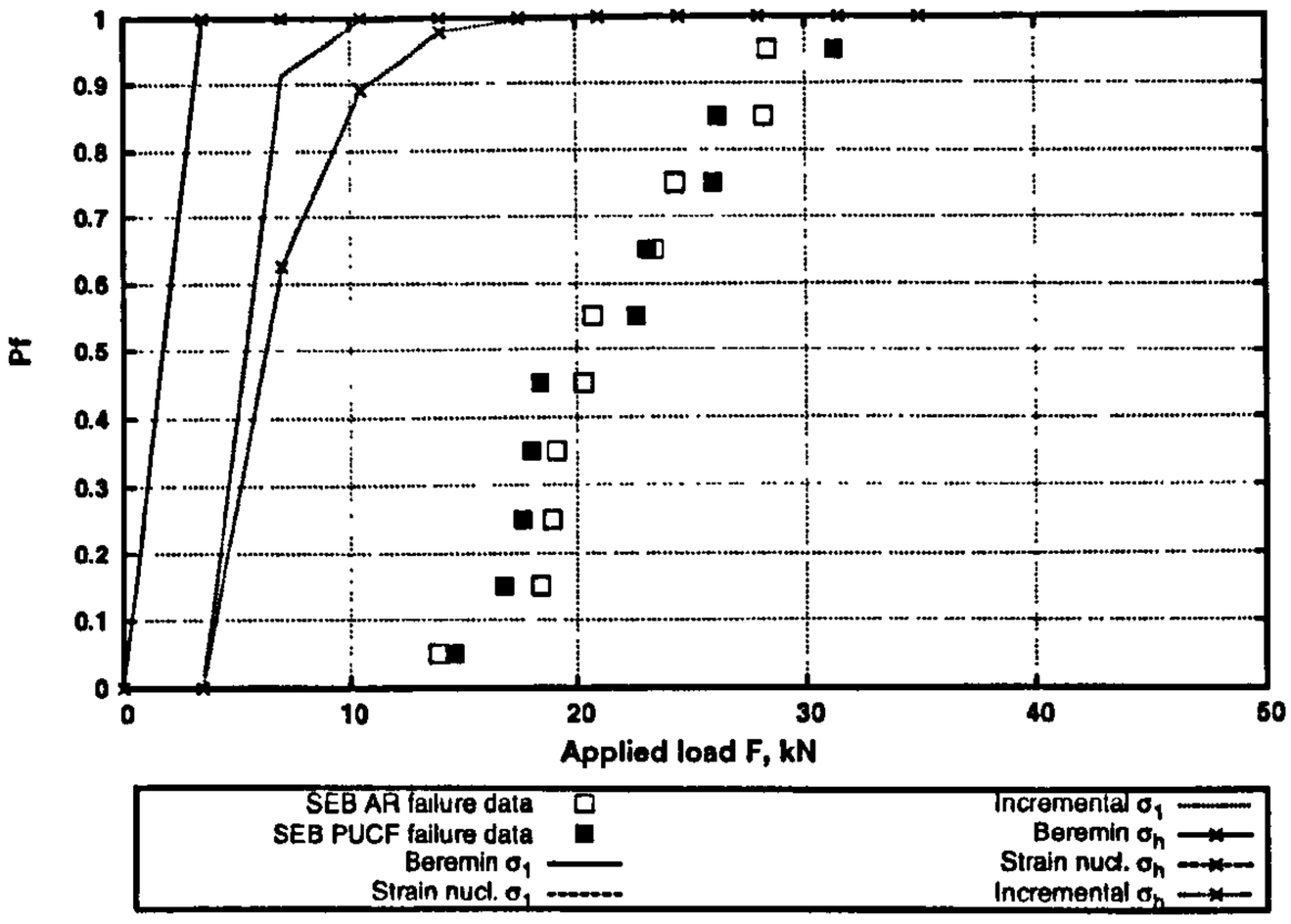

Figure 4.17: Prediction of SEB specimen failure after PUCF load cycle, based on local approach models. Beremin = equation 2.37, Strain nucl. = equation 4.6, Inc. = equation 4.8.

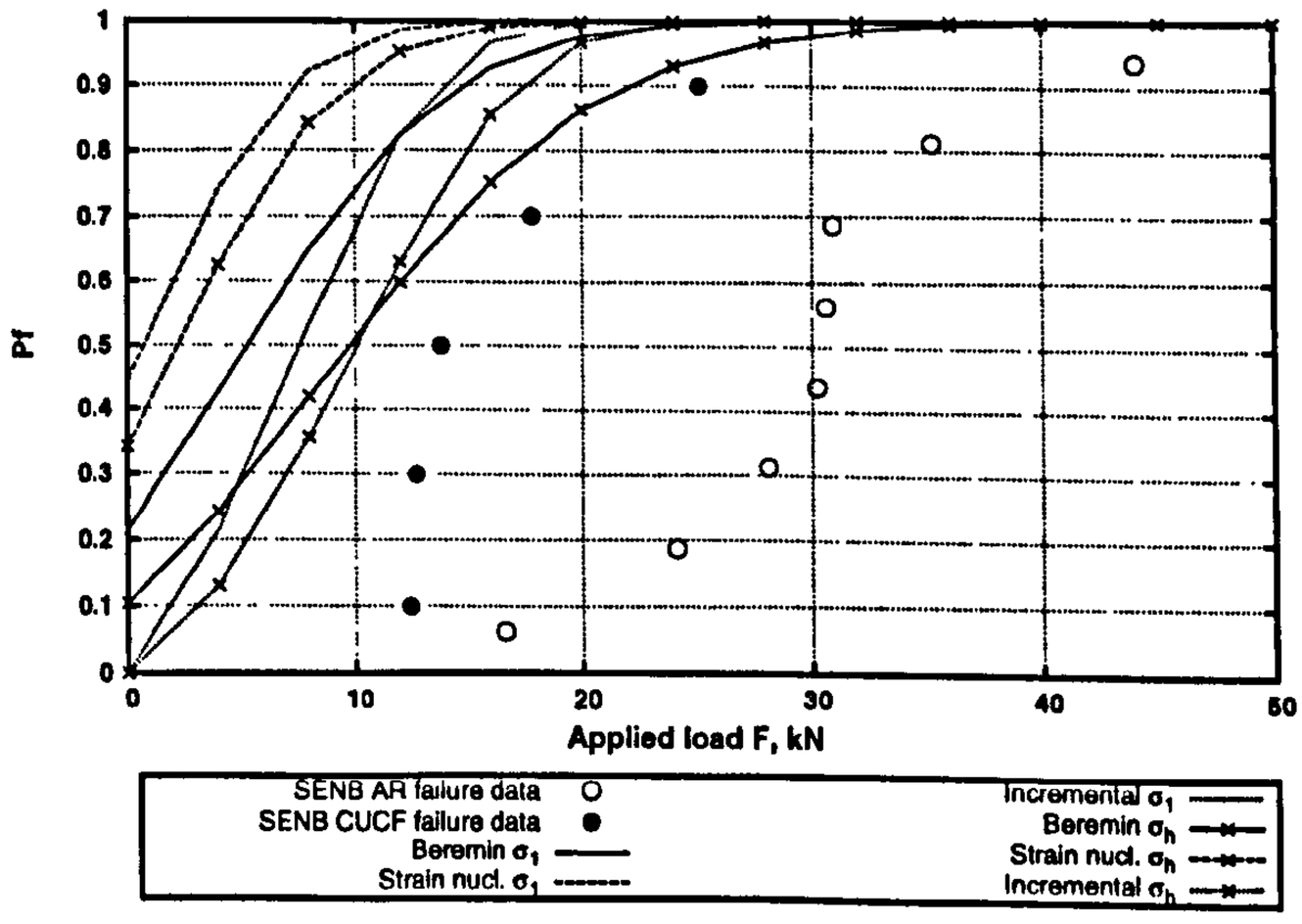

Figure 4.18: Prediction of SENB specimen failure after CUCF load cycle, based on local approach models with a threshold stress. Beremin = equation 2.37, Strain nucl. = equation 4.6, Inc. = equation 4.8.

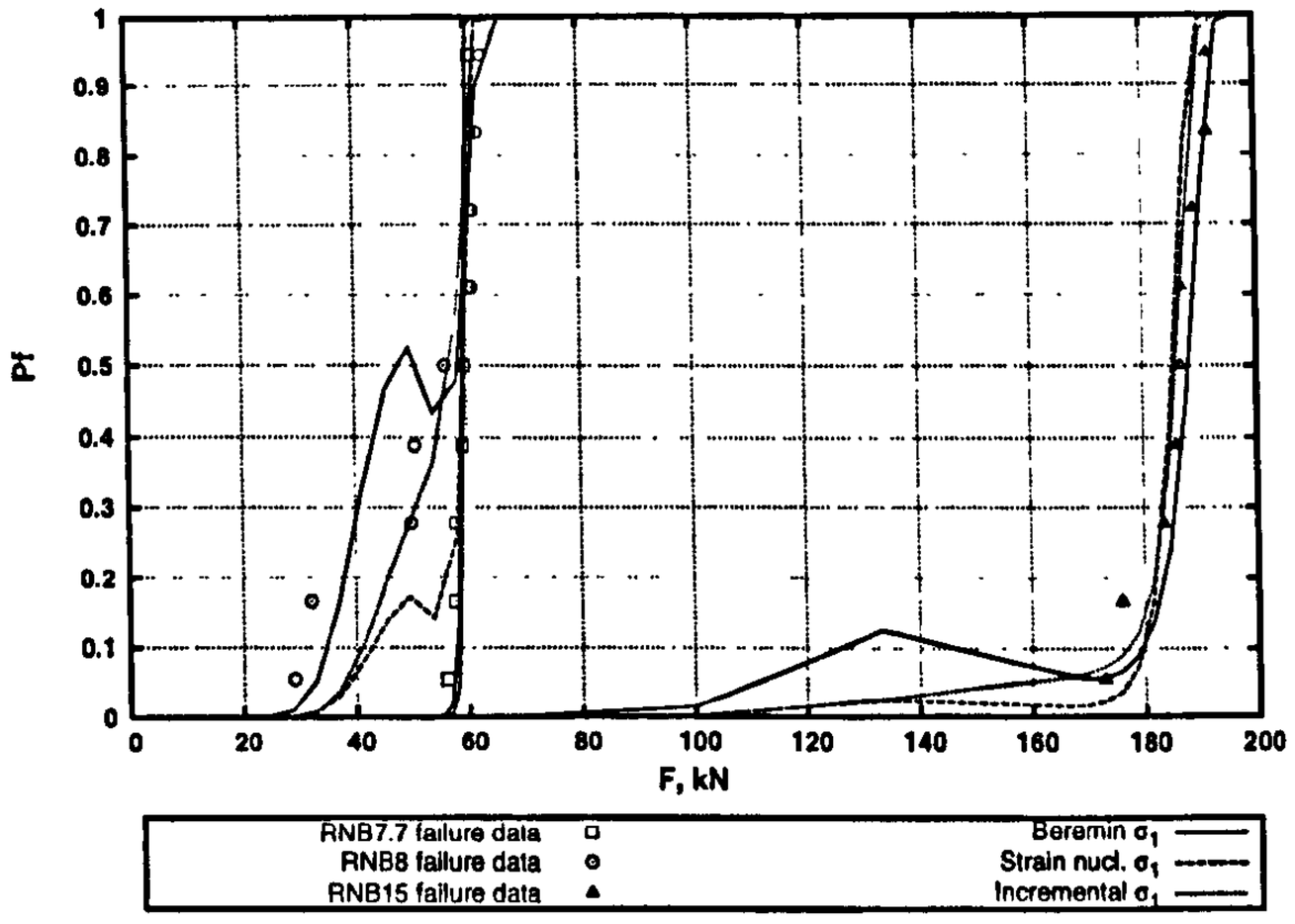

Figure 4.19: Agreement of local approach model fits based on σ_1 with AR failure data for RNB specimens. Beremin = equation 2.37, Strain nucl. = equation 4.6, Inc. = equation 4.8.

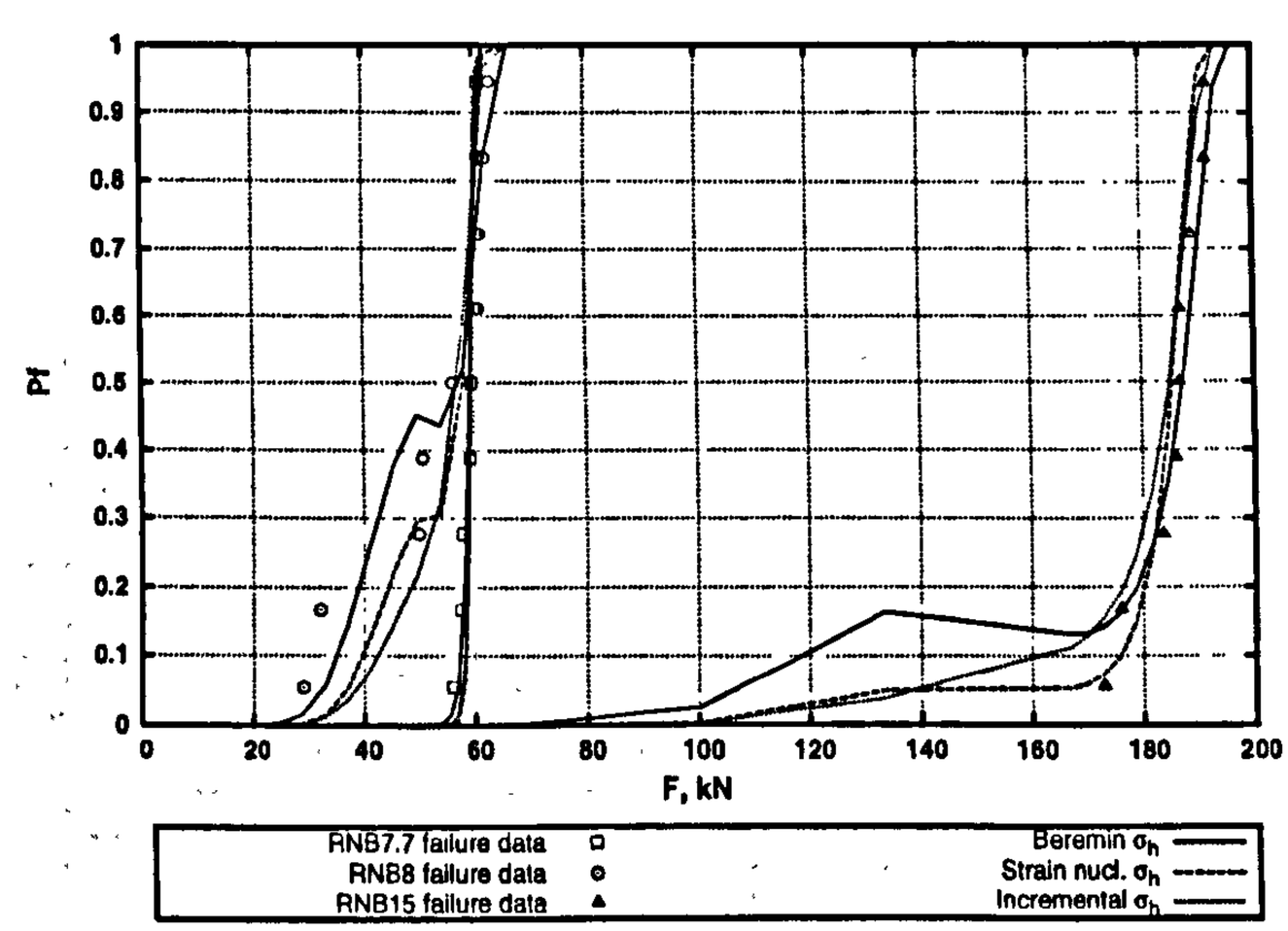

Figure 4.20: Agreement of local approach model fits based on σ_h with AR failure data for RNB specimens. Beremin = equation 2.37, Strain nucl. = equation 4.6, Inc. = equation 4.8.

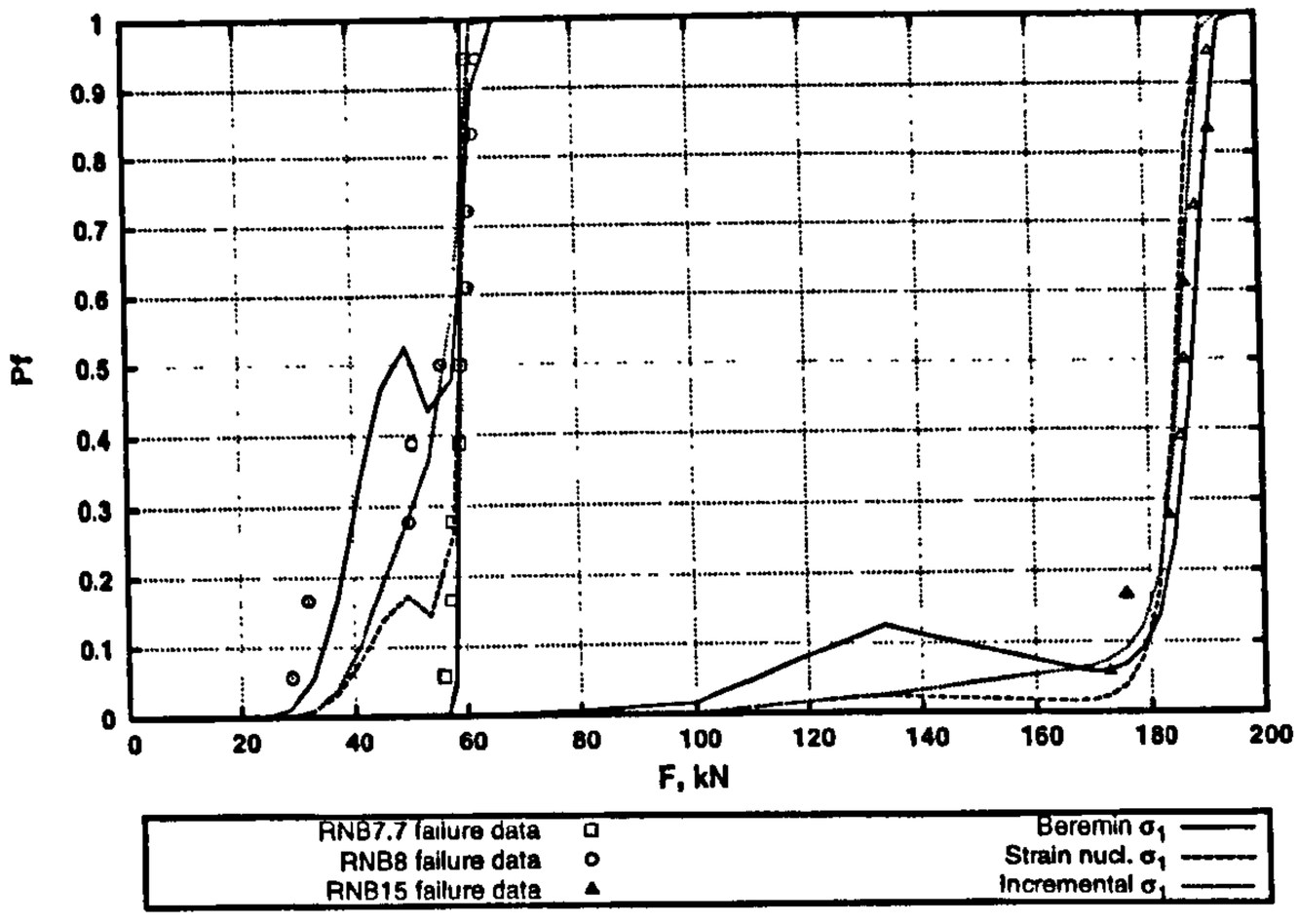

Figure 4.21: Agreement of local approach model fits based on σ_1 with AR failure data for RNB specimens. Models including local threshold stress. Beremin = equation 2.37, Strain nucl. = equation 4.6, Inc. = equation 4.8.

4.7 Effect of crack introduction

The results of FE modelling on pre-compressed SENB specimens showed that the value of J_m calculated using JEDI was strongly affected by the method of crack introduction.

In the analyses presented, the crack was introduced in 4 increments. Modelling the cutting process in a single step resulted in an increase in the values of J_m, as illustrated in figure 4.23. As this has the potential to significantly alter predictions of fracture in the presence of residual stress, a numerical investigation was undertaken into the effects of the method of crack introduction on J and K values.

4.7.1 Crack growth modelling

To further investigate the implications of how a crack is introduced into an existing residual stress field, a further numerical investigation was undertaken. For simplicity, the specimen for modelling was chosen to approximate a semi infinite plate. The model dimensions were as in figure 4.24. Finite element meshing was undertaken using two dimensional plane strain elements with a

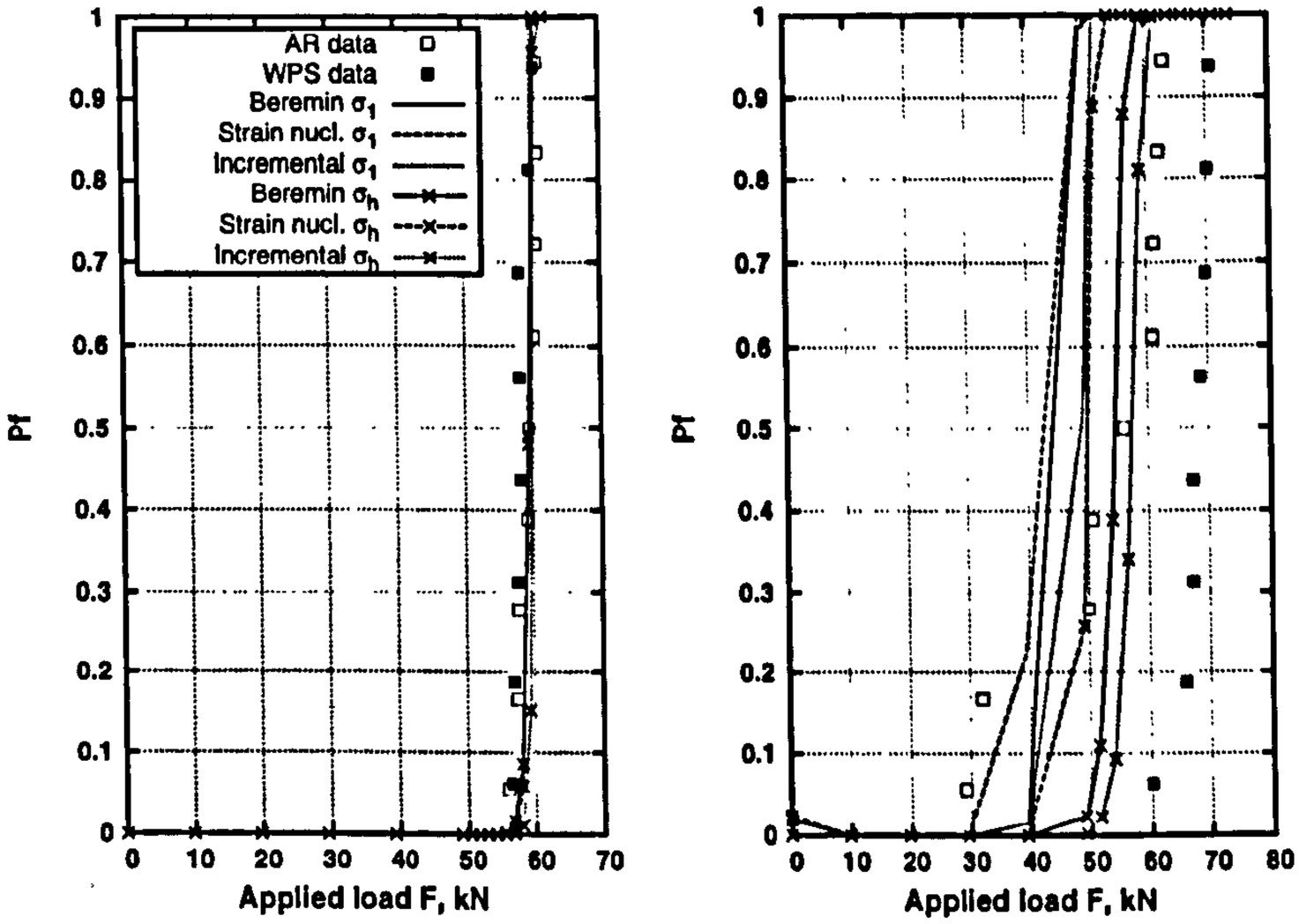

(a) RNB7.7 geometry

(b) RNB8 geometry

Figure 4.22: Prediction of RNB failure following warm prestressing using local approach methods. Lines in b) correspond to local approach models as described by the key in a). Beremin = equation 2.37, Strain nucl. = equation 4.6, Inc. = equation 4.8.

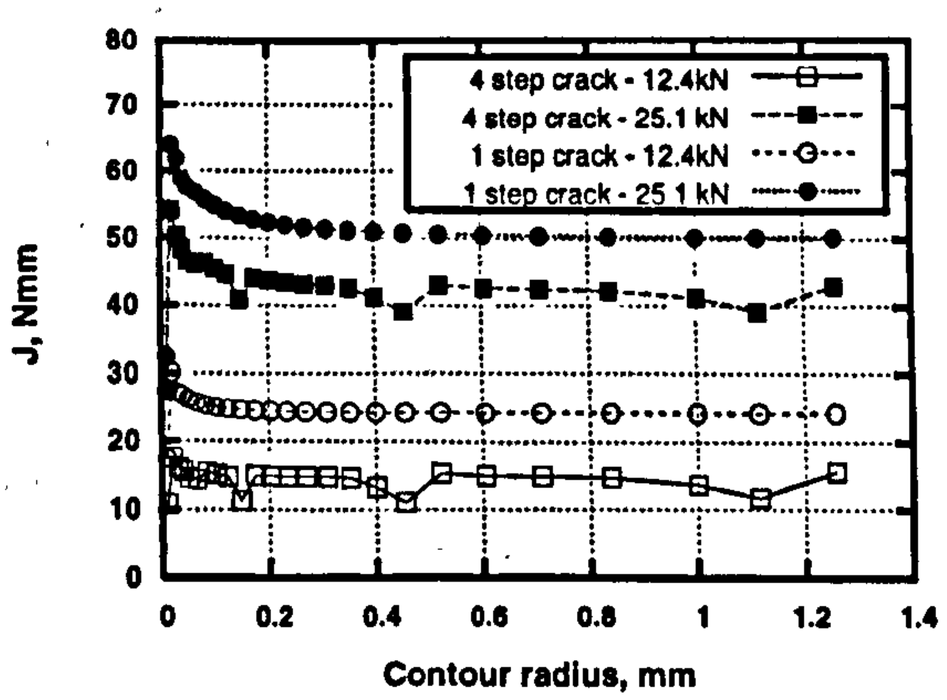

Figure 4.23: Effect of incremental crack introduction on J_m contours at varying applied loads for SENB specimens with CUCF load cycle.

minimum element size of $10\mu m$ at the crack tip.

The combination of a deep cracked geometry and plane strain conditions was chosen to maximise in-plane and out of plane constraint. The postulated reason for variation in calculated J_m values was the dissipative effect of the plastic wake created as the crack grows through the stress field. In the experimental test considered, crack 'growth' occurred by means of wire EDM cutting but one would expect the same plasticity effects to occur. By maximising constraint, the effects of plasticity should be minimised, effectively producing a lower bound estimate of the effect of the method of crack insertion.

A far field residual stress field was simulated by applying varying prescribed displacements to the plate edges. A region of uniform displacement of magnitude $D1$ was applied along 37.5mm from the plate edge with a further uniform displacement, $D2$, applied up to 50mm from the edge as in figure 4.24. The result was a tensile residual stress field normal to the intended direction of crack propagation. Three load levels were applied, with displacements according to table 4.7. The crack was introduced into the generated stress field in three different ways.

1. Introduction in a single step (1 step).

2. Introduction in 9 steps: 4×5.25mm, 4.0mm, 3.0mm, 1.0mm, 0.8mm, 0.2mm (9 step).

3. Initial introduction in 6 steps over 28mm 4×5.25mm, 4.0mm, 3.0mm. Final 2mm of growth by releasing nodes one at a time (incremental).

The material was assumed to be low temperature A533B ferritic steel, as for the SENB specimens.

4.7.2 Observations

The geometry of the crack tip was found to be significantly altered by the size of growth increment. The crack tip opening displacement CTOD, taken from the displacement on the element immediately behind the crack tip, was found be $19.87\mu m$ for single step crack introduction, $9.09\mu m$ for the 9 step model and $2.82\mu m$ for the incremental introduction model.

Values of J_m were calculated using the JEDI postprocessor, assuming non-proportional loading. The initial state was taken to be that of the uncracked body, prior to crack introduction. Values were also calculated using elastic

finite element analyses to calculate J, as well as a weight function analysis to estimate the effect of the residual stress field in the absence of plasticity during crack growth.

Stress intensity factors were calculated using the stresses in the uncracked body from the FE analysis and the weight function for semi-infinite plates in [146].

$$K_I = \int_0^a h(x,a)\sigma(x)dx \tag{4.16}$$

The weight function was also used to characterise the load magnitude by defining an equivalent uniform stress σ_{eq} across the crack region, displayed in table 4.7.

$$\sigma_{eq} = \frac{K_I}{\int_0^a h(x,a)dx} \tag{4.17}$$

From the variation of the stress and strain fields (figure 4.25) it can be seen that crack introduction method has a greater effect on the plastic strain field than on the stresses. The reduction in peak plastic deformation with increasing number of increments is in keeping with the estimated CTOD values. It can be seen that incremental introduction of the crack results in reduced peak values of stress and strain, dissipating the energy further away from the tip, as can be seen from the raised stresses and strains at a distance of 0.1mm from the crack tip.

The effect of this increased dissipation on J and K_J values can be seen in figure 4.26. Even when using the modified J_m formulation, significant path independence can be seen. Sizable perturbations are also present in the contour values as the contour grows to enclose previous crack tip locations - i.e. where a previous growth increment ended.

This oscillation is not too concerning as an overall constant value is maintained, however the significant decrease in J_m with decreasing increment size is important. It was observed that strong path dependence emerged following incremental crack introduction, taking the initial state for J_m as the uncracked body. It is seen in figure 4.26(a) that when the initial state is defined after crack introduction, this path dependence is largely removed, however the resulting steady value is still markedly lower than for the other models.

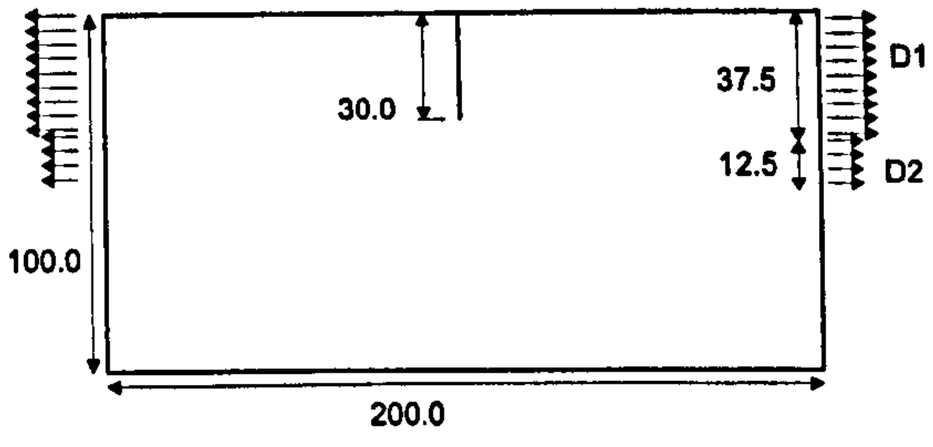

Figure 4.24: Model used to investigate the effect of crack introduction modelling, dimensions in mm.

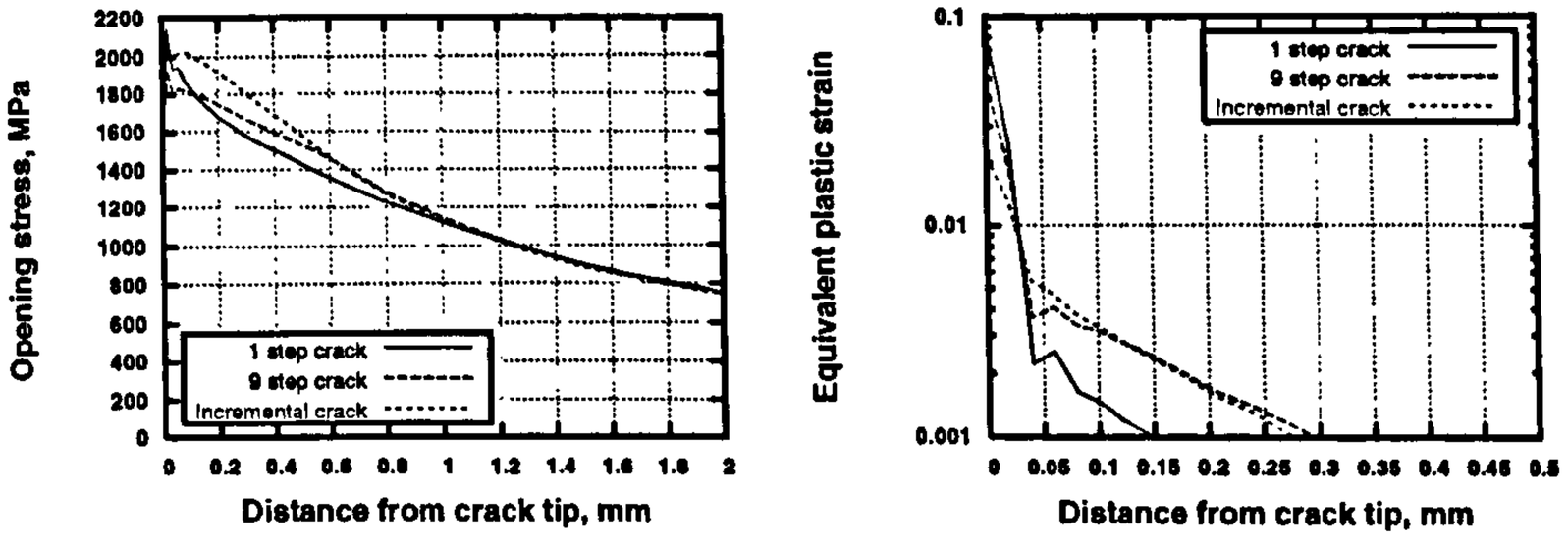

Figure 4.25: Effect of crack introduction method on stress (a) and strain (b) ahead of the crack tip, $\sigma_{eq} = 245.2$ MPa.

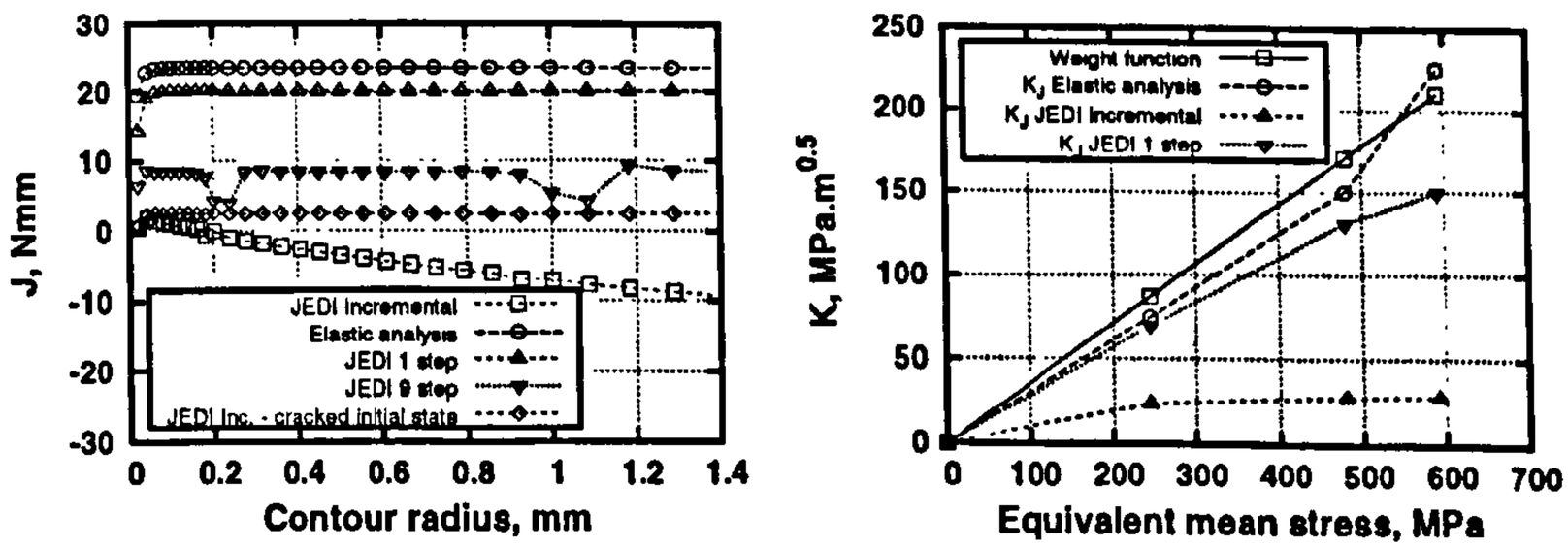

Figure 4.26: Effect of crack introduction method on J integral contours, $\sigma_{eq} = 245.2$ MPa (a) and variation of stress intensity factor with load (b).

4.8 Discussion

The results for the fitting of local approach models have highlighted a number of inadequacies in the methods used. The m intercept method was found to perform adequately for the high constraint CT fracture data, with less success for the lower constraint SENB and SEB data and no viable fitting results for the lowest constraint RNB data.

The lack of correlation between the m used to calculate σ_w and the slope of the linearised plot described by equation 4.11 suggests a problem with the Weibull formulation. Regardless of the model used, the use of σ_w and the Weibull distribution to describe failure as in equation 2.36 is reliant on the failure probability of any single element of volume being small, as demonstrated in appendix A. In samples where the overall probability of failure is dominated by a small material volume, this assumption may be violated.

This may also explain the divergence of the $m*$ values used in calculation and m obtained from fitting at higher $m*$ (figures 4.6(a)-4.6(c)). As the value of $m*$ used to calculate σ_w increases, failure probability becomes increasingly dominated by the most highly stressed regions, therefore the overall failure probability will be almost entirely dependent on a small volume of the most highly stressed material.

To further analyse the failure of the fitting process of section 4.5.1 to characterise the whole RNB data set, fitting was performed to each RNB AR data set separately. For the incremental model, figure 4.27 shows converged m values were determined for the RNB7.7 and RNB15 data but not for the RNB8 data. Furthermore, the calibrated values of m varied considerably between data sets, which may also explain the lack of convergence when analysing all three data sets together (figure 4.6(c)). This highlights the danger of selecting parameters based on a single geometry, especially when sample sizes are small, such as in this case.

The fact that the fitted $m*$ values in figures 4.6(b) and 4.6(c) are lower than those used to calculate σ_w is more concerning as many authors [141, 142, 143, 144] have noted that the method of section 4.5.1 has a tendency to overestimate the 'true' value of m.

The alternative method of maximisation of R^2_{Pf}, equivalent to maximising agreement between Pf from equation 4.12 and that from the calibrated model, is seen to be unsatisfactory in many cases as highlighted by figure 4.7. This is particularly apparent for the high constraint CT data where R^2 provides

essentially no guidance as to the optimum value of m. Further work is needed to investigate the influence of the data used for fitting on the validity of this approach. Parameter calibration by determining intercepts for different data sets on a plot of σ_0 against m also warrants further investigation.

The modified J integral has been shown to produce path independent values for a range of load histories. However, based on figures 4.10 and 4.14 the resulting values are unable to accurately characterise fracture following cyclic plastic deformation. This is highlighted by the negative J_m values produced for the LUCF load cycle in figure 4.10.

A notable exception is the SENB data following the CUCF cycle where a reasonable prediction was obtained. This is likely to be due to the introduction of the crack into an existing residual stress and plastic strain field. This allows the 'initial state' for J_m to be clearly defined as that of the uncracked body, just prior to crack insertion. For the PUCF and LUCF cycles for the CT data, defining the initial state as that following preloading and cooling, but prior to the final loading to fracture, has only a small effect on the values of J_m (figure 4.9(b)). A similar effect was also seen for the SEB PUCF load cycle (figure 4.13).

For the PUCF and LUCF cycles, the preloading cycle is applied to the cracked body. It then becomes considerably more difficult to separate the components of plastic strain which are incompatible with the current stress field as discussed by Lei [38]. Inclusion of all accumulated plastic strain results in large J values, unrepresentative of the energy available for crack propagation. Furthermore, derivation of the J_m formulation (equation 2.25) is reliant on the assumption that $\epsilon_{ij} \approx du_i/dx_j$. Where deformations are large, such as in many of the preload cycles discussed where significant plastic deformation occurs, this assumption is no longer valid.

The Eshelby force, F_k shows some ability to accurately predict the effects of load history, correctly predicting an increase in fracture load for the CT LUCF cycle and a decrease in fracture load for the SENB CUCF cycle. This is likely to be linked to the dependence of F_k on elastic strains only. The resultant value is therefore dependent on the current stress field only and not the plastic strain history.

The local approach methods used were, in general, able to accurately model failure in the AR state for all specimens. For the CT data, figures 4.11 and 4.12 show that the model fits to the AR data are nearly identical for all

model variants employed. The prediction of failure based on the Beremin model correctly suggests an increase in fracture load for the LUCF cycle and a decrease for the PUCF case. The strain nucleation model however incorrectly predicts a decrease in apparent strength for the LUCF case. This is attributed to the model's assumption that the number of local defects is proportional to the total accumulated plastic strain. In cases with plastic deformation history, this may result in predictions of high failure probability although local stresses may be low.

For the SEB and SENB specimens, it can be seen in figure 4.15 that the two models based on local strains (the strain nucleated and incremental models) were better able to capture the variation in fracture load for the two AR geometries. All models predicted a significant drop in fracture load following the PUCF cycle (figure 4.17), but such a change was not manifested in the experimental data. For the CUCF load cycle (figure 4.16), the strain based model dramatically under predicts the fracture loads. An improved, but still conservative, prediction is obtained from the Beremin and incremental models. For both preload cycles, models based on hydrostatic stress predicted higher fracture loads following room temperature preloading than those based on maximum principal stress.

The model fits to the RNB data (figures 4.19 and 4.20) show some anomalous behaviour for the Beremin and strain nucleated models with a decrease in failure probability with load for the RNB15 and RNB8 specimens. This is likely to be due to local stress redistribution, as a result of yielding, lowering peak local stresses. As failure probability must be a monotonically increasing function of time, this phenomenon highlights a clear problem with the non-incremental formulations. It should be noted that the effect is more pronounced for models based on σ_1, although this is likely to be an effect of the considerably higher m values strongly weighting the predicted Pf towards small regions of peak stress.

Predictions of the warm prestress effect for the round notched bar specimens, displayed in figure 4.22, show that all the models used predict little change in fracture load for the RNB7.7 specimens, as also seen in the experimental data. For the RNB8.8 geometry, the local approach models were able to correctly predict a change in shape for the load/failure probability curves but consistently under predicted the overall size of the fracture loads. The incremental model provides the best predictions of failure and, as before, models

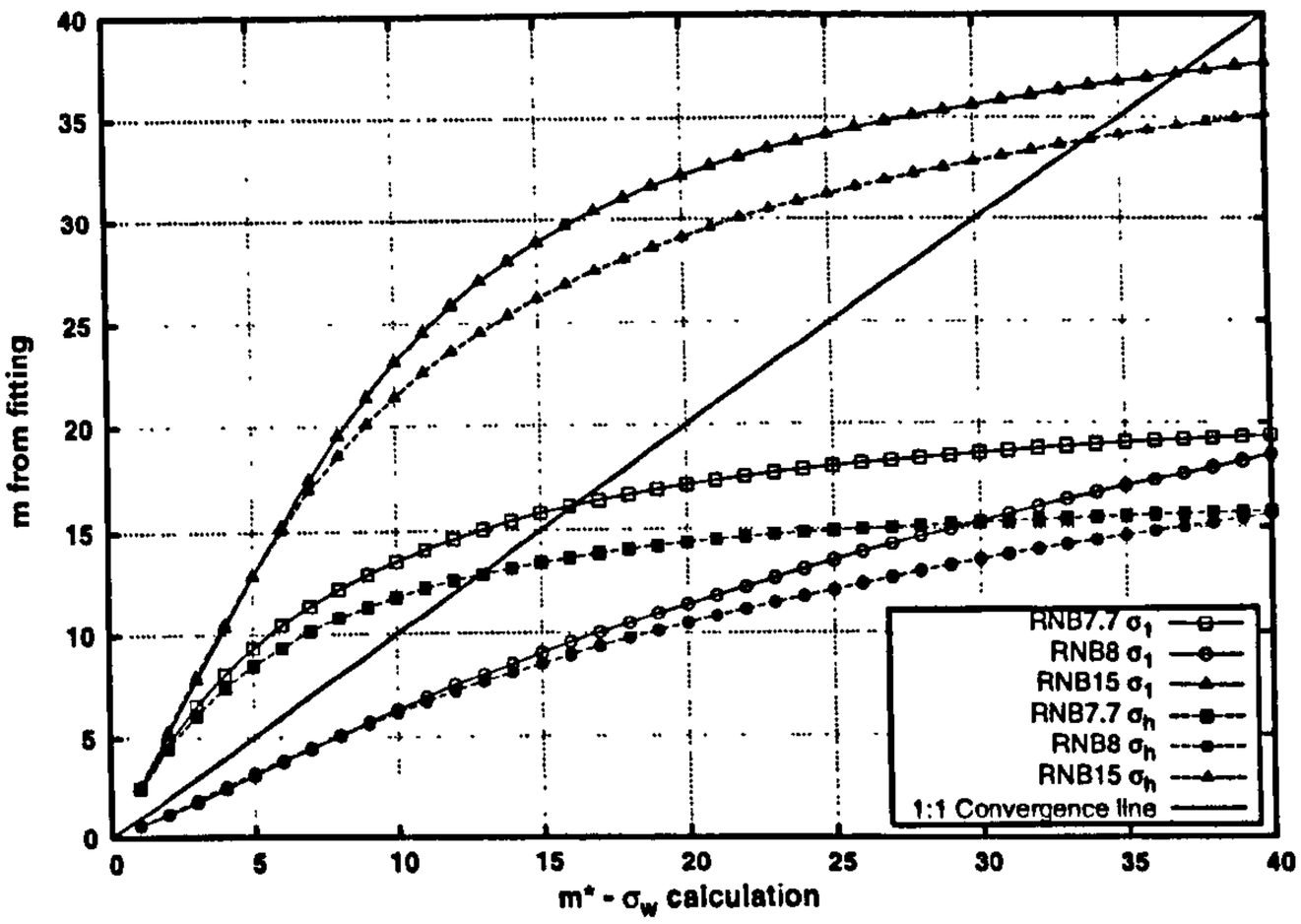

Figure 4.27: Weibull slope m from best fit plotted against $m*$ used to calculate Weibull stress σ_w. Values calculated using the incremental Weibull stress model, applied to A508 RNB data.

based on hydrostatic stress suggest higher overall fracture loads.

The investigation into the effect of modelling assumptions, for cracks introduced into existing residual stress fields, highlighted a large potential variation in the J_m values which may be obtained. A definite trend was observed with the apparent effect of residual stress decreasing as the increment of crack growth grew smaller.

As the crack is introduced in increasingly fine increments, the situation becomes closer to that of a growing crack. As noted in a number of previous works e.g. [147] the energy available for fracture becomes zero for continuing crack growth. This phenomenon may explain the marked decrease in K_J with decreasing crack growth increment.

From a practical point of view, the dependence on growth increments results in significant ambiguity as to the proper determination of J_m for a crack introduced into a residual stress field. The most accurate modelling of the crack introduction process would appear to result in very low values of J_m, which in turn may significantly underestimate the effect of the residual stress field.

4.9 Conclusions

A range of previously published cleavage fracture data for ferritic steels, with and without load history has been studied. Using a number of models for cleavage fracture to analyse and predict failure, the following conclusions have been drawn

1. Use of a modified J integral was shown to provide path independent values for cyclic and monotonic load cycles, with significant non-proportional stressing. In cases where significant plastic deformation occurs prior to failure, such as in cyclic loading, the value of J_m is significantly increased.

2. Significant plastic deformation invalidates the small strain assumptions used in deriving J_m and plastic dissipation casts significant doubt on it's interpretation as an energy release rate. This is highlighted by very large or even negative values produced following preloading.

3. Modelling of crack growth into a residual stress field showed a significant effect of the increment size of crack growth. Where the growth was finely modelled, better approximating continuous growth as would be the case for an EDM wire cut, the resulting J_m values due to residual stress decreased significantly.

4. Local approach methods were generally able to correctly predict a change in shape of plots of estimated experimental failure probability against load following load history, as well as the overall increase or decrease in fracture load.

5. Calibration of the Weibull exponent m by matching values from linearised fitting with proposed values was problematic for lower constraint data sets. Converged values could not be found for the lowest constraint RNB samples, this may be an indicator of a problem with the Weibull model in the context of the local approach to fracture, or a problem associated with calibrating to more than one geometry via this method.

6. Linking local defect population to the total accumulated equivalent plastic strain was found to under predict specimen strength following preloading. This was attributed to an overestimate of local defect density following significant plastic deformation.

7. Use of an incremental strain formulation to describe defect nucleation was found to improve prediction of load history effects compared with the commonly used Beremin local approach model.

8. Introduction of a local threshold stress for defect propagation did not significantly effect agreement with data in the AR condition or quality of prediction of load history effects although correct determination of threshold stresses requires further investigation.

9. Use of hydrostatic stress, rather than maximum principal stress, to characterise fracture behaviour resulted in improved prediction of load history effects and reduced conservatism.

10. The work has highlighted the problems of empirical determination of local approach parameters and the unsatisfactory nature of many current methods for calibration to experimental data. Further investigation is needed to provide guidance as to the algorithms and experimental data used to calibrate local approach models in order to minimise error and maximise transferability of the models between geometries and load cycles.

Chapter 5

Fracture experiments

5.1 Design of experiments

In designing and undertaking any programme of experimental tests, it is important that the aims of the work are well defined at the outset. The fracture testing undertaken in this work was devised to resolve a number of questions raised by the reanalyses of previously published data in chapter 4.

Principal among these was the issue of the calibration of local approach models. The ability of varying methods to predict the effects of load history is difficult to accurately determine if model constants cannot be reliably calibrated.

The aim of the test program in this thesis was twofold. The first was to provide suitable data for rigorous calibration of numerous models for failure and to ensure geometric independence of the calibrated values. Secondly, it was required to obtain data for fracture following significant load history against which to compare calibrated model predictions. To meet these objectives, a total of 121 fracture tests were performed, as summarised in table 5.1.

5.1.1 Specimen geometry and loading

Monotonic load cycles

To accurately determine local approach parameters, ensuring geometric independence of the fracture model in question, it is necessary to have data from at least two specimen geometries. Preferably, high and low constraint data is needed. Most importantly, the structure of the stress/strain fields in the two geometries should be sufficiently different to avoid problems of self similarity

when calibrating local approach models [75].

To this end, two standard CT geometries were selected. A set of 20mm thick specimens was chosen to determine a 'baseline' plane strain fracture toughness according to ASTM E399 [27]. A further set of 10mm thick CT specimens was manufactured to provide a low constraint cracked geometry. Both standard CT geometries are illustrated in figures 5.1(a) and 5.1(b).

To ensure consistency between specimens EDM wire cutting, rather than fatigue precracking, was used to introduce the final 'crack' into the CT specimens. Cutting was undertaken using a wire of 0.1mm diameter, selecting the slowest available erosion speed to ensure accuracy. Twenty of these specimens were examined under high optical magnification, showing a mean final notch diameter of 0.19mm with standard deviation of 0.007mm.

Although the 10mm CT specimens were of lower constraint than required for standard fracture toughness testing, the presence of an existing macro-scale crack creates a region of high triaxiality ahead of the crack tip. This tends to produce a region with very high local stresses but relatively low plastic strain, compared to a similar uncracked geometry. To better study the relationship between stress and plastic strain in the eventual cleavage fracture event, failure of round notched bar (RNB) specimens - representing very low constraint levels - was also studied. Three V-notched RNB specimen types, with decreasing notch width, were fabricated and are shown in figure 5.2

Specimens with load history

The effects of prior loading on fracture behaviour can be decomposed into effects due to a change in the local stress field, strain hardening and the generation of residual stresses, as well as any changes to the material microstructure resulting from plastic strain. It is assumed that the effects of thermal loading in terms of creep or microstructure change are negligible.

In an attempt to decouple the strain effect from that of residual stress it was necessary to produce specimens with a well defined plastic strain history, but negligible residual stress. The effect of strain hardening was minimized by using a 20mm thick CT geometry, where levels of near tip triaxiality maintain high local stresses, such that increasing yield stress was expected to have a secondary effect on the peak stresses. A tensile prestrain was applied to large specimens of uniform cross section before extracting specimens of CT geometry, as in figure 5.1(a).

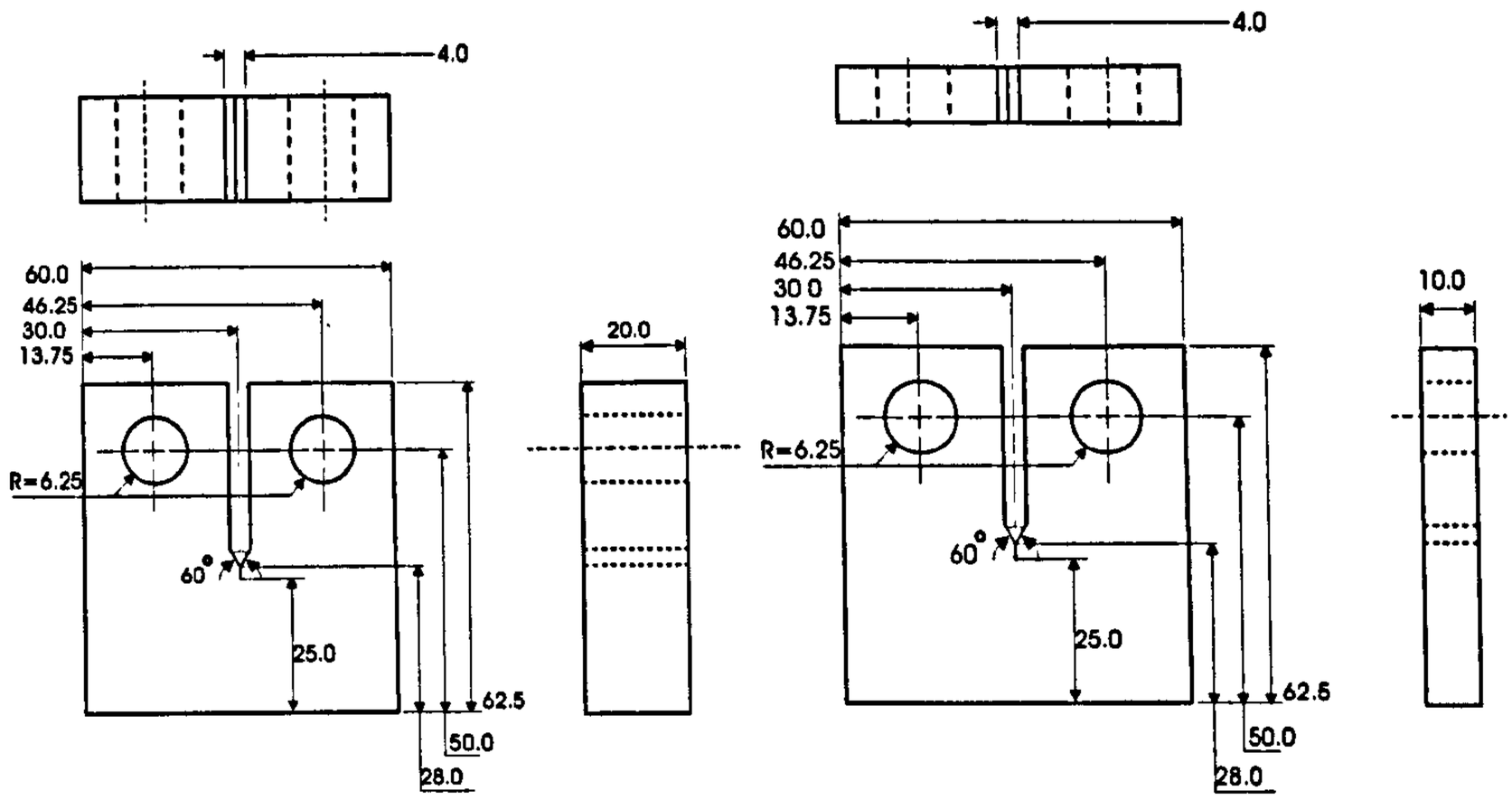

(a) CT20 specimens.

(b) CT10 specimens.

Figure 5.1: Geometry of CT specimens, dimensions in mm.

To investigate the effect of combined residual stress and plastic strain, two modified CT specimen types were also tested. Following a number of previous works, e.g. [148], notched CT (NCT) specimens were preloaded to induce yielding at the notch root. Upon unloading, a residual stress field is created. The initial specimen geometry and load type is shown in figure 5.3. Both tensile and compressive preloads were applied, resulting in compressive and tensile residual stress fields at the notch root. The 'crack' was inserted into the specimens after the preload cycle, using EDM cutting. This was intended to provide a well defined 'initial state', to allow analysis of the residual stress effect on fracture using, for example, the modified J integral or a weight function analysis to determine K due to residual stress.

Preloading of precracked specimens was also investigated. In this case the commonly used LUCF warm prestress (WPS) cycle was employed. The load cycle was applied to CT specimens, of geometry as in figure 5.1(a), with a tensile preload applied and then unloaded at room temperature before cooling and loading to fracture.

5.1.2 Material selection

As cleavage fracture was the failure mode of interest, a material with a BCC crystal structure was preferred. Specimens were therefore fabricated from

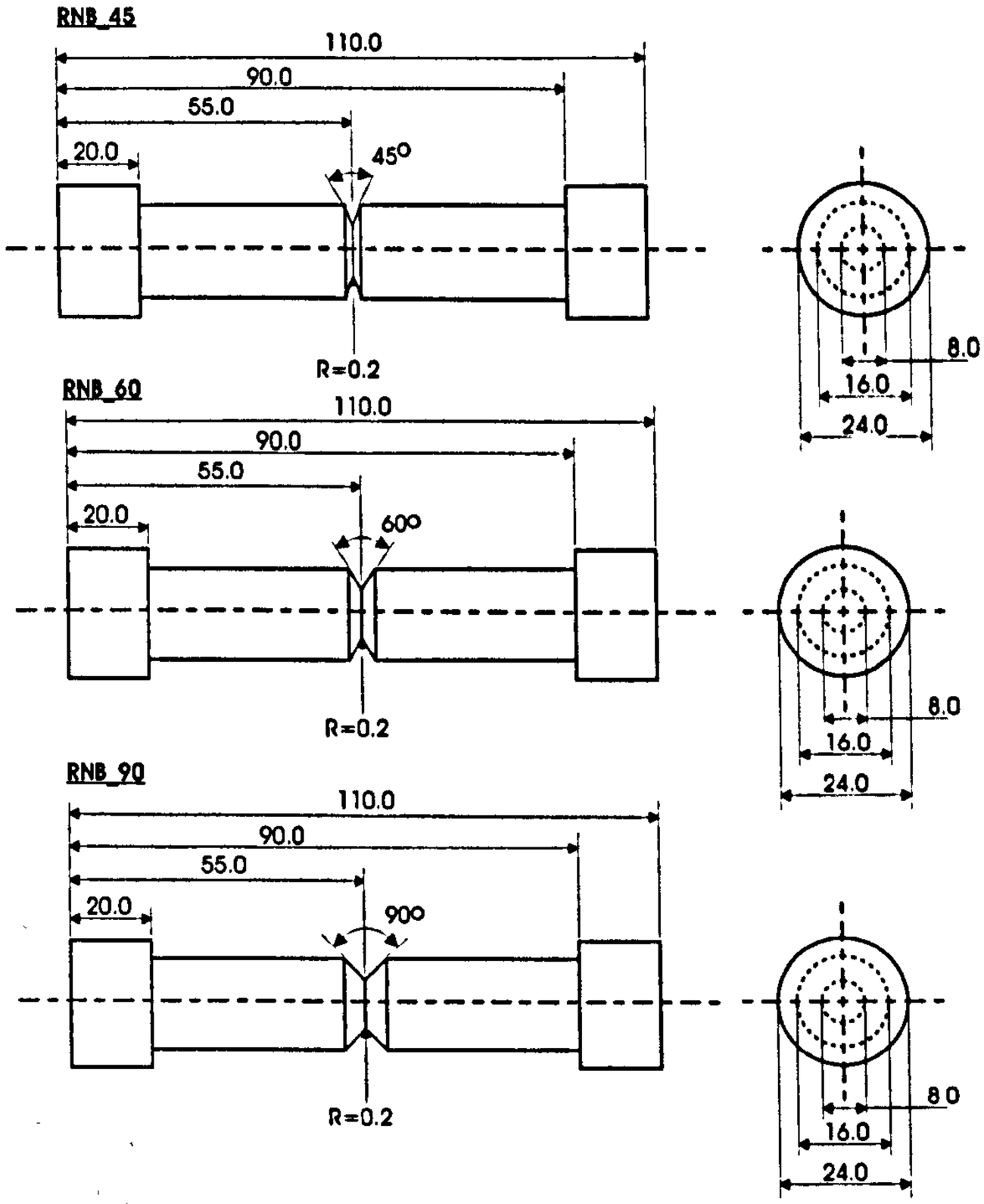

Figure 5.2: Geometry of RNB specimens, dimensions in mm.

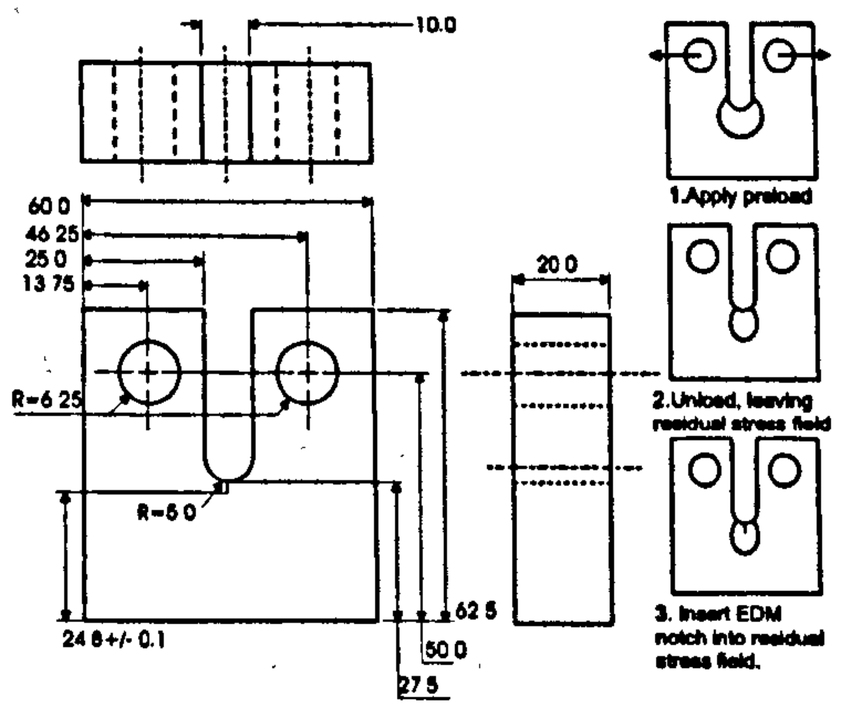

Figure 5.3: Geometry of notched, modified CT specimens, dimensions in mm.

A533B ferritic steel. This material was selected as it has been the subject of a number of previous investigations e.g. [145, 149, 150, 13] and is typical of the types of high strength steel used in many safety critical applications such as the manufacture of reactor pressure vessels.

The material in this work was previously used by Mirzaee-Sisan [74], and as such the material properties were well characterised. However, the centre of the billet was used in [74], whereas two sections from the top and bottom of the casting were used in this work. In addition, the material properties quoted for A533B steel in [74] were measured as part of an earlier project and corresponded to a different batch of steel. Therefore, it was deemed wise to perform separate tests to confirm the physical properties of the material used in this work.

Tensile testing at room temperature was undertaken according to ASTM E8 [113], using a mechanical extensometer to monitor the true strain over the centre section of the specimens. The geometry of the room temperature tensile test specimens is shown in figure 5.4 A. Tensile tests were also performed at low temperature on virgin material, as well as following varying degrees of tensile prestrain at room temperature. To allow testing within an appropriate low temperature chamber, an alternative grip arrangement was designed as shown in figure 5.5. Tensile test specimens for low temperature testing are shown in figure 5.4 B.

Room temperature tensile tests were carried out on specimens aligned with and transverse to the rolling direction in the material parent plate, labelled 'Longitudinal 20°C' and 'Transverse 20°C' in figure 5.6. The results show little anisotropy in material response and good agreement with the data previously reported in [135, 74]. Tests at −150°C showed an increased material yield strength, as well as noticeable yield point elongation. The results differ appreciably with those reported previously and so data obtained in this work was used for modelling low temperature material response. A number of specimens were subjected to tensile prestrain of 0.5%, 3% and 4.5% at room temperature before tensile testing at −150°C. The work hardening effect of the room temperature prestrain was very close to that which would be expected from applying the same plastic deformation at low temperature, as can be seen in figure 5.6. To ensure consistency, all fracture specimens were cut with L-S orientation relative to the original plate.

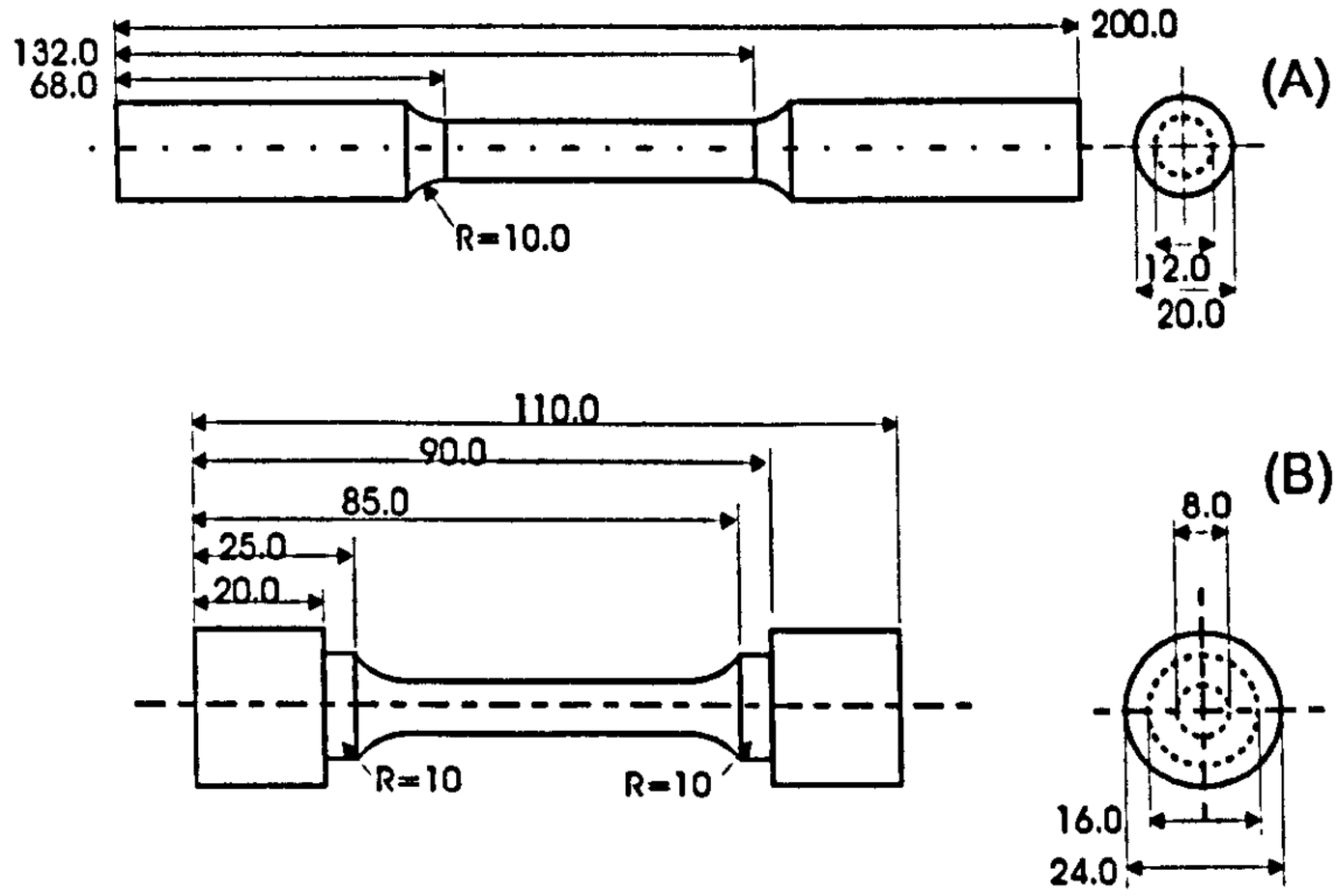

Figure 5.4: Tensile test specimens used to determine tensile behaviour (A) at room temperature and (B) at −150°C. Dimensions in mm.

5.2 Experimental method

5.2.1 CT Specimens - 20mm thickness

Fracture tests for the AR state CT20 specimens were carried out using an Instron tensile test machine with load capacity 250kN. All other tests were undertaken on a Dartec 500kN capacity machine.

All tests were undertaken at −150°C, achieved by encasing the specimen grips in a nitrogen cooled low temperature chamber. Although the internal air temperature was automatically controlled and monitored, there was concern that the steel samples would cool at a considerably slower rate due to differing specific heats. To ensure constant temperature during loading to fracture, a K-type thermocouple was fixed to the specimens using a spring loaded clip. The thermocouple voltage was used to determine the current specimen temperature relative to the air outside the chamber and thereby determine when a steady state specimen temperature had been reached.

Loading was applied to the CT specimens via pins, manufactured from hardened EN24 steel to ensure elastic response across the load levels used. The crosshead displacement rate was 0.2mm/min for all specimens to approximate static loading.

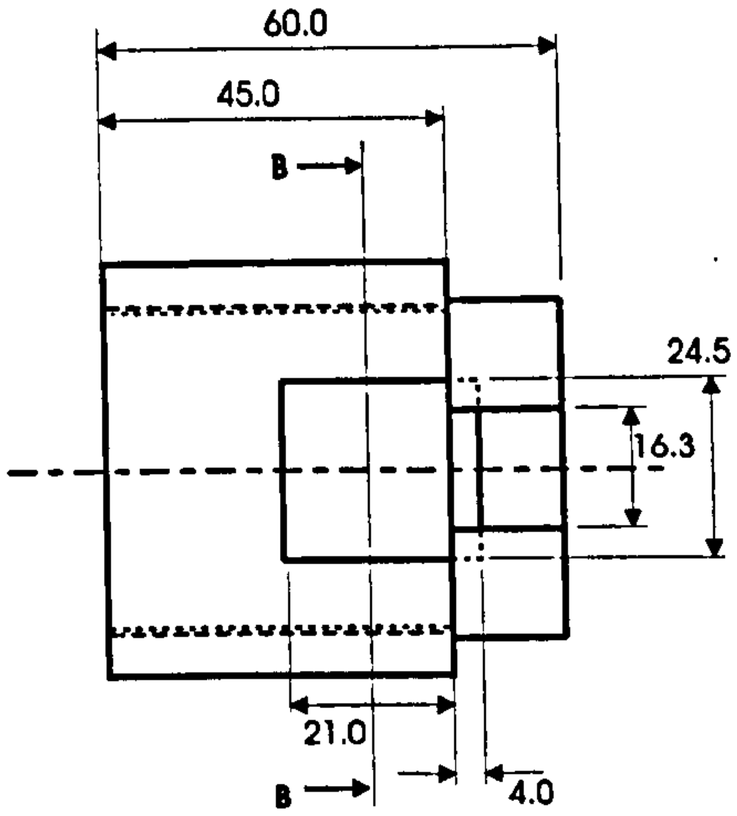

A: Clamps for RNB specimens showing slot for specimen insertion / removal

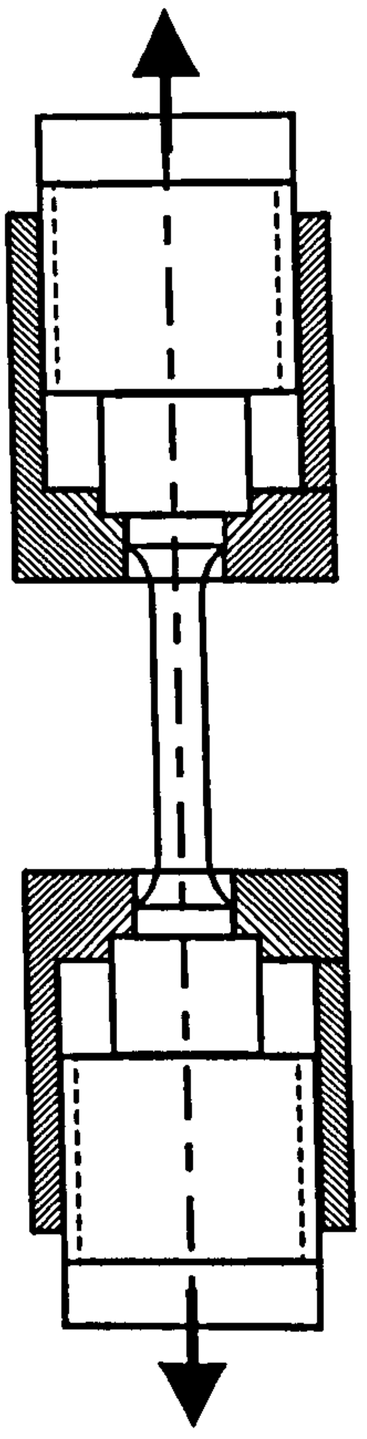

B: Loading assembly for RNB and tensile test specimens

Figure 5.5: Clamping arrangement for low temperature tensile specimens. Dimensions in mm.

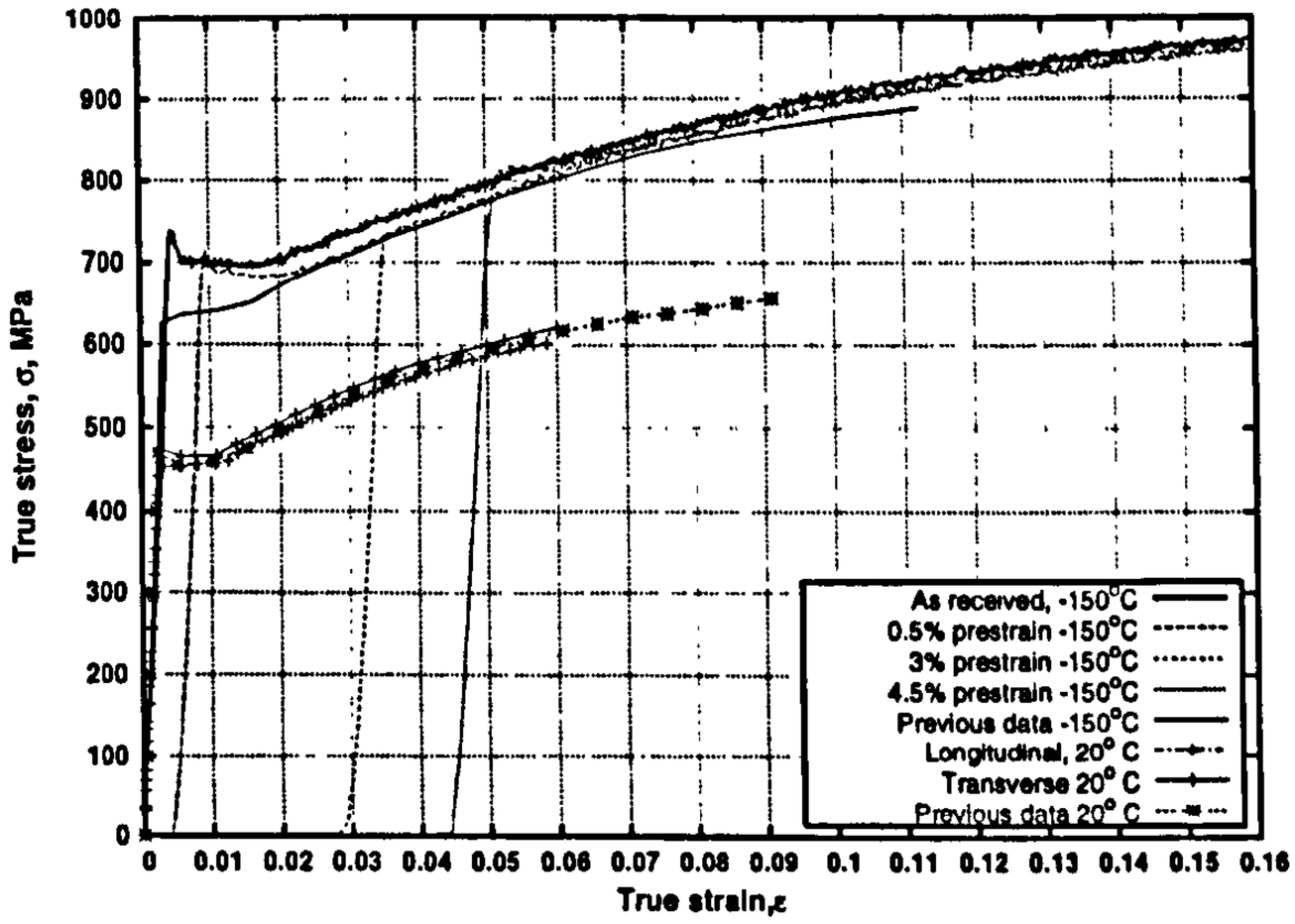

Figure 5.6: Tensile test data for A533B steel obtained in this work and previously used by Mirzaee-Sisan.

The pin loading arrangement and low temperature chamber are shown in schematic form in figure 5.7. Good repeatability in load/displacement behaviour was observed in most samples tested, as plotted in figure 5.8. Experimental data are displayed in table 5.2. Analytical K and stiffness solutions for CT specimens are provided in [22],

$$K_I^{el} = \frac{P}{B\sqrt{W}} f\left(\frac{a}{W}\right) \tag{5.1}$$

$$f\left(\frac{a}{W}\right) = \frac{2+\frac{a}{W}}{(1-\frac{a}{W})^{\frac{3}{2}}}\left[0.886 + 4.64\left(\frac{a}{W}\right) - 13.32\left(\frac{a}{W}\right)^2 + 14.72\left(\frac{a}{W}\right)^3 - 5.60\left(\frac{a}{W}\right)^4\right]$$

$$\Delta = \frac{P}{BE'} Z\left(\frac{a}{W}\right) \tag{5.2}$$

$$\begin{aligned} Z\left(\frac{a}{W}\right) \;=\; & \left(\frac{1+\frac{a}{W}}{1-\frac{a}{W}}\right)^2\left[2.163 + 12.219\left(\frac{a}{W}\right) - 20.065\left(\frac{a}{W}\right)^2\right. \\ & \left. -0.9925\left(\frac{a}{W}\right)^3 + 20.609\left(\frac{a}{W}\right)^4 - 9.9314\left(\frac{a}{W}\right)^5\right] \end{aligned}$$

where P is the applied load, B and W the specimen thickness and width, E' is Young's modulus for plane stress conditions and Δ is the specimen load line displacement. Based on equations 5.1 and 5.2 the experimental loading rate was found to be equivalent to 0.315 MPa.m$^{0.5}$/min.

In six of the tests, 'pop in' was observed - characterised by a sudden reduction in load at a given displacement, followed by a continued linear increase in load/displacement. This may be a result of stable crack growth prior to the final fracture event or some 'settling' in the loading apparatus. The effect on load/displacement behaviour was not severe in most cases, the exceptions being specimens 4 and 10, as seen in figure 5.8(a).The fact that the specimen stiffness was not appreciably altered would suggest that significant crack growth had not occurred. The fact that, of the six cases with a drop in load, five occurred in sequential tests further suggests an issue with the load apparatus. Regardless of the reason, the fact that unloading occurred prior to fracture raises questions about the validity of the tests.

Examining the complete data set, there is no systematic change in final fracture load between specimens where pop-in was or was not observed, as shown in figure 5.9. However, the fact that some crack growth appears to have occurred prior to final failure results in ambiguity as to the crack configuration just prior to failure. Therefore, only the data where no crack growth occurred prior to failure were used for the analyses which follow. The entire data set with estimated ranked fracture probabilities, as well as the 'no pop-in' data only are displayed in figure 5.9 and it can be seen that the effect of 'sanitising' the data on the overall distribution is small.

5.2.2 Prestrained CT specimens

In order to create a uniform strain field with no nominal residual stress, a number of large scale tensile specimens, as in figure 5.10, were fabricated. Tensile prestrain was applied at room temperature using a 1000kN Losenhausen tensile test rig. Strain in the centre of the specimens was monitored using a mechanical extensometer, to enable a desired level of macroscopic plastic deformation to be attained. Permanent tensile strains of 1%, 3% and 5% were imparted to 6 samples - 2 for each prestrain level.

A total of 3 CT20 specimens, of geometry as in figure 5.1(a), were then extracted from the centre of the tensile samples, as shown in figure 5.10. The CT specimens were aligned such that the direction of crack propagation was

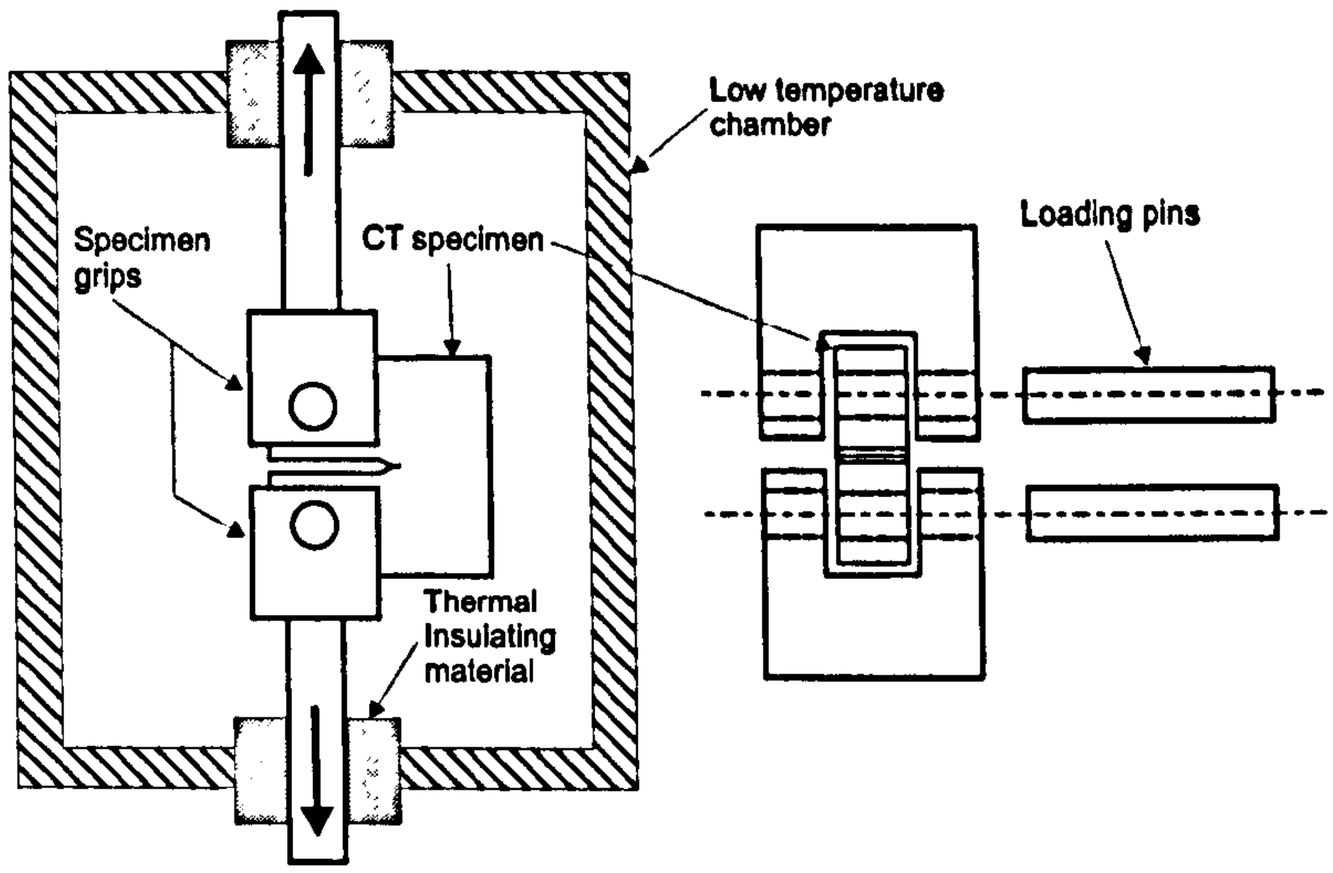

Figure 5.7: Schematic of experimental apparatus for CT specimens.

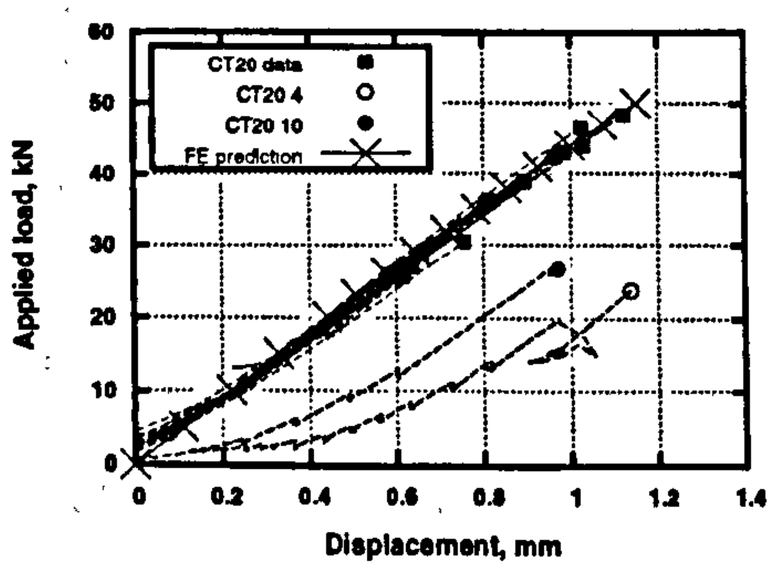

(a) Tests 1-15

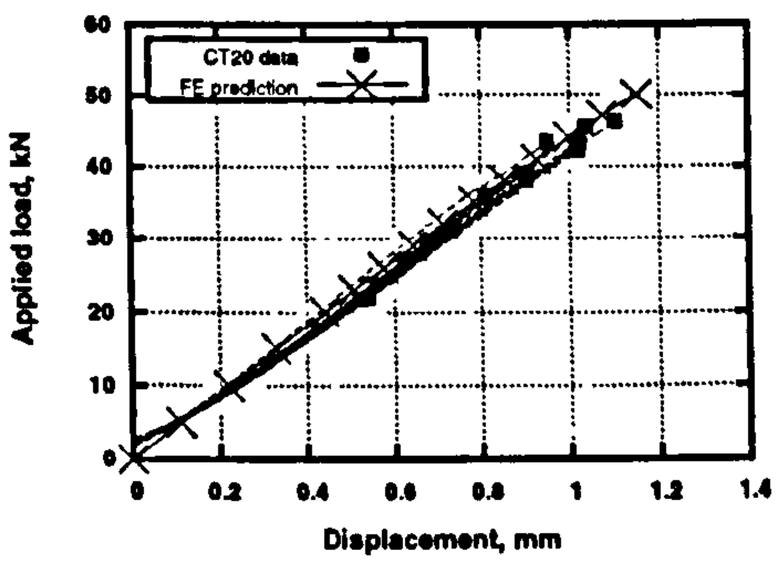

(b) Tests 16-30

Figure 5.8: Applied load vs. crosshead displacement from fracture testing of CT20 specimens compared with finite element predictions.

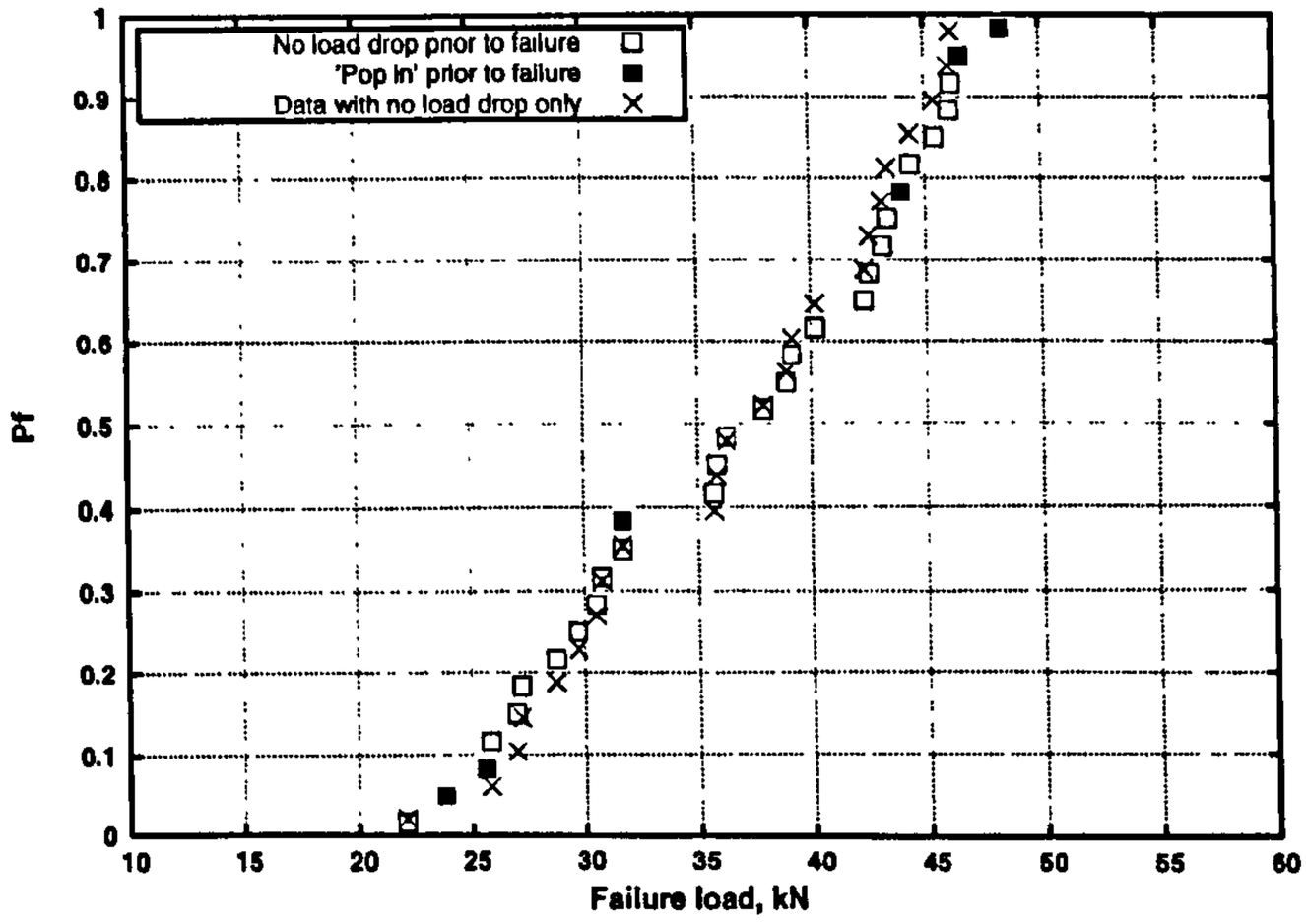

Figure 5.9: Test results from CT20 specimens

normal to the direction of the prestrain. Specimens were fractured using an identical experimental procedure to that in section 5.2.1, cooling to −150°C, monitoring temperature via a thermocouple and loading to fracture at a rate of 0.2mm/min. The results for the three levels of prestrain are reproduced in tables 5.4, 5.5 and 5.6.

Experimental load-displacement plots, as in figure 5.11(a), showed consistent response across all specimens, with the notable exception of the 5% prestrain sample CT20_51b which exhibited a greatly reduced stiffness. This was traced to a reduction in crosshead clamping force and, once this was remedied, the traces for the remaining specimens were consistent with those previously tested. As the behaviour remained linear for specimen CT20_51b and the fracture load is consistent with the remainder of the 5% prestrain data, the fracture load and K_I at fracture are taken to be reliable.

5.2.3 CT Specimens - 10mm thickness

The experimental apparatus and test conditions for the CT10 specimens were as detailed in section 5.2.1. Experimental data are presented in table 5.3 and experimental load/displacement results in figure 5.11(b).

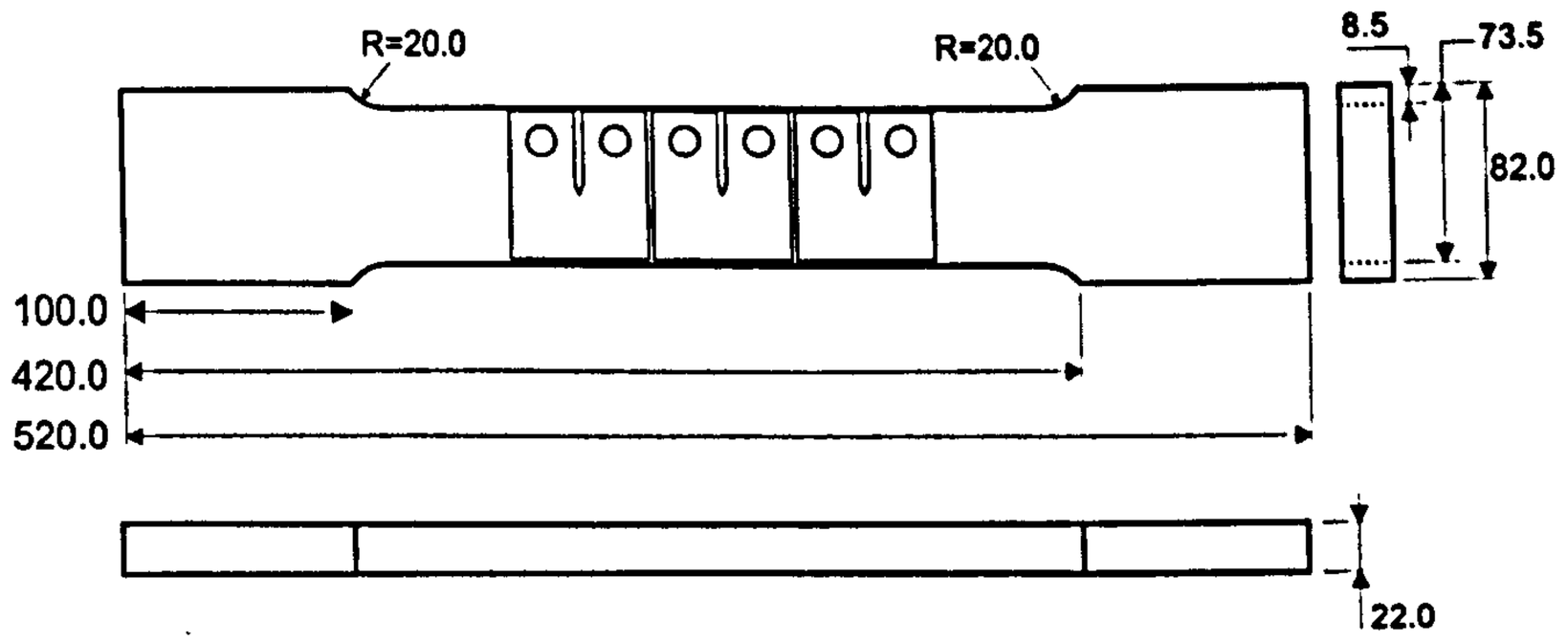

Figure 5.10: Large scale tensile specimens, used to impart uniform prestrain, showing locations of extracted CT specimens. Dimensions in mm.

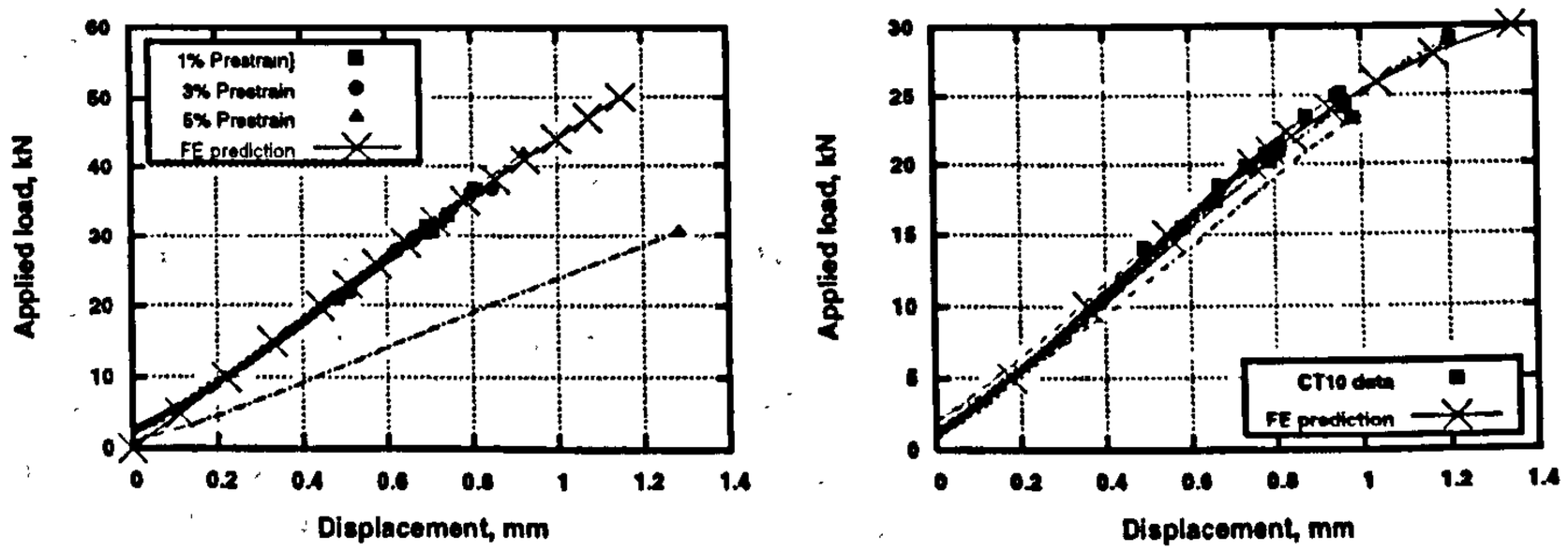

Figure 5.11: Applied load vs. crosshead displacement from fracture testing of a) prestrained CT20 specimens b) CT10 specimens.

5.2.4 RNB specimens

All three RNB fracture geometries, as shown in figure 5.2, were loaded using the grips illustrated in figure 5.5. The same low temperature chamber and thermocouple arrangement as detailed in section 5.2.1 were used and the crosshead displacement rate was 0.2mm/min as for the CT specimens.

Measurement of the minimum cross section of the specimens showed some slight deviation from the nominal dimensions of figure 5.2. For the RNB45 geometry, the minimum diameter was found to be 7.9mm for the RNB45 specimens and 8.1mm for the RNB90 specimens.

Load displacement traces for all three RNB geometries are plotted in figure 5.12 and experimental data are presented in table 5.7. In general, results were consistent between specimens, one exception being the specimen labelled RNB90_5 which failed at a noticeably higher load than the rest of the RNB90 data set and also displayed differing yielding behaviour, as can be seen in the upper most curve of figure 5.12(c). This would suggest that the specimen geometry may have deviated somewhat from the others, or some material anomaly may have occurred. As a result of the difference in specimen response, this sample (RNB90_5) was not included in subsequent fracture analyses.

5.2.5 Warm prestressed CT specimens

The first step in the experimental testing of the WPS CT specimens was to determine an appropriate level of preload, such that the effect of load history could be seen experimentally, but with minimal risk of specimen damage during preload. Taking K_{IC} to be 78.31 MPa.m$^{0.5}$ (the mean value from table 5.2), the analytical model of Chell [46] was employed to make predictions of the effect of varying levels of preload. The analytical formula used to implement the model for the LUCF cycle was that also used by Smith and co-workers [150].

An initial preload of 50kN was imposed. This was above the maximum failure load in the AR state and equal to an analytical elastic K_I of 108 MPa.m$^{0.5}$. The Chell model predicted a subsequent increase of K_{IC} to 132.8 MPa.m$^{0.5}$ - a fracture load of around 61 kN. A similar analysis, taking K_{IC} as the minimum and maximum values from table 5.2 suggested a likely variation in toughness following preload of 123.5 - 139.0 MPa.m$^{0.5}$, a fracture load variation of 57.2-64.35 kN. This was deemed to provide a suitable increase in toughness, such that it would be distinguishable from experimental scatter in the AR CT20

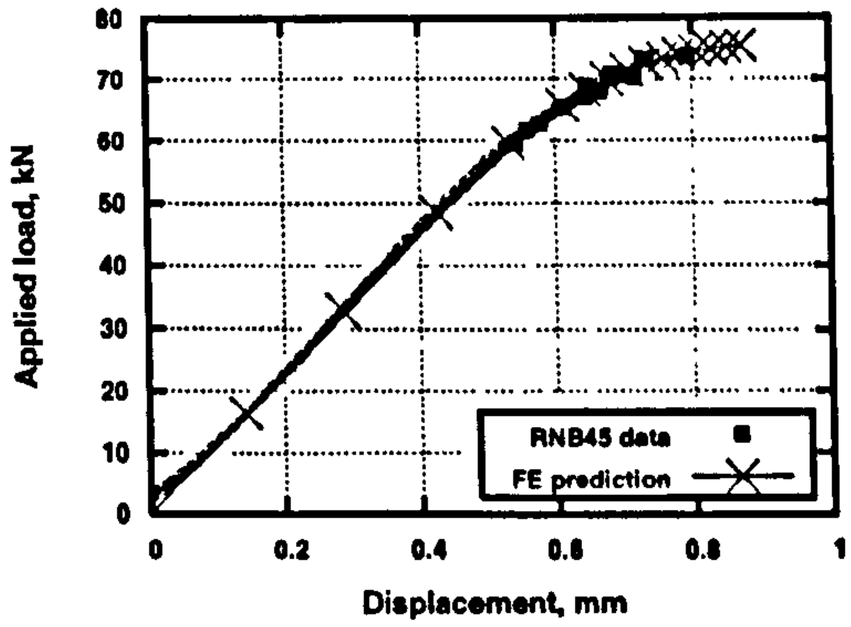

(a) RNB45 data

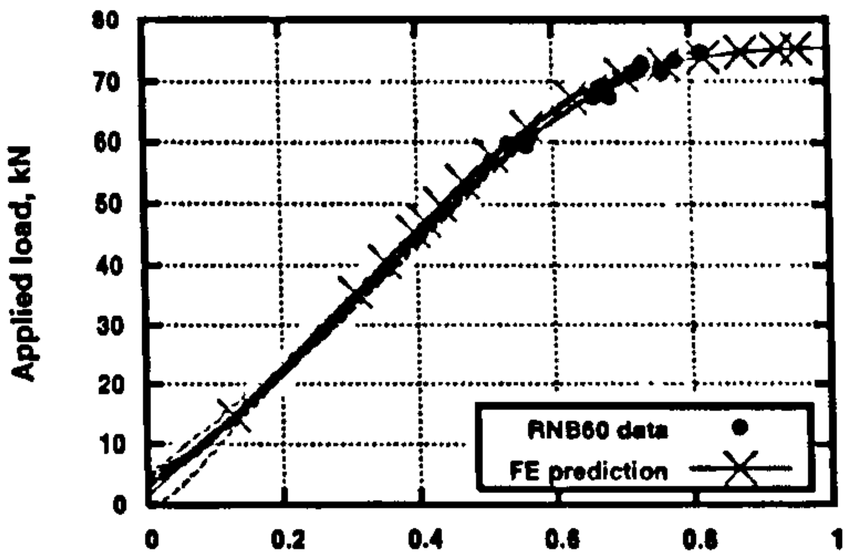

(b) RNB60 data

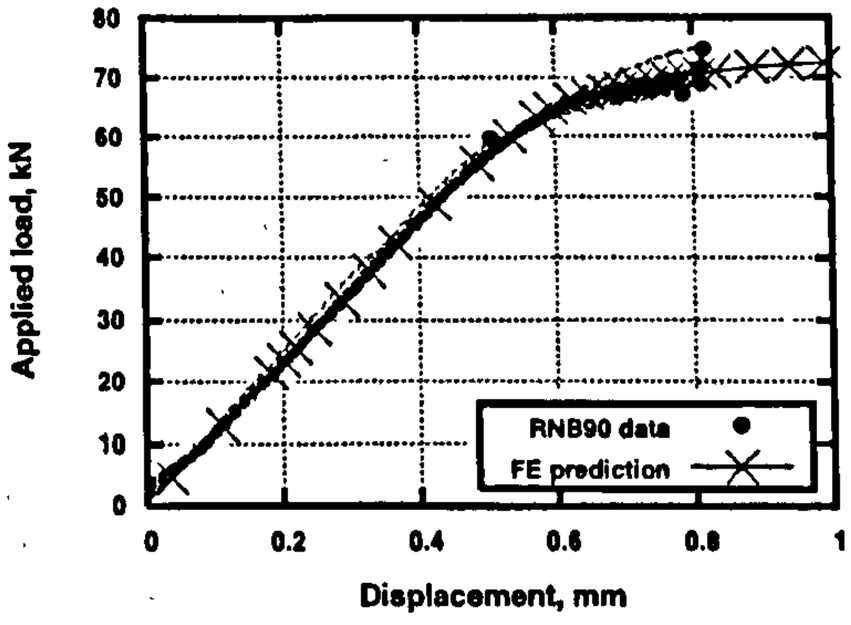

(c) RNB90 data

Figure 5.12: Applied load vs. crosshead displacement from fracture testing of RNB specimens.

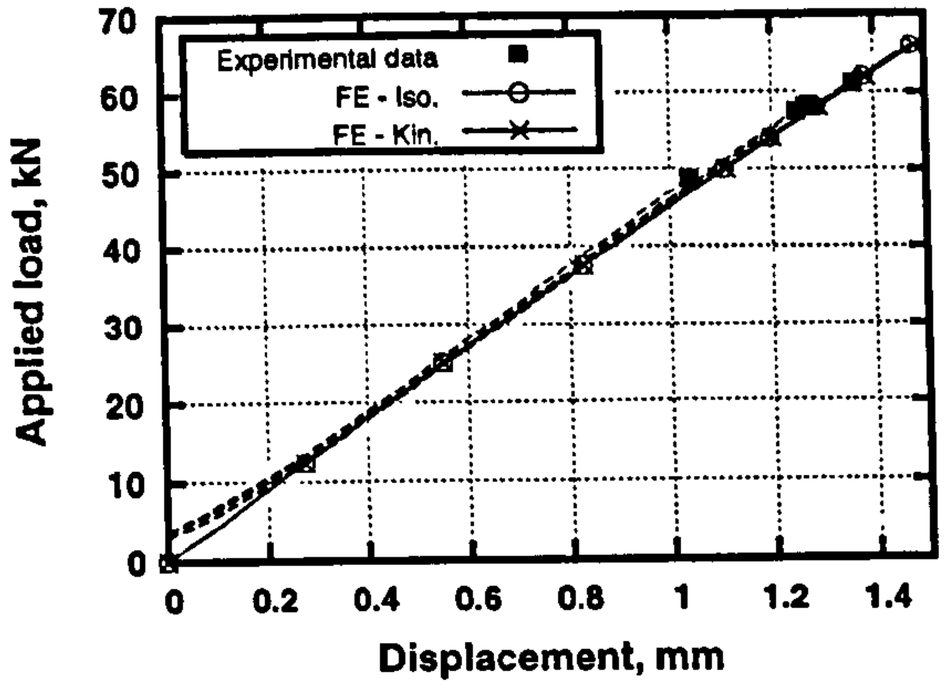

Figure 5.13: Load displacement from experimental tests and finite element predictions for warm prestressed CT20 specimens.

data, even with the small sample size of 5 specimens.

A nominal tensile preload of 50 kN was applied to 5 CT20 specimens at 20°C. Following unloading, the specimens were cooled to -150°C and loaded to failure as described in section 5.2.1. Fracture data are presented in table 5.8 and load displacement results in figure 5.13.

5.2.6 Preloaded, modified CT specimens

By preloading the modified notched CT (NCT) specimens shown in figure 5.3, it was intended to create a residual stress field on unloading that would result in an alteration of the measured fracture toughness (i.e. experimental fracture load). As an EDM 'crack' was to be introduced into the residual stress field, it was important that the tensile or compressive region at the notch root should extend beyond the tip of the inserted crack.

To ensure this was the case, a number of finite element simulations were conducted to obtain estimates of the variation of residual stress in the direction of the applied load. Selected results are shown in figure 5.14. Tensile and compressive preloads of 60kN were selected as they produced high magnitude residual stresses over the expected extent of the final crack. This was selected to be 2.5mm from the notch root, giving an a/w ratio of 0.5, as for the standard CT specimens tested.

Preloading and loading to fracture was undertaken using the apparatus in figure 5.7. The load rate for preloading and loading to fracture was 0.2mm/min.

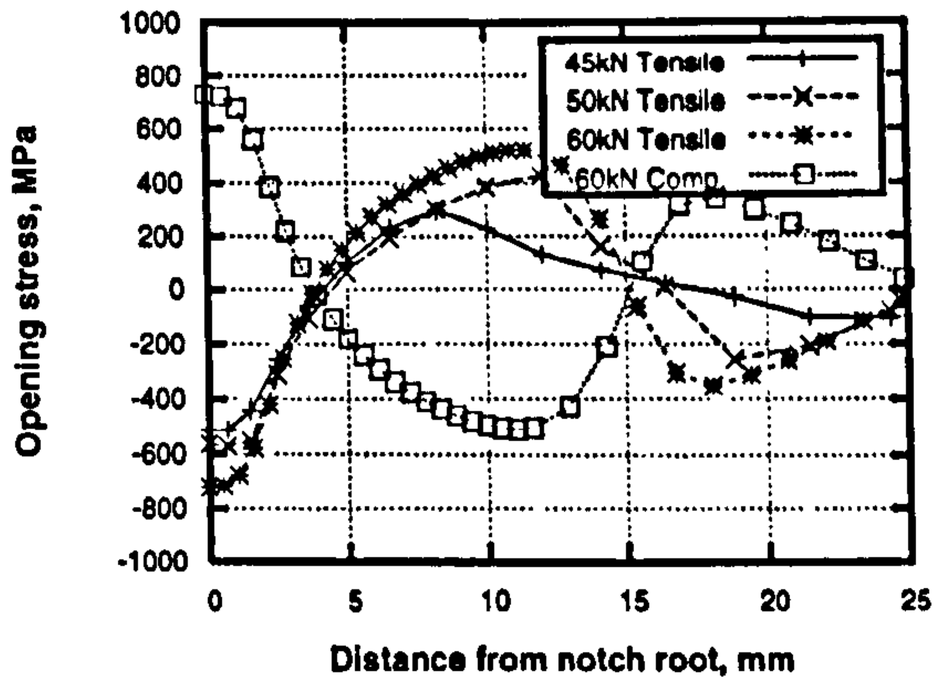

Figure 5.14: Variation of residual stress with applied preload for NCT specimens.

After the initial load and unload an EDM notch was inserted as shown in figure 5.3. Specimens were then cooled to -150°C (monitored by a thermocouple) and loaded to fracture.

It is also apparent that several of the pre-compressed specimens did not fail catastrophically (figure 5.15). Initial crack growth in these samples was seen to occur at low loads, it is therefore postulated that the effect is due to advancement of the crack beyond the near-tip tensile stress field into a region of compressive stress, causing the crack to arrest. At higher loads, the potential energy released at crack advance is higher, such that crack propagation continues through this region. The fracture data are displayed in table 5.9. Non-catastrophic failure occurred in specimens NCT_C1, NCT_C6 and NCT_C10, the displayed loads and stress intensity factors for these specimens correspond to those for initial crack propagation. The EDM notch on pre-compressed specimen NCT_C9 was found to be mis-aligned and so this sample was discarded.

5.3 Imaging of fracture surfaces

Following testing, it was necessary to ensure that the data used to calibrate fracture models corresponded to the same micro-mechanism of failure. For example, if a model for failure by cleavage fracture is applied to a data set where some values correspond to failure by ductile mechanisms, considerable error may be introduced.

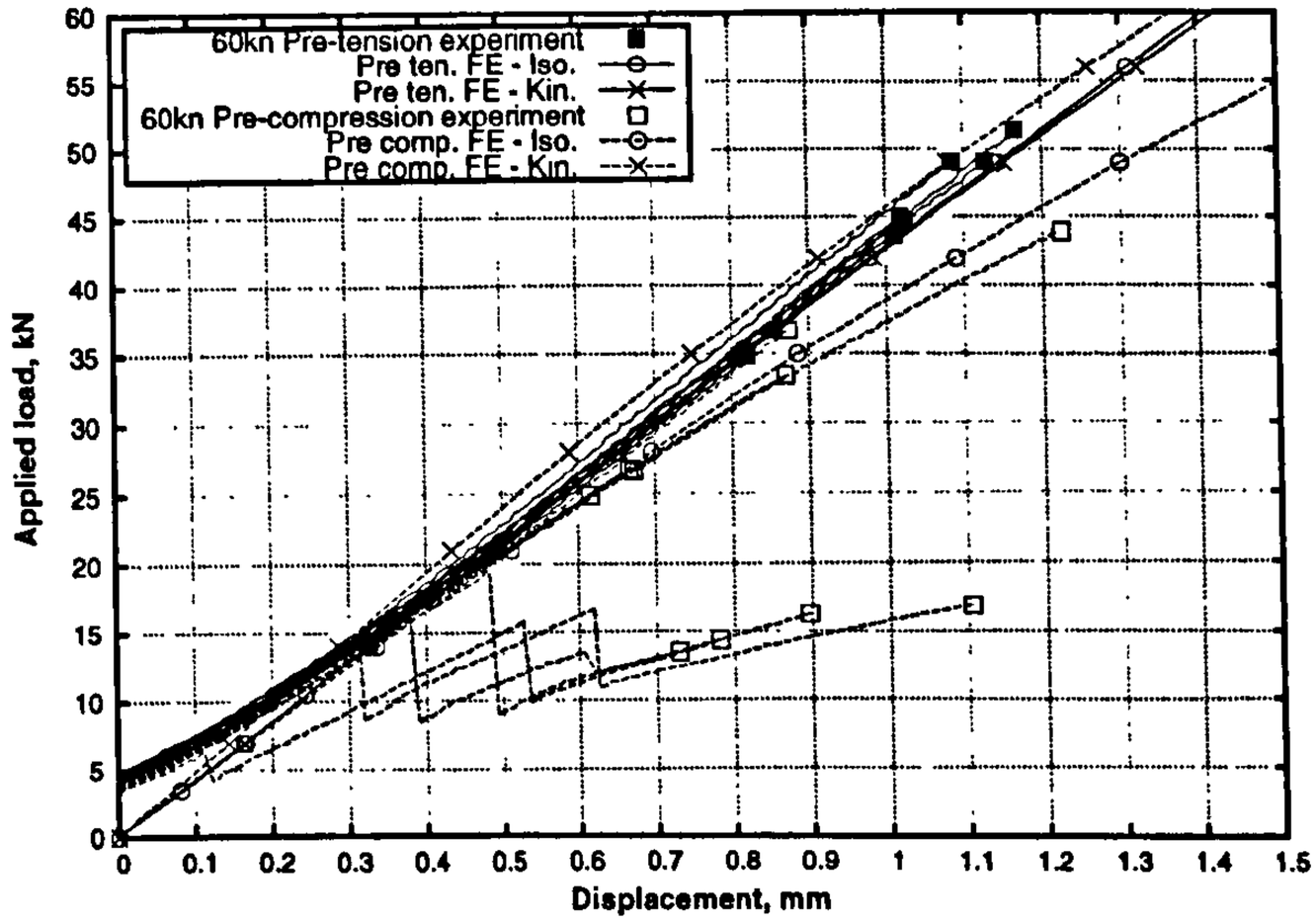

Figure 5.15: Applied load vs. crosshead displacement from fracture testing of pre-loaded notched CT20 specimens with finite element predictions for isotropic and kinematic hardening.

To ensure failure was attributable to transgranular cleavage, as initially supposed, fracture surfaces were examined under high magnification using a Hitachi S-2300 scanning electron microscope (SEM).

As imaging of the fracture surfaces of all the tested specimens would have proved extremely time consuming, SEM imaging was only carried out where fracture by ductile means was deemed most likely. In general this meant those specimens which failed at high loads or displayed significant nonlinearity of loading, indicating significant plastic deformation.

5.3.1 CT20 specimens - AR condition

Typical observations of the fracture surfaces of the 20mm thick CT specimens are shown in figures 5.16(a) and 5.16(c), corresponding to failure loads representing the lower (CT20_8) and upper (CT20_24) ends of the spectrum of measured values.

In both cases, failure was observed to occur by cleavage over the majority of the ligament with some evidence of arrested micro cracks (figure 5.16(a)). In both cases it was also observed that there were some localised microvoid clusters, indicated in figures 5.16(b) and 5.16(d). It is therefore likely that the

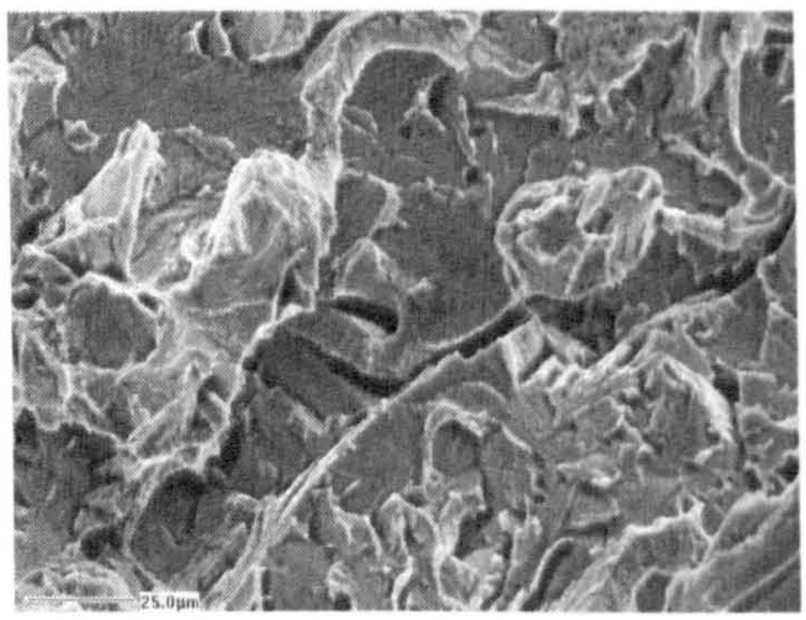

(a) Typical fracture surface observation, specimen CT20_8.

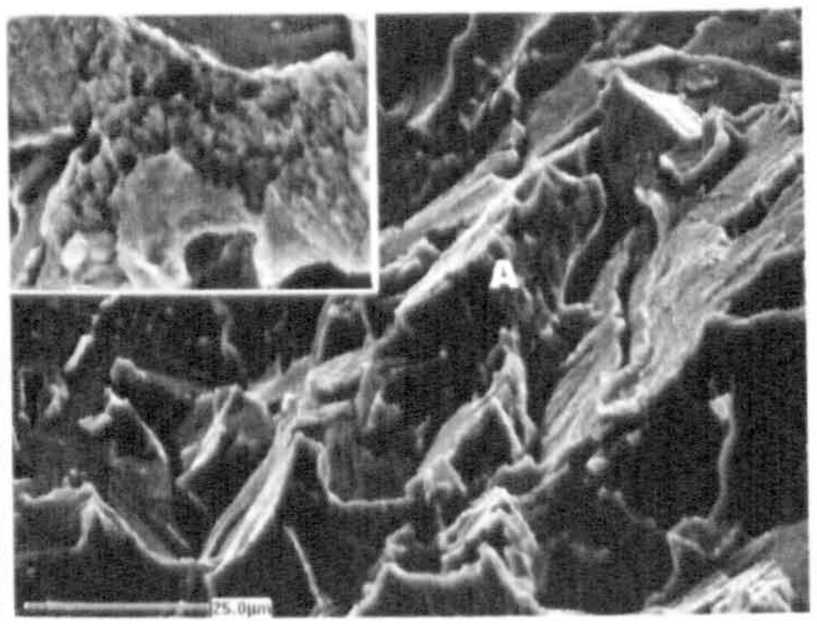

(b) Typical fracture surface observation, specimen CT20_8, showing region of microvoidage (A) and detail of microvoid region (inset).

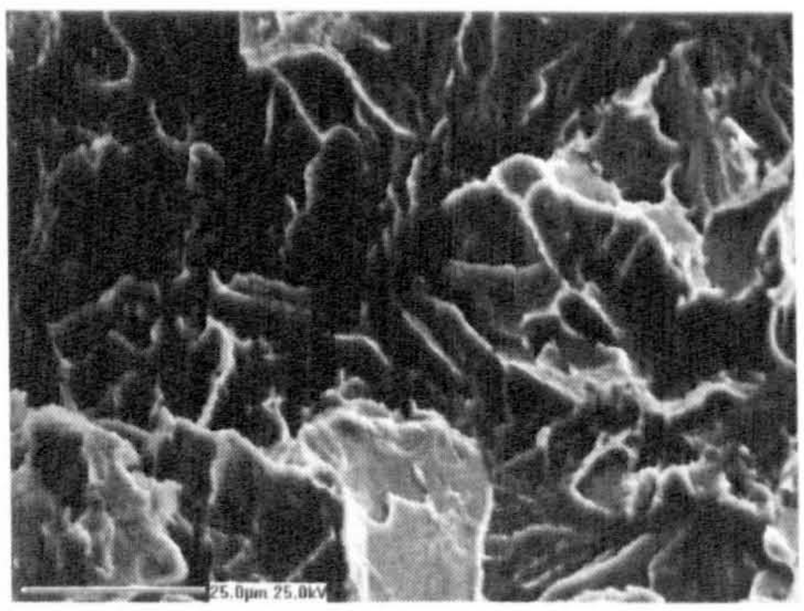

(c) Typical fracture surface observation, specimen CT20_24.

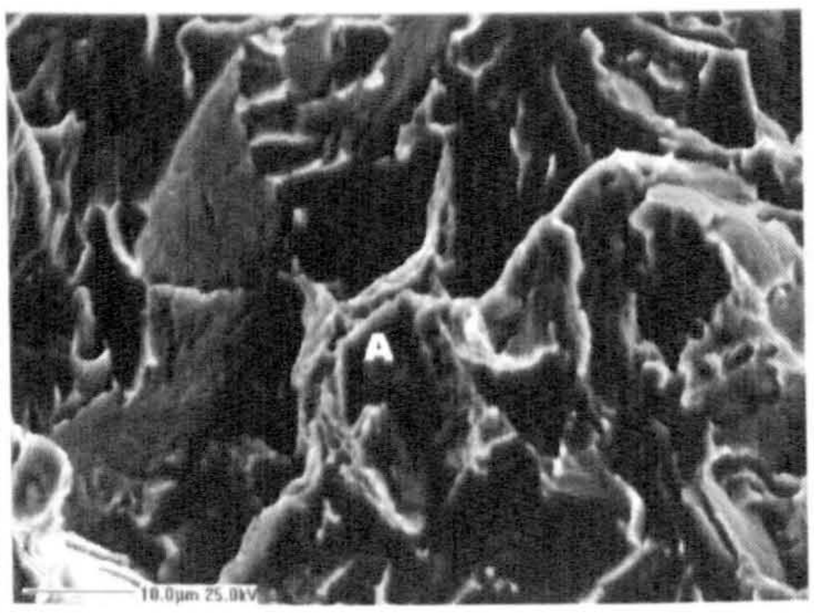

(d) Typical fracture surface observation, specimen CT20_24, showing region of microvoidage (A).

Figure 5.16: SEM images from fracture surfaces of CT20 specimens.

true failure mechanism was 'quasi cleavage', as observed previously by Kumar [14], rather than pure cleavage.

5.3.2 CT20 specimens - prestrained

Following all three investigated levels of room temperature prestrain, the nature of fracture remained predominantly trans-granular cleavage, as illustrated by figures 5.17(a), 5.18, and 5.19(a). As in the as-received case, there was also evidence of microvoid clusters forming in the region near to the crack tip, as shown in figures 5.17(b) and 5.19(b), both of which correspond to areas within 0.5mm of the initial crack tip.

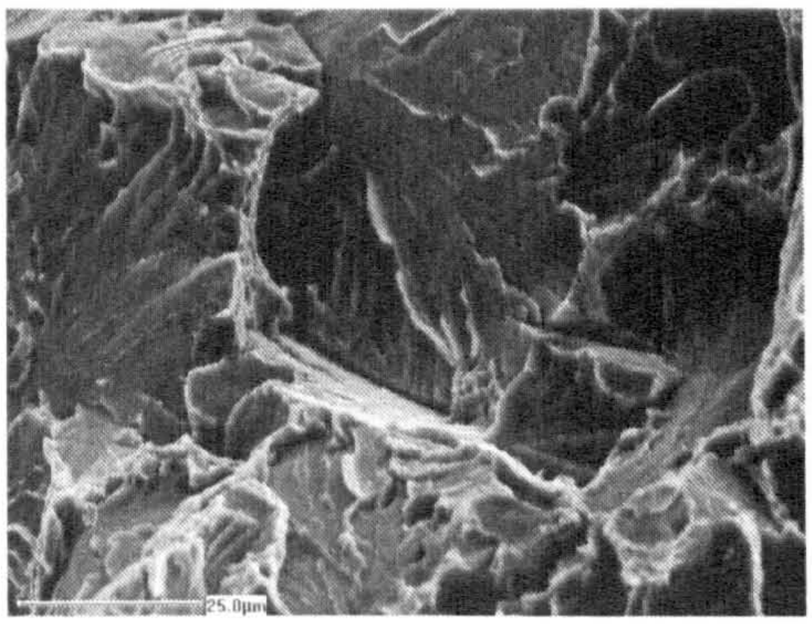

(a) Typical fracture surface observation, CT20 specimen after 1% room temperature prestrain.

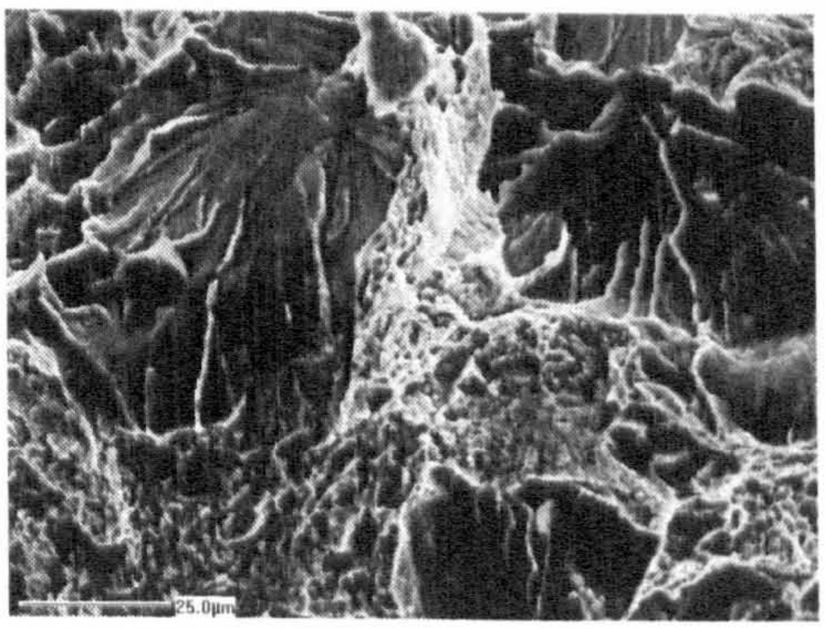

(b) Fracture surface observation, CT20 specimen after 1% room temperature prestrain, showing microvoid cluster in the near-tip region.

Figure 5.17: SEM images from fracture surfaces of CT20 fracture toughness specimens with 1% prior strain.

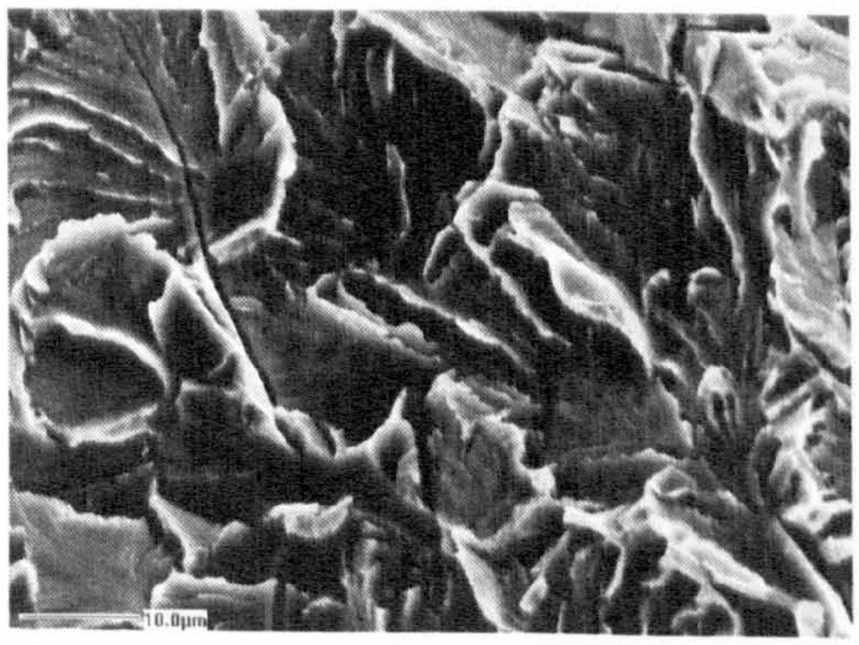

Figure 5.18: Typical fracture surface observation, CT20 specimen after 3% room temperature prestrain.

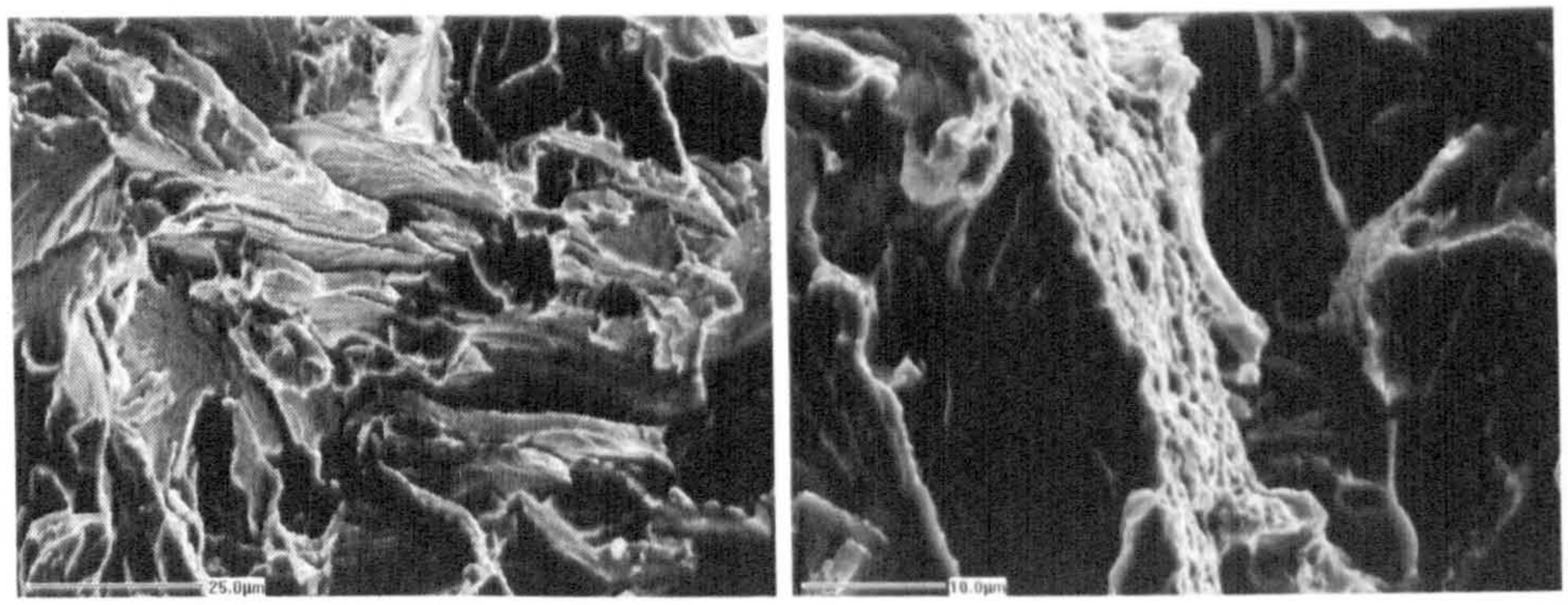

(a) Typical fracture surface observation, CT20 specimen after 5% room temperature prestrain.

(b) Fracture surface observation, CT20 specimen after 5% room temperature prestrain, showing microvoid cluster.

Figure 5.19: SEM images from fracture surfaces of CT20 fracture toughness specimens with 5% prior strain.

5.3.3 CT10 specimens - AR condition

Specimen CT10_9 was selected for examination as it exhibited the largest fracture load of all specimens tested (table 5.3). As with the 20mm thick specimens, fracture surface observations on the 10mm thick CT geometry indicated that crack propagation occurred primarily by transgranular cleavage. A typical observation is shown in figure 5.20(a), where evidence of arrested micro cracks can also be seen. Some localised regions of void formation were also observed, as in figure 5.20(b).

5.3.4 RNB specimens

The RNB specimens displayed considerable nonlinearity in load/displacement behaviour during testing, indicating significant plastic deformation prior to fracture. There was therefore some concern that the fracture mechanism may have altered from transgranular cleavage. To confirm fracture by cleavage, the fracture surfaces of specimens RNB60_5 and RNB90_4 were examined. These specimens were chosen as they attained the highest loads prior to fracture and so were deemed most likely to have experienced considerable ductile damage prior to failure.

Specimen RNB60_5 clearly indicated cleavage fracture at the centre of the specimen (figure 5.21(a)), with only small regions of localised ductile rupture at the tip of the notch, as can be seen in figure (figure 5.21(b)). As the width

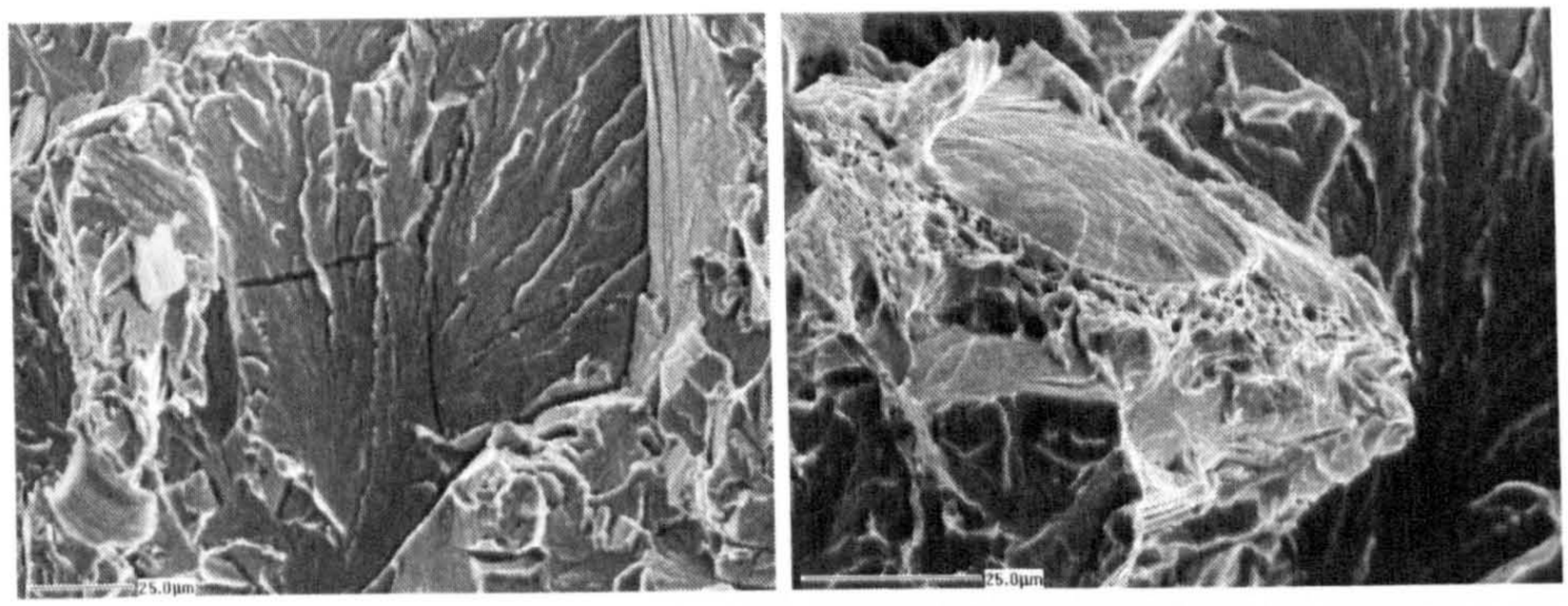

(a) Fracture surface showing cleavage fracture and arrested microcracking in the near tip region, specimen CT10_9.

(b) Fracture surface observation showing microvoid cluster CT10_9.

Figure 5.20: SEM fracture surface observations for 10mm thick CT specimens.

of the ductile region was small ($\approx 10\mu$m, figure 5.21(c)), it is concluded that fracture can be assumed to be dominated by cleavage mechanisms.

Similar observations were noted for specimen RNB90_4 with cleavage at the centre of the specimen (figure 5.21(d)) and limited microvoid formation at the notch tip (figure 5.21(e)). Some evidence of arrested cracking was also noted as seen in figure 5.21(f).

5.4 Discussion

In general, the experimental testing can be regarded as successful, however a number of problems were encountered during the testing.

One such issue is the determination of a valid fracture load where small scale decreases in load may occur prior to the final fracture event. In the case of the CT20 specimens, it is likely that the load drop was due to the experimental apparatus. Regardless of the reason, the fact that cyclic loading occurs introduces considerable uncertainty as to the stress and strain state in the specimen at failure.

In the CT20 specimens the drop in load was only small and, even if attributed to crack growth, cannot be regarded as 'failure'. In the case of the NCT tests, a number of pre-compressed samples displayed a sudden significant drop in load at fixed displacement. As the applied displacement increased, a reduction in sample stiffness was observed - a clear indication of significant

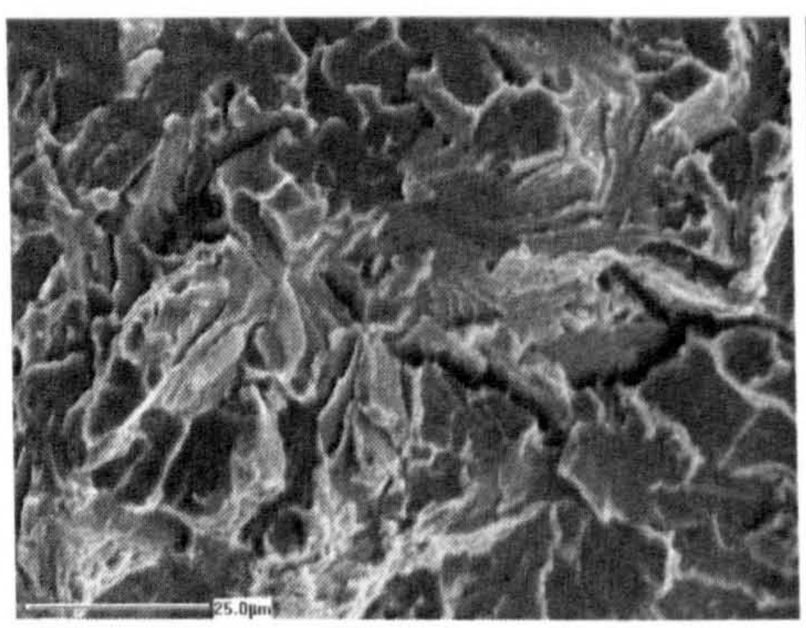

(a) Cleavage fracture at centre of RNB60_5.

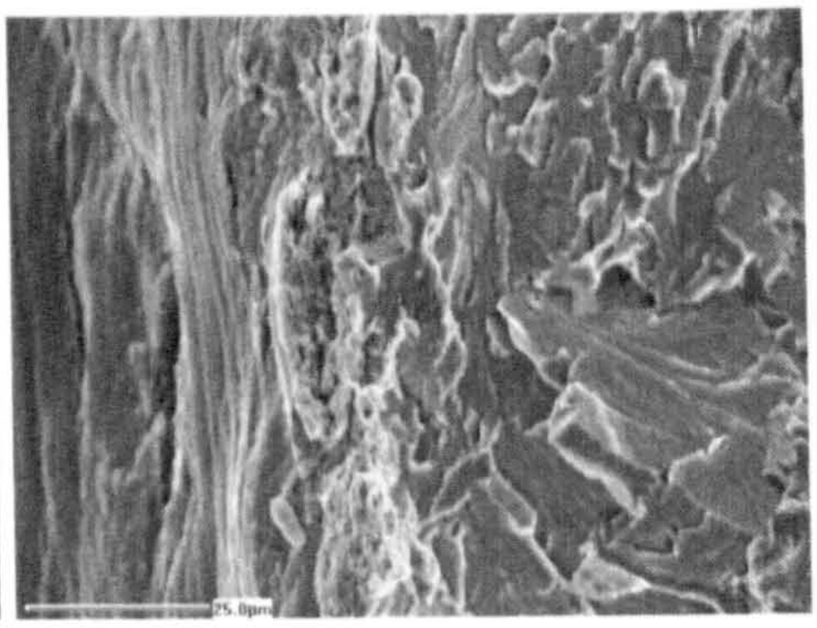

(b) Localised ductile rupture at notch tip of RNB60_5.

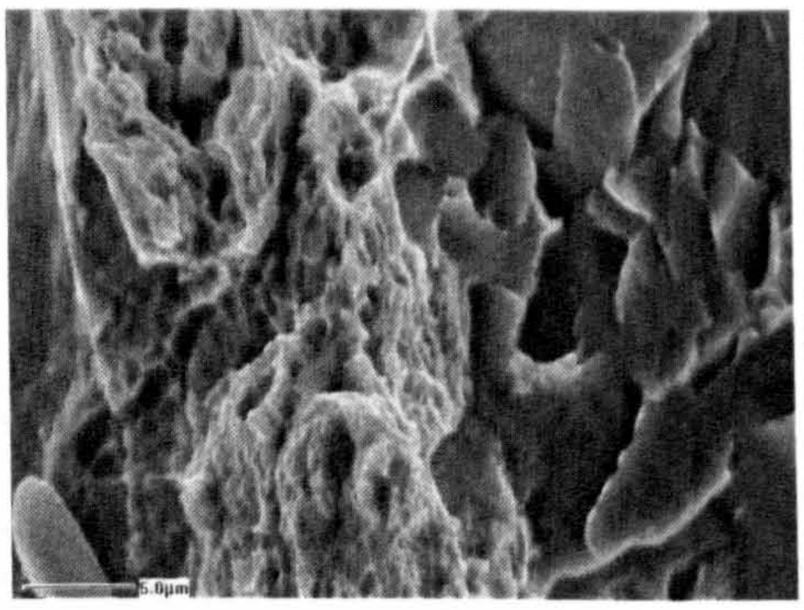

(c) Detail on ductile voids at notch tip of RNB60_5.

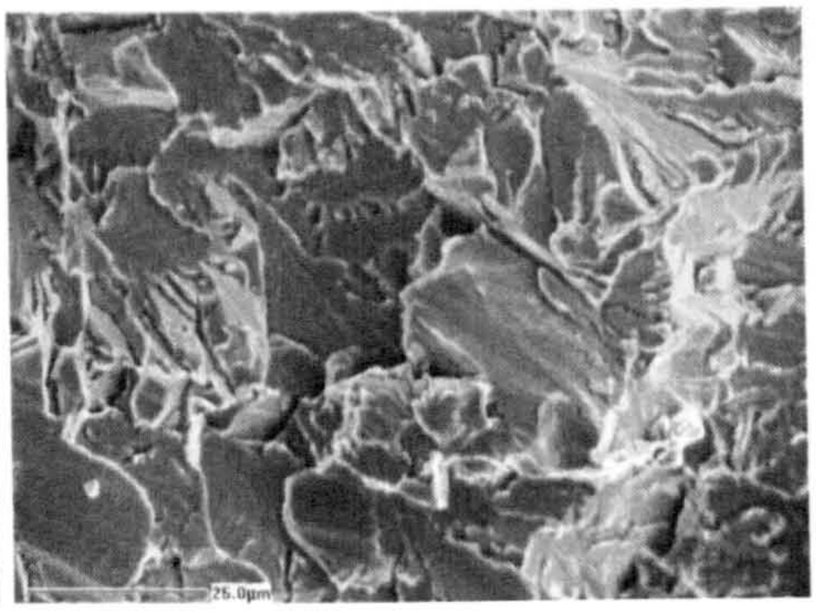

(d) Cleavage fracture at centre of RNB90_4.

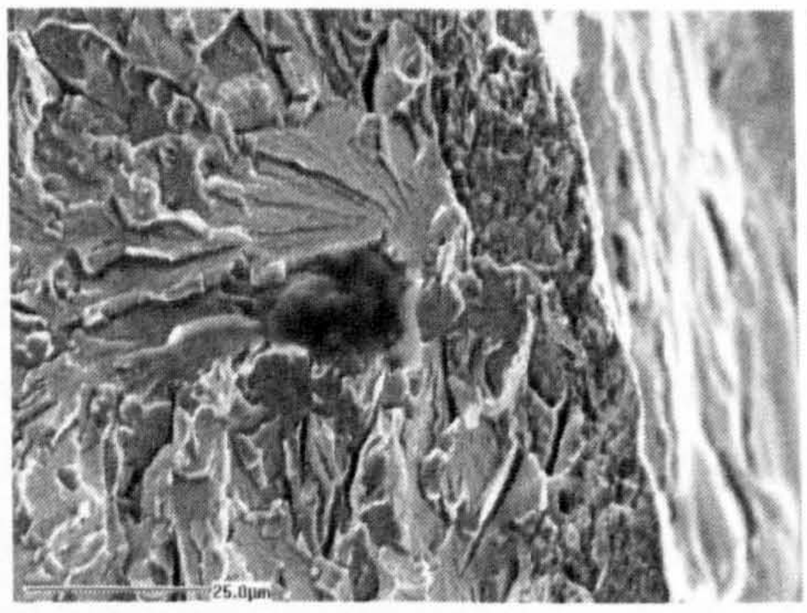

(e) Ductile voids at notch tip of RNB90_4.

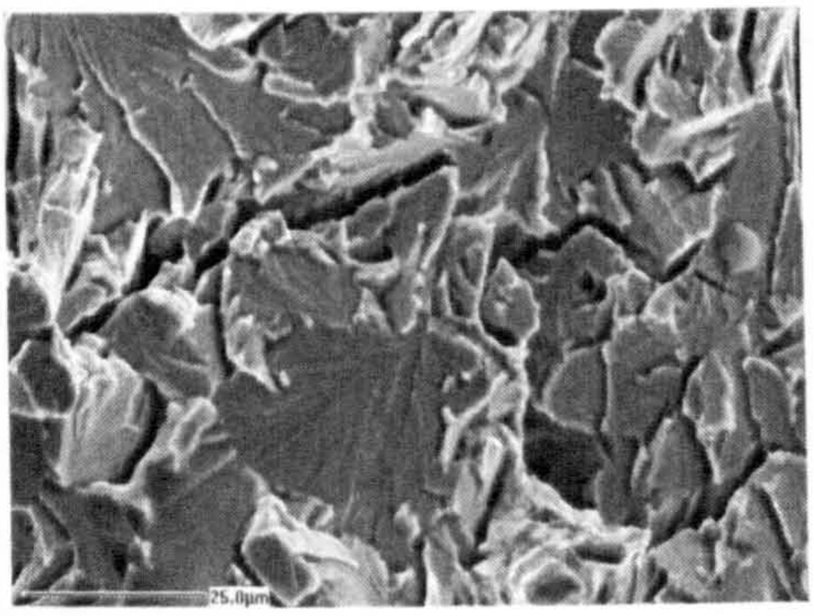

(f) Arrested microcrack in specimen RNB90_4.

Figure 5.21: SEM fracture surface observations for RNB60 and RNB90 specimens.

crack growth.

Examination of these specimens showed a clear tendency for crack re-orientation following pre-compression, with the crack path being much straighter in the pre-tensioned specimens as shown in figure 5.22. This is likely to be related to the relative magnitudes of the fracture loads. Following pre-tension, the compressive residual stress field at the crack tip inhibits fracture. In the case of pre-compression, fracture is promoted at lower loads by tensile crack tip residual stresses. Fracture occurring at higher loads results in the release of a much greater amount of potential energy, driving the crack in the lowest energy failure mode i.e. a straight line. When fracture is promoted locally by high stresses, under low applied load, the crack may propagate into a region of much lower, even compressive stress where it may arrest (as seen in 3 of the pre-compressed tests) or re-orientate to a more preferable direction of propagation.

In the manufacture of the prestrained samples, it was assumed that as plastic deformation was homogeneous at a macroscopic scale, there would be no significant residual stress remaining. Although this may be true in terms of the engineering definition - i.e. type I stresses - there may still be a significant build up of stresses within grains [151, 152]. This is manifested in neutron diffraction results made on a number of the prestrained 'blanks' for the prestrained CT specimens, as described in chapter 3. Residual strains, as measured in specimens with varying plastic strain, are displayed for various diffraction peaks in figure 5.23. It would therefore seem that even if macroscopic strain is homogenous, a considerable inhomogenity at the scale of material grains may exist. This, in turn, may have a considerable effect on fracture initiation after plastic deformation.

Upon examination of the SEM images taken from a range of tested specimens, it is apparent that the fracture mechanism in all cases appears to be 'quasi-cleavage', where cleavage facets are present in addition to localised regions of microvoidage. Quasi cleavage is generally considered to be characterised by frequent microcrack nucleation and localised propagation, as opposed to pure brittle fracture where a single, catastrophic nucleation and propagation is considered [6]. This is supported by the presence of arrested microcracks in a number of the SEM images, suggesting that the critical event for failure is the propagation of cracks from a micro to macro scale, rather than initial nucleation or propagation of defects at a granular scale.

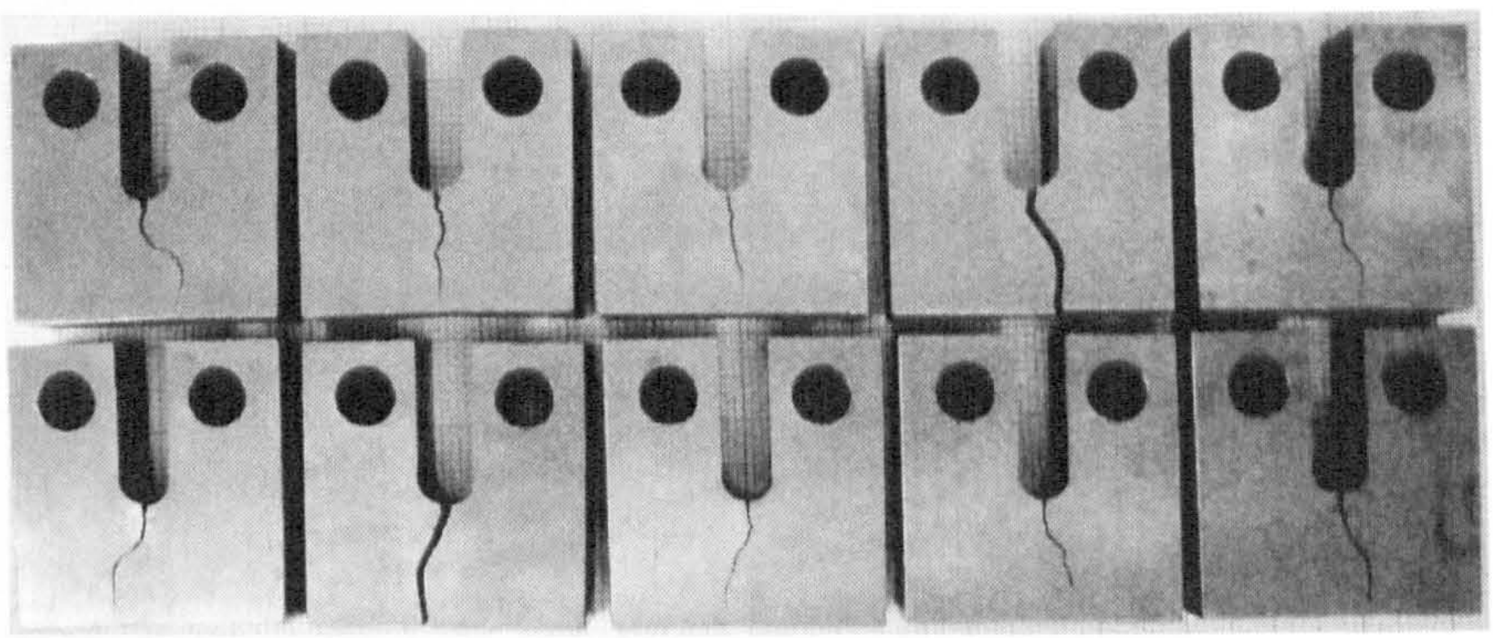

(a)

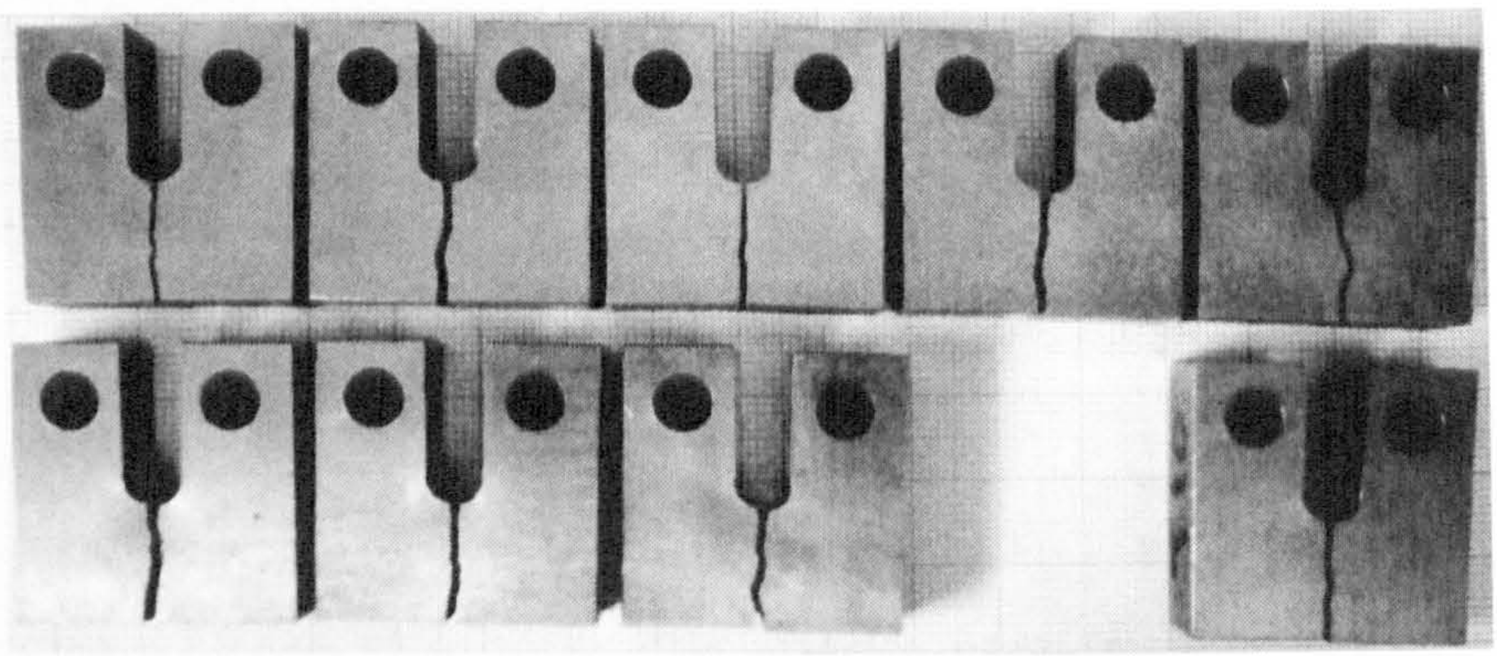

(b)

Figure 5.22: Fractured NCT specimens following compressive preload a) and tensile preload b).

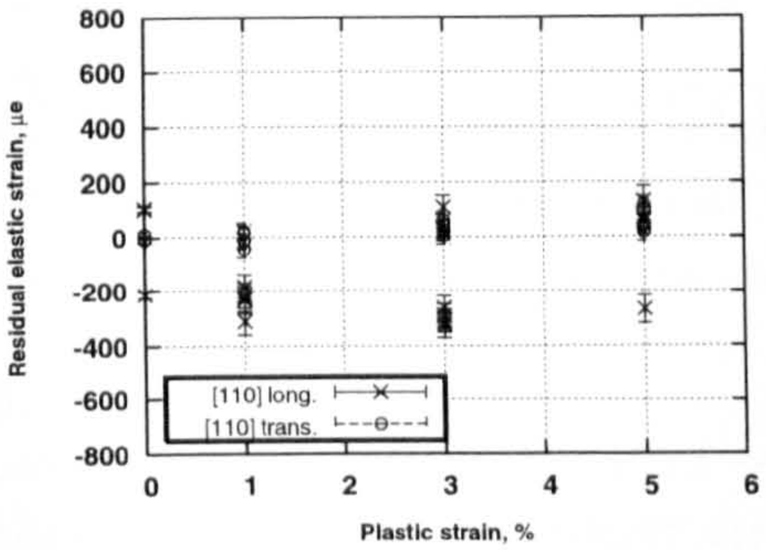

(a)

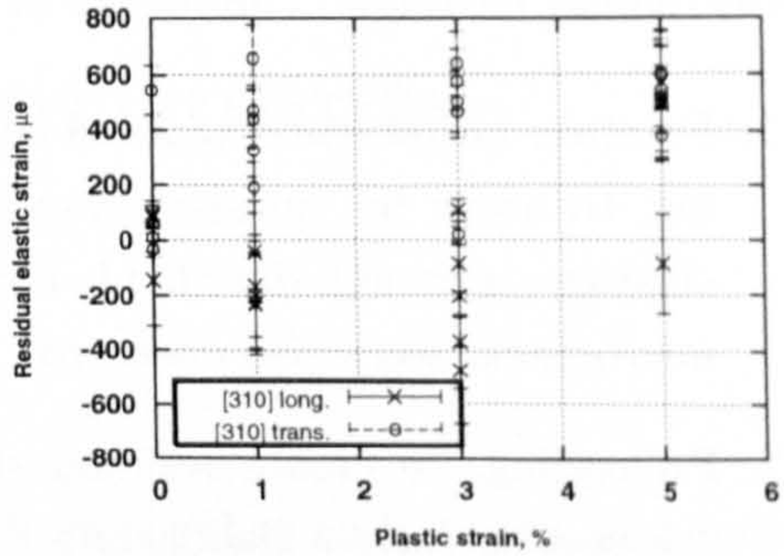

(b)

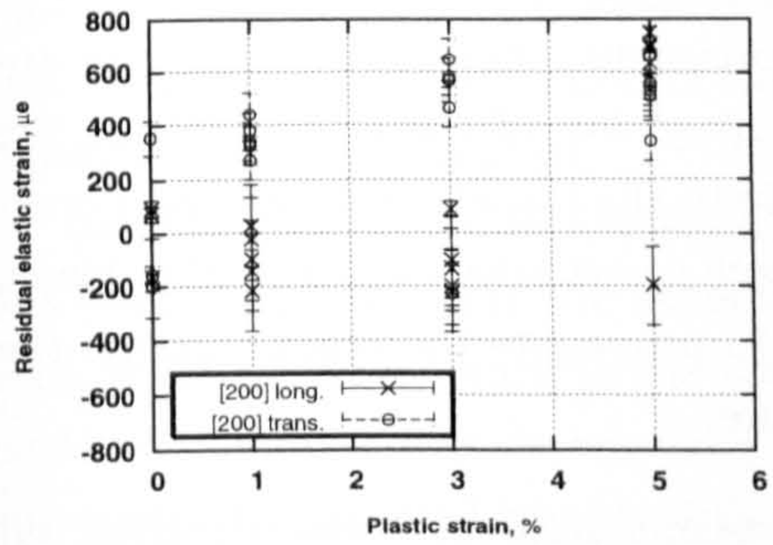

(c)

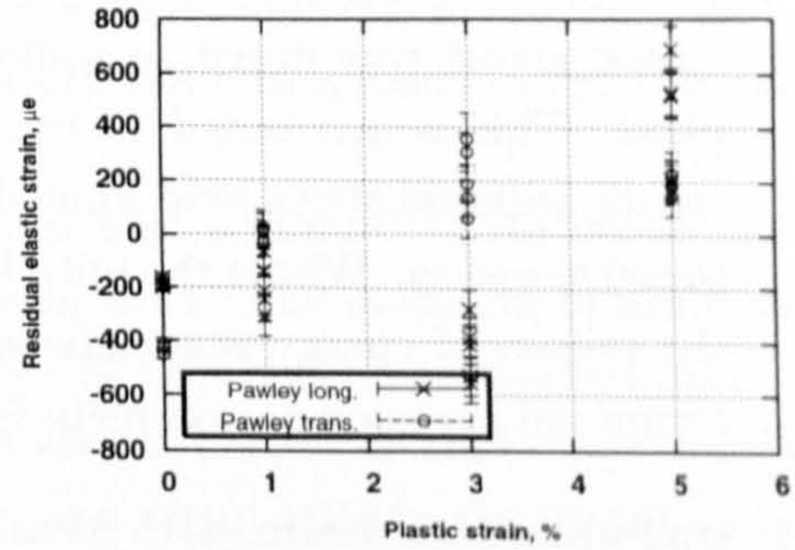

(d)

Figure 5.23: Remnant residual stress in prestrained CT blanks, measured using neutron diffraction in directions longitudinal and transverse to the direction of plastic deformation. Results based on the a) {110}, b) {310} and c) {200} diffraction peaks as well as d) Pawley refinement of multiple diffraction peaks.

5.5 Conclusions

A large number of experimental fracture tests (120) were carried out on a large number of specimens fabricated from A533b ferritic steel. A wide range of specimen geometries were used to obtain results for high and low constraint conditions to provide a benchmark for accurate calibration of fracture models. All tests were conducted at -150°C in order to ensure fracture occurred by transgranular cleavage. The results of the testing are summarised as follows:

1. Fracture across the range of specimens was observed, by SEM imaging, to occur by 'quasi-cleavage'. Crack propagation was primarily by cleavage, although ductile phenomena such as void clusters and arrested microcracks were also observed.

2. Preloading, to create residual stress in the fracture initiation region, was seen to have a sizable effect of the fracture loads and therefore the measured fracture toughness.

3. Crack arrest was noted in some specimens where preloading was applied. This is attributed to the propagation of the crack through the tensile residual stress field immediate to the initial crack tip into a compressive region. Where the initial crack growth occurred at higher loads, the release of energy was sufficient to propagate the crack through the compressive region to complete failure.

4. Uniform plastic strain, with no macroscopic residual stress, was observed to alter the distribution of measured toughness data, compared with material in the as-received condition. It was however noted that although plastic deformation was uniform in an engineering sense, a build up of residual strain may still occur at the scale of single grains.

Chapter 6

Analysis of experiments

6.1 Introduction

This chapter details the analytical work undertaken to interpret and understand the fracture tests described in chapter 5. An important tool in the interpretation of many engineering tests is finite element modelling, used in this work to estimate variation of the stress and strain fields in the test specimens as loads were applied.

In addition to complex numerical modelling, a number of statistical methods were used to analyse the experimental data. The intention of using such tools was to add structure to the analysis of trends in the scattered data. Of particular interest was determining between a perceived shift, due to inherent scatter in a limited sample data set, and a statistically significant shift in toughness due to load history.

6.2 Finite element modelling

6.2.1 Model geometry and mesh

Modelling of all fracture tests was undertaken using the ABAQUS finite element software package. To properly capture the high stress and strain gradients in many of the test geometries, a high level of mesh refinement was required. To ensure solutions could be reached within reasonable timescales, the symmetry of the test geometries was used to reduce the problem size.

For the CT and NCT geometries, one quarter of the entire geometry was modelled with symmetry assumed about the plane of the crack and through

the middle thickness of the specimens. The symmetry boundary conditions are shown for these geometries in figures 6.1 and 6.2. For the RNB geometries, the rotational and linear symmetries were exploited to make axisymmetric models of half of the specimens, as illustrated in figure 6.3.

Identical mesh structures were employed for the CT20 specimens in the AR, prestrained and WPS states. The mesh structure and detail of the near tip area is displayed in figure 6.1. The EDM notches were modelled with diameter of 0.19mm following the specimen measurements made in chapter 5. The minimum element size immediate to the notch tip was approximately 20μm. In the near crack region, 48 layers of elements were used though the specimen thickness, reduced to 16 layers in the bulk of the specimen as detailed in figure 6.1 b). The mesh and geometry for the 10mm CT specimens was identical to that for the 20mm thick specimens, except for a reduction in the number of through thickness element layers to 24 and 8 respectively.

The mesh for the NCT geometry is shown in figure 6.2. As for the CT specimens, a high level of refinement was employed near the EDM notch tip. As the EDM notch was introduced into the specimens after preloading, it was necessary to account for redistribution effects as the cut advanced through the residual stress field. Following [134] and chapter 4, the introduction of the EDM cut was modelled in several discrete steps by removing elements from the cut region. This allowed dissipation of strain energy as a plastic 'wake' behind the growing crack. If the growth of the EDM 'crack' is modelled in a single step, the release of energy will be concentrated around the crack tip, resulting in unrealistically high deformation in this region as discussed in [134] and chapter 4. To accommodate the removal of elements, a fine mesh structure was needed over the whole region surrounding the EDM cut. Furthermore, the number of through thickness elements was increased to 30, reducing to 10 in regions far from the crack tip.

For the RNB specimens, a fine mesh was employed in the region around the minimum section, in particular around the notch tip were large deformation was expected prior to failure (figure 6.3 a). As axisymmetric assumptions were employed, the mesh was essentially two dimensional. The overall structure of the mesh is illustrated in figure 6.3. Although the notch geometry varies slightly between the RNB45, RNB60 and RNB90 specimens, a very similar mesh structure was used in all three cases. Specimens were modelled with minimum diameters as measured on the test specimens as discussed in chapter

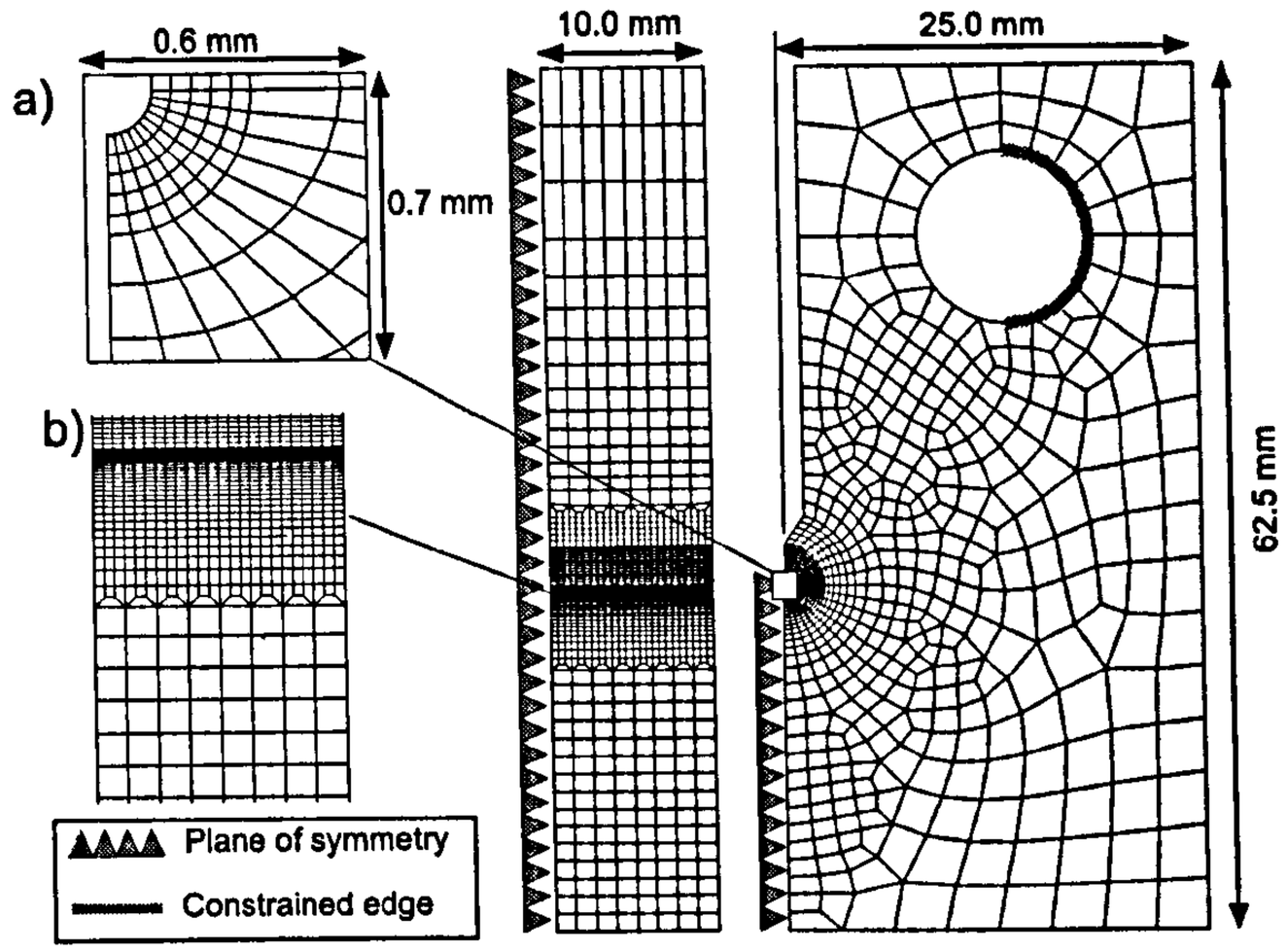

Figure 6.1: Mesh and boundary conditions for modelling CT20 geometry.

5, corresponding to 7.9mm (RNB45), 8.0mm (RNB60) and 8.1mm (RNB90) rather than the nominal diameter of 8.0mm.

For all analyses, second order elements were used to most accurately capture local variations is the strain field. Where three dimensional modelling was employed (CT and NCT specimens), 20 node brick elements were used (ABAQUS element type C3D20R). This formulation used 8 integration points per element. As calculations for local approach methods were based on integration point values, using such elements was anticipated to reduce error compared to linear formulations with 1 integration point per element. For the RNB geometries, second order axisymemtric elements with 8 nodes and 4 integration points each were used (ABAQUS element type CAX8R).

6.2.2 Loading

Loading of the CT and NCT geometries was applied via pins through the loading holes the specimens. To explicitly simulate the pin loading arrangement, including contact between the pins and the specimens, would have considerably added to the complexity of the modelling. Therefore, the loading was approximated by applying a point load to the interior of the hole and constraining the contact surface to translate and rotate as a single, rigid section.

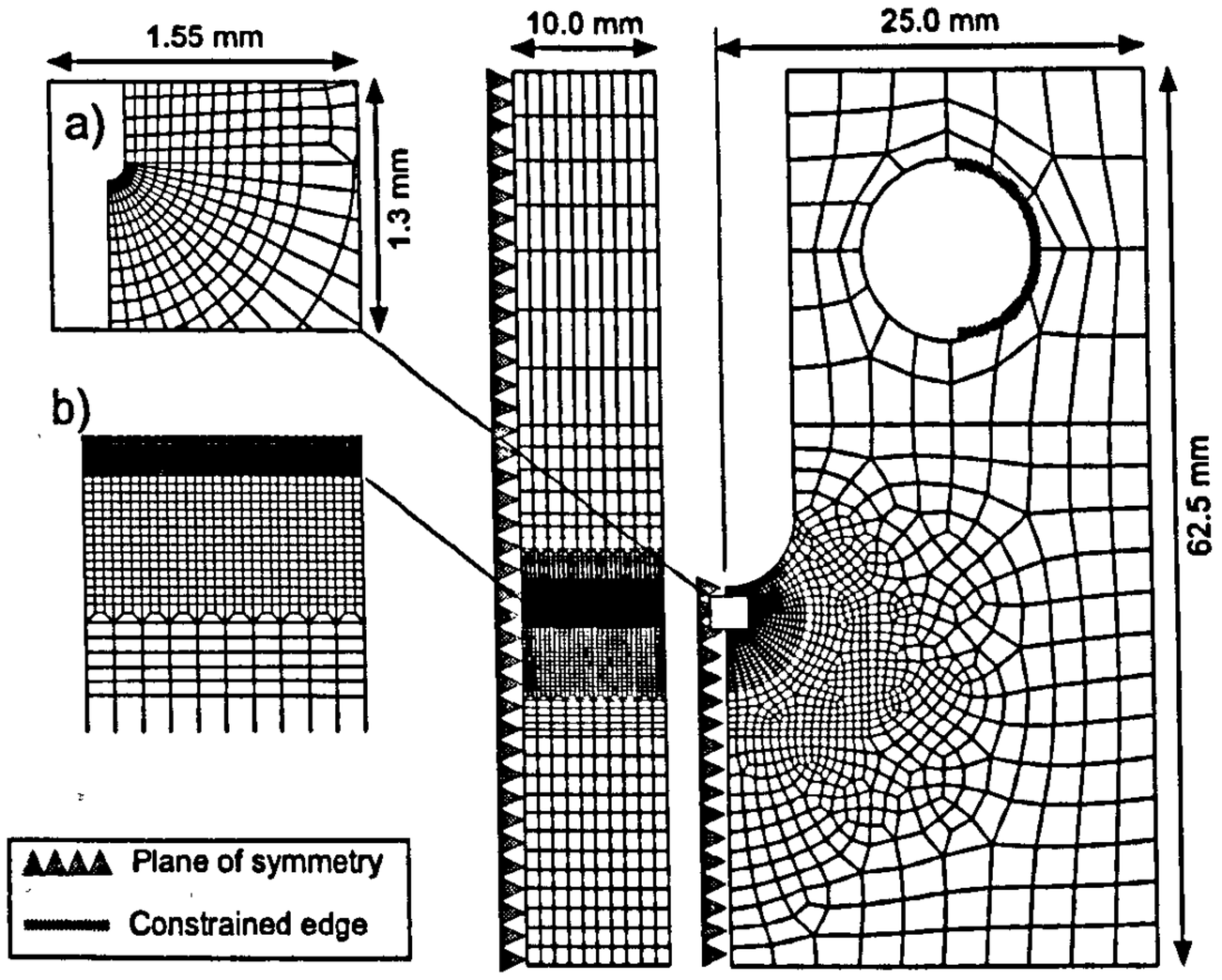

Figure 6.2: Mesh and boundary conditions for modelling of notched CT geometries.

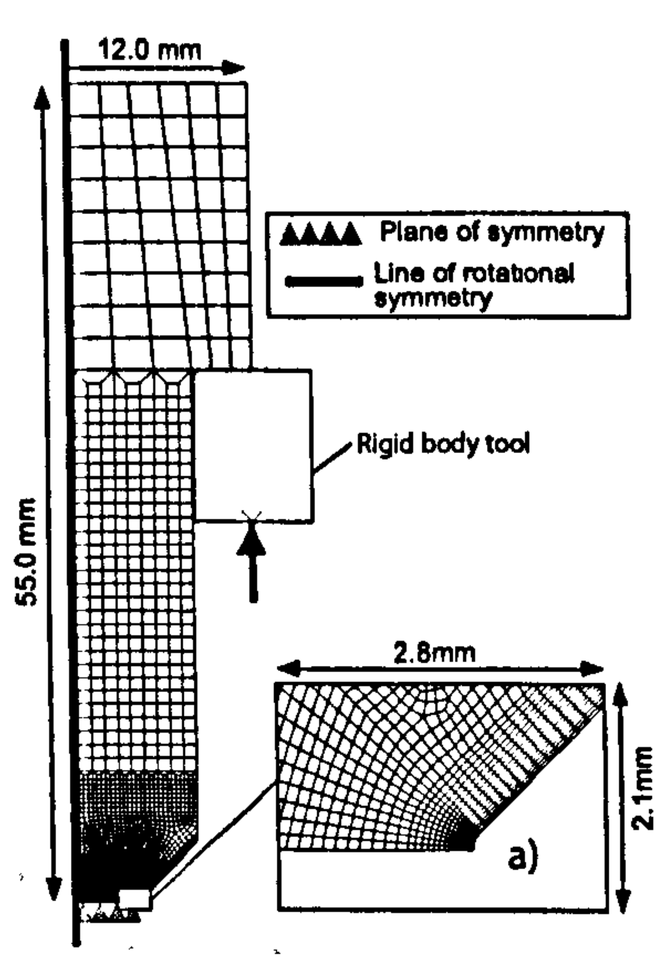

Figure 6.3: Mesh and boundary conditions for modelling of RNB geometries.

The constrained regions are shown in figures 6.1 and 6.2. In the case of the pre-compressed NCT samples, separate constraint boundary conditions were applied to the opposite side of the hole for the compressive load.

The RNB specimens were loaded using a collar arrangement, as shown in figure 5.5. To approximate this, a rigid body tool was used to apply loads to the finite element model. Contact between the tool and the specimen was assumed to be frictionless. As load was only applied normal to the contact plane, this was felt to be a reasonable simplification. As considerable yielding was seen to occur in the RNB geometries, with load not always rising monotonically with displacement, convergence problems were encountered when applying specified loads to models. To avoid such numerical difficulties, displacements were specified instead.

To model WPS CT20 load cycle, separate steps were assigned for the preload at room temperate, subsequent unload, cooling and final load to fracture.

For the notched CT tests, room temperature preload and unload were followed by the EDM cutting. This was modelled as 4 successive steps in which elements were removed. Alternative models were also employed, with the cut occurring in 8 increments, but the effect of this on the resulting crack tip stresses and strains was small, as shown in figure 6.4. The stress and strain fields were allowed to redistribute to satisfy equilibrium and compatibility conditions following each growth increment, before removing the next set of elements. A step for cooling of the specimen, modelled by a change in material properties, was then followed by the final loading to fracture.

For the prestrained CT specimens, the entire process of prestraining, extraction and loading was not modelled. Instead, the effects of the prestrain process were approximated by modifying the stress/strain curve, increasing the yield stress as will be discussed in section 6.2.3.

6.2.3 Material response

The tensile tests, described in chapter 5, provided stress/strain data for the A533B ferritic steel used. The resulting data used to describe the material in the FE analyses are given in table 3.4. For the response at 20°C, values at high strain were extrapolated based on a power law hardening behaviour $\sigma = 461.3\epsilon^{0.17}$.

For the prestrained CT samples, room temperature prestrain was assumed

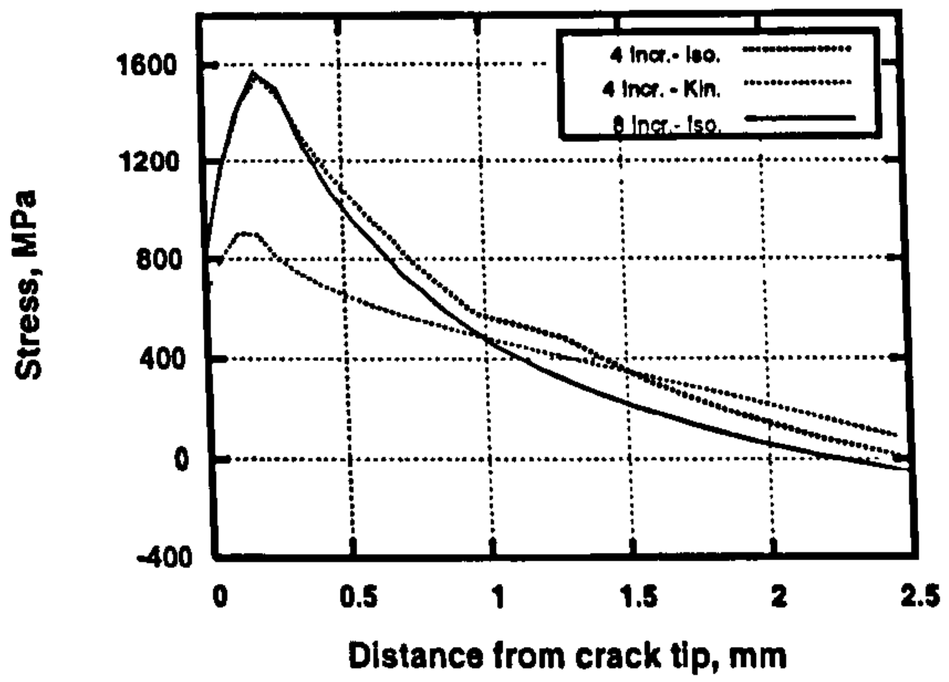

Figure 6.4: Effect of crack introduction on crack tip stresses in pre-compressed NCT specimens.

to move the low temperature yield point up the stress/strain curve according to the level of permanent deformation. This was supported by the low temperature tensile tests on prestrained material, discussed in section 5 and displayed in figure 5.6. The low temperature response in the AR and prestrained states, as used in the analyses, are shown in figure 6.5.

In the NCT and WPS CT tests, where cyclic loading occurred, the material hardening model assumed had the potential to significantly affect results. Two variations were used in this work. As an initial estimate, a simple isotropic hardening model was used. By allowing expansion but no translation of the yield surface, this was expected to provide an upper bound estimate for the stresses resulting from load histories. A lower bound estimate was obtained using nonlinear kinematic hardening, such that the yield surface could translate but the size was fixed.

6.2.4 Comparison with experimental response

In order to draw accurate conclusions from finite element results, it is important to ensure that the simulation is an accurate representation of reality. A simple test in terms of fracture testing is to ensure that the load/displacement response predicted from modelling is in good agreement with that obtained by experiment.

For the fracture tests undertaken in this work, displacement was recorded at the crosshead of the test apparatus. As a result, the recorded displacement

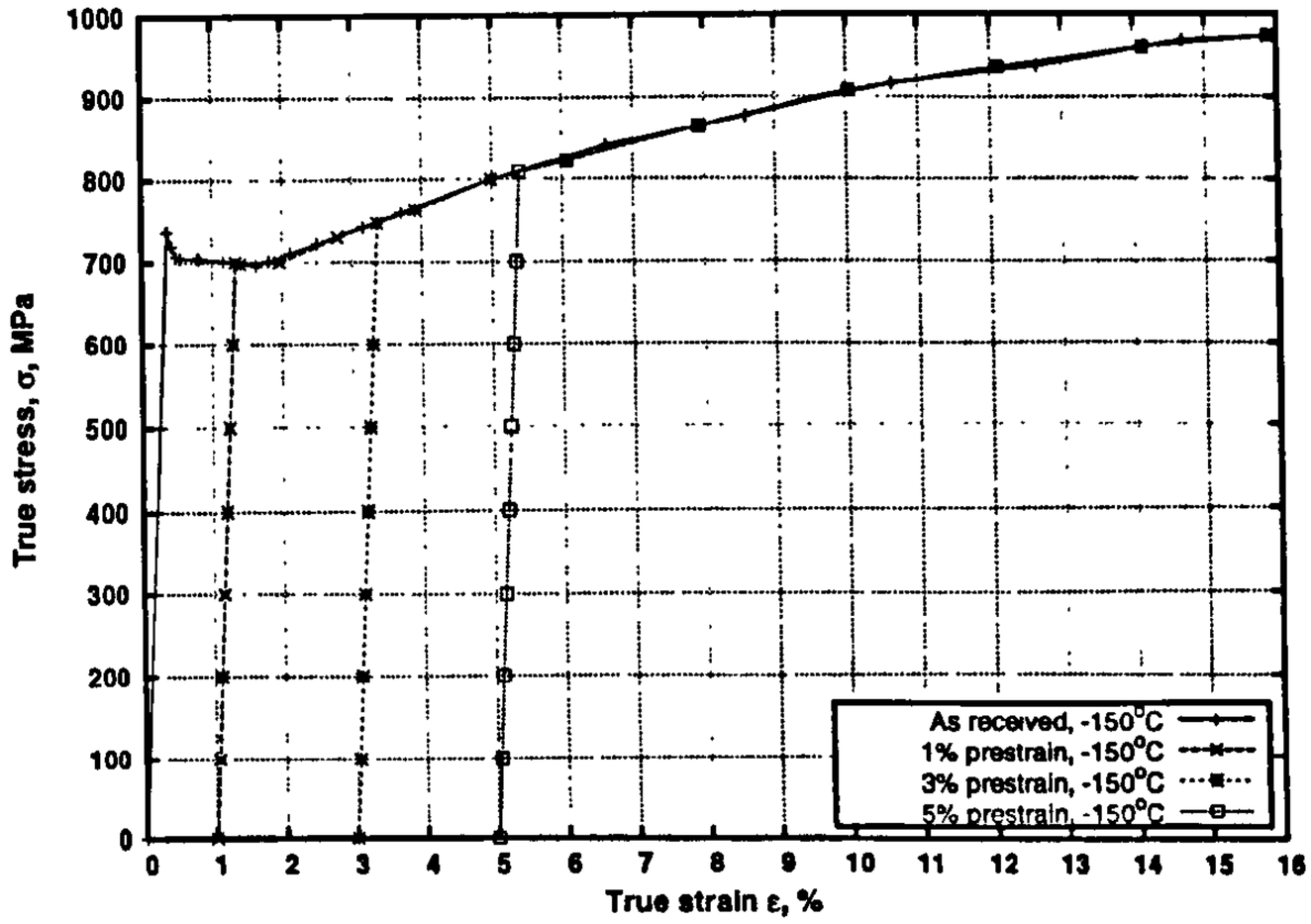

Figure 6.5: Low temperature stress/strain response assumed in finite element analyses.

included some compliance of the machine supports as well as an amount of play in the system. Therefore, a degree of adjustment was necessary before the experimental data could be compared with the FE predictions. To correct for initial takeup of play in the system, it was assumed that a line fitted to the linear region of the load/displacement curve should pass through the origin. This produced a corrective constant, added to the displacement. To correct for the linear elastic response of the machine and gripping arrangement, a constant elastic displacement was added. From room temperature tensile testing, comparisons between the response measured at the clip gauge and that at the crosshead suggested the stiffness of the loading apparatus was 160kN/mm. The response of the pin loading arrangement, used for testing the CT and NCT samples, was found to be well approximated by a stiffness of 80kN/mm. The displacement was added to the FE predictions of load line displacement for comparison with the experimental results. The corrections applied are displayed in schematic form in figure 6.6.

Resulting comparisons between response from finite element predictions and those from the experimental tests are shown for specimens in the AR state in figures 5.8, 5.11(b) and 5.12. In general, it can be seen that the experimental response is well approximated by the models.

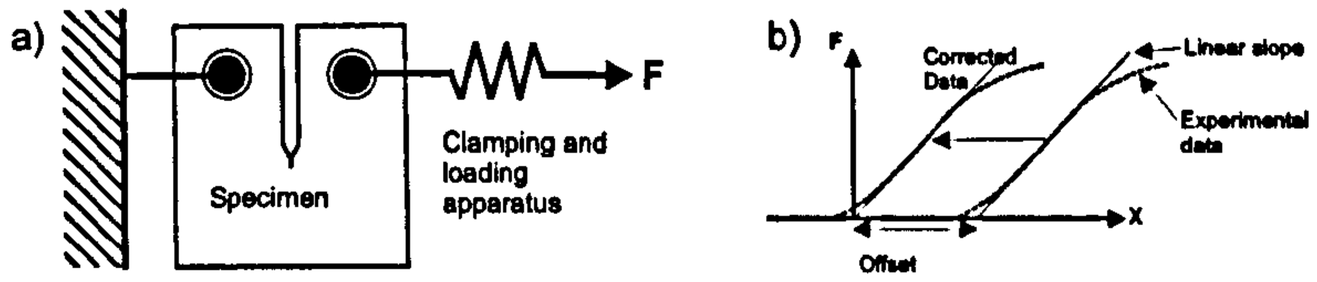

Figure 6.6: a) Schematic of experimental load/displacement response. b) Correction to remove play.

6.2.5 Effect of material hardening model

The effect of isotropic and kinematic hardening assumptions on the stress fields in the WPS CT and NCT specimens can be seen in figures 6.7 and 6.8. Opening stress $\sigma_{\theta\theta}$ is defined as in figure 2.2. Minimal effect is seen upon initial load, but it is evident that kinematic hardening produces a significant reduction in the peak residual stresses upon unloading.

In terms of the predicted load/displacement response, the effect of hardening on the WPS specimens is minimal (figure 5.13). In the case of the NCT specimens the effect for tensile preload is also minimal (figure 5.15). For the pre-compressed NCT data, figure 5.15 shows a considerable increase in specimen stiffness under kinematic hardening assumptions with the experimental data best approximated by isotropic hardening. It can be seen from figure 6.8(b) that, regardless of the hardening model, there is a transition to compressive stress approximately 2.5mm from the EDM crack tip. This compared well with the region where the crack path was seen to deviate in figure 5.22(a).

6.3 Statistical Analyses

To gain deeper insight into the effects of differing geometry and load cycles, it is often useful to apply statistical methods. This is especially useful where experimental scatter is significant, as is apparent in much of the data obtained in this work. The aim in this case was to investigate the statistical significance of the load history or specimen type in terms of the change in stress intensity factor at fracture.

Based on the work of Smith and Booker [49], it was elected to use statistical t and F tests to investigate changes between data sets from differing specimen types.

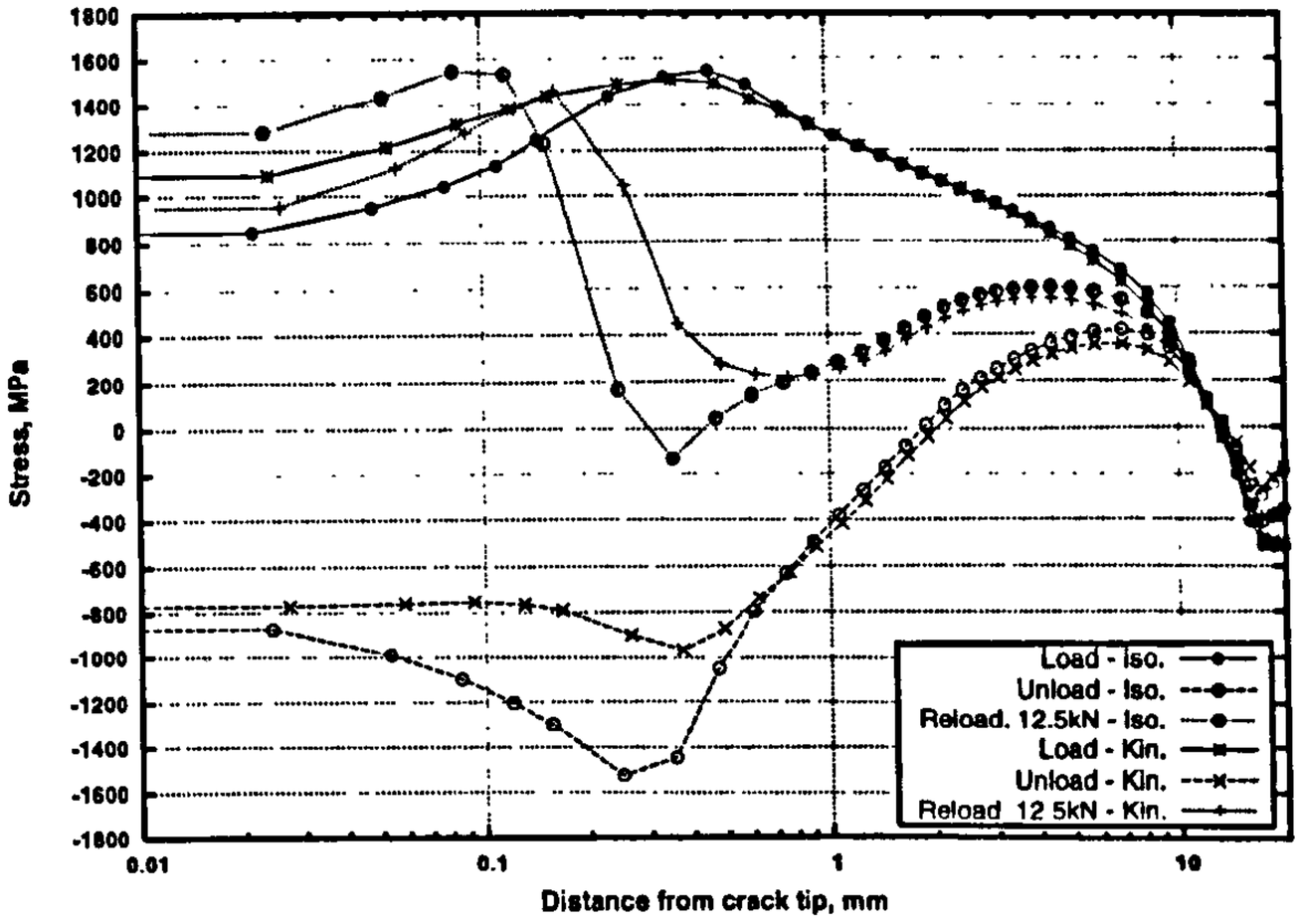

Figure 6.7: Opening stresses, $\sigma_{\theta\theta}$, in WPS CT specimens from finite element analyses based on isotropic and kinematic hardening assumptions.

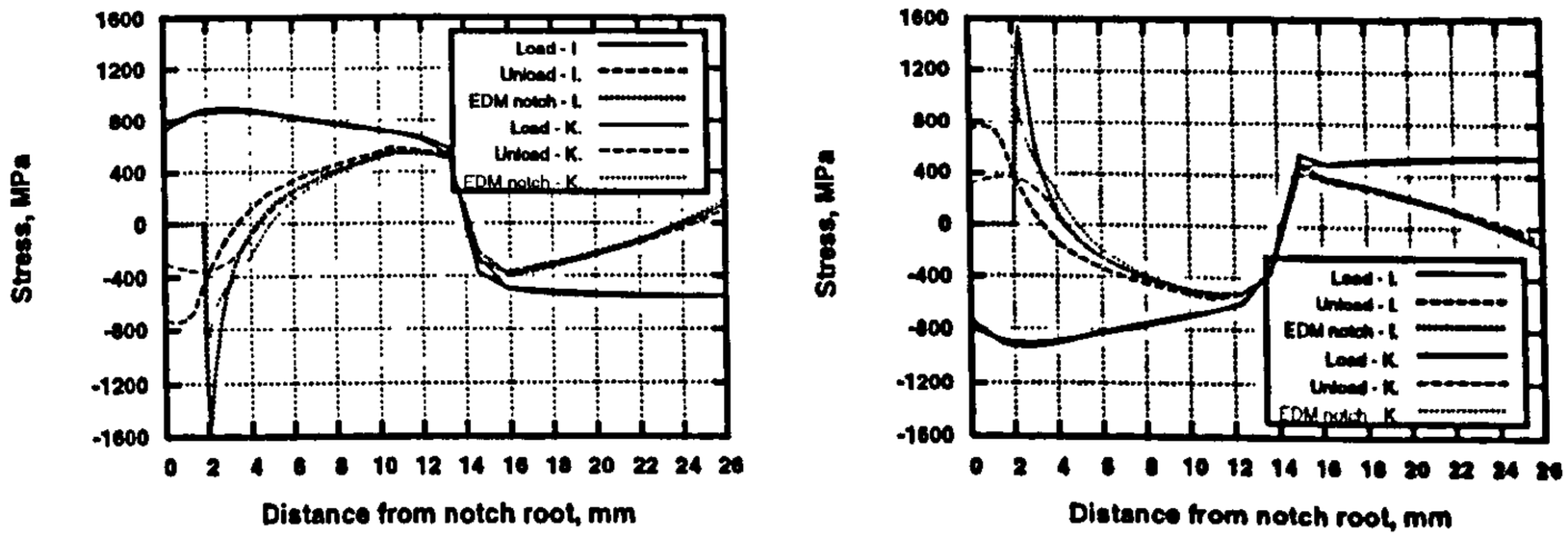

(a) Tensile preload

(b) Compressive preload

Figure 6.8: Variation of opening stress $\sigma_{\theta\theta}$ ahead of the notch root for preloaded NCT specimens, using isotropic and kinematic hardening models.

6.3.1 Method

When sampling from two normally distributed data sets, the F test allows the variances of two sample sets to be compared. The value of the F statistic allows the likelihood that the parent populations (from which samples are drawn) have the same variance to be estimated. The F statistic is given by the ratio between the two sample variances

$$F = \frac{s_1^2}{s_2^2} \tag{6.1}$$

where s_1 and s_2 are the standard deviations of sample sets 1 and 2 and $s_1 > s_2$. A critical value, F_c, may be determined for the test from inversion of the F distribution, dependent on the level of significance required and the degrees of freedom associated with the two data sets. If $F > F_c$, the hypothesis that the population variances are the same is rejected.

In this case, as the population variances must be estimated from the sample data, the degree of freedom for each data set is $n - 1$ where n is the number of samples. Critical values may be determined from tables, as in [153] for example, however in this case the MATLAB software package was used to generate F_c. A 10% level of significance was chosen, providing 90% confidence that any change in variance is due to random error. To compare sample means, the t statistic is determined from

$$\begin{aligned} t &= \frac{|\bar{x_1} - \bar{x_2}|}{\sqrt{S_p^2(1/n_1 + 1/n_2)}} \qquad F < F_c \\ t &= \frac{|\bar{x_1} - \bar{x_2}|}{\sqrt{s_1^2/n_1 + s_2^2/n_2}} \qquad F > F_c \end{aligned} \tag{6.2}$$

where S_p^2 is an unbiased estimator of the variance of the two samples.

$$S_p^2 = \frac{(n_1 - 1)s_1^2 + (n_2 - 1)s_2^2}{n_1 + n_2 - 2} \tag{6.3}$$

A critical t value was determined from Student's t distribution using a 10% level of significance, with $n_1 + n_2 - 2$ degrees of freedom. Using this criterion, if $t < t_c$, it can be stated with 90% confidence that any difference in sample means is due to random error.

Linear regression was used to fit equation 4.12 to data from varying spec-

imen types. As the F and t tests assume normally distributed parent populations, equivalent normal parameters were estimated from the 3 parameter Weibull distribution [153] using

$$\mu = K_m + (K_0 - K_m)\Gamma(1 + 1/M) \tag{6.4}$$

$$\sigma = (\mu - K_m)M^{-0.926} \tag{6.5}$$

Where Γ represents the Gamma function. For the ensuing analyses, $\bar{x} = \mu$ and $s^2 = \sigma^2$. The results of the analyses, comparing numerous data sets with the 'baseline' CT20 data, are presented in table 6.1. In addition, the fitted Weibull probability density functions are plotted for the fracture data sets in figure 6.9. The CT20 distribution cumulative density function, along with 95% prediction intervals from the fitting process, are plotted with fracture data in figure 6.10.

6.3.2 Results

Based on the statistical testing, table 6.1 highlights a mean shift in K_I^{el} at fracture relative to the CT20 data for all specimen types apart from the compressed NCT and 5% prestrained CT data sets. Figure 6.10 shows both of these data sets lying outside the prediction interval for the CT20 data fit, suggesting that there is indeed a significant shift in the apparent toughness. The fact that this is not highlighted by t testing may be related to the small data set size, generally $n = 30$ is set as a minimum for statistical significance. Also, the need to approximate non-normally distributed data sets as normal is likely to bias the results. Figure 6.9 shows appreciable asymmetry in many of the fits, suggesting that the normal approximation is not appropriate.

The Weibull modulus values in table 6.1 show a marked reduction in scatter following tensile preload for WPS CT20 and NCT pre-tensioned data. For the pre-compressed NCT data, a decrease in M indicates an increased scatter. This is in keeping with the results of [49] where tensile/compressive residual stresses increased/decreased scatter. It can also be seen that a decrease in scatter is also present in 2 of the 3 prestrained CT data sets, even in the absence of residual stresses.

This can be interpreted in terms of the size of the volume active in the fracture process. Where residual stresses are tensile, even at very low loads, a small region may exist where fracture can occur with this region increasing in

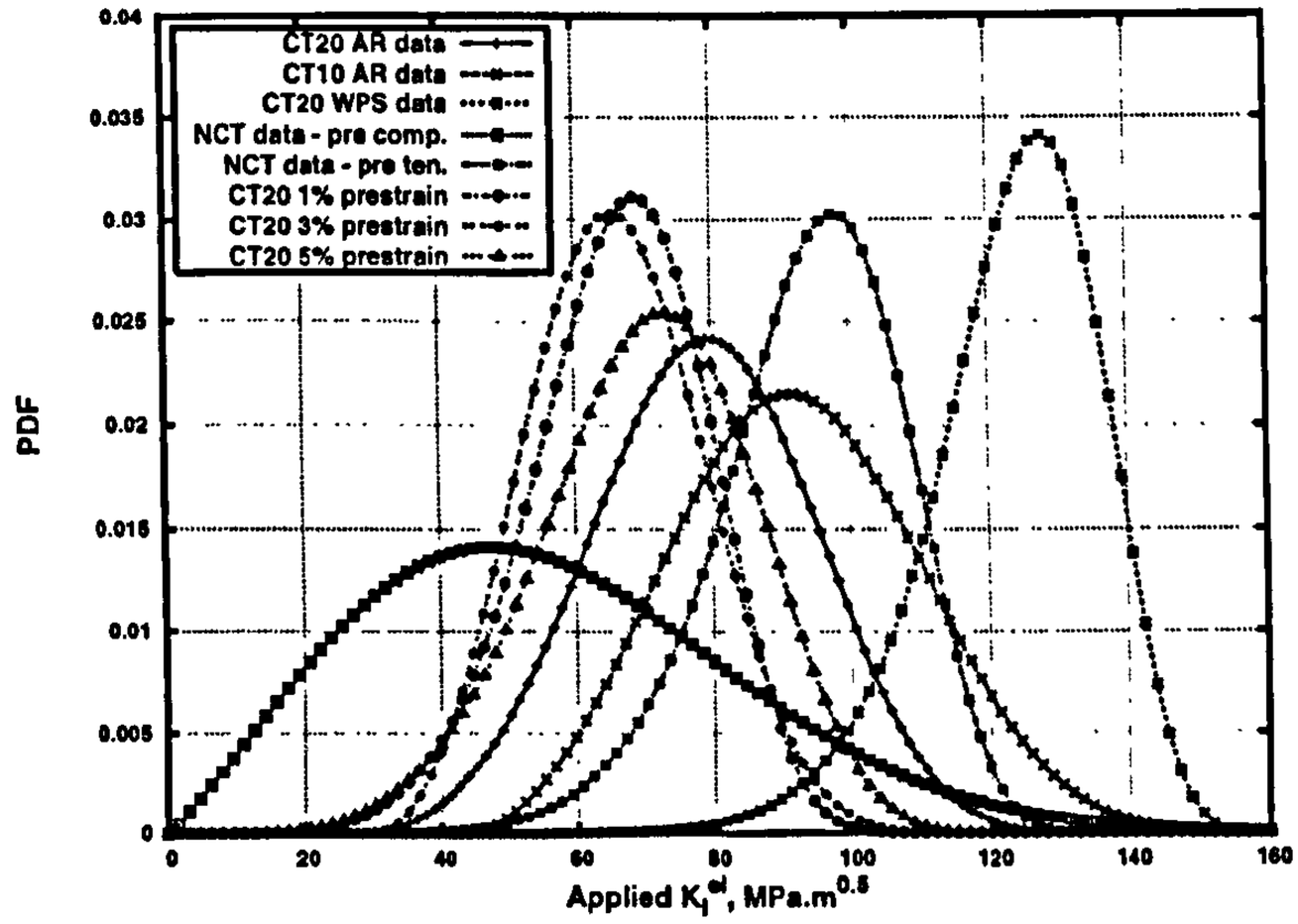

Figure 6.9: Weibull probability density functions for experimental fracture data.

size with load. In this case, the stress field may be thought of as a sharp peak, centred at the crack tip with the fracture event controlled by the presence, or otherwise, of defects within the process zone. Hence, fracture may occur a very low loads if a defect is preferentially located, as well as at higher loads when the process zone has grown to encompass further defects.

Where residual stresses at the crack tip are compressive in nature, the sharp peak in stress is 'blunted' to a degree such that a larger, more uniformly stressed region is active in the fracture process. In this case, the active zone is far more likely to contain viable defects and fracture will be controlled by a high enough stress being attained. Therefore, a sharper increase in fracture probability will occur at a load where a high enough stress is reached over a sizeable region.

6.4 Conclusions

A series of analyses of the experimental fracture tests discussed in chapter 5 were conducted. Finite element analyses were used to model the evolution of stresses and strains throughout the experimental tests and statistical methods were used to analyse trends and scatter in the experimental data. From these

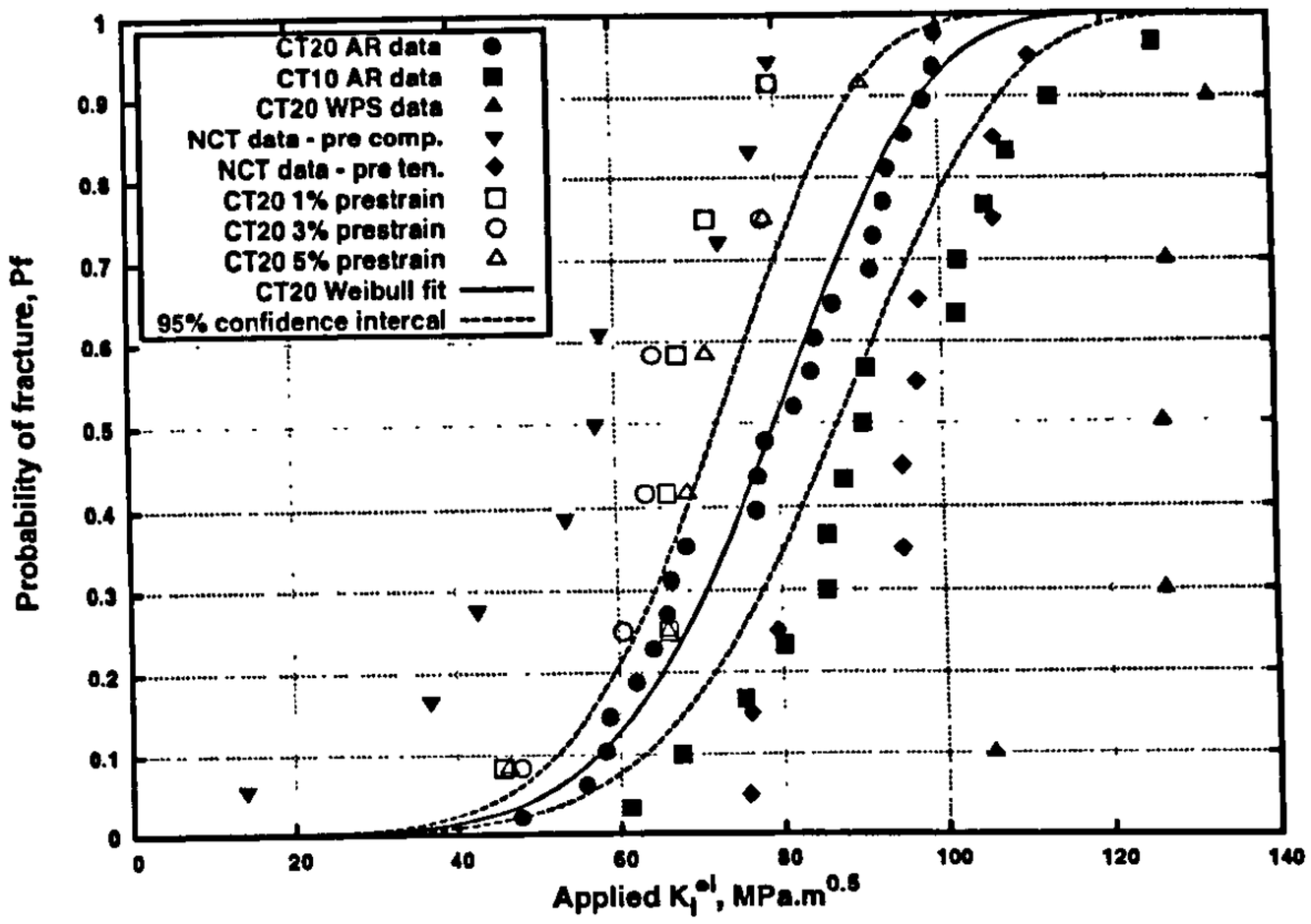

Figure 6.10: Experimental fracture data with three parameter Weibull fit to AR CT20 results, showing 95% prediction limits.

analyses, the following conclusions were drawn:

1. Variation of load line displacement (LLD) with applied load was approximated from experimental load/crosshead displacement measurements by correcting for compliance and nonlinearities in the test machines used. The resulting LLD-load traces were found to be in good agreement with those predicted from FEA, giving confidence in the validity of the numerical models of the tests.

2. The results of the finite element modelling showed that, when cyclic loading occurred, differing material hardening assumptions could have a significant influence on the stress field ahead of the crack tip.

3. Statistical analysis of the experimental fracture load data showed that scatter was reduced by tensile preloading and increased by compressive preload, based on fitting of Weibull distributions to the fracture load data.

4. Use of statistical T and F tests showed that a statistically significant shift in mean measured toughness occurred following preloading in the majority of the data sets examined. The small size of the data sets examined ($N < 30$) and the need to approximate distributions as Gaussian,

is suggested to be a factor where statistically significant shifts were not found.

Chapter 7

Calibration of model parameters

7.1 Introduction

In order to draw accurate conclusions as to the validity of local approach models for prediction of fracture, reliable values must be obtained for the model parameters. For practical application to structural integrity assessments, model parameters must also be transferrable between differing component geometries.

A study of previously published data (chapter 4) illustrated the problems associated with determination of the parameters σ_0 and m. This chapter presents a study of the variation and reliability of differing calibration methods. Various techniques were applied to the fracture data obtained from the tests described in chapter 5 and analysed in chapter 6.

7.2 Models considered

Using the Weibull distribution to describe fracture probability as in equation 2.36, a number of definitions were employed for the Weibull stress σ_w. As well as the standard 'Beremin model' definition of equation 2.37, the incremental definition of equation 4.8 was also used.

By calculating equation 4.8 with $\sigma_{th} = 0$, the effect of strain nucleation on model accuracy was investigated. In addition, to produce a best estimate model, the threshold value was determined from the fracture data obtained.

The non-incremental model of Gao and co-workers ([85], equation 4.6) was not applied in this case as the results of chapter 4 showed the assumption of a constantly increasing active defect population results in a significant under-estimation of fracture strength following load history.

In addition to the two Weibull stress formulations, an alternative model based on equation 4.8 was also employed. This was intended to avoid the problems associated with discrete implementation of models and large failure probabilities of individual volume elements (as discussed in chapter 4).

The probability of failure in a material volume element i is given by

$$Pf^i = \int_{V^i} \left[\int \frac{\sigma_1^m - \sigma_{th}^m}{\sigma_0^m} d\epsilon_e^p \right] dV \tag{7.1}$$

the overall fracture probability is then expressed as

$$Pf = \prod \left(1 - Pf^i\right) = \prod \left(1 - \int_{V^i} \left[\int \frac{\sigma_1^m - \sigma_{th}^m}{\sigma_0^m} d\epsilon_e^p \right] dV \right) \tag{7.2}$$

7.2.1 Calculation methods

Calculation of all local approach model values was carried out based on finite element results. The Beremin and Incremental strain models were calculated using the discrete formulae detailed in chapter 4. For equation 7.2, the change in fracture probability associated with a single integration point I over load step k is.

$$\Delta Pf^{I,k} = \begin{cases} \left(\frac{(\bar{\sigma}_1^m)^{I,k} - \sigma_{th}^m}{\sigma_0^m} \right) (\Delta \epsilon_e^p)^{I,k} V^I & \bar{\sigma}_1^{I,k} > \sigma_{th} \\ 0 & \bar{\sigma}_1^{I,k} < \sigma_{th} \end{cases} \tag{7.3}$$

where V^I is the element volume associated with the integration point, $(\Delta \epsilon_e^p)^{I,k}$ is the increment of equivalent plastic strain between k and $k-1$ and $\bar{\sigma}_1^m$ is the mean value of σ_1^m over the load increment. The total integration point fracture probability after load step K is then

$$Pf^{I,K} = \sum_{k=1}^{K} \Delta Pf^{I,k} \tag{7.4}$$

Accordingly, the total fracture probability at load step K is

$$Pf^K = \prod_I \left(1 - Pf^{I,K}\right) \tag{7.5}$$

7.3 Fitting algorithms

7.3.1 Maximising coefficient of determination

The coefficient of determination, R^2, provides a measure of the variance in the experimental data which is accounted for by the model under examination. In this case, correlation between the estimated ranked probability of the fracture data Pf_r and the predicted Pf from the model under investigation is maximised. The linearisation and grid search approaches discussed in chapter 4 were employed, with a linear fit to equation 4.14 used to determine σ_0 for a range of values of m. The best estimates for m and σ_0 are then taken to be those for which R^2_{Pf} is a maximum.

In the case of equation 7.2, determination of σ_0 by linearisation is not possible. Therefore a 'brute force' approach was adopted in which a value of m was selected and R^2 was calculated for a wide range of σ_0 until a maximum of R^2_{Pf} was obtained. This process was then repeated for many m values (typically covering the range $m = 1 - 30$) until the optimum combination of m and σ_0 was found.

7.3.2 Maximum likelihood estimation

An alternative method, avoiding the use of estimated fracture probabilities Pf_r, is maximum likelihood estimation (MLE). Constants are chosen in order to maximise the probability of obtaining the experimental data set to which the model is being calibrated. The probability density function (PDF) for equation 2.36 is

$$p(\sigma_w) = \frac{m(\sigma_w)^{m-1}}{(\sigma_0)^m} \exp\left(-\left(\frac{\sigma_w}{\sigma_0}\right)^m\right) \tag{7.6}$$

with the likelihood estimator for the data set LE given by $LE = \prod_{i=1}^{N} p(\sigma_w^i)$. To avoid the long-winded differentiation involved in maximising LE, the logarithmic likelihood estimator LLE is usually maximised ($LLE = \ln(LE)$) which is equivalent to

$$LLE = N\left[\ln(m) - m \cdot \ln(\sigma_0)\right] + \sum_{i=1}^{N}\left[(m-1)\ln(\sigma_w^i) - \left(\frac{\sigma_w}{\sigma_0}\right)^m\right] \tag{7.7}$$

fixing the value of m , the value of σ_0 is found from

$$\frac{dLLE}{d\sigma_0} = \sum_{i=1}^{N} m\frac{(\sigma_w^i)^m}{\sigma_0^{m+1}} - \frac{Nm}{\sigma_0} = 0 \tag{7.8}$$

which leads to

$$\sigma_0 = \sqrt[m]{\frac{\sum_{i=1}^{N}(\sigma_w^i)^m}{N}} \tag{7.9}$$

The optimum value of σ_0 is then determined for each m, the optimum m value is taken to be that which results in the maximum value of LLE. Alternatively, m may be found for a given data set using.

$$\frac{dLLE}{dm} = \sum_{i=1}^{N}\ln(\sigma_w^i) - N\left(\frac{\sum_{i=1}^{N}\ln(\sigma_w^i)(\sigma_w^i)^m}{\sum_{i=1}^{N}(\sigma_w^i)^m}\right) + \frac{N}{m} = 0 \tag{7.10}$$

The optimum m value is then found using an iterative process as discussed for equation 4.11 (section 4.5.1). A proposed value, $m*$ is used to calculate σ_w for the fracture data. If this value is the same as the m which satisfies equation 7.10, then $m*$ is assumed to be characteristic value for the material.

7.3.3 Determination of threshold stresses

The threshold stress σ_{th} in equations 4.8 and 7.2 may be found by similar means to m and σ_0 - i.e. by maximising a chosen 'goodness of fit' statistic. For multiple, interdependent parameters this is not a desirable approach and may lead to significant error in subsequent predictions. Of particular concern is the potential for dangerous over-estimates of lower bound fracture strength.

In particular, in introducing a non-zero threshold, one must be sure that any improvement is not merely a result of adding an additional arbitrary degree of freedom to the model fitting. Therefore it was decided that σ_{th} should be determined independently of the other fitted constants. To do so, the maximum values of σ_1 and σ_h at fracture were determined from finite element analyses. The results are plotted in figure 7.1. The peak stresses are noticeably greater for the two cracked geometries with lower stresses in the

RNB geometries.

If a threshold stress is assumed to exist, it follows that fracture only becomes a possibility when the peak stress exceeds the threshold. Therefore the maximum stress, at a load where fracture just becomes possible, can be taken as the threshold value. The minimum values from figure 7.1 at fracture are $\sigma_1 = 1364$ MPa and $\sigma_h = 907$ MPa (taken from the RNB90 data). As the minimum experimental load cannot be taken to be the true minimum fracture load, care must be taken to avoid introducing a dangerous level of non-conservatism by over estimating threshold values.

When using K_I in statistical fracture models, a threshold value of $K_{min} = 20$ MPa.m$^{0.5}$ is commonly used [76]. Although not based on any micromechanical arguments, many test programmes have shown fracture occurring only above this limit [154] even at extremely low temperatures [19]. Therefore, the maximum stresses in the CT20 geometry at $K_I = 20$ MPa.m$^{0.5}$ were also determined and found to be $\sigma_1 = 1275$ MPa and $\sigma_h = 787$ MPa. The $K_{min} = 20$ MPa.m$^{0.5}$ threshold was found to hold in [19] for specimens at -253°C, therefore this value is likely to be conservative for fracture at -150°C, as examined in this case.

Values used in the analyses in this work were taken to be $\sigma_1 = 1200$ MPa and $\sigma_h = 700$ MPa, as these are sufficiently below those observed in testing and also maintain the $K_{min} = 20$ MPa.m$^{0.5}$ limit. This is in keeping with [19] where a threshold principal stress of 1450 MPa was found for a similar reactor pressure vessel steel.

7.4 Fitting to single data sets

To examine the variation in the parameters m and σ_0 that may be obtained from varying calibration data sets, fitting was undertaken to fracture data from single specimen geometries. Fitting results of the linearisation method, described in section 4.5.1, are plotted in figure 7.2. It can be seen from both Beremin model variants (figures 7.2(a) and 7.2(b)) that there is a considerable variation in the value of m found from the linear fitting process. This supports the findings of chapter 4 where this method was unable to provide converged values when fitting to more than one specimen geometry. With the exception of the RNB60 geometry, there is relatively good agreement for the incremental strain model (figures 7.2(c) and 7.2(d)). A greater spread is apparent after a

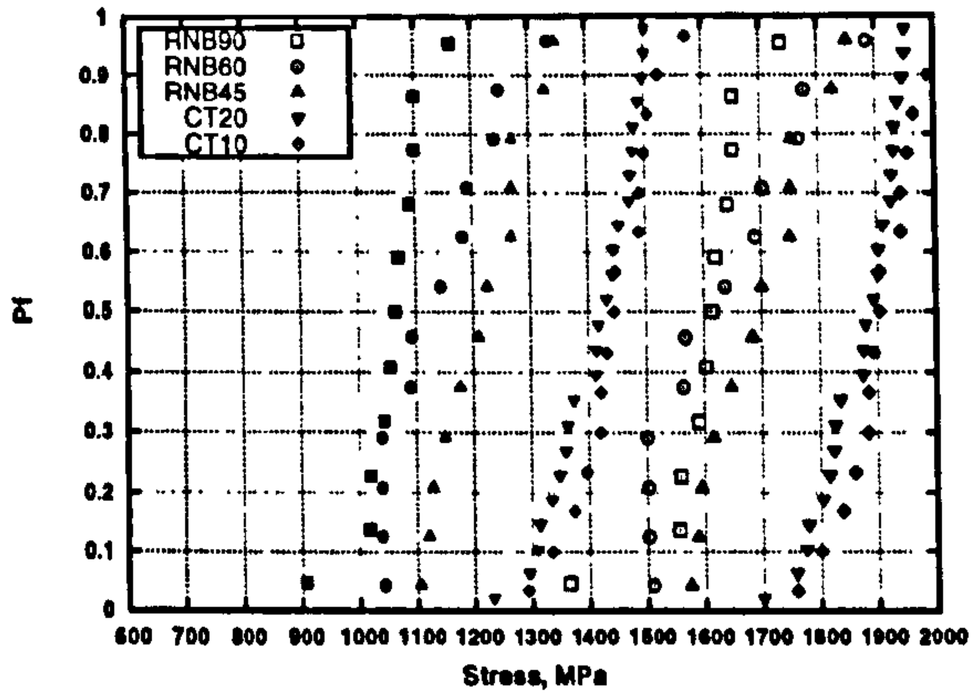

Figure 7.1: Maximum values of σ_1 (open points) and σ_h (filled points) at fracture for data without load history.

non-zero threshold stress is introduced (figures 7.2(e) and 7.2(f)).

From the variation in the coefficient of determination (figure 7.3), it is apparent that R^2_{Pf} is not a reliable indicator of the optimum value of m for fits to single geometries. The overall tendency is to favour low values of m however, as is apparent in figure 7.4, this does not coincide with similar best fit values of σ_0.

Figures 7.4(c)-7.4(f) show a marked effect of introducing a threshold stress, greatly reducing the separation between the high and low constraint geometries at low m. This points to an excessive influence, at low m, of regions of high strain but low stress in the RNB geometries. In the CT geometries, where a small and highly stressed region near the crack tip is dominant, the effect of threshold introduction in minimal. It can be seen from figures 7.4(c)-7.4(f) that although the various specimen curves do not coincide at a single point, there is certainly a clear region of intersection.

Values of the likelihood estimator LE for varying $m*$ are displayed in figure 7.5. The likelihood estimator was calculated using LLE as in equation 7.7 and normalised for data set size.

$$LE = \exp\left(\frac{LLE}{N}\right) \tag{7.11}$$

It can be seen that when fracture probability is described by σ_h, rather than maximum principal stress, there is a consistent increase in the likelihood estimator. It can also be seen in all cases that the RNB60 data set shows a much

reduced likelihood compared to the other specimen data sets. A similar separation of this data set can be seen in figure 7.2. In contrast to the variation of R^2, the LE parameter shows more obvious peak values and so provides some indication of the best value of m. There is, however, still no clear agreement between m values from differing specimens.

Variation in σ_0, as in equation 7.2, with $m*$ for individual specimen geometries can be seen in figure 7.6. It is apparent from comparison with figures 7.4(e) and 7.4(f) that assuming a Weibull distribution does not appear to have a significant effect on the normalising stress σ_0.

7.5 Fitting to multiple data sets

In applying the R^2 maximisation method to data from multiple specimen types, there is a degree of ambiguity as to how the ranking probability equation (equation 4.12) should be applied. Data may be ranked separately, for example by fracture load, and then brought together for parameter fitting. Alternatively, data from multiple specimen types may be treated together as a single material data set and then ranked by another suitable variable such as σ_w.

The way in which data are ranked may have a sizeable effect on the results of fitting processes, as illustrated in figure 7.7. It can be seen that when there is no differentiation applied to data from differing geometries, deficiencies in model fits may become more difficult to detect. The illustrative example in figure 7.7 highlights how, when information about the two separate geometries is retained, the separation between the distributions of σ_w is clear. In this case, the effect of ranking all data together (hence referred to as type 1 fitting) and ranking separately by geometry (type 2 fitting) were investigated, designated T1 and T2 in figures 7.9 and 7.10.

A key practical concern in reliable determination of model constants is an appropriate choice of fracture data, upon which fitting should be based. A degree of pragmatism is needed to balance the requirement for large data sets to improve confidence and minimise the cost and time needed to obtain experimental data. In this case, it was assumed that the 'best' values were obtained by calibrating to the entire AR data set (CT20, CT10 and all RNB data).

For comparison, fits were also carried out based on only the highest and

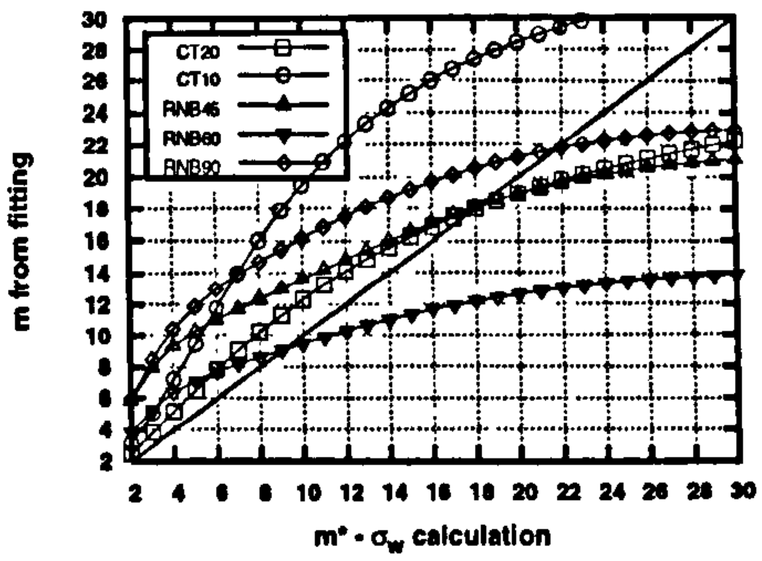

(a) Beremin model - σ_1

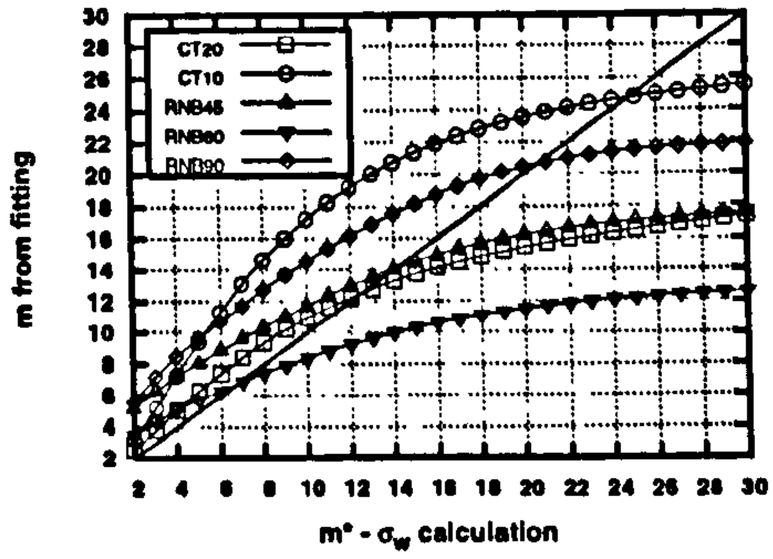

(b) Beremin model - σ_h

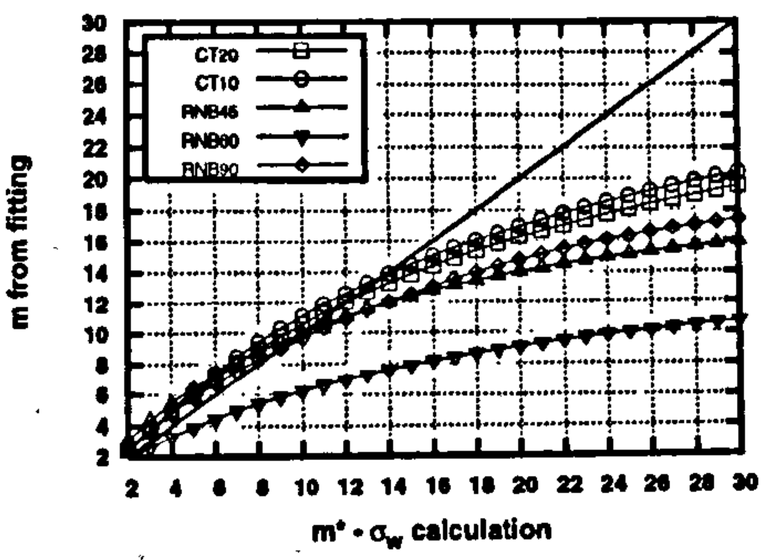

(c) Incremental model - σ_1

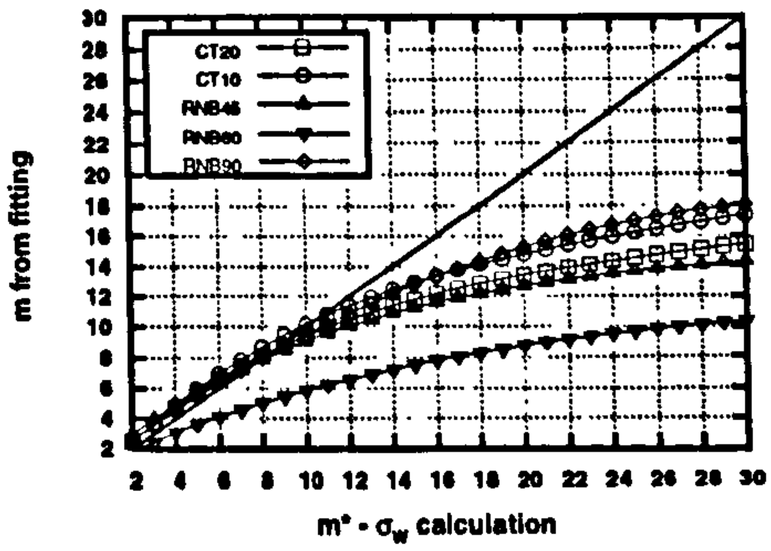

(d) Incremental model - σ_h

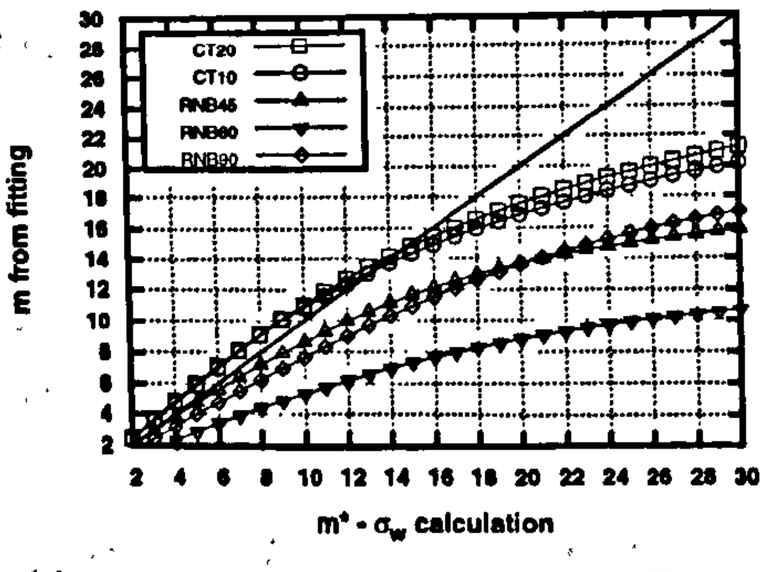

(e) Incremental model, σ_{th}=1200MPa- σ_1

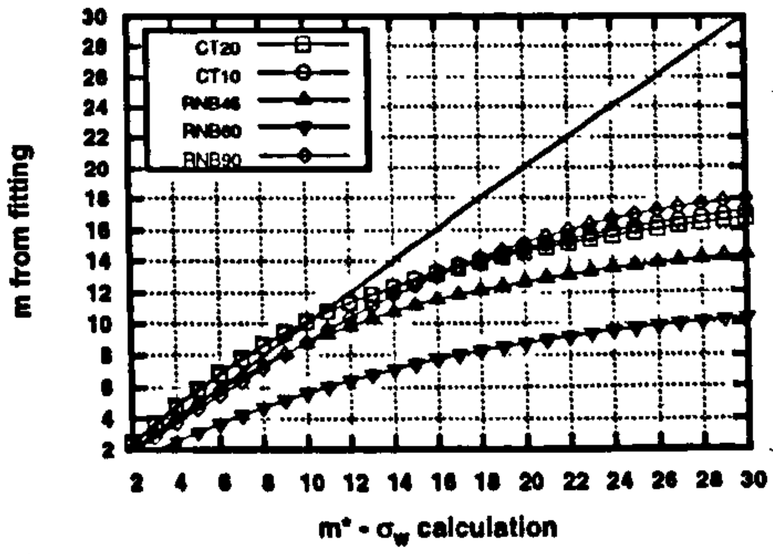

(f) Incremental model, σ_{th}=700MPa - σ_h

Figure 7.2: Variation of m from linearised fitting with $m*$ used to calculate σ_w for various local approach models.

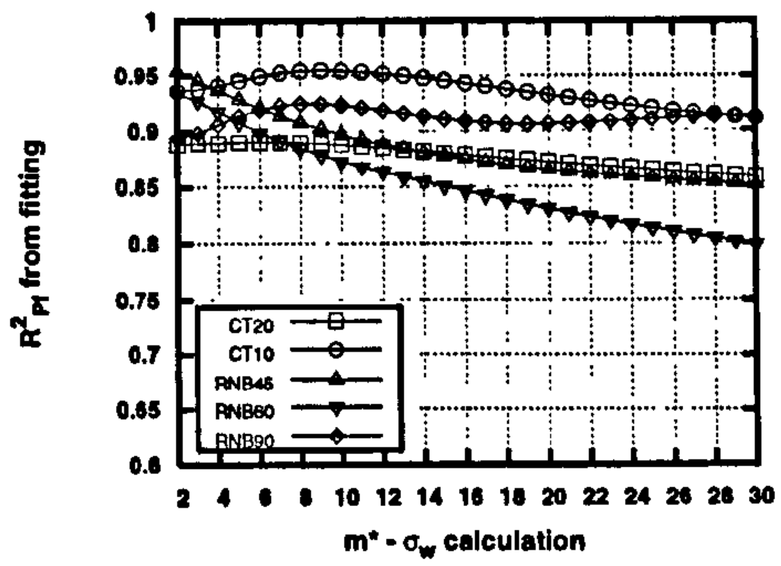

(a) Beremin model - σ_1

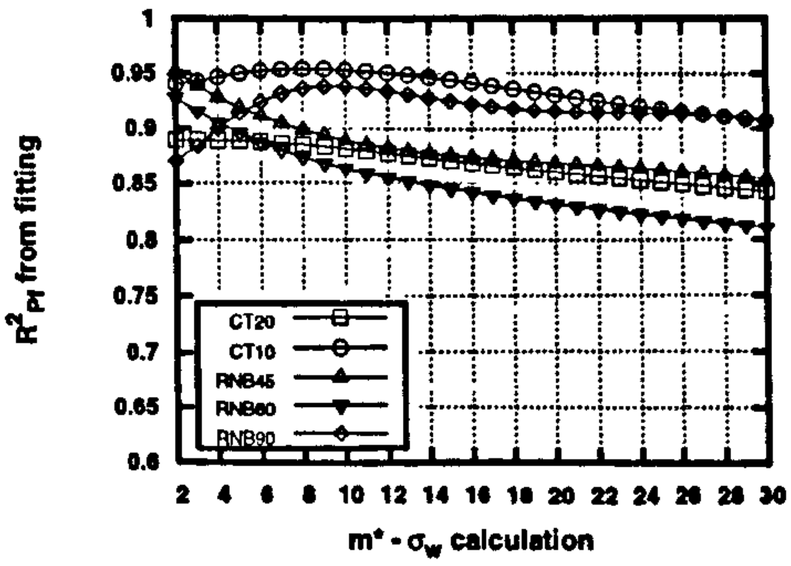

(b) Beremin model - σ_h

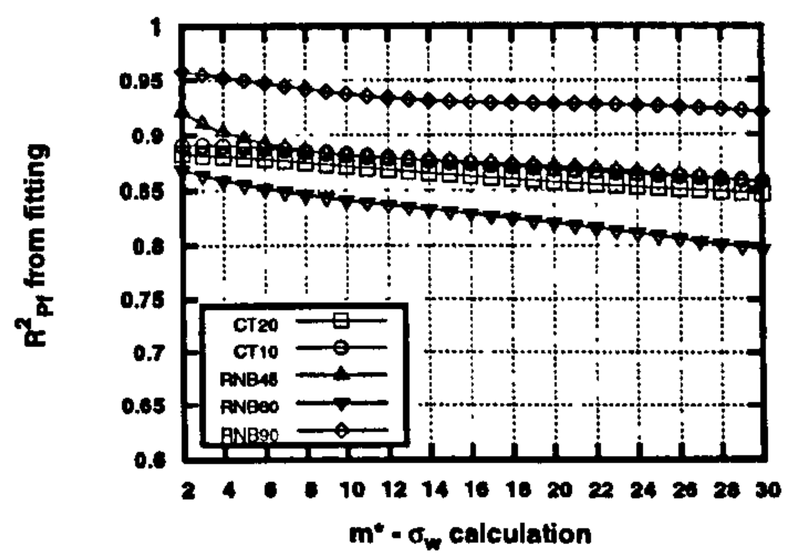

(c) Incremental model - σ_1

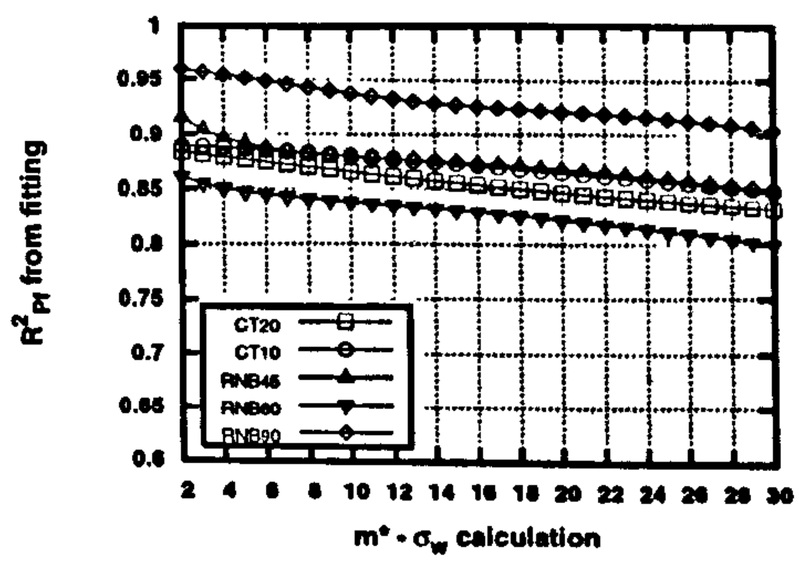

(d) Incremental model - σ_h

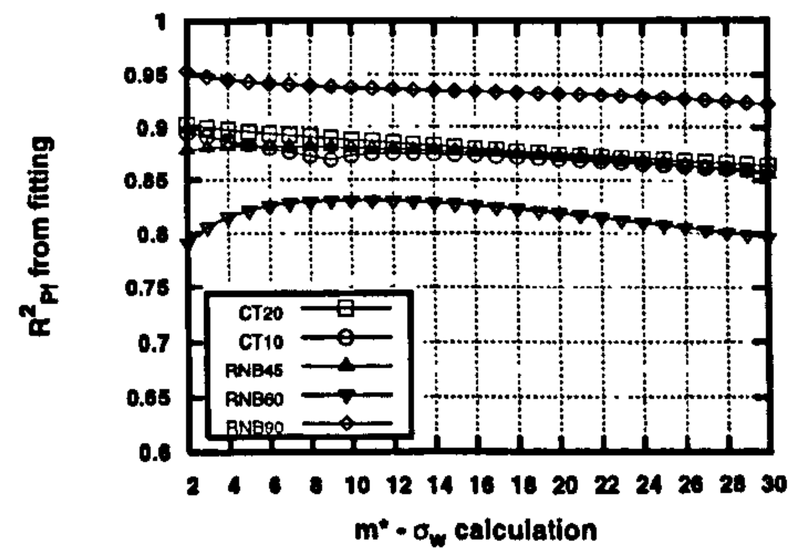

(e) Incremental model, σ_{th}=1200MPa- σ_1

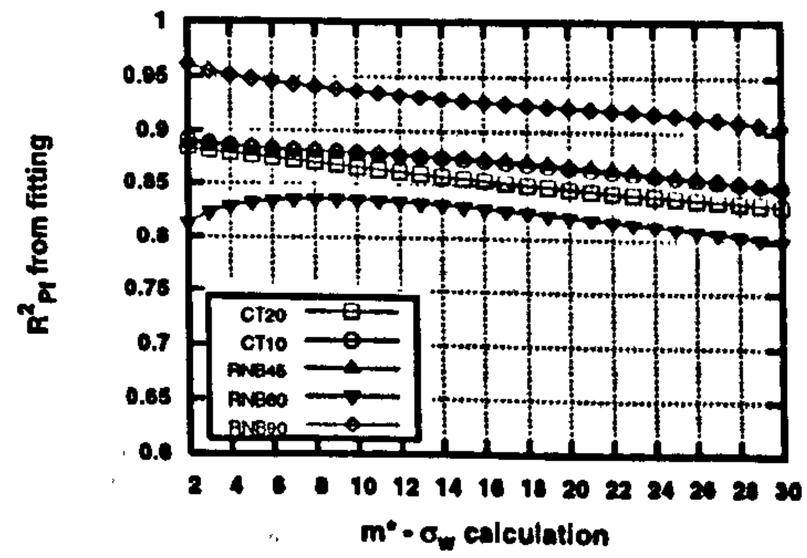

(f) Incremental model, σ_{th}=700MPa - σ_h

Figure 7.3: Variation of coefficient of determination R^2_{Pf} with $m*$ used to calculate σ_w for various local approach models.

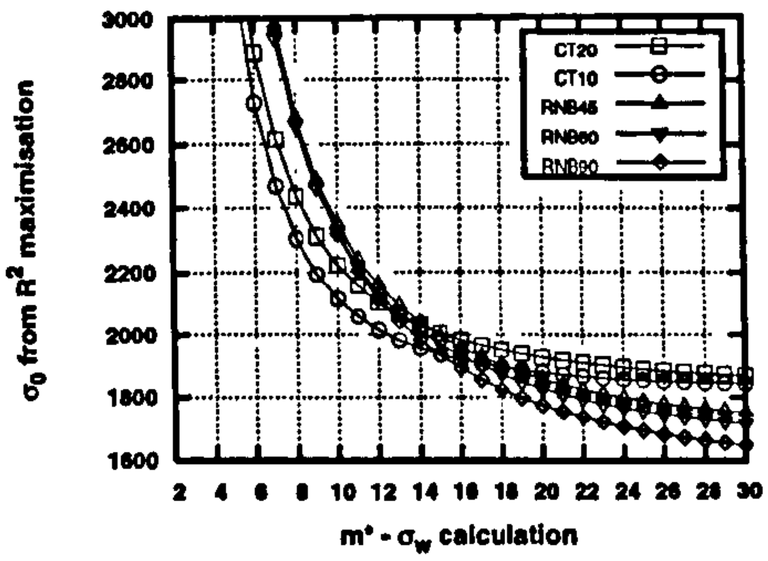

(a) Beremin model - σ_1

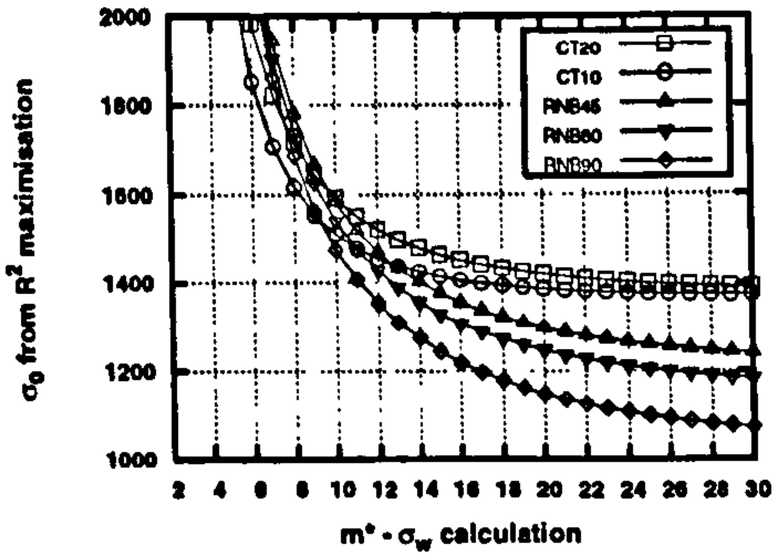

(b) Beremin model - σ_h

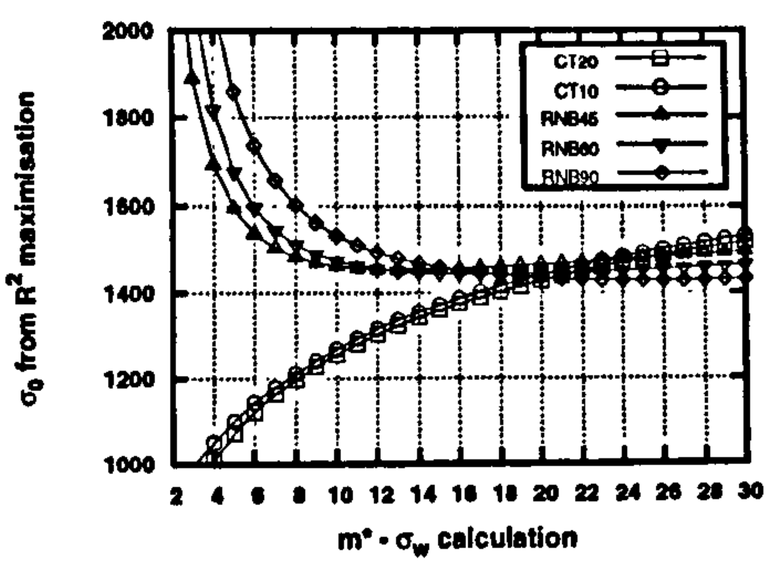

(c) Incremental model - σ_1

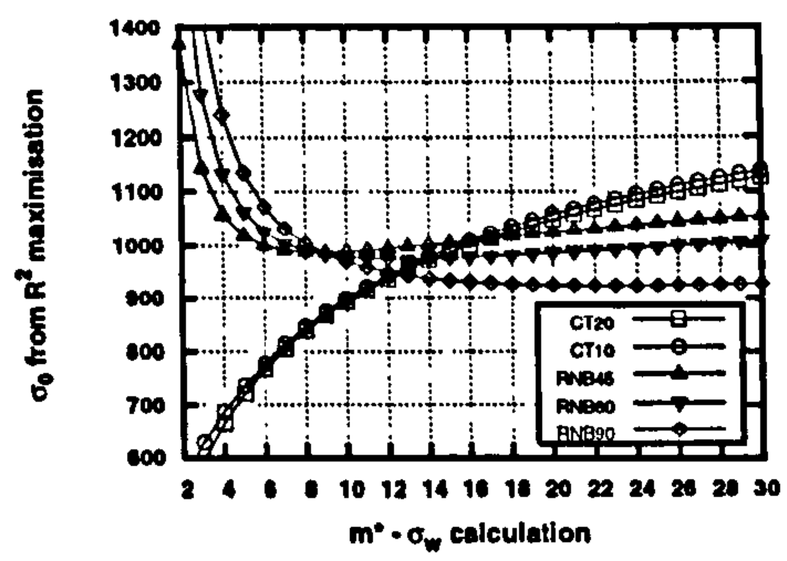

(d) Incremental model - σ_h

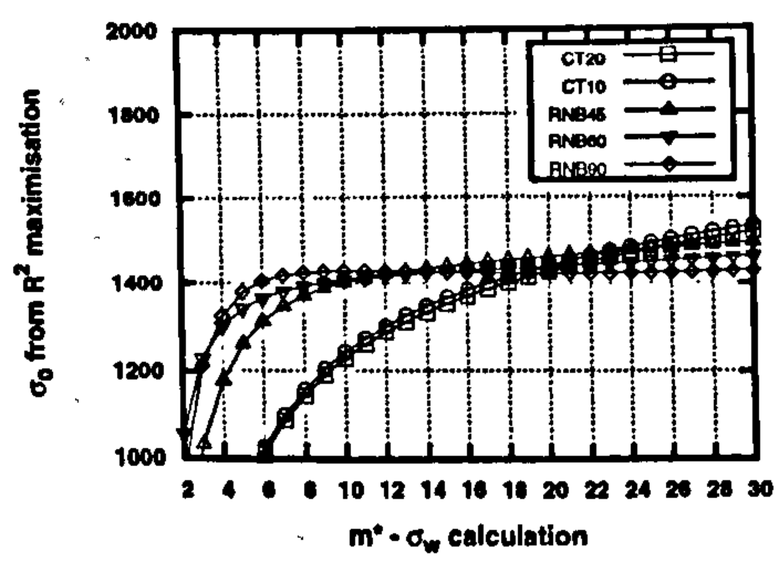

(e) Incremental model, σ_{th}=1200MPa- σ_1

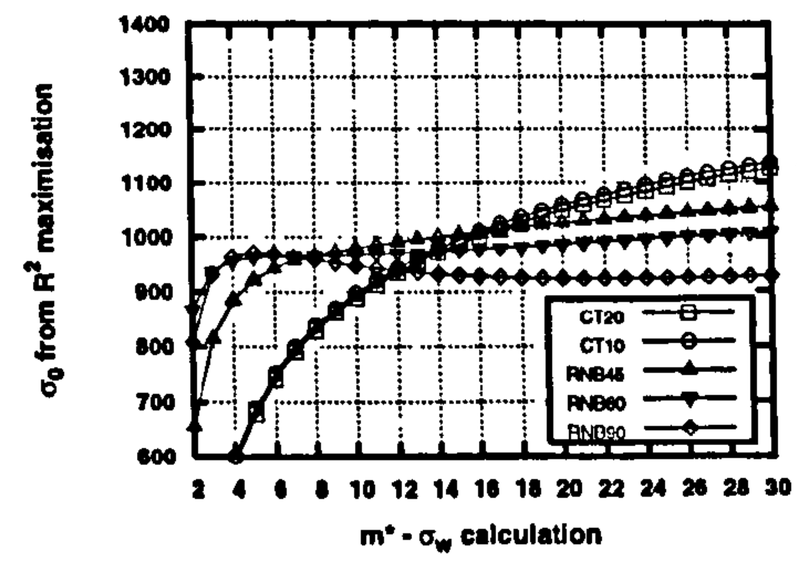

(f) Incremental model, σ_{th}=700MPa - σ_h

Figure 7.4: Variation of σ_0, from R^2_{Pf} maximisation, with $m*$ used to calculate σ_w for various local approach models.

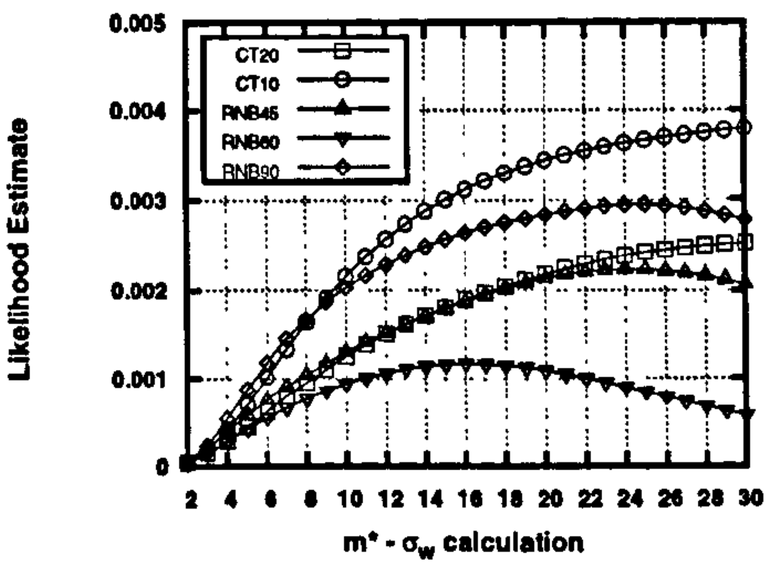

(a) Beremin model - σ_1

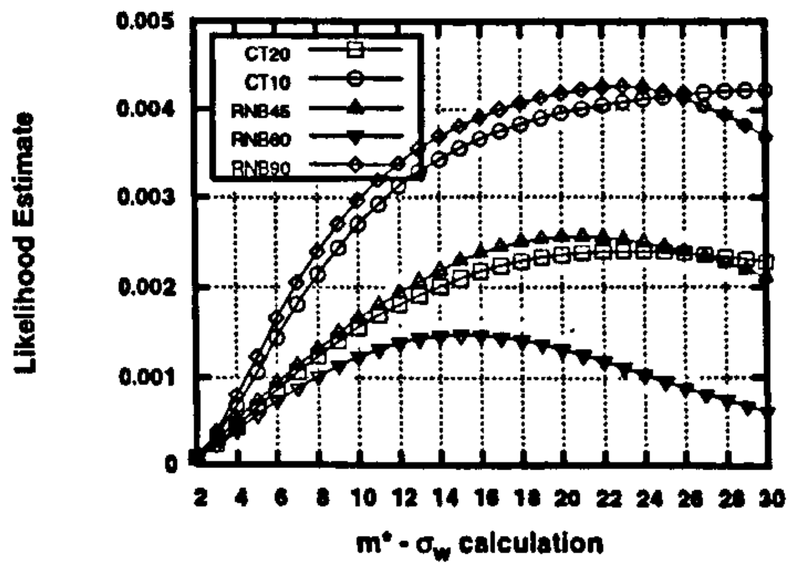

(b) Beremin model - σ_h

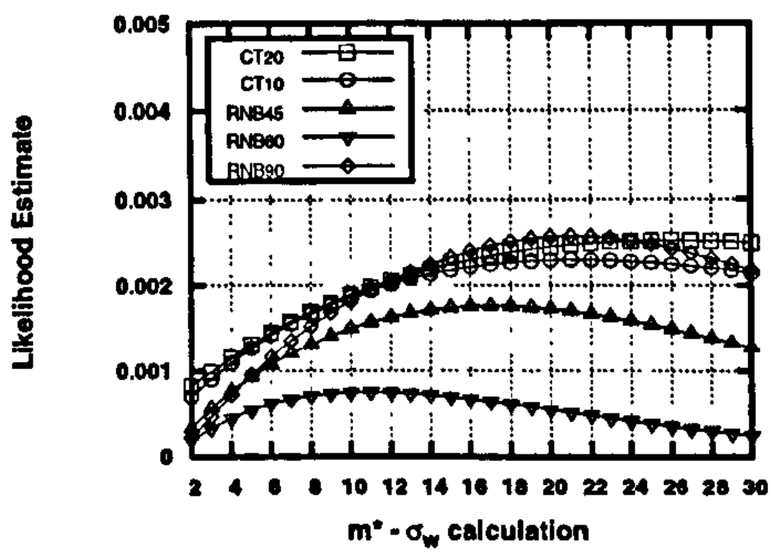

(c) Incremental model - σ_1

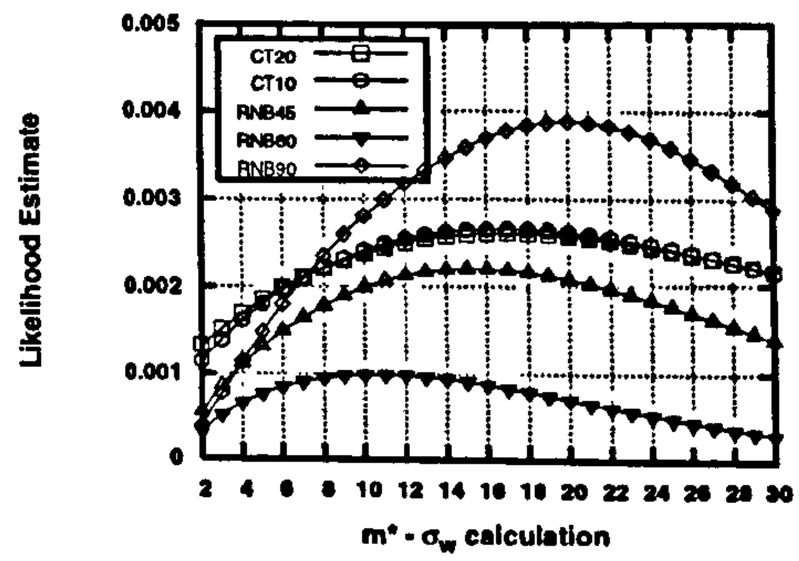

(d) Incremental model - σ_h

(e) Incremental model, σ_{th}=1200MPa- σ_1

(f) Incremental model, σ_{th}=700MPa - σ_h

Figure 7.5: Variation of likelihood estimator LE with $m*$ used to calculate σ_w for various local approach models.

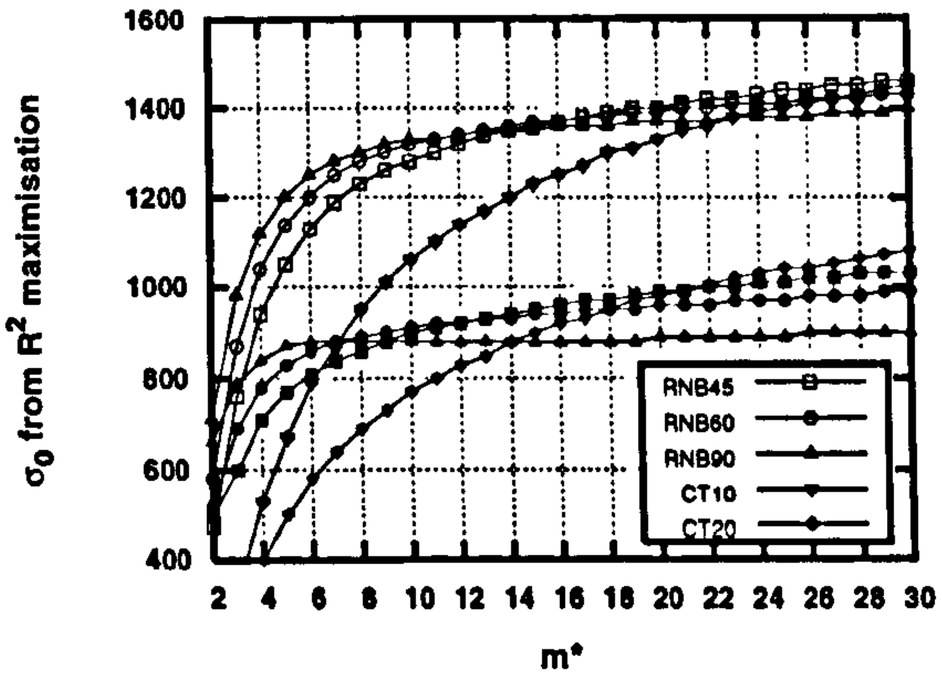

Figure 7.6: Variation of σ_0 in equation 7.2, from R^2_{Pf} maximisation, for differing specimen types.

lowest constraint fracture data. Figure 7.8 shows the variation of plastic zone size with ranked fracture probability for the AR state fracture data. A clear difference is apparent between the two CT geometries and the three RNB geometries. The highest range of constraint, based on this plot, is presented by the CT20 and RNB90 data sets. Fit details for the high and low constraint data set are shown in figure 7.9 and fits to all data in figure 7.10. Variation of LE with $m*$ for the two fit data sets is shown in figure 7.11.

For the alternative model of equation 7.2, fitting data are shown for the CT20 and RNB90 and complete data sets in figure 7.12. Data in this case were ranked using the 'T2' method - i.e. ranking each geometry type separately with the resolution of the search method used to find σ_0 set to 10 MPa.

Details of the fitted parameters are presented in tables 7.1 to 7.4. Confidence limits on σ_0 were obtained from the linear fitting process used to obtain its value. As m is specified, the linear fit did not provide confidence limits. As such, errors were estimated from the function $R^2_{Pf} = f(m*)$, taking bounding values from the two solutions to $f^{-1}(0.99R^2_{max})$.

7.6 Assessment of fit quality

Ideally, one would wish to calibrate model parameters to fracture data and then apply the model to assess the integrity of complex structures, without the need for extensive fracture testing. To have confidence in values obtained from empirical fits, it is important that the ability of the model used to accurately

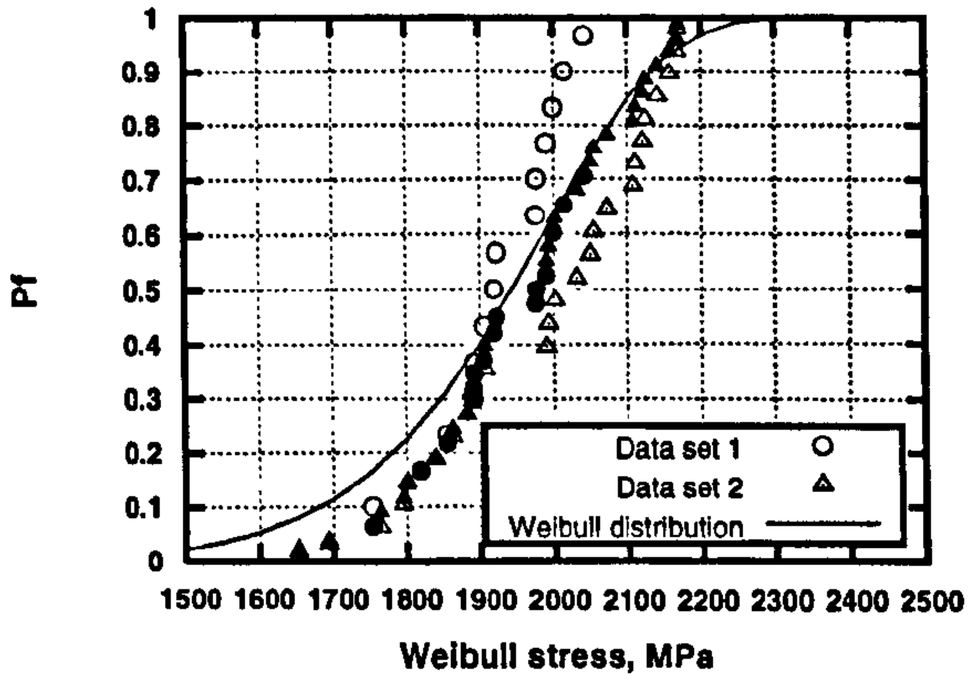

Figure 7.7: Effect of ranking method on distribution of fracture data. Open points ranked as individual geometries, closed points ranked as a single combined data set.

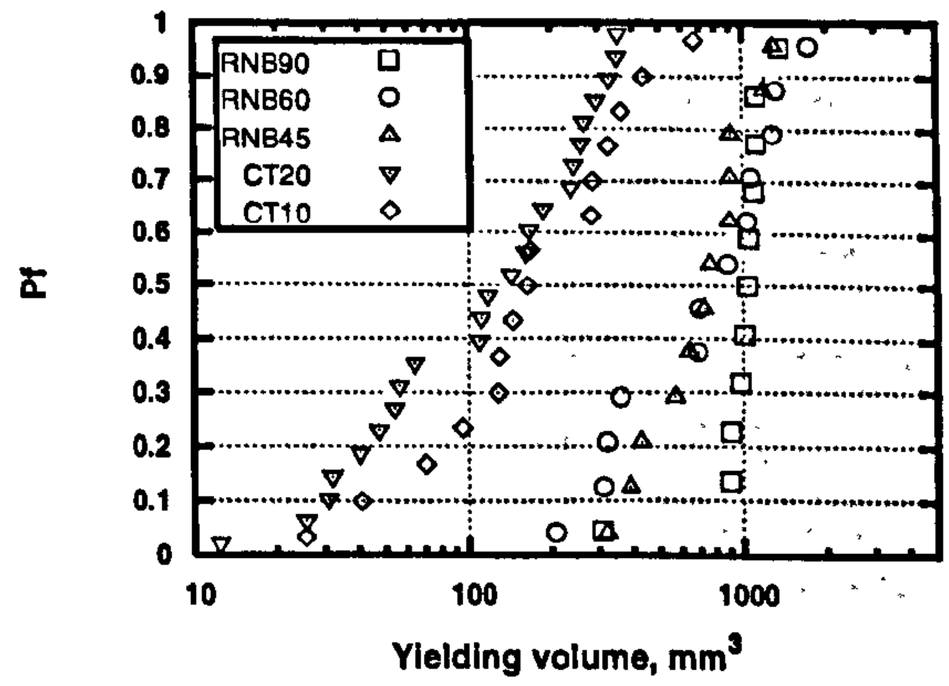

Figure 7.8: Variation of plastic volume size with failure probability for fracture data in the AR state.

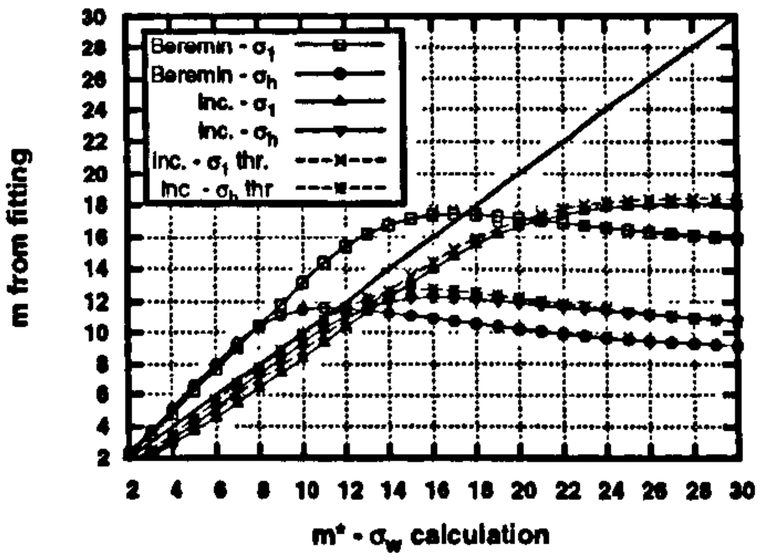

(a) Variation of $m*$ and m from linearised fitting (T1).

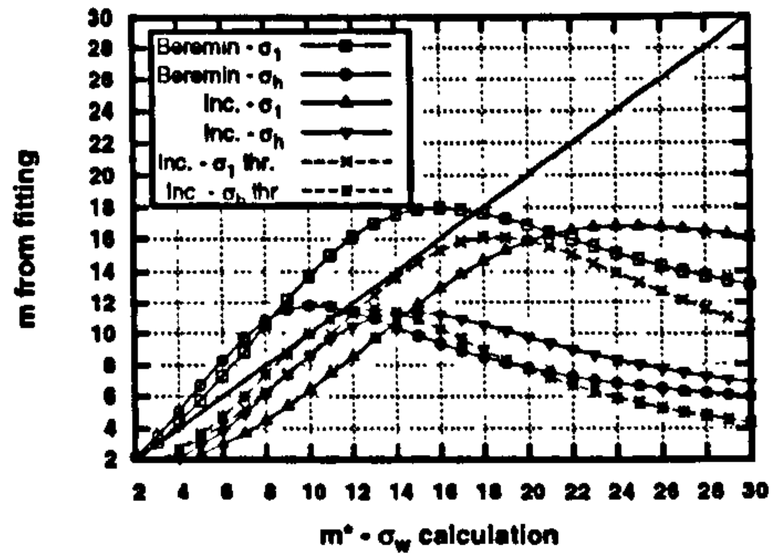

(b) Variation of $m*$ and m from linearised fitting (T2).

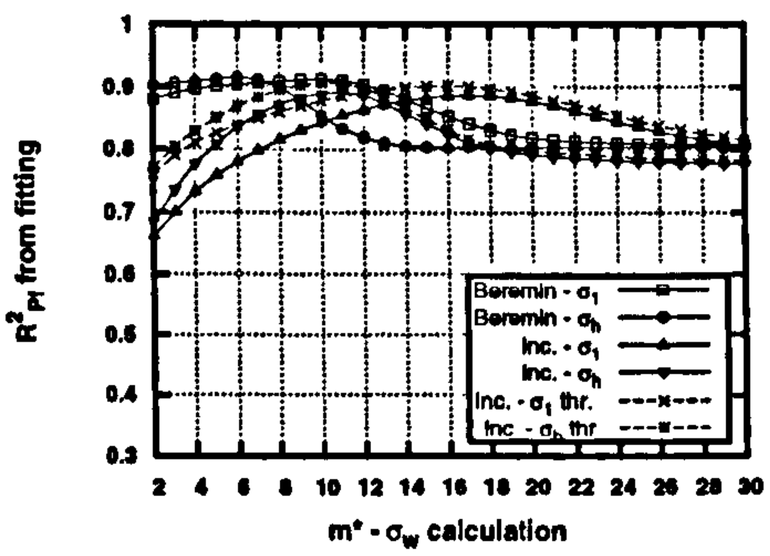

(c) Variation of R^2, between predicted and ranked Pf, with $m*$ (T1).

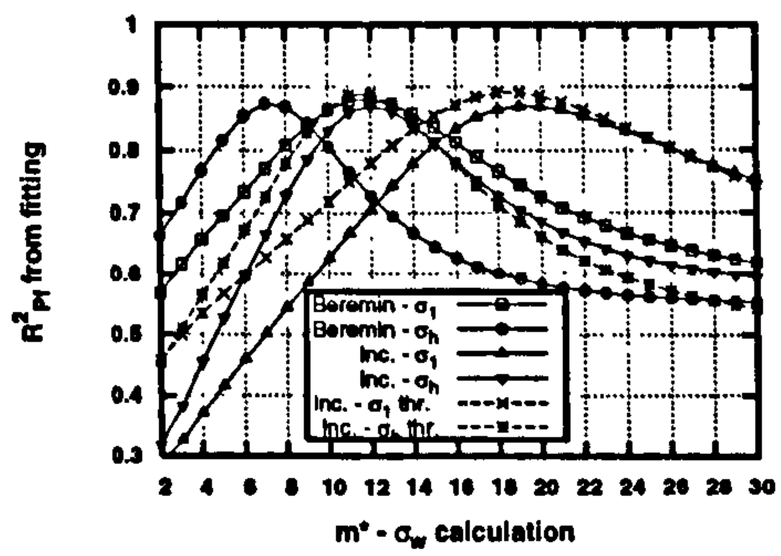

(d) Variation of R^2, between predicted and ranked Pf, with $m*$ (T2).

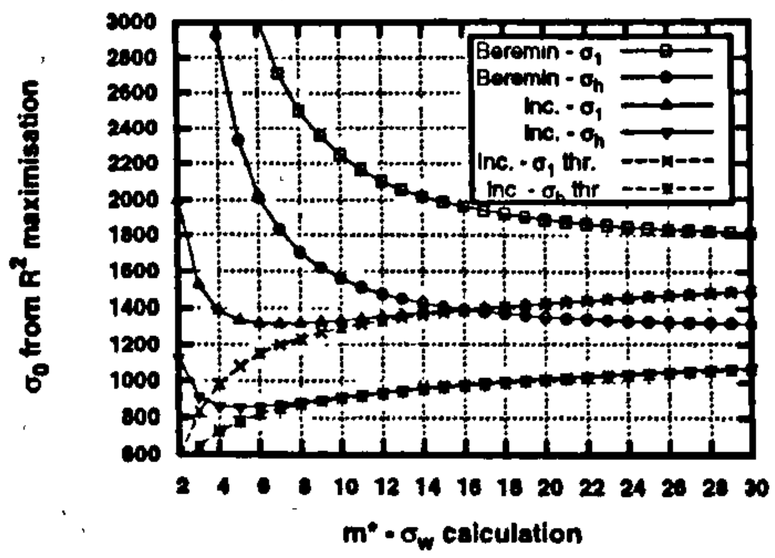

(e) Variation of σ_0, from R^2 maximisation, with $m*$ (T1).

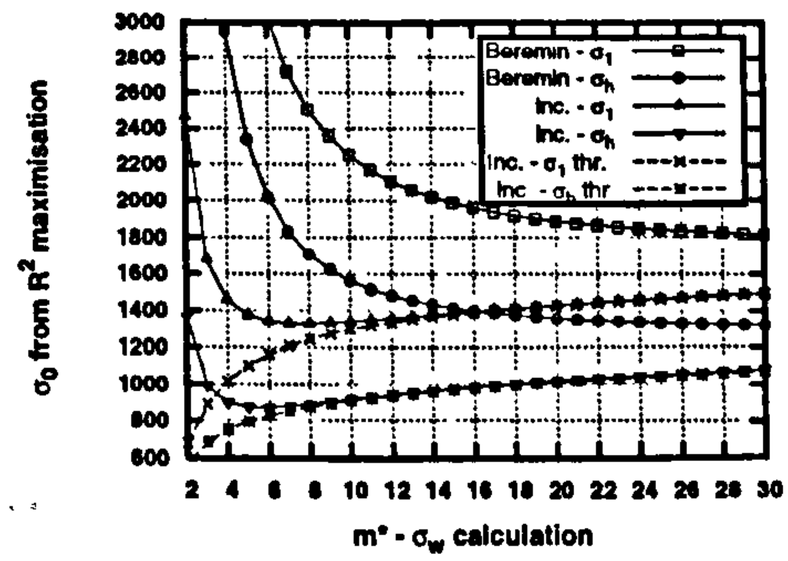

(f) Variation of σ_0, from R^2 maximisation, with $m*$ (T2).

Figure 7.9: Model fit data based on CT20 and RNB90 fracture data.

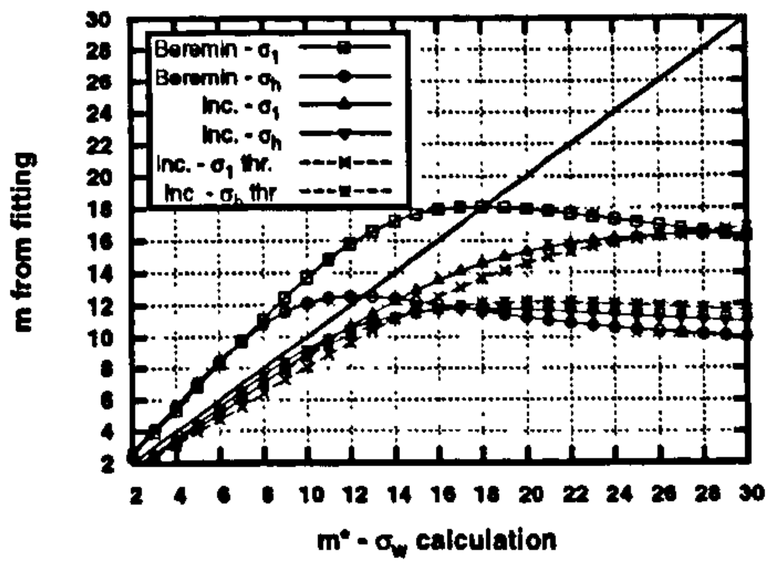

(a) Variation of $m*$ and m from linearised fitting (T1).

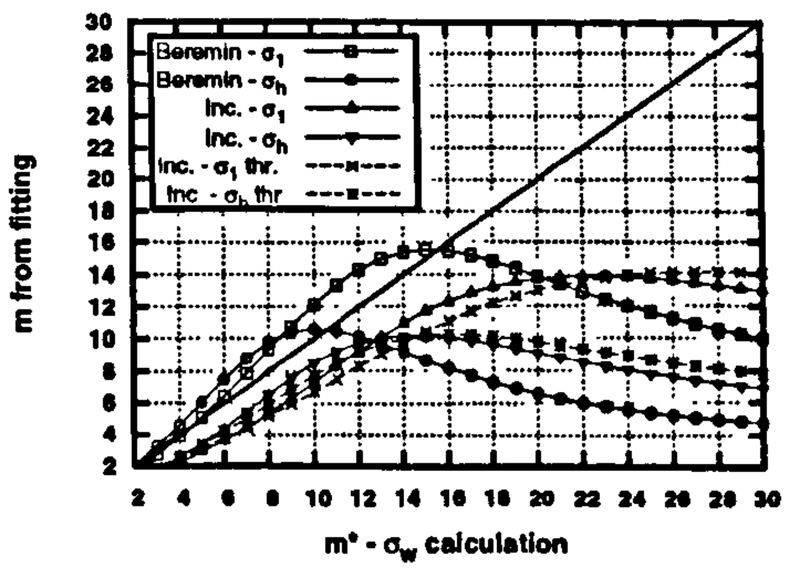

(b) Variation of $m*$ and m from linearised fitting (T2).

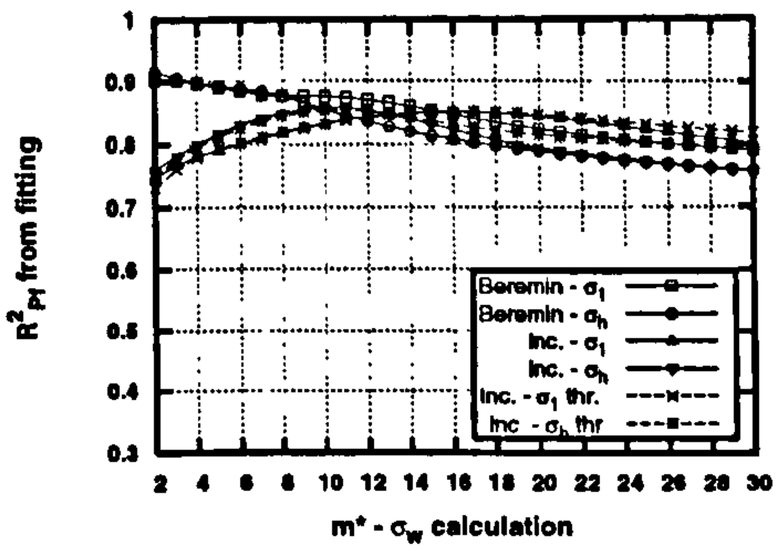

(c) Variation of R^2, between predicted and ranked Pf, with $m*$ (T1).

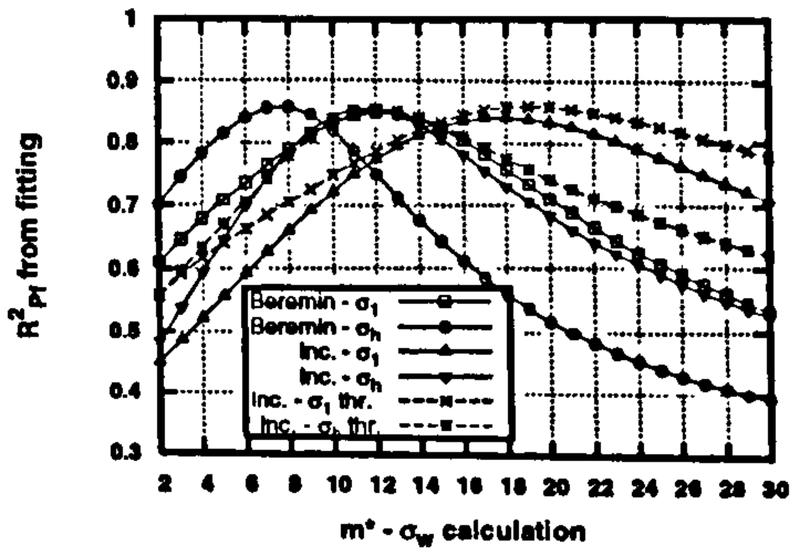

(d) Variation of R^2, between predicted and ranked Pf, with $m*$ (T2).

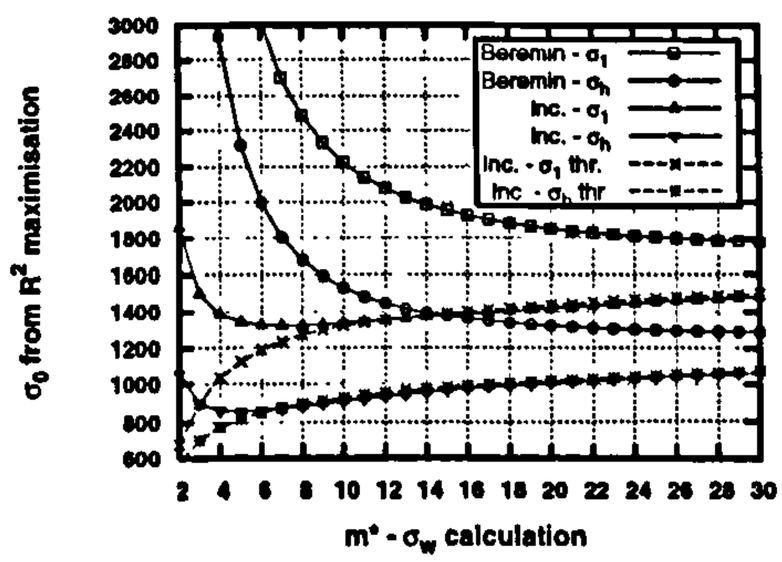

(e) Variation of σ_0, from R^2 maximisation, with $m*$ (T1).

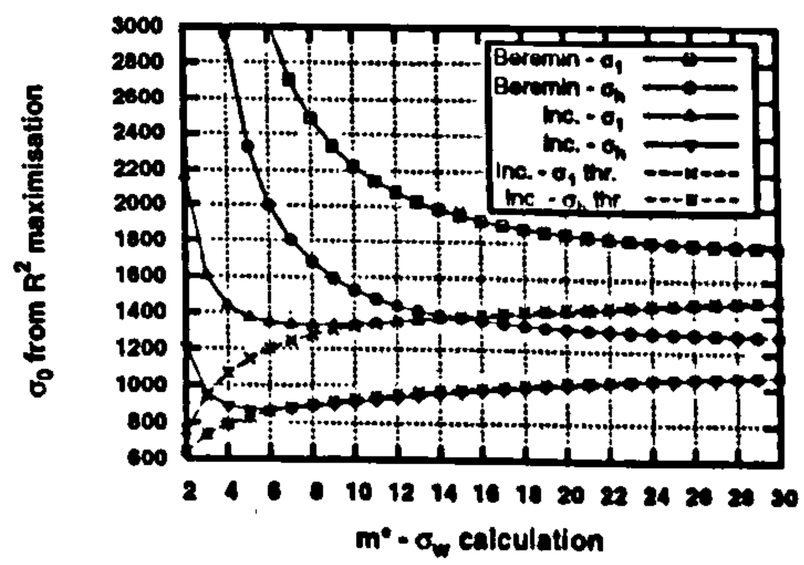

(f) Variation of σ_0, from R^2 maximisation, with $m*$ (T2).

Figure 7.10: Model fit data based on all AR fracture data.

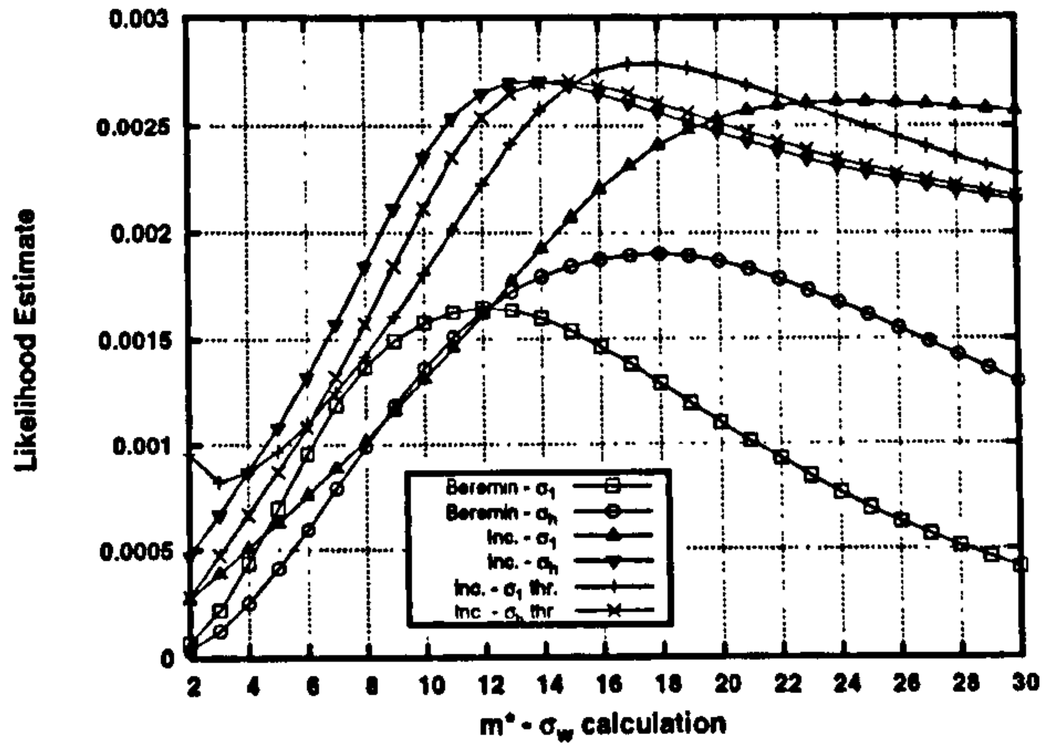

(a) CT20 and RNB90 data.

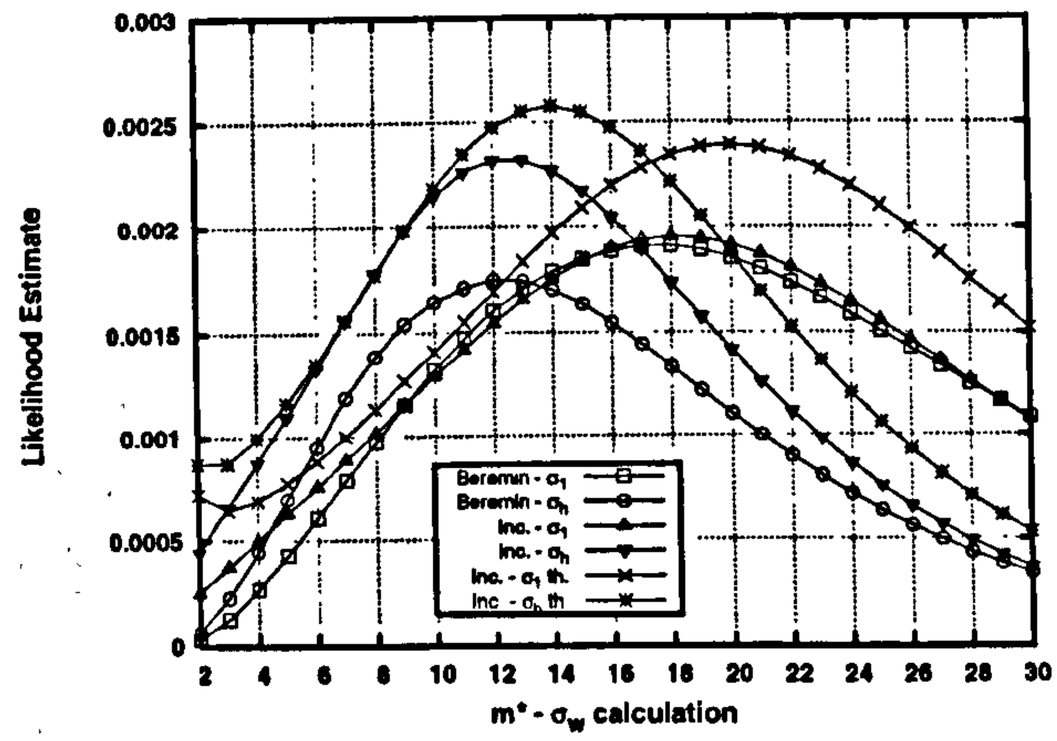

(b) All AR fracture data.

Figure 7.11: Variation of likelihood estimator LE with $m*$ for fits to multiple specimen types.

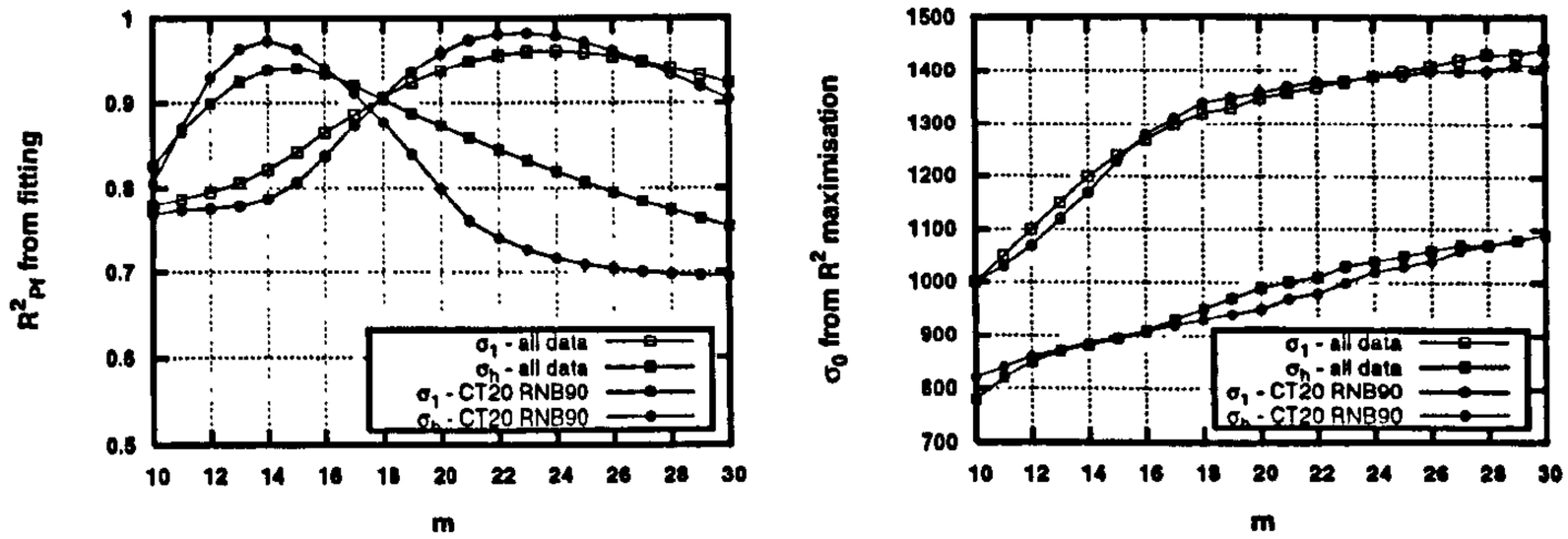

(a) (b)

Figure 7.12: Variation of coefficient of determination a) and normalising stress σ_0 b) with m for the non-Weibull local approach formulation of equation 7.2.

represent the data can be verified.

In the case of probabilistic fracture assessments, the probability of fracture from the model may be compared with the estimates of Pf obtained by applying ranking equations to experimental data. This is non-trivial as the use of any ranking equation - in this case equation 4.12 - introduces error between the 'true' probability of fracture at a given load and that obtained from applying the ranking equation to a relatively small sample of data. The error introduced by estimating Pf may however be estimated numerically. To this end, a Montecarlo analysis of the error introduced by the ranking equation 4.12 was undertaken:

1. Select a data set size, N, to be examined and generate N random failure probability values (values between 0 and 1).

2. Calculate the ranked failure probabilities associated with this data set - in this case $Pf = (i - 0.5)/N$. Each randomly generated 'true' fracture probability now corresponds to an estimated value from ranking.

3. Repeat steps 1 and 2 to generate many 'true' Pf values for each ranked value. Based on this, confidence limits for the true fracture probability associated with each ranked value may be determined.

4. Steps 1-3 should be repeated as necessary, to ensure enough random data sets are generated for the confidence limits to reach convergent values.

Convergence of the confidence limits with increasing number of data sets are shown for set size 5 in figure 7.13(a) - 10^5 tests were chosen for converged

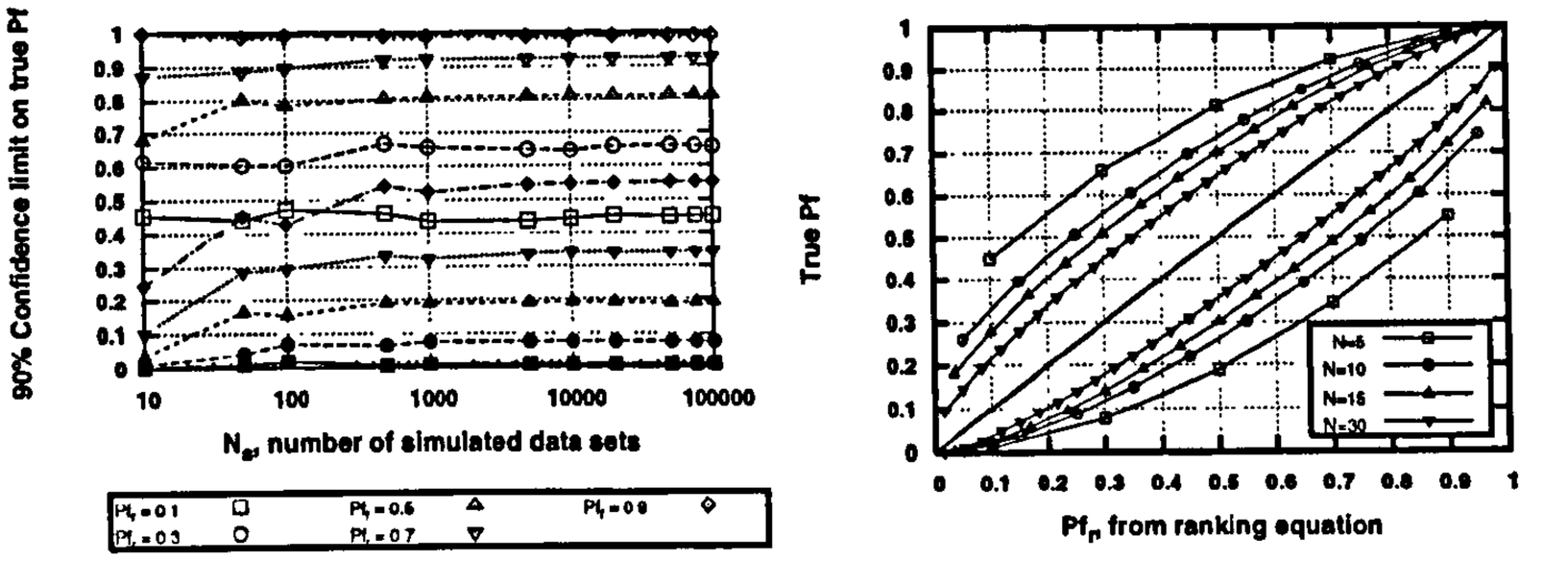

(a) Convergence of values, N=5 (b) Variation of limits with N

Figure 7.13: 90% Confidence limits for the fracture probability associated with the estimated probability of fracture from the ranking equation $Pf_r = (i - 0.5)/N$.

values in this work. The variation of the converged limits with set size N is shown in figure 7.13(b).

Predicted probabilities of fracture (for models fitted to the CT20 and RNB90 data) are plotted against those from the ranking equation in figure 7.14. It is assumed that if a model fit is reliable, 90% of the fracture data should lie within the limits corresponding to the correct data set size. For example the RNB90 data set (11 samples) may have 1.1 (i.e. 1) data points outside the limits corresponding to $N = 11$. Based on this criterion, it can be seen that the fit to the standard Beremin model should be rejected (figure 7.14(a)).

7.7 Discussion

From the investigation of parameter variation from single geometries (figures 7.2 to 7.6), it is apparent that the results obtained from single geometry data sets can vary considerably. In comparing the fitted slope m from linearisation to $m*$ (figure 7.2) it can be seen that inclusion of strain to control defect nucleation improves the overall grouping between specimens (figures 7.2(c) and 7.2(d)). There is a notable exception for the RNB60 data where there is no agreement between m and $m*$ at any point. This has important implications if fitting is applied to multiple specimens where the inclusion of the RNB60 data may unduly influence the overall trends. To examine the sensitivity of the

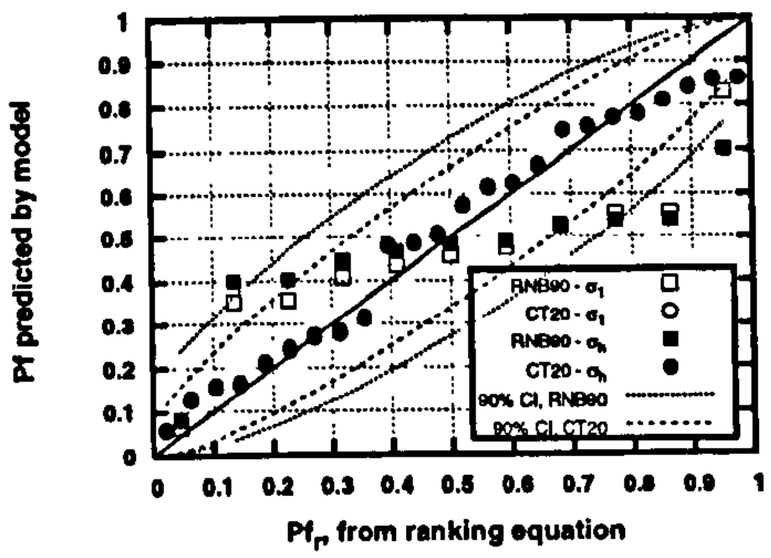

(a) Beremin model

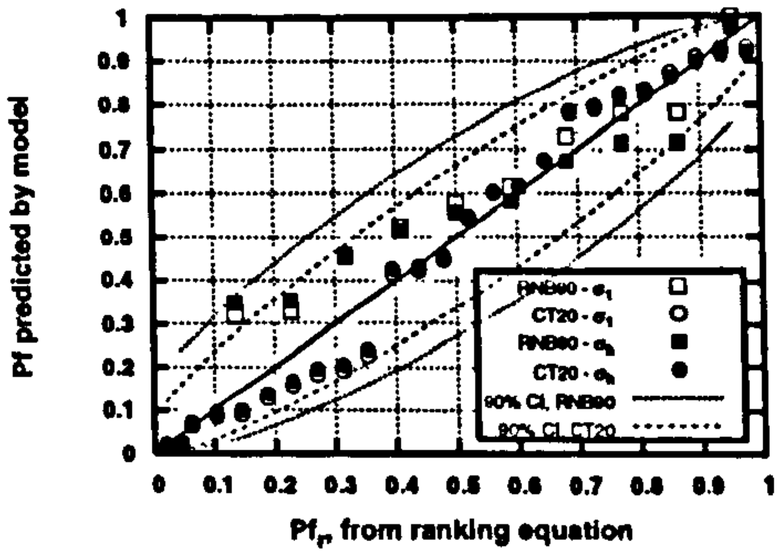

(b) Incremental model

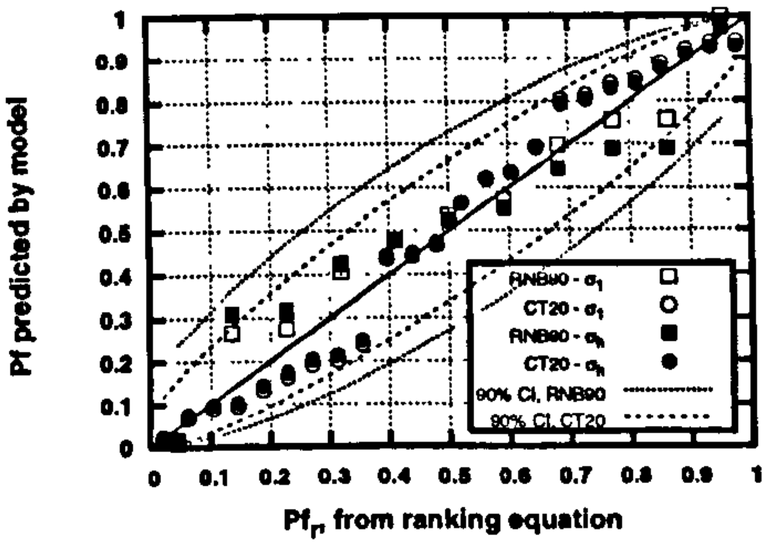

(c) Incremental model with threshold

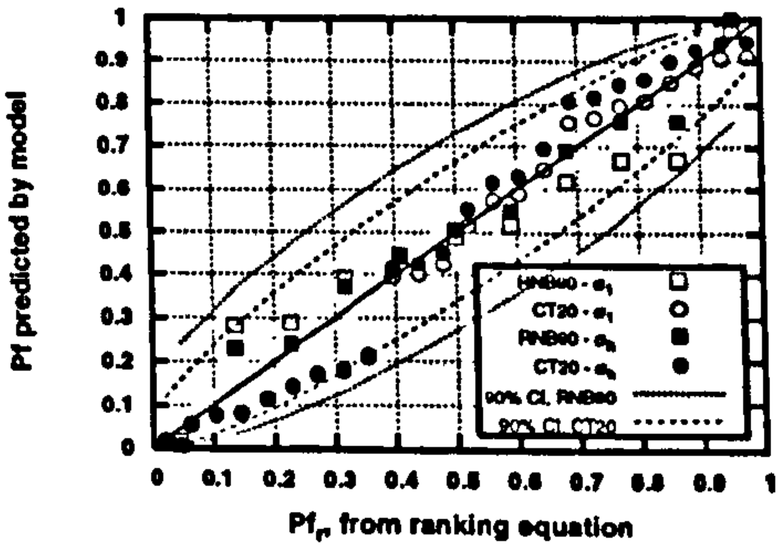

(d) Non Weibull model, equation 7.2

Figure 7.14: Assessment of model fit quality, CT20 and RNB90 data, based on 90% confidence intervals for probability ranking equation.

process to the FE model used, an alternative simulation of the RNB60 failure was undertaken, increasing the minimum diameter from 8.0mm to 8.1mm. It was felt to be a reasonable assumption that a variation of this size may have existed in the experimental specimens. The effect of this change, in the context of the incremental strain model (fitted to the CT20 and RNB90 data) with $\sigma_{th} = 1200$MPa, is shown in figure 7.7.

It can be seen that a small variation in geometry has a sizeable effect on the fracture predictions. Although both predictions can be said to agree reasonably well with the fracture data, the change may be significant in terms of fitting. For example, if the error between predicted and ranked fracture probability is to be minimised, the agreement of the 8.1mm diameter prediction is much better. If determination of minimum fracture load is necessary, then the 8.0mm model may be preferred. This highlights one of the potential issues with geometries where the fracture loads are grouped very tightly - i.e. where the increase in Pf is a sudden, step like function. In such cases, the gradient of the $F - Pf$ response means that a small error in fracture load can result in a large variation between predicted and ranked fracture probability. It may therefore be more appropriate to minimise error in fracture load, for a given P_f, rather than minimising error in probability at fixed loads.

The variation of σ_0 with $m*$ for single geometries (figure 7.4) highlights the variation which may occur across differing specimen types, particularly at low $m*$. The variation of maximum values of R^2_{Pf}, as in figure 7.3, tends towards low $m*$ values which illustrates the danger of using a single geometry. The maximum values of LE correspond better to the regions where values of σ_0 were similar and so, if a single geometry must be used, an investigation finding m from the slope of the linearised data and maximising LE would seem to be the best option.

Examining the variation of σ_0 between the incremental threshold model (figures 7.4(e) and 7.4(f)) and the non-Weibull model (figure 7.6), suggests that the effect of the Weibull distribution assumption is small.

When multiple data sets are taken into account, it is clear from figures 7.9(c), 7.9(d), 7.10(c) and 7.10(d) that ranking data by geometry (T2) produces much clearer peak values for R^2_{Pf}. As the maximum values are not greatly altered, it is apparent that the additional degree of freedom introduced by allowing data from differing geometries to 'float' increases the apparent quality of fit. The effect of the ranking assumption on σ_0 was minimal.

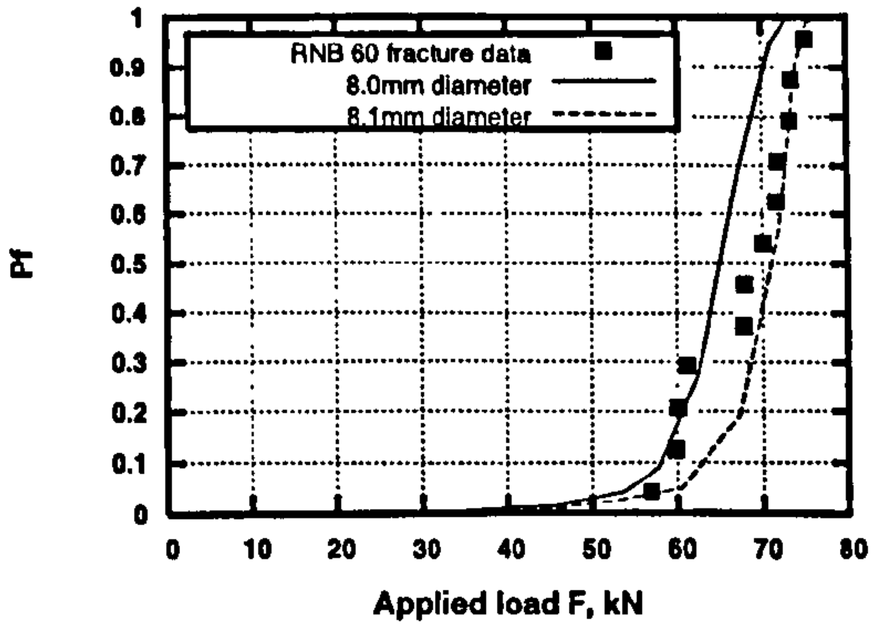

Figure 7.15: Effect of variation in minimum diameter on failure prediction of RNB60 fracture data - incremental strain model, based on σ_1, with threshold stress.

As for fitting to single specimen types, the difference between the incremental model and non-Weibull model is small (figures 7.9(f), 7.10(f) and 7.12(b)).

The peak values of LE for multiple data sets (figure 7.11) were approximately coincident, in terms of best fit value of m, with those from R^2_{Pf}. As mentioned previously, it is desirable to be able to reliably approximate material parameters based on limited fracture data. A review of tables 7.1-7.4 suggests that the R^2 maximisation approach provides the most stable solutions between the RNB90 and CT20 data set and the complete AR fracture data set. It is also noticeable that the confidence limits (from linear fitting of equation 4.14) on σ_0 are much reduced when the sample data size is increased.

7.8 Conclusions

1. Comparing m values from fitting to linearised Weibull stress data with those used to calculate Weibull stresses results in acceptably consistent converged values, but the resulting estimates for m were found to vary considerably between specimen types.

2. The coefficient of determination R^2 between predicted and ranked fracture probabilities was found to be insensitive to the choice of m for single geometries and so is not a useful measure of fit quality in such cases.

3. Plots of best fit σ_0 against m for multiple single geometries were found to provide good indications of the optimum m value for the whole data

set.

4. Introduction of a local threshold stress was seen to improve agreement between high and low constraint geometries for the strain nucleation model, especially at low m.

5. Maximisation of R^2 was found to provide good indication of m values when applied to high and low constraint data. In such cases it is recommended to assign ranked failure probabilities to specimen geometries separately, rather than grouping all values as a single material data set.

6. Use of a non-Weibull formulation for failure probability was not found to significantly affect the model parameters.

7. Using a Montecarlo analysis, the error introduced by estimating fracture probability using a ranking equation was estimated. It is suggested that confidence limits on this error may be used as a criteria to accept or reject model fits.

8. Maximising R^2 was found to be the most stable method of estimating model parameters for a large data set from limited high and low constraint data.

Chapter 8

Predictions of fracture

This chapter investigates the ability of the varying local and global fracture methods considered to predict the results of the fracture tests described in chapter 5. One of the intentions was to investigate the benefits, if any, that may be obtained from using local approach methods in place of simpler K and J based methods. As K values in particular are relatively easily obtainable from analytical functions, it is useful to understand the practical gains resulting from the considerable extra effort involved in using the local approach.

For stress intensity factor methods, a number of approaches were employed to determine effective plane strain stress intensity factor values for specimens of differing constraint or combined applied and residual stresses. For local approach techniques it was assumed that, in a practical assessment, a relatively limited data set is often available for parameter calibration. Therefore, models were calibrated to the high constraint CT20 and low constraint RNB90 data sets, as described in chapter 7.

As well as investigating the descriptions of the overall variation of fracture probability, estimates of lower bound fracture load were also determined using various predictive approaches and the R6 structural integrity assessment code.

8.1 J and K based predictions of fracture

8.1.1 Determining K from the modified J integral.

The J_m formulation of equation 2.24 was used for the WPS CT and NCT specimens to account for the effect of preload cycles. In the case of the NCT specimens, the initial state was set as that of the uncracked body, after creation

of the residual stress field but prior to introduction of the crack. No initial state was defined for the WPS case as preloading was applied to the cracked structure. The resulting variation in J_m upon reloading for these load cases are plotted in figure 8.1. Equivalent K values for combined loading due to residual stress and external loads were then defined using equation 4.15.

8.1.2 Thickness correction

It is well documented that many materials display a pronounced reduction in strength with specimen size, due to the increasing probability of defects being present in larger specimens. Working on this principle, Wallin [48] suggested a thickness correction for cleavage fracture toughness. Based on the probabilistic equation 4.3, with $m = 4$, an effective toughness, corrected for specimen thickness is.

$$K_{eff} = K_{min} + (K - K_{min}) \left(\frac{B}{B_0}\right)^{1/4} \tag{8.1}$$

Where B is the thickness of the specimen being considered and B_0 is the thickness of a reference specimen type. A fit to the CT20 data, using the elastic analytical values of K from equation 5.1, results in K_{min}=21.4 MPa.m$^{0.5}$ and K_{min}=84.3 MPa.m$^{0.5}$ with m fixed at 4. Taking B=10mm and B_0=20mm, the fracture of the 10mm CT specimens may be predicted from.

$$Pf = 1 - \exp\left(-\frac{10}{20}\left[\frac{K_I - 21.4}{84.3 - 21.4}\right]^4\right) \tag{8.2}$$

8.1.3 Weight function analyses

Weight function analyses allow stress intensity factors to be estimated, based on the stresses which would exist in an uncracked body. When a crack is introduced into a residual stress field, the stress intensity factor due to residual stress, K_{res}, may be estimated from the uncracked body stresses over the cracked region. In this work, the method was used to estimate the effect of preloading on the NCT specimens.

The stress intensity factor may be determined using equation 8.3, where $m(a, x)$ is the weight function for the specimen in question. For CT geometries, a, x and W are defined in figure 8.2. The function $m(a, x)$ was presented for CT specimens by Wu [146].

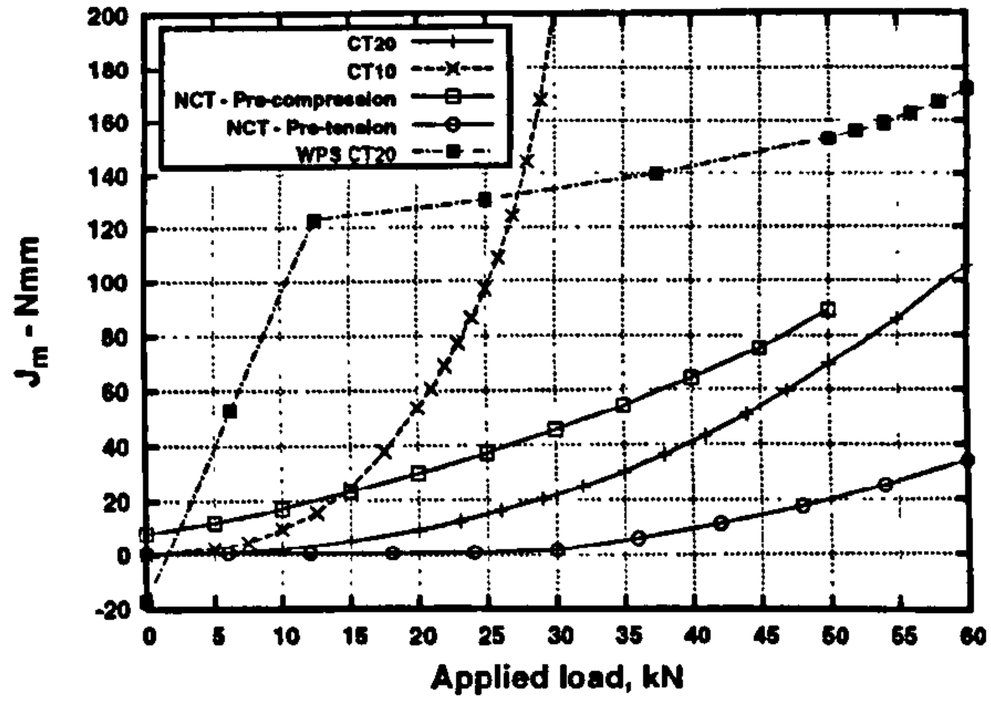

Figure 8.1: Variation of the J integral of equation 2.24 with applied load for CT and NCT data with varying load histories.

$$K = \sqrt{W} \int_0^a \sigma(x) m(a,x) dx \tag{8.3}$$

$$m(a,x) = \frac{1}{\sqrt{2\pi a}} \sum_{i=1}^{4} \beta(a_i)(1 - x/a)^{i-1.5} \tag{8.4}$$

Where β are constants for a given crack length. In this work, the variation in stress in the uncracked body $\sigma(x)$ was estimated from finite element analyses of the NCT geometry, as in figure 6.8. As the analysis presented here is two dimensional, the stresses at mid-thickness of the specimens were used in the calculation of K_{res}. The resulting residual stress intensity factors were 50.8 MPa.m$^{0.5}$ for the pre-compressed samples and -49.2 MPa.m$^{0.5}$ for samples with tensile preload. The effective stress intensity factor for the samples was then estimated to be

$$K_{eff} = K_I^e + K_{res} \tag{8.5}$$

where K_I^e is the applied, elastic stress intensity factor. It should be noted that this does not account for any relaxation of K_{res} due to yield upon reloading and as such, the effect of the preloading would be expected to be over-estimated. The resulting predictions are plotted in figure 8.4.

8.1.4 Displacement superposition

The model for prediction of the warm prestress effect proposed by Chell [46] is based on superposition of displacement states at different stages in the load

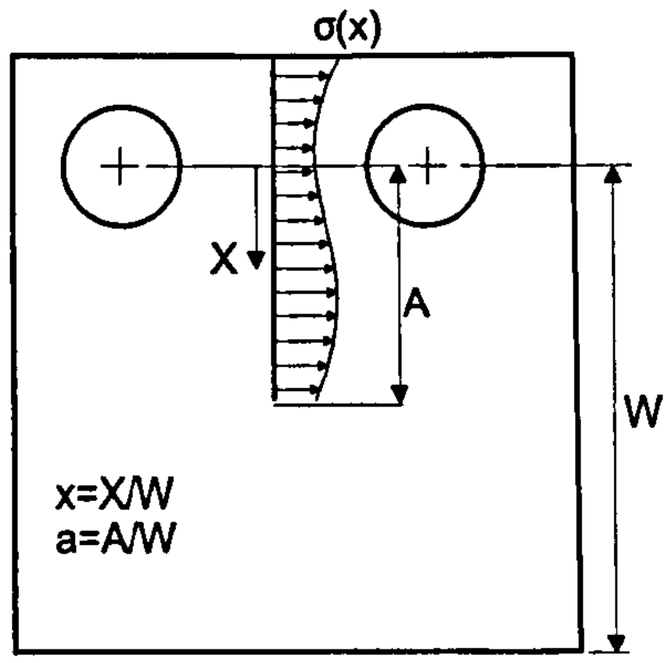

Figure 8.2: Nomenclature used for weight function calculation of K due to residual stress.

history. The relevant states for the LUCF cycle are preload, unload and reload. The model was applied to the CT20 specimens following warm prestressing using the method described in appendix B, also outlined in [150].

In brief terms, the stress intensity factor at fracture is a function of the preload SIF K_I, material K_{IC} and yield stresses at the preload and failure temperatures σ_{Y1} and σ_{Y2}

$$\frac{K_{IC}^2}{\sigma_{Y2}} = \frac{K_{IC}^2}{\sigma_{Y1}}(1 - f(R_1/R_2)) - \frac{K_1^2}{2\sigma_{Y1}}(1 - f(R_3/R_2)) + \frac{K_f^2}{\sigma_{Y1} + \sigma_{Y2}} \quad (8.6)$$

further detail is presented in appendix B. For a given K_I and K_{IC}, equation 8.6 can be solved numerically to find a single K_f for fracture. However, definition of K_{IC} as a single value is difficult in this case as fracture of the CT20 specimens showed considerable scatter. Therefore, K_f values were found assuming K_{IC} was equal to the minimum, maximum and mean values from the CT20 tests (47.6 MPa.m$^{0.5}$, 104.13 MPa.m$^{0.5}$ and 78.31 MPa.m$^{0.5}$ - table 5.2). This resulted in a range of K_f from 123.5-139 MPa.m$^{0.5}$. Polynomial interpolation was then used to calculate the variation in K_f values following preloading with the fracture SIF in the AR state. This relationship was used with equation 4.3 to produce a probabilistic prediction of fracture for LUCF loading. In addition, direct calculation of K_J based on J_m was employed to characterise fracture following the LUCF load cycle. All results, along with those for the CT10 specimens, are shown in figure 8.3.

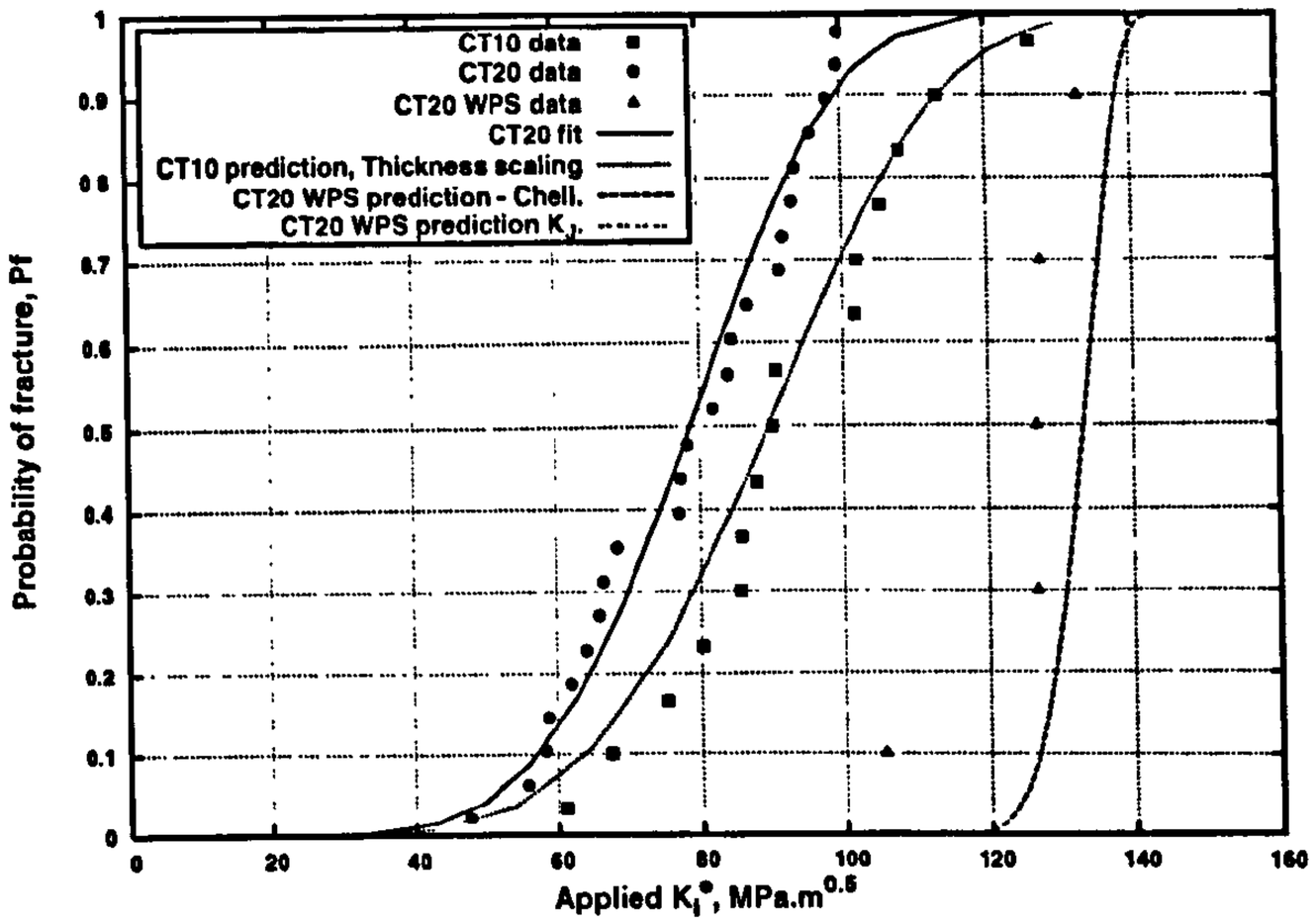

Figure 8.3: Prediction of CT10 specimen fracture and WPS CT20 fracture, based on stress intensity factor methods.

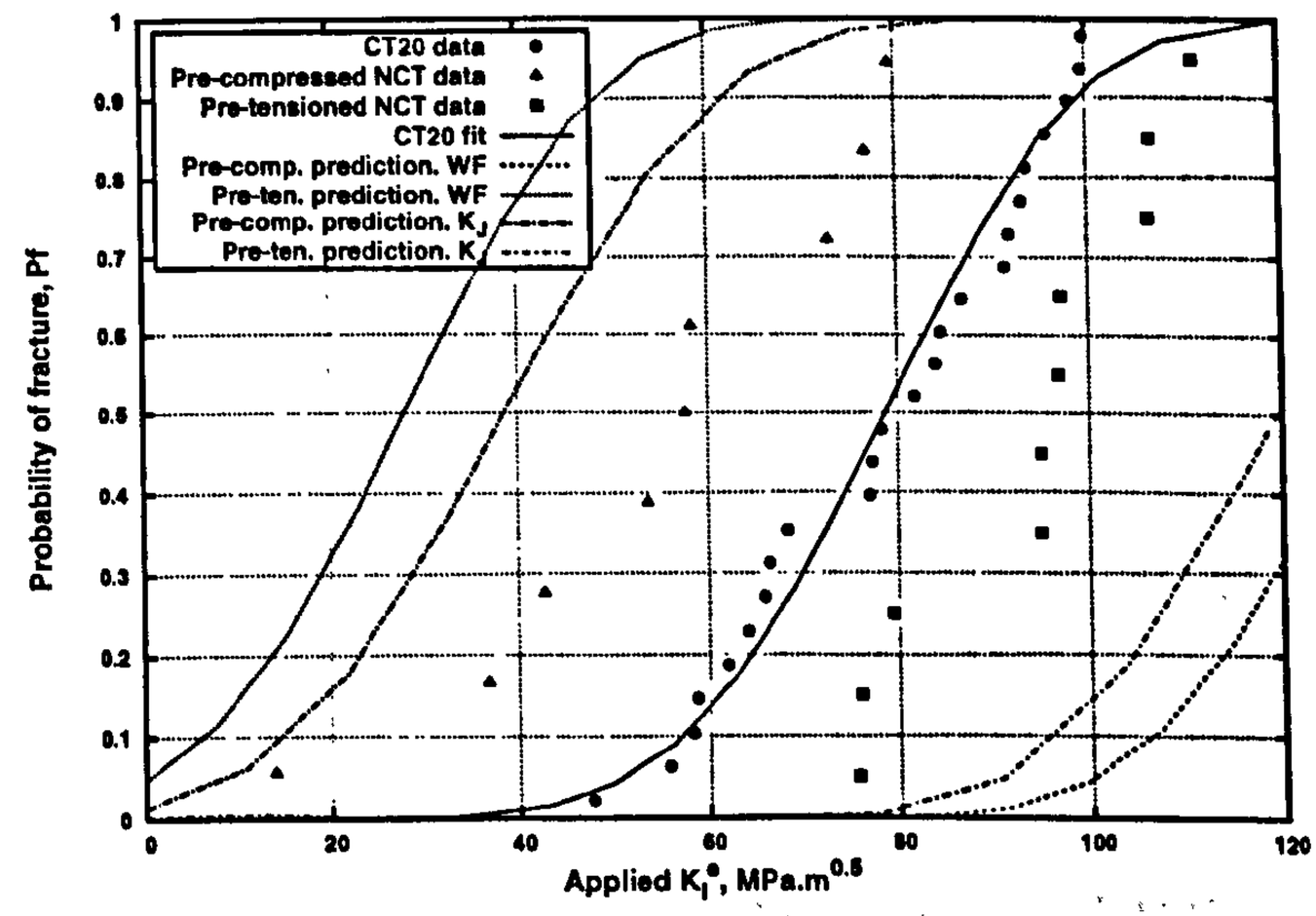

Figure 8.4: NCT specimen fracture, based on weight function analysis of residual stress effect.

8.2 Local approach predictions of fracture

Fracture predictions using the local approach were performed with model constants calibrated to the CT20 and RNB90 data, using the R^2_{Pf} maximisation approach. This method and the resulting constants m and σ_0 are detailed in chapter 7. Predictions are displayed based on the Beremin model, as well as the incremental strain formulation with zero and non-zero threshold.

The fit agreement with the CT20 and RNB90 data is presented in figures 8.5 and 8.6. Predictions of the remaining specimens in the AR state (RNB45, RNB60 and CT10) are plotted in figures 8.7-8.9. Predictions of the prestrained CT specimen tests are shown in figure 8.10. The warm prestressed CT specimen tests are predicted in figure 8.11 and the notched CT samples in figures 8.12 and 8.13.

Agreement with the calibration data (figures 8.5 and 8.6) is reasonable for all models, although there is a notable change in the shape of the predicted curves between the Beremin and strain based models. It is immediately apparent that prediction of failure in the AR state is reasonable for most specimens, with the notable exception of the CT10 specimens where the Beremin model is unable to reproduce the experimental data at higher loads. The Beremin model also appears to over-estimate fracture probability at low loads for the RNB45 and RNB60 data

The predictions following load history are noticeably poorer. For the prestrained CT data, there is effectively no predicted effect for 1% prestrain. The agreement for the 3% and 5% cases are reasonable, however. For the LUCF cycle, figure 8.11 shows that an increase in fracture load is correctly predicted by all the models used, although the overall nature of the predictions is conservative.

For both NCT specimens, where preloading is applied to the uncracked body, the effect of the load history is slightly over-estimated in both cases. This is of particular concern for the case of tensile preload where the predictions are non-conservative.

8.3 Implications for structural integrity assessment

In determining safe operating loads, predictive tools are most often applied in the context of structural integrity assessment codes. The guidelines and procedures in such codes are usually the result of extensive analytical and ex-

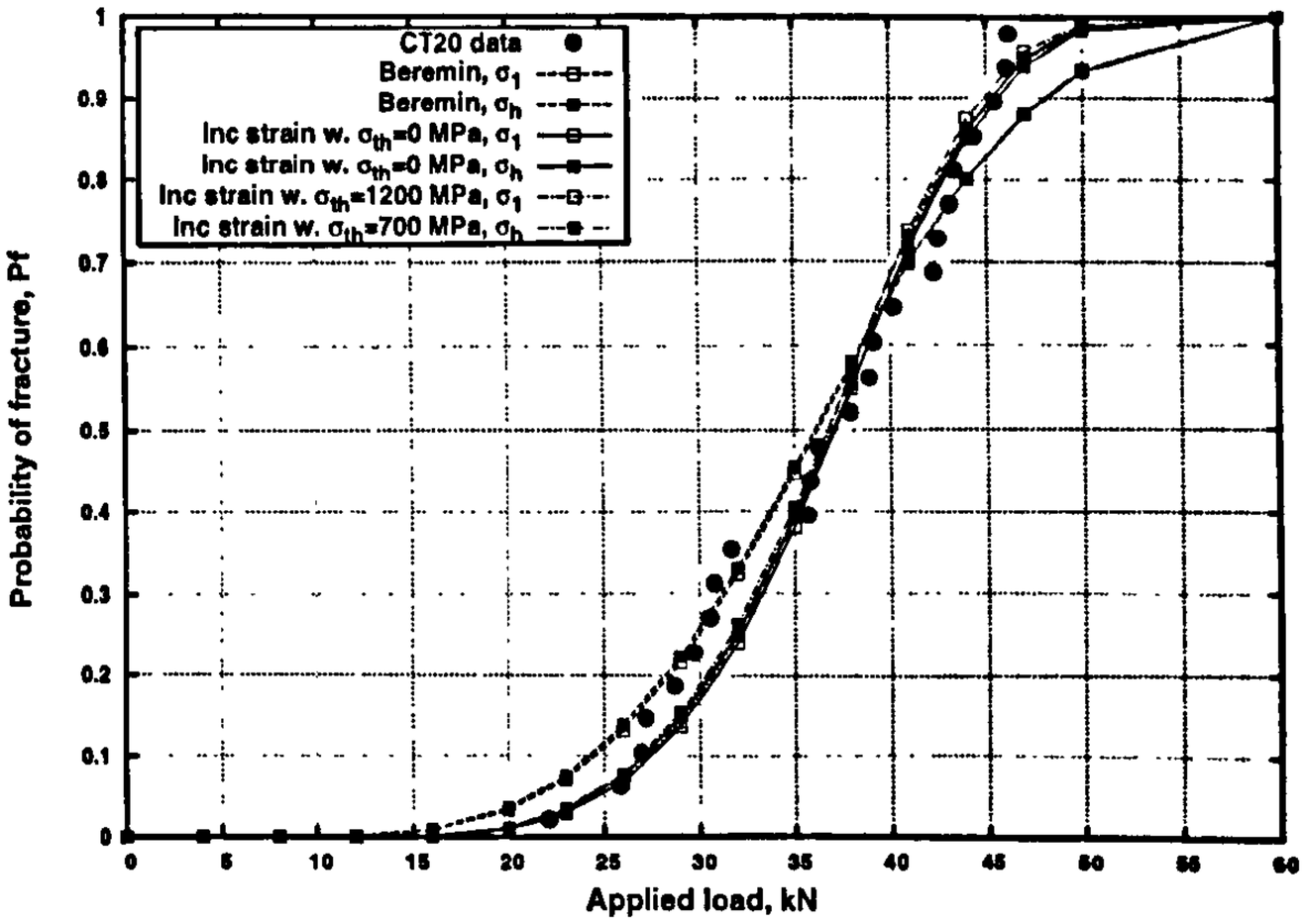

Figure 8.5: Prediction of CT20 specimen failure from local approach models.

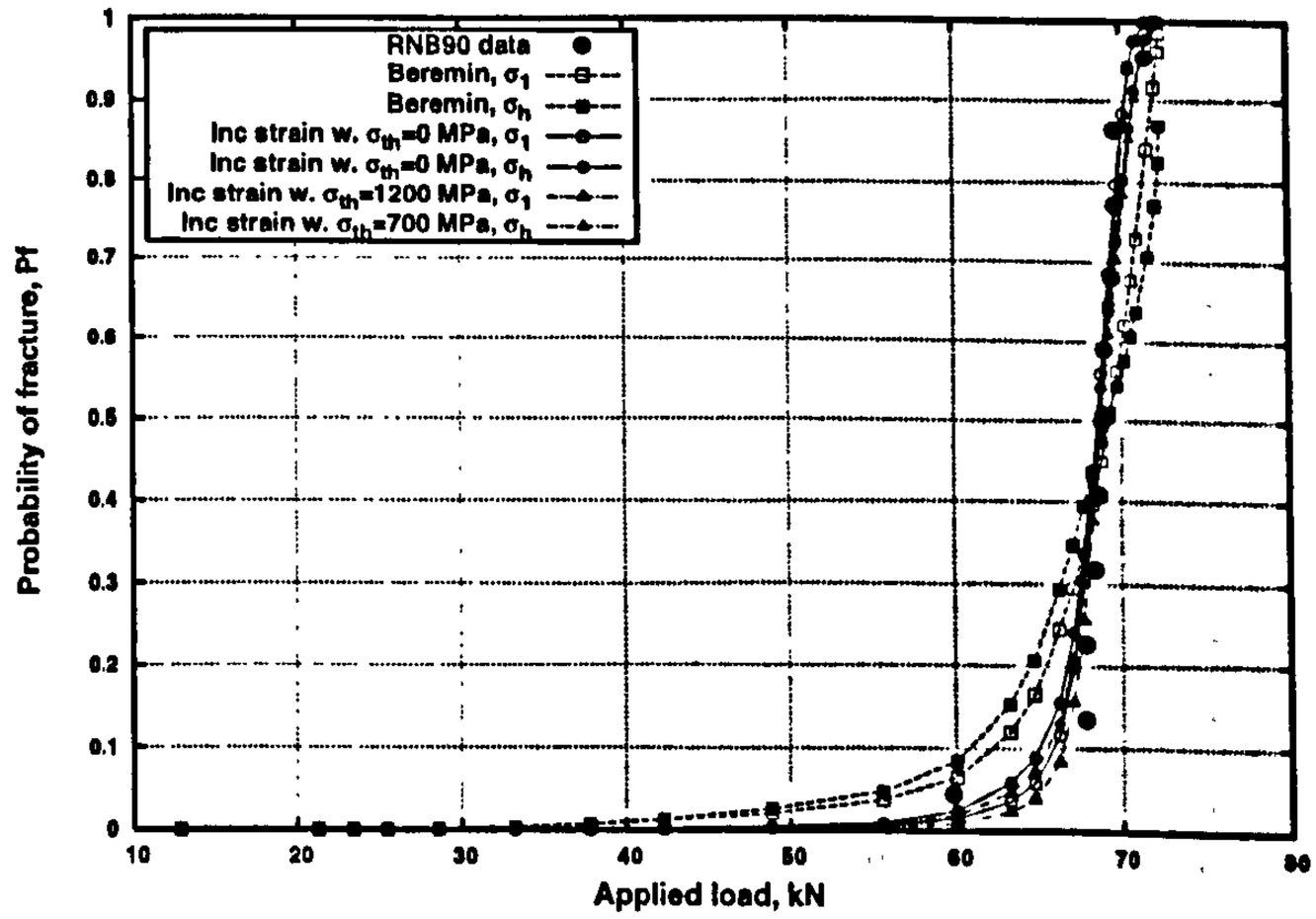

Figure 8.6: Prediction of RNB90 specimen failure from local approach models.

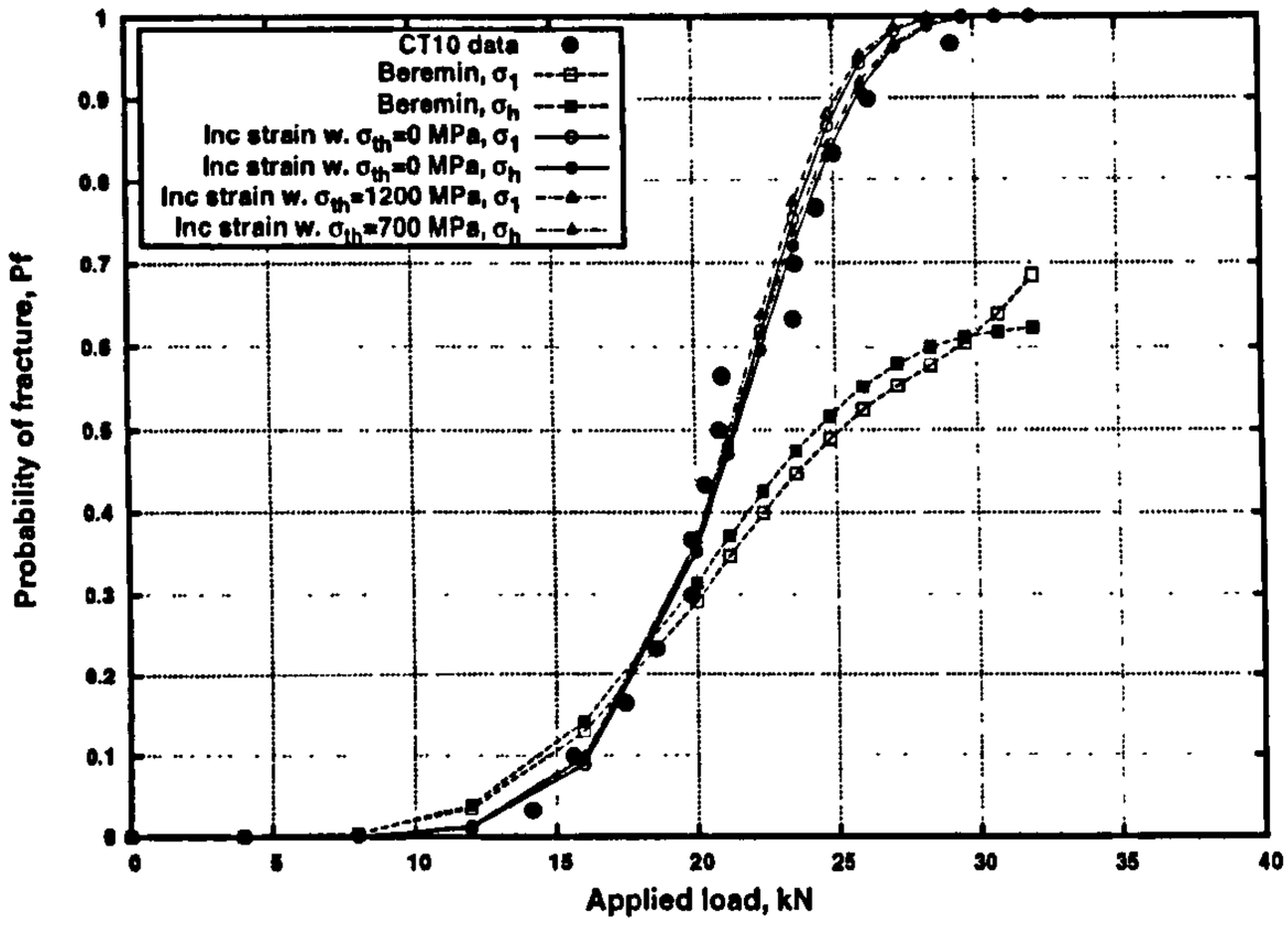

Figure 8.7: Prediction of CT10 specimen failure from local approach models.

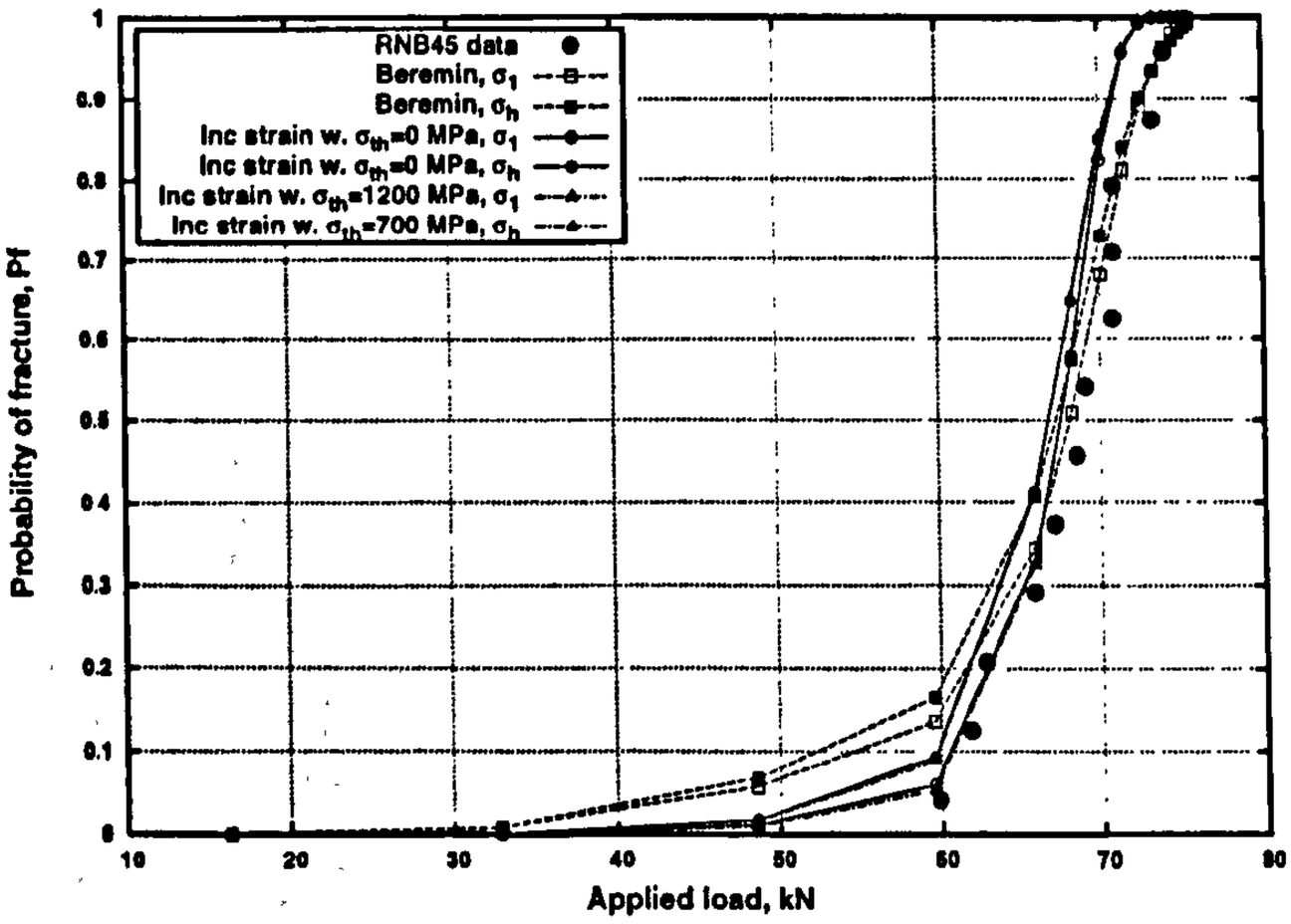

Figure 8.8: Prediction of RNB45 specimen failure from local approach models.

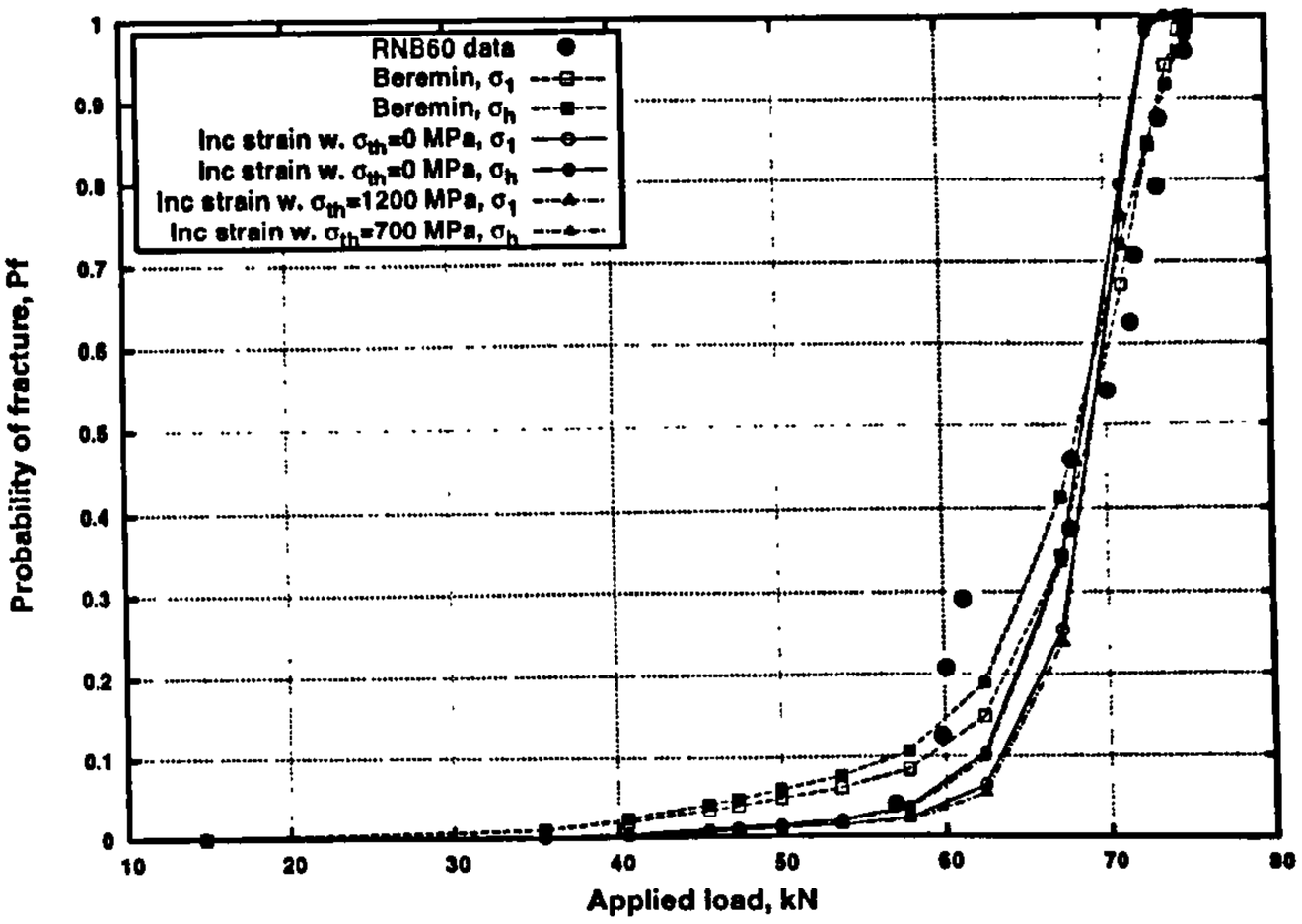

Figure 8.9: Prediction of RNB60 specimen failure from local approach models.

perimental review. To ensure safety, the guidelines in such documents are generally weighted strongly towards conservatism, aiming to form a lower bound for failure as seen, for example, in [108].

Rigorous review and validation of new failure criteria is required before regulatory authorities permit their use in safety assessments. Consequentially, and necessarily, the methods used in SI codes are some years behind the most recent developments in fracture modelling and tend to be largely based on K theory.

To examine the potential benefits of more complex local approach analyses on safety assessments, the predictive methods discussed in section 8.2 were interpreted using the R6 [107] structural integrity assessment code.

The R6 procedure is based on the use of a failure assessment diagram (FAD). A failure envelope is described in terms of two parameters, K_r and L_r, describing a structure's proximity to failure by fracture and plastic collapse respectively. The proximity to plastic failure is given by

$$L_r = \frac{F}{F_y} \tag{8.7}$$

where F is the applied load and F_y the load corresponding to general yielding of the structure. The fracture parameter K_r is determined from the ratio of

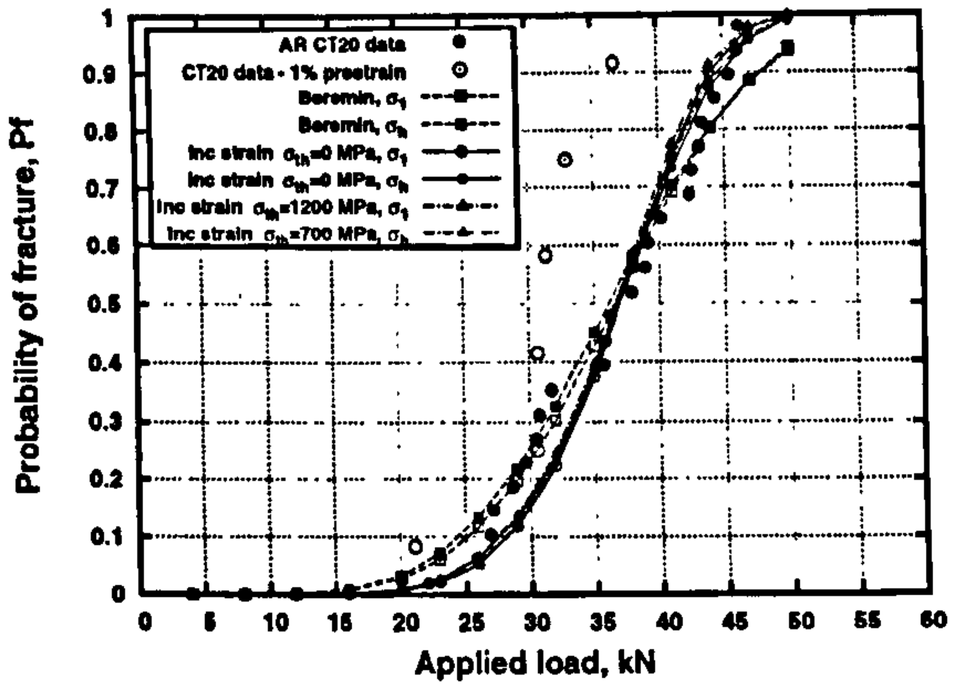

(a) 1% Prestrain

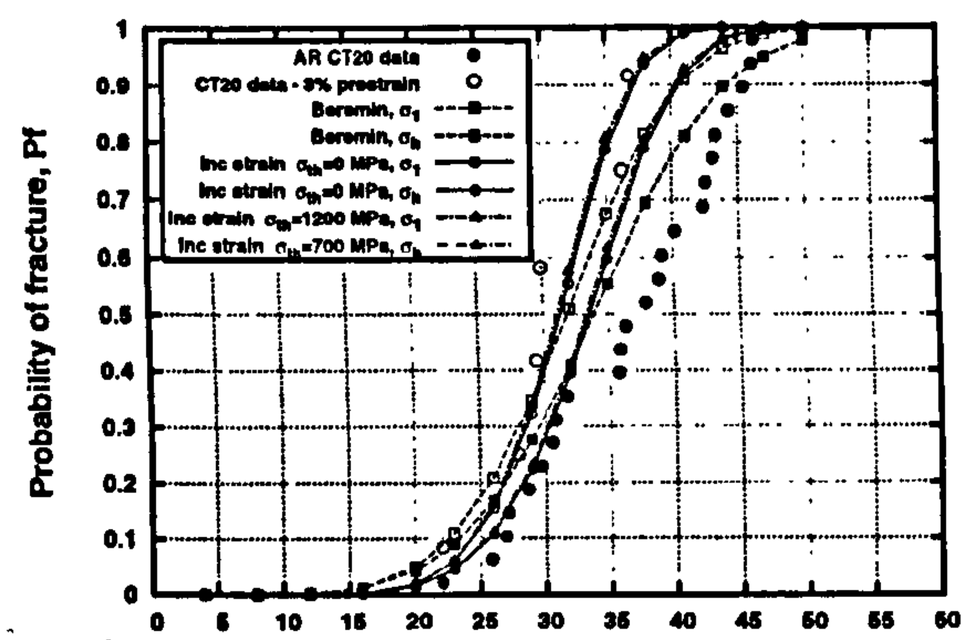

(b) 3% Prestrain

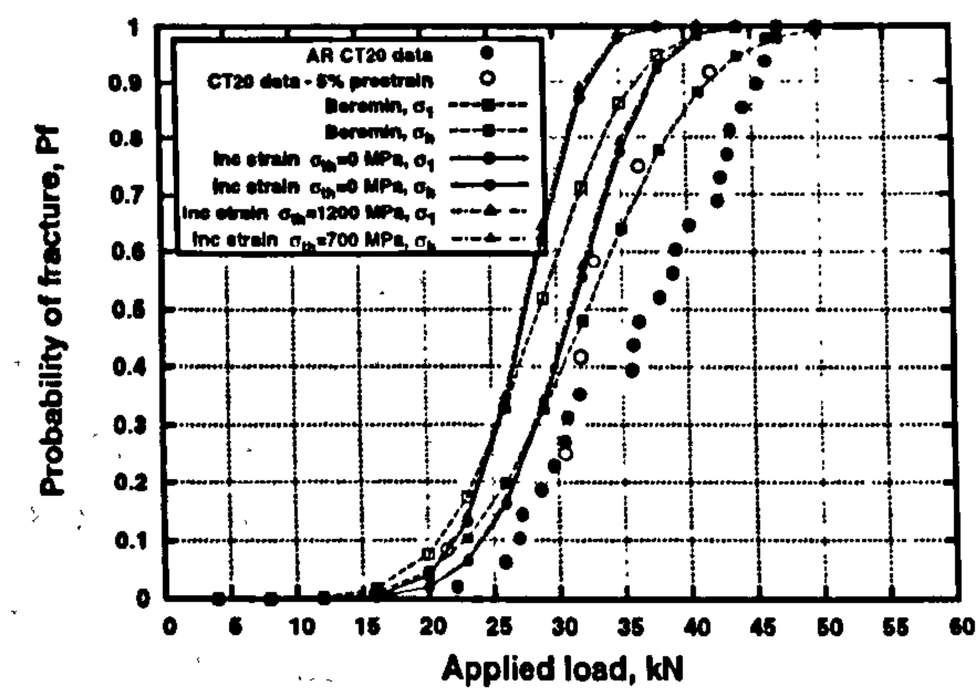

(c) 5% Prestrain

Figure 8.10: Prediction of prestrain effect on CT20 specimen failure, using local approach methods.

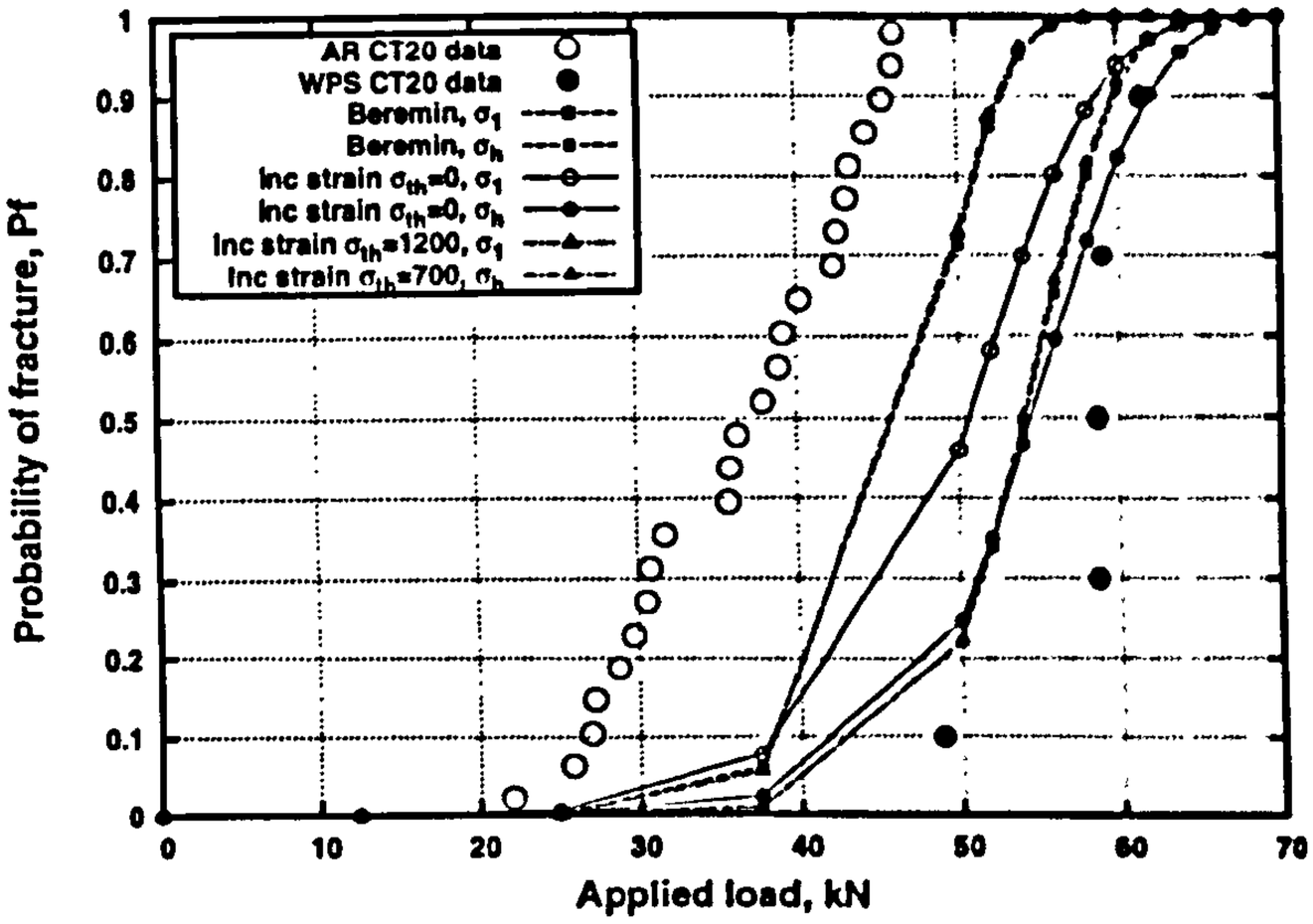

(a) Isotropic hardening

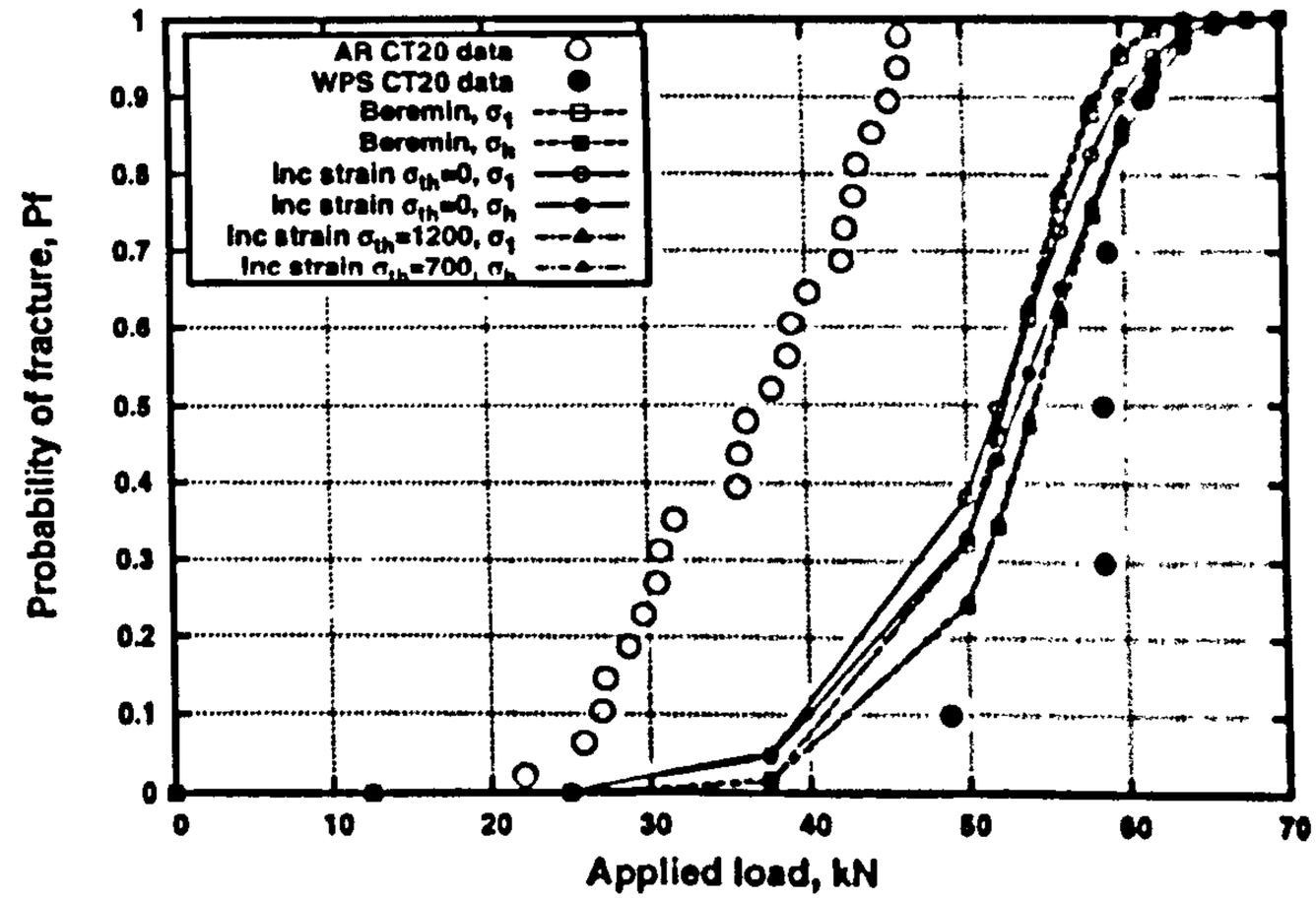

(b) Kinematic hardening

Figure 8.11: Prediction of CT20 specimen failure, following LUCF load cycle, from local approach models.

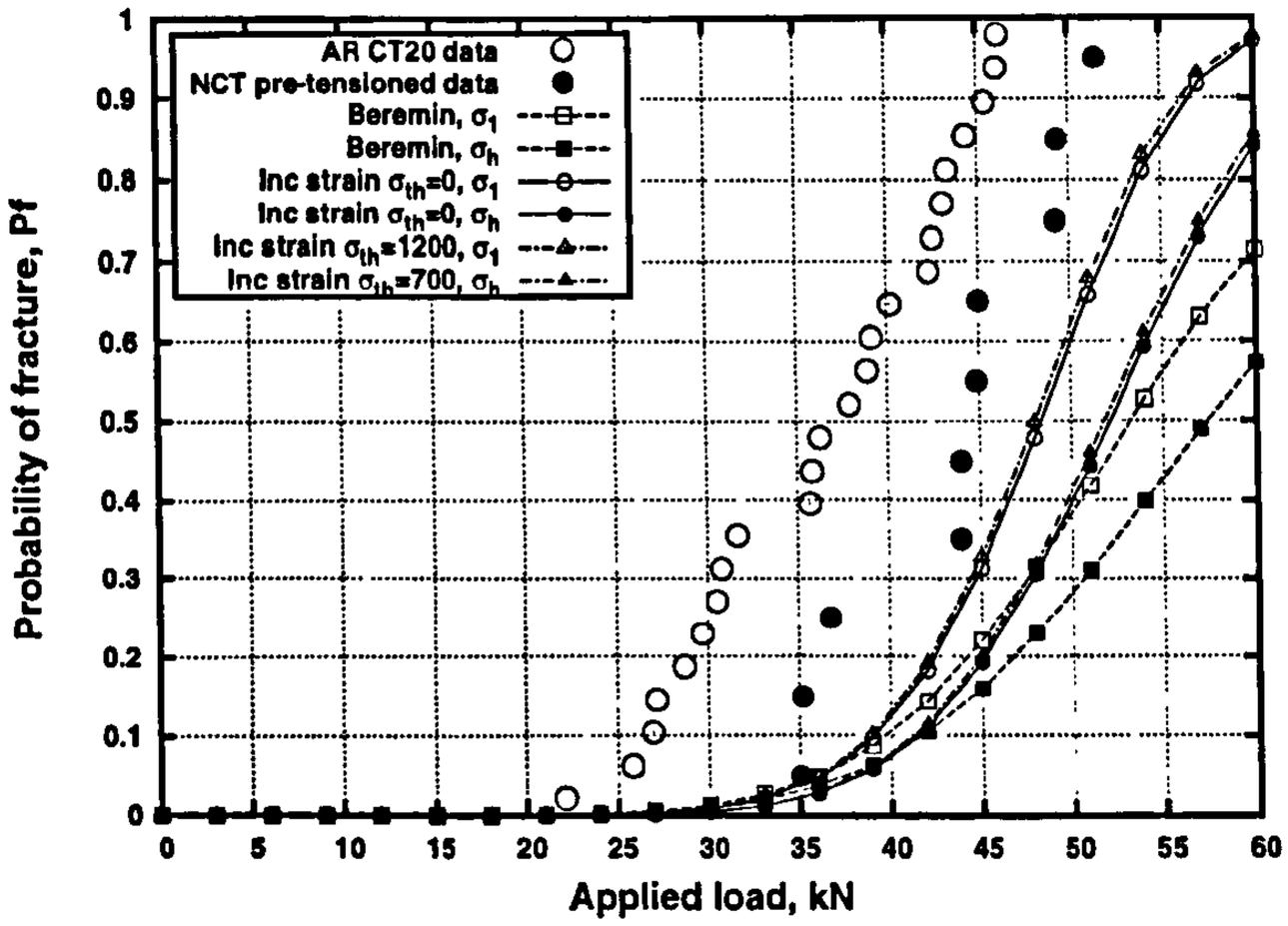

(a) Isotropic hardening

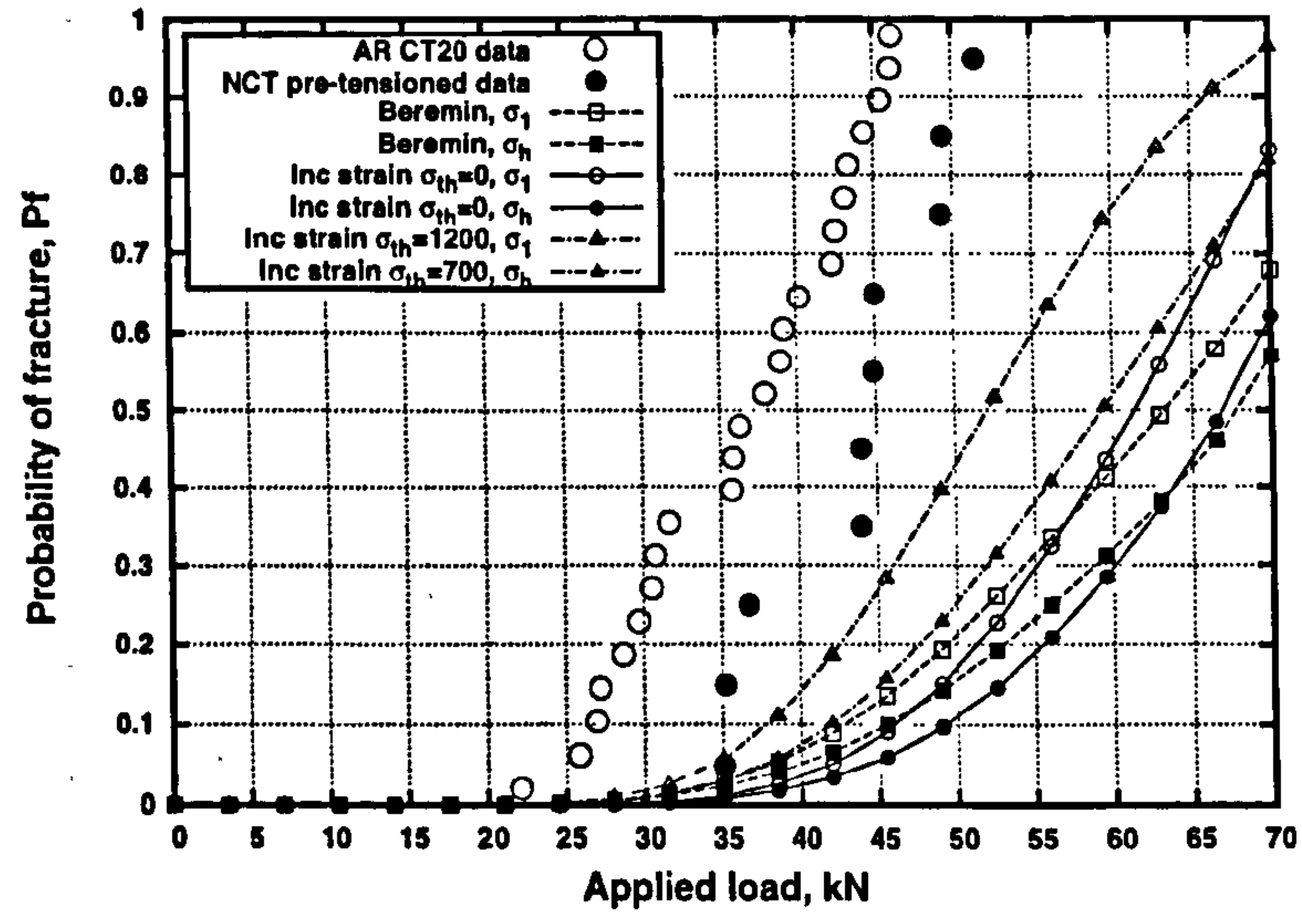

(b) Kinematic hardening

Figure 8.12: Prediction of NCT specimen failure, following tensile preload, from local approach models.

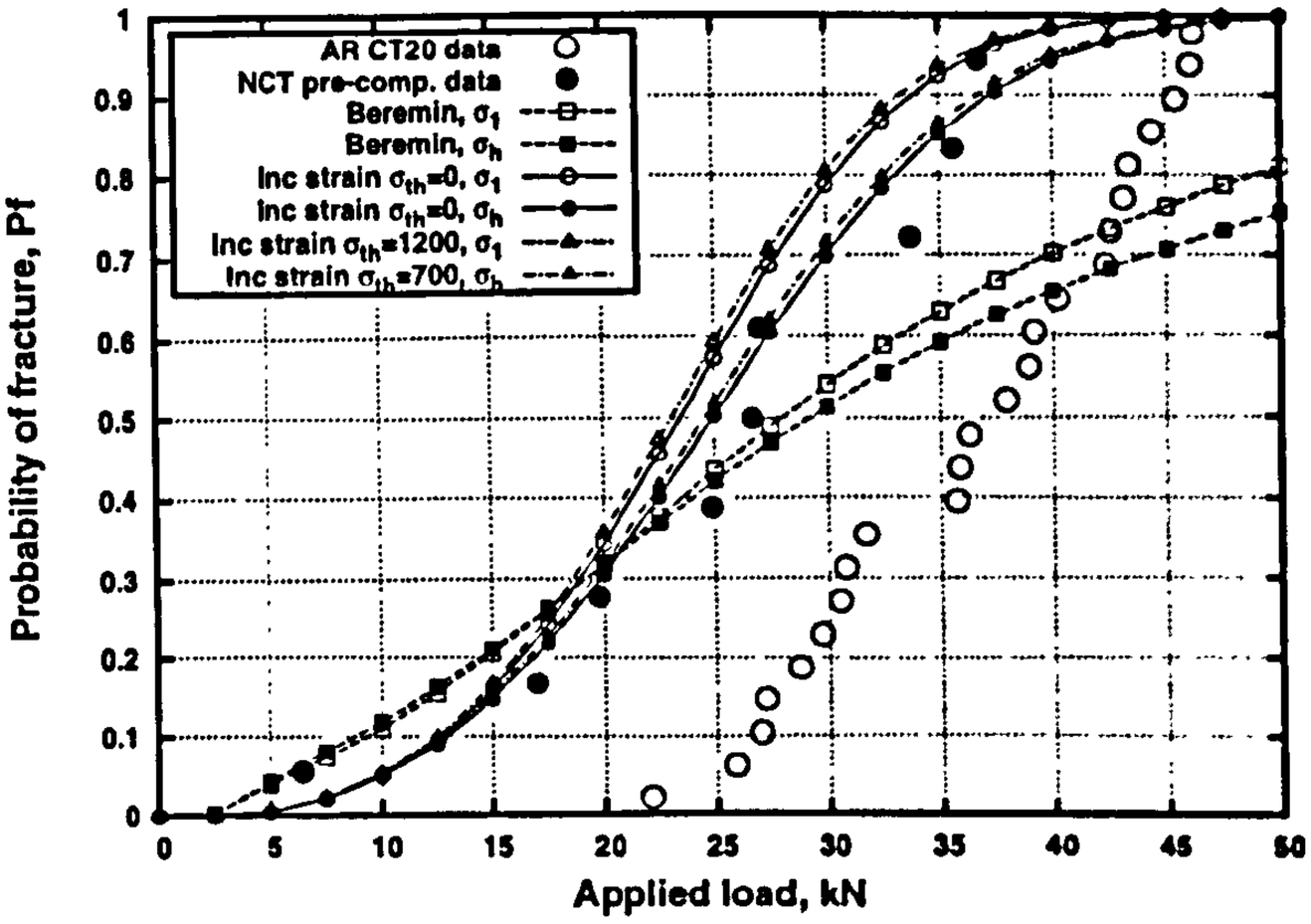

(a) Isotropic hardening

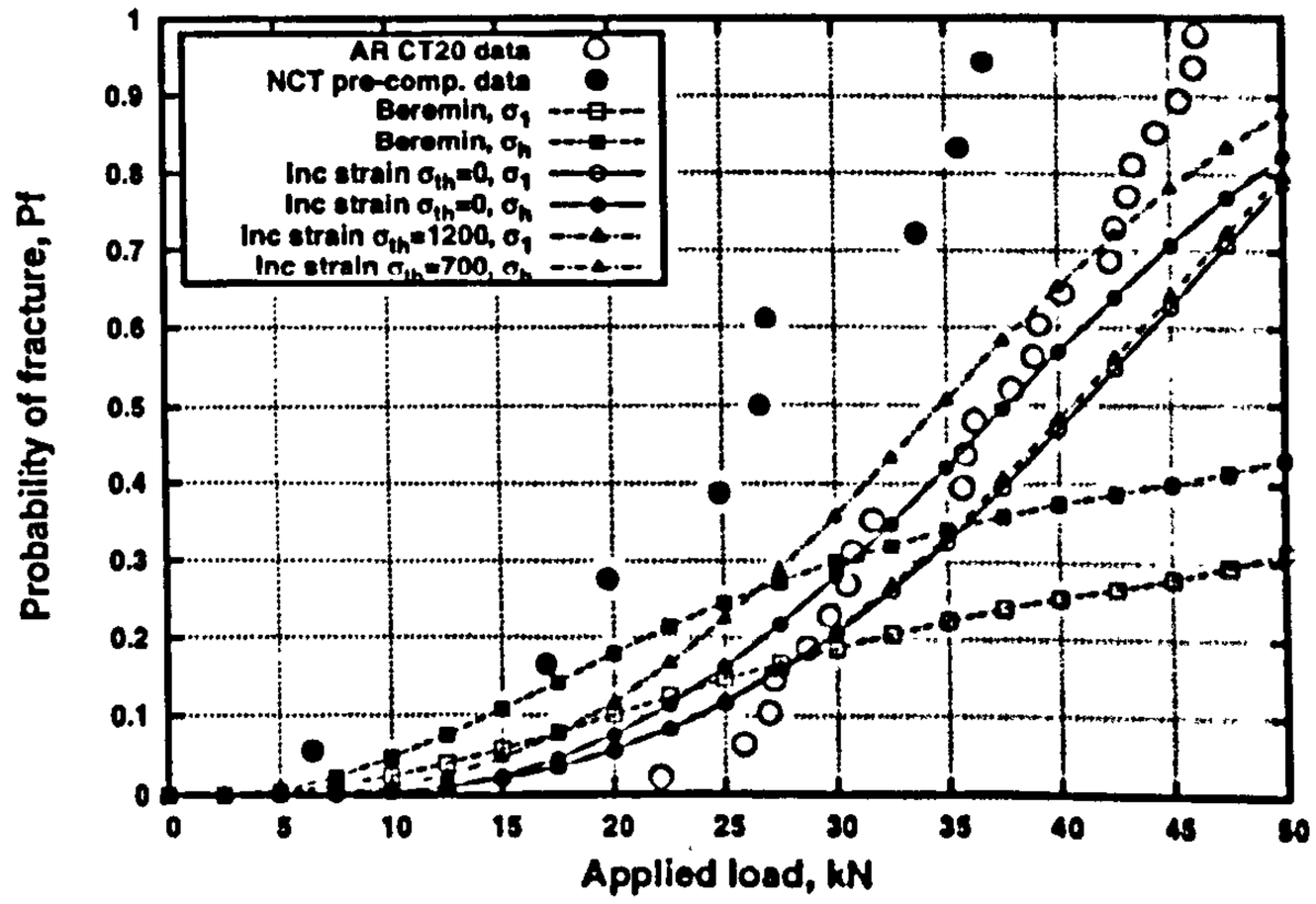

(b) Kinematic hardening

Figure 8.13: Prediction of NCT specimen failure, following compressive preload, from local approach models.

the applied K to the material fracture toughness parameter, referred to in the R6 code as K_{mat}. In the presence of residual stress, K is decomposed into those due to primary (K_I^p) and secondary (K_I^s) stresses

$$K_r = \frac{K_I^p + K_I^s + \rho}{K_{mat}} \tag{8.8}$$

where ρ is a correction factor to allow for plasticity. An alternative definition for plasticity correction is also available, replacing ρ with a multiplication term V i.e. $K_I^s + \rho$ becomes VK_I^s. In determining primary and secondary stress intensity factors, [107] defines primary stresses as those contributing to plastic collapse and secondary stresses as those which do not. In this case, residual stresses due to load history were considered as secondary stresses, all other loadings were assigned as primary stresses.

A failure envelope in terms of K_r and L_r is given in general terms as

$$K_r \geq \left[1 + 0.5L_r^2\right]^{-1/2} \left[0.3 + 0.7\exp\left(-0.6L_r^6\right)\right] \tag{8.9}$$

Equation 8.9 is independent of geometry and material and is termed the 'Option 1' curve in [107]. An alternative material and geometry specific curve ('Option 3' in [107]) is

$$K_r \geq \left(\frac{J_e}{J_{pl}}\right)^{1/2} \tag{8.10}$$

where J_e and J_{pl} are J integral values from elastic and elastic-plastic analyses.

As the R6 procedure is formulated for analysis of cracked structures it was not applicable to the RNB geometries. Instead, the method was used to predict failure of the CT10, WPS CT20, and NCT specimens. Limit load values for calculation of L_r were found using the analytical solutions for CT geometries in [107],

$$F_y = WB\sigma_Y \frac{2a}{\sqrt{3}W}\left[\sqrt{2.702 + 4.599\left(\frac{a}{W}\right)^2} - \left(1 + 1.702\frac{a}{W}\right)\right] \tag{8.11}$$

where a, W, B and P are as defined for equation 5.1 and σ_Y is the material yield stress. For A533B steel at -150°C, F_y=94.7kN for CT20 data and 47.4kN for CT10 data. To obtain estimates for safe loads for these cases, K_{mat} was

taken as 5% lower bound from the measured values, determined as

$$K_{mat,5\%} = \bar{K}_{mat} - t_5 S_K \tag{8.12}$$

where $\bar{K}_{mat}$ is the mean value obtained from experiment, S_K is the standard deviation of these values and t_5 is the value of the Student distribution for a 5% level of significance. The appropriate degree of freedom for the Student distribution is $N-1$ where N is the number of K_I values used to determine K_{mat}. The resulting value of $K_{mat,5\%}$ was found to be 51.08 MPa.m$^{0.5}$ based on a mean value of 78.3 MPa.m$^{0.5}$. A similar method was employed, using fracture loads in equation 8.12, to produce a lower bound estimate for the fracture load, $L_{r,5\%}$, for each data set.

8.3.1 K based analyses

Predictions of fracture based on K were applied to the CT10 specimens using equation 8.1 to correct for thickness relative to the CT20 specimens. Corrected K values were then normalised by $K_{mat,5\%}$ to produce K_r. This procedure was applied to K values from elastic analyses as well as K_J values from elastic-plastic analyses. As a baseline comparison, a prediction based on uncorrected K_J values is also plotted on the FAD (figure 8.15).

To obtain K_r values for the NCT specimens, the weight function method of section 8.1.3 was used to determine K_I^s, based on FE stresses using isotropic hardening. The plasticity correction factor ρ was calculated as described in [107],

$$\rho = 0.1x^{0.714} - .007x^2 + .00003x^5, \quad x = \frac{K_I^s}{K_I^p/L_r} \tag{8.13}$$

yielding values of $\rho = 0.038$ for the pre-compressed specimens (K_I^s =50.8 MPa.m$^{0.5}$). For the specimens with tensile preload, as $K_I^s < 0$, the R6 procedure requires that $\rho = 0$ or $V = 1$. In addition to the approach based on elastic K values, K_r was also determined from K_J, based on J_m values accounting for primary and secondary stresses. The FAD plots for the NCT data are presented in figures 8.19 and 8.20.

For the prestrained CT data, variation of K_I^s with load is unchanged from the AR state. Values of J and therefore K_J also displayed essentially no effect of prestrain. In terms of the R6 assessment, the limit load for the CT specimens is altered by the prestrain process due to a change in yield stress.

The altered F_y values following 1%, 3% and 5% strain were 90.2kN, 96.64kN and 105.65kN.

For the WPS CT20 data, K_r values were obtained using the method of Chell, as discussed in section 8.1.4. The relationship between K_I, the AR fracture SIF and K_f, the fracture SIF after preloading was determined from equation 8.6 (figure 8.16 (a)). Inverting this relationship allows the apparent applied K_I (equivalent to K_f) to be related to the effective SIF K_{eff} - i.e. that describing proximity to failure (figure 8.16 (b)). From this, the applied load can easily be related to K_{eff} using the analytical relationship between K_I^{el} and applied load (figure 8.16 (c)). This is easily converted to the $L_r vs K_r$ relationship as plotted in figure 8.18. In addition K_r was also calculated from K_J, based on J_m from isotropic FE analyses, such that $K_r = K_J/K_{mat,5\%}$.

8.3.2 Local approach analyses

To make use of local approach models in the R6 procedure, it was necessary to express the values of σ_w or Pf in terms of stress intensity factor, such that predictions could be interpreted in the context of the failure assessment diagram. It was assumed that the appropriate reference measure was K_{IC}, i.e. plane strain fracture toughness. A number of scaling approaches have been suggested, using Weibull stress to describe changes in J or K at failure, [155, 156].

In [156] it is suggested

$$\sigma_w^m = CBJ_{av}^2 g(b\sigma_Y/J_{av}) \tag{8.14}$$

where C is a material constant, B the crack front length and J_{av} the through-thickness averaged value of J. The function g describes loss of constraint in terms of b the uncracked ligament length, the yield stress σ_Y and J_{av}. Under small scale yielding conditions $g = 1$ such that J^2 is a linear function of σ_w^m.

Probabilistic models may also be employed, assuming that under small scale yielding conditions,

$$Pf = 1 - \exp\left(-\left(\frac{\sigma_w}{\sigma_0}\right)^m\right) = 1 - \exp\left(-\left(\frac{K - K_{min}}{K_0 - K_{min}}\right)^4\right) \tag{8.15}$$

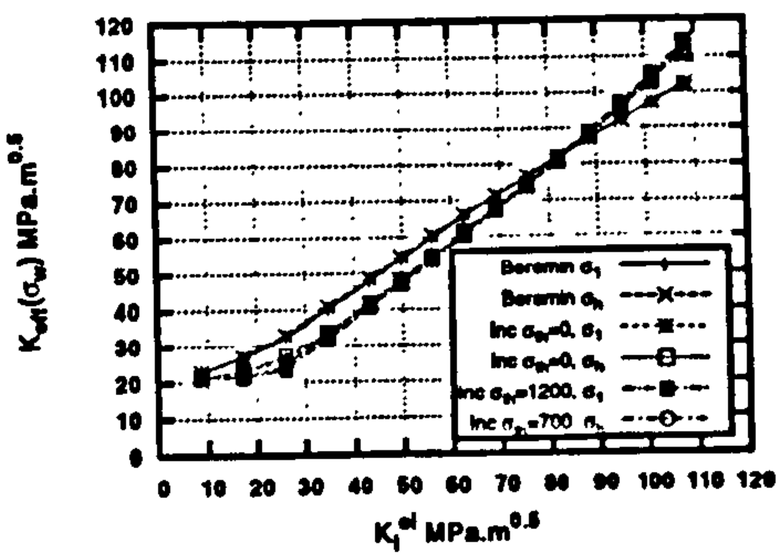

(a) Equation 8.16

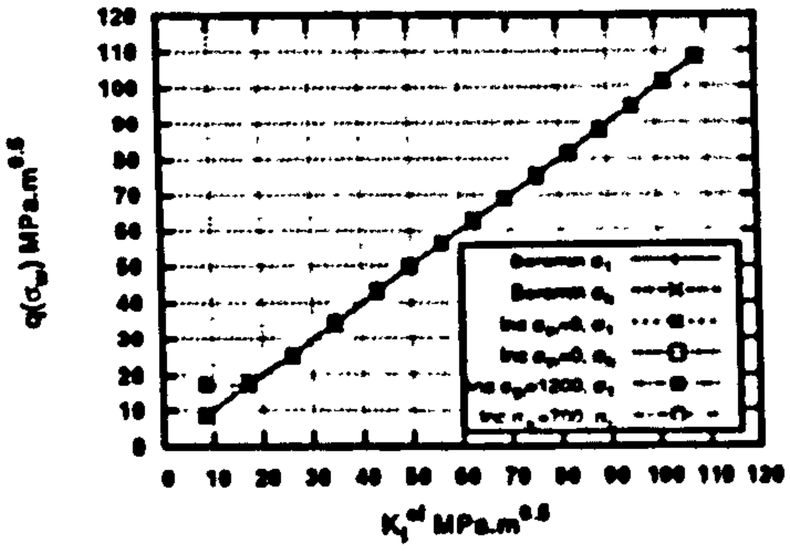

(b) Equation 8.17

Figure 8.14: Functions describing variation of equivalent elastic K with σ_w.

Under general conditions, an effective K may then be expressed as.

$$K_{eff} = \left(\frac{\sigma_w}{\sigma_0}\right)^{m/4} (K_0 - K_{min}) + K_{min} \tag{8.16}$$

Alternatively the increase in σ_w with applied elastic K_I may be calculated for cases of small scale yielding. The resulting relationship

$$K_I^{el} = q(\sigma_w) \tag{8.17}$$

may then be applied to other geometries to calculate the effective small scale yielding value of K. The function q was calculated in this case based on finite element analyses of the CT20 specimens. As this data set was used to determine K_{mat}, used in the R6 analysis, using this data as a benchmark for q was deemed appropriate. The function q was calculated separately for the varying definitions of σ_w used. The relationships according to equations 8.16 and 8.17 are plotted in figure 8.14. In this case, cubic polynomial functions were used to describe q. It can be seen that the results are broadly similar, excepting equation 8.16 based on the Beremin model (figure 8.14 (a)). This suggests that inclusion of strain in the local approach improves agreement between probabilistic models of CT20 failure based on K and σ_w.

The calculated q functions were used to estimate K_{eff} and therefore $K_r = K_{eff}/K_{mat,5\%}$ for all applicable data. The resulting R6 analyses are plotted in figures 8.15-8.20.

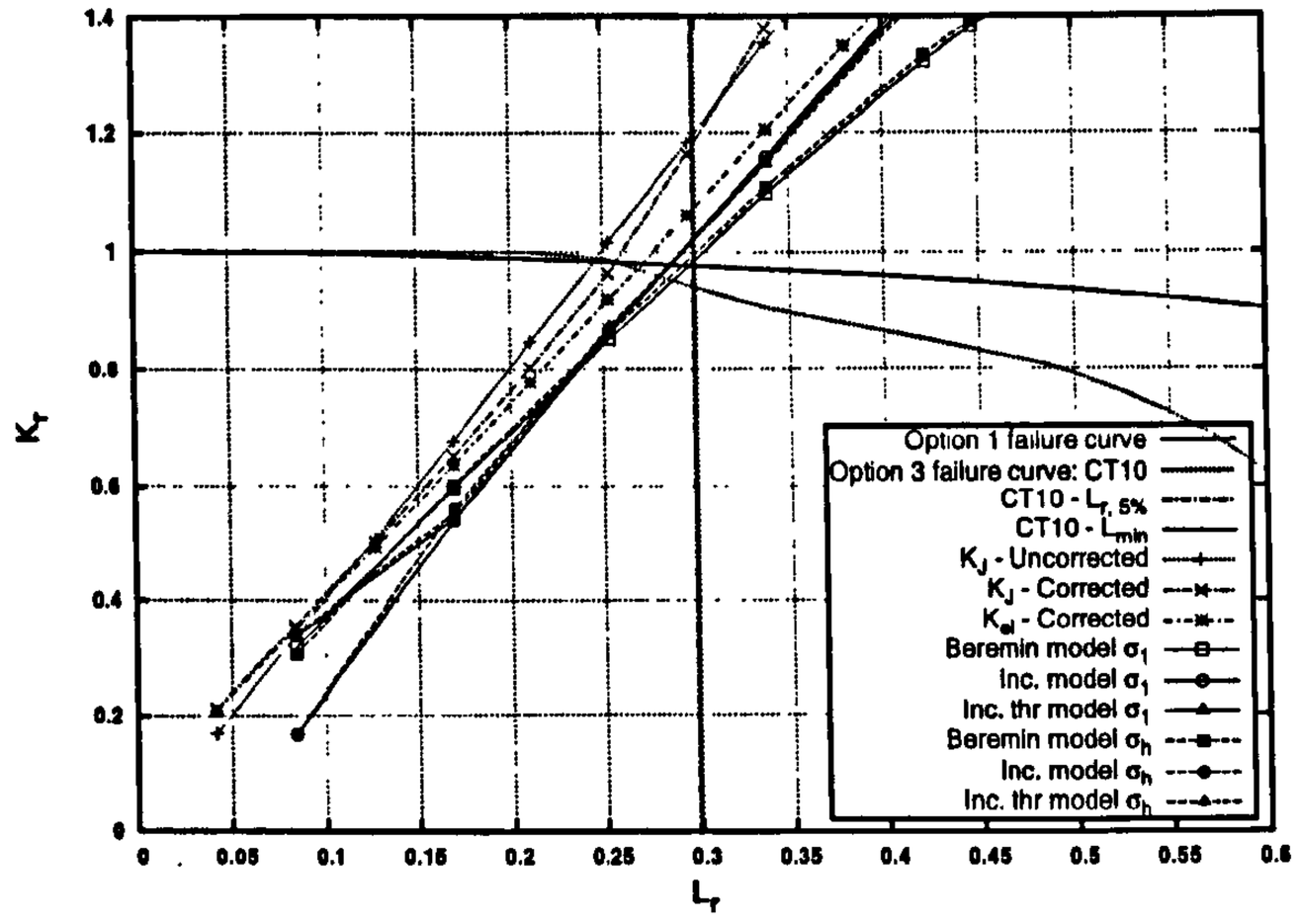

Figure 8.15: Prediction of safe load for CT10 data, based on R6 assessment failure assessment diagram.

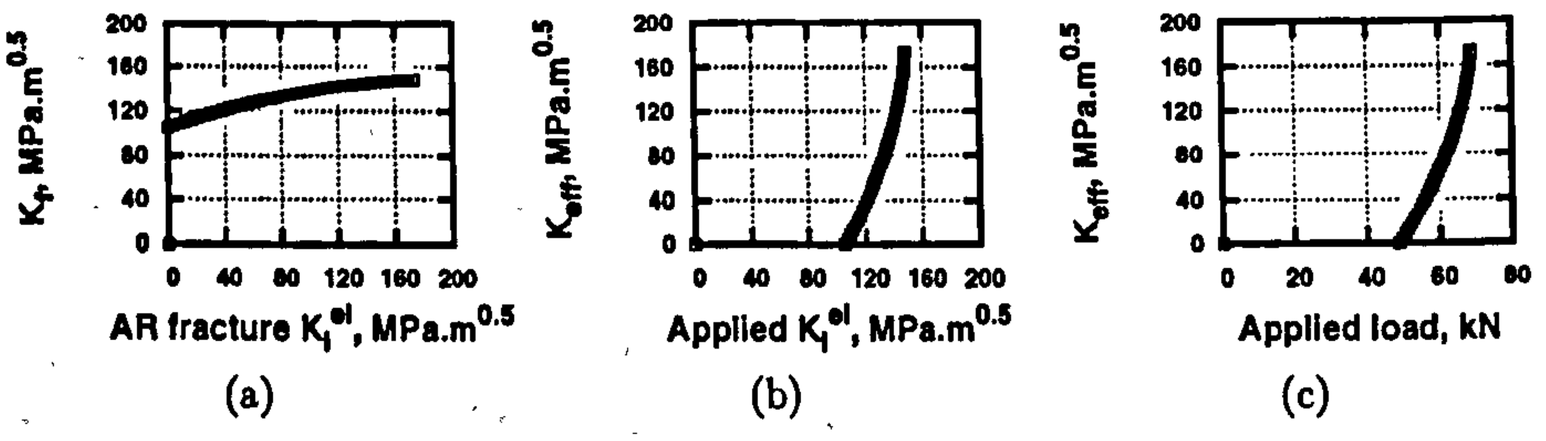

Figure 8.16: Determination of variation of effective stress intensity factor with load for WPS CT20 specimens.

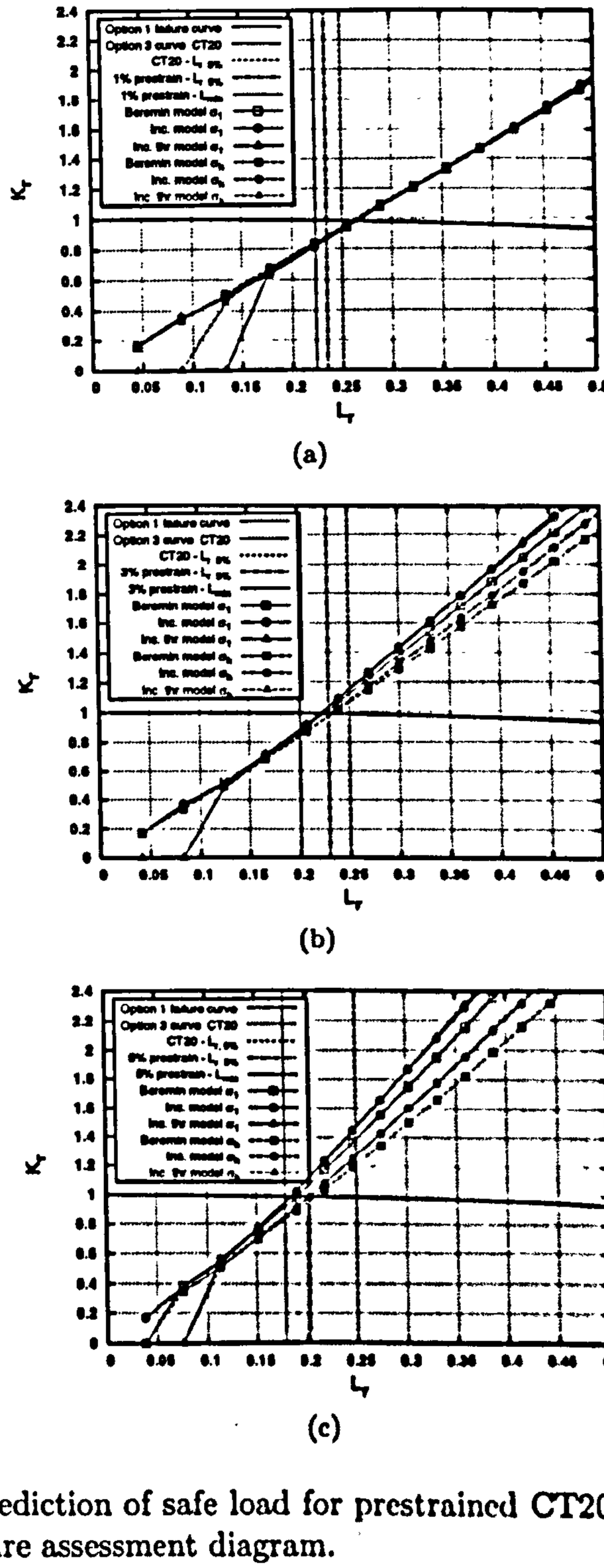

Figure 8.17: Prediction of safe load for prestrained CT20 data, based on R6 assessment failure assessment diagram.

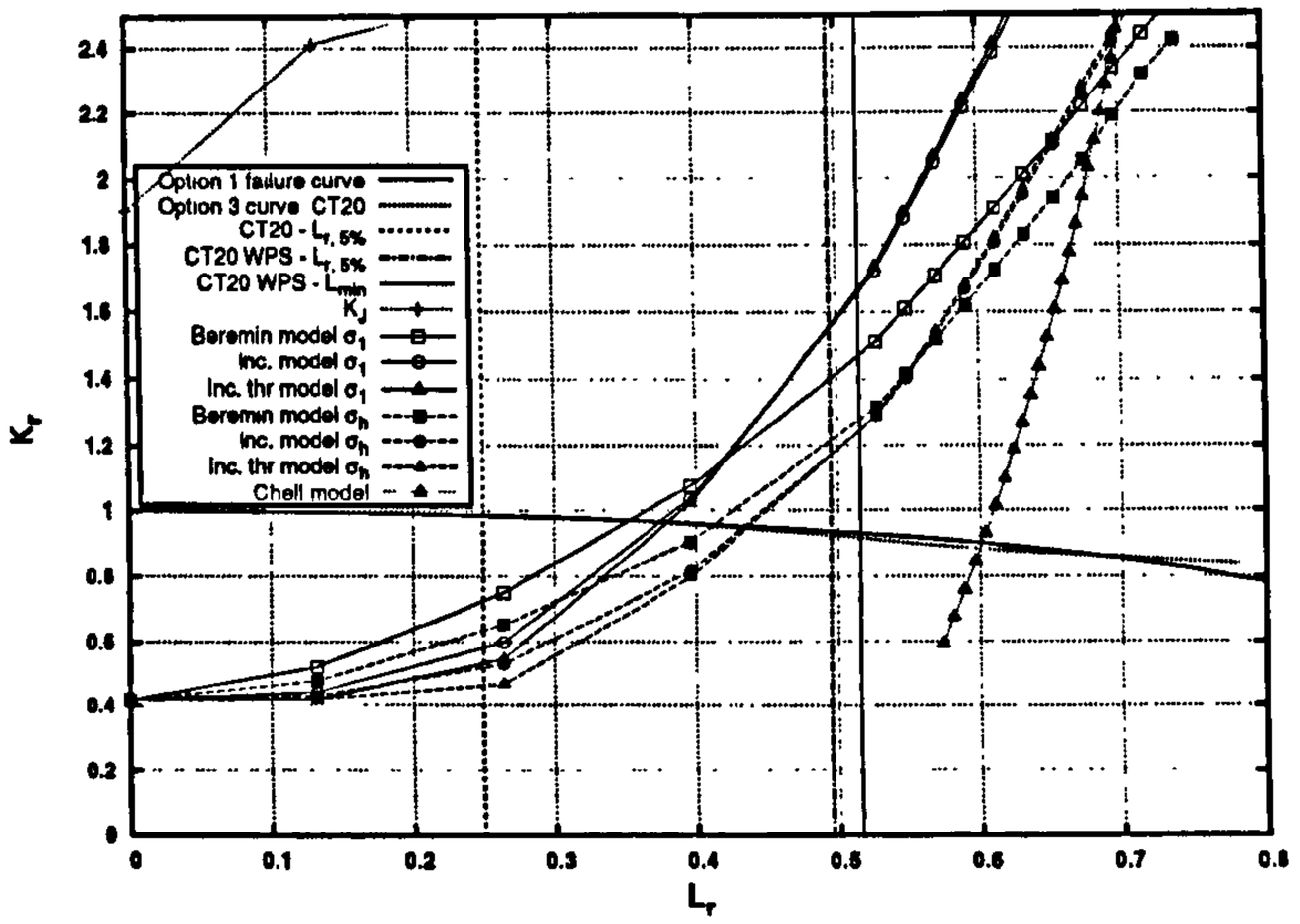

Figure 8.18: Prediction of safe load for WPS CT20 data, based on R6 assessment failure assessment diagram.

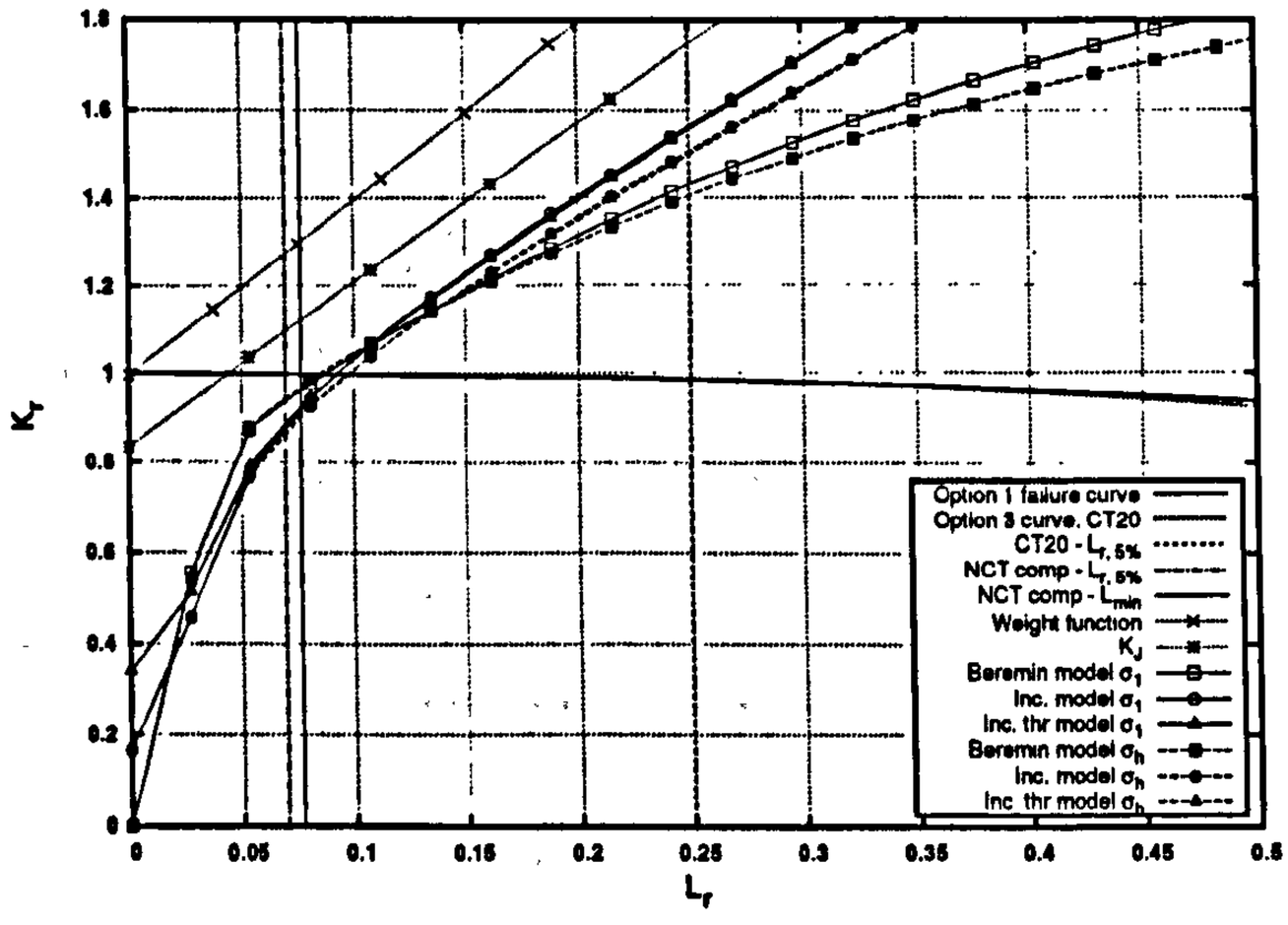

Figure 8.19: Prediction of safe load for NCT data with compressive preload, based on R6 assessment failure assessment diagram.

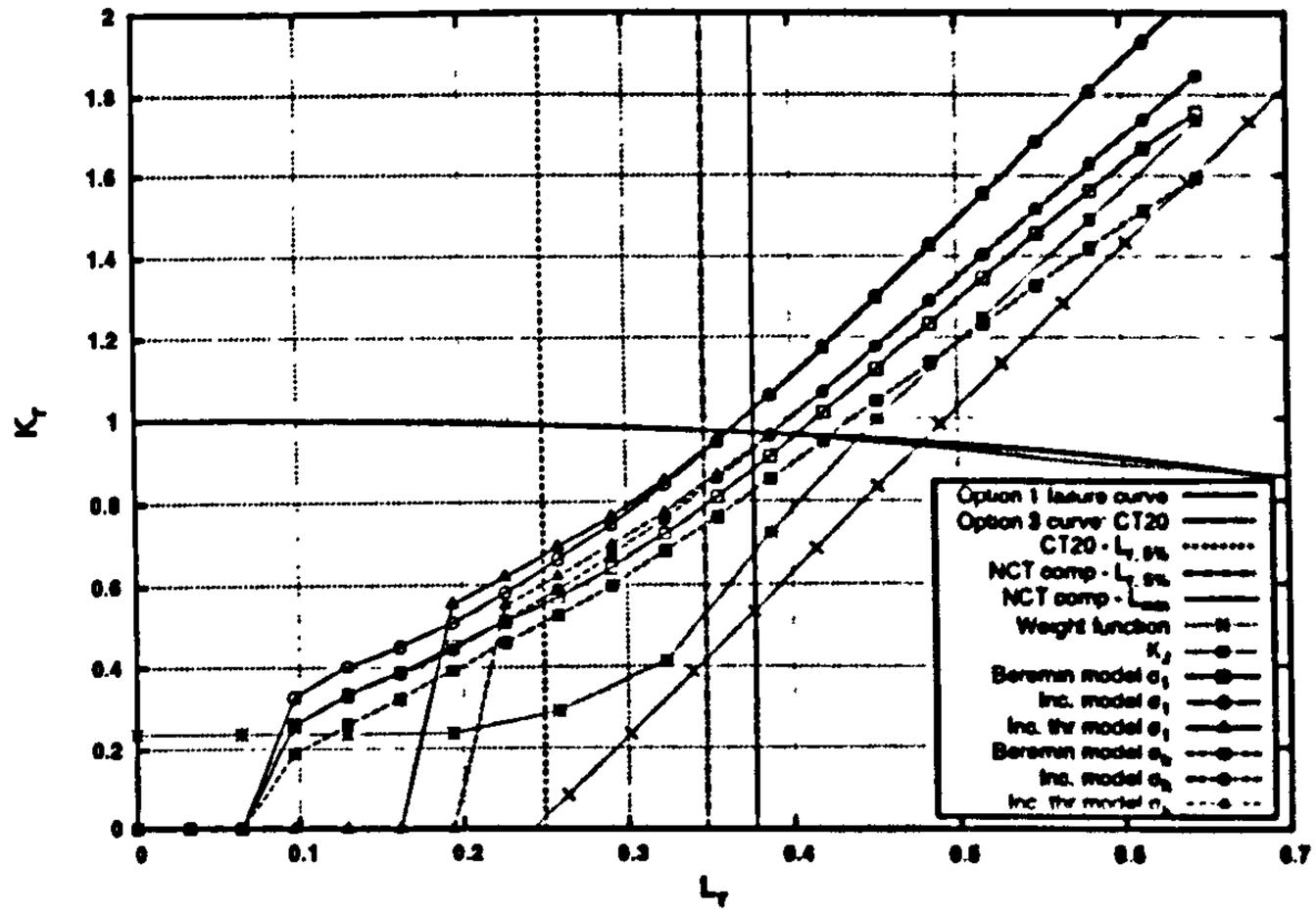

Figure 8.20: Prediction of safe load for NCT data with tensile preload, based on R6 assessment failure assessment diagram.

8.4 Discussion

An immediate observation from figures 8.3 and 8.4 is that simple K superposition arguments provide acceptable qualitative estimates of the effect of load history. The thickness scaling model also provides acceptable predictions of fracture for the CT10 data.

It is apparent that the predictions in all cases over-estimate the effect of the residual stresses on ensuing fracture behaviour. The predictions are therefore non-conservative for the WPS CT20 data and NCT data with tensile preload (where strength is increased) and overly pessimistic for the pre-compressed NCT data. It is likely that the over-estimation of preloading effects results from the elastic nature of the analyses. In the experiments, plasticity would be expected to reduce the mismatch causing the residual stress field and so reduce K_{res}.

When predictions are based on K_J, figure 8.4 shows that the increase or decrease in fracture load is correctly predicted for the NCT specimens, although the magnitude of the preloading effect is over-estimated in both cases. The values of K_J for the WPS case suggested a significant drop in fracture load that was not manifested in the experimental data, shown in figure 8.3. This is in keeping with the results for the LUCF load cycle in chapter 4.

This result suggests the unsuitability of J_m for cyclic loadings, where a clear initial material state cannot be defined. Physically, it becomes difficult in such cases to differentiate between the accumulated plastic strain which does and does not contribute to the current failure probability.

In the case of compressive residual stress, the work energy density W remains positive. Essentially, the energy input associated with compressive hydrostatic strain remains apparently available to drive fracture, even though this seems physically unlikely.

Predictions from the local approach methods tested were generally encouraging, however the disparity between predictions for data with and without load history warrants further consideration. This result may be attributable to the increased potential for inaccuracy in modelling complex cyclic loading in FE, compared to monotonic load histories.

The fact that agreement between predictions and experimental data is excellent for the AR state specimens, in particular for the incremental strain models, suggests the models and calibration are valid. Given the sensitivity of the RNB geometries used to variations in the FE analyses, the level of agreement is particularly encouraging.

The somewhat reduced accuracy of the Beremin model predictions may be related to the fit analyses in chapter 7. Figure 7.14 suggested an inability of this model to characterise the calibration data set and therefore the poorer geometric independence of the model is perhaps unsurprising.

For preloaded specimens, the simplest case is perhaps that of the prestrained CT data. The experimental data shows a consistent reduction of the fracture load following prestrain (figure 8.10). This reduction in fracture load appears roughly independent of the level of prestrain, within the limits studied in this case. The predictions suggest little effect at 1% prestrain, provide generally good estimates of the effect of 3% prestrain and somewhat overestimate the drop in fracture load after 5% prestrain. Analysis of the size of the volume active in the fracture process V_a (i.e. the currently yielding volume where the threshold stress is exceeded) sheds some light on the mechanisms of this effect. Figure 8.21 shows a reduction in active volume at a given σ_w with increasing prestrain. This suggests that the increase in yield stress reduces the active volume size but also increases the stresses within this volume. Figure 8.21 (b) shows that this remains the case when a threshold stress is introduced.

The overall effect of this process on σ_w will be dependent on the value

of m. For low m the reduction in yielding volume will dominate, producing a strengthening effect with prestrain. At high m, the effect of higher peak stresses will dominate, resulting in a reduction in predicted specimen strength. It should be noted that these effects are based solely on changes to the stress/strain curve and do not account for any other micromechanical effects of strain history. The lack of predicted effect following 1% prestrain may be related to the stress strain curve used. The stress strain behaviour exhibits yield point elongation up to around 1.1% plastic strain. It may be that the assumptions regarding the effect of room temperature strain on subsequent low temperature behaviour may be invalid in this region.

Where load history produced significant residual stress, the effect of the hardening model on the predictions was considerable. This was especially true of the pre-compressed NCT specimens, although there is an overall increase in predicted strength for all cases where kinematic hardening was assumed. Based on figures 8.11, 8.12 and 8.13 the effect of hardening model on principal stresses is more pronounced than for hydrostatic stress.

Based on the data analysed in chapter 4, the predictions were expected to be conservative, however the NCT failure loads are consistently over-estimated following tensile preloading. As previously noted, hydrostatic stress predicts higher fracture loads following load history. In general this improves the agreement between prediction and experiment however in the case of figure 8.12 it increases the level of non-conservatism.

When predictions are used in a FAD analysis, the results for the CT10 data are generally conservative. The predictions from elastic K methods are reasonable but intersect the failure curve well below the 5% probability fracture load, $L_{r,5\%}$. This is seen to be virtually equivalent to the minimum experimental load $L_{r,min}$. The conservatism of the K based predictions varies from 18% for the uncorrected K_J values to 15% for the thickness corrected K_J^t data. Local approach predictions reduce the level of conservatism to 3.7%, based on the elastic-plastic option 3 curve.

For the prestrained data, all approaches are slightly non-conservative following 1% prestrain (figure 8.17). Predictions for 3% and 5% prestrain (figures 8.17 (b) and (c)) are slightly conservative based on σ_1 and slightly non-conservative when σ_h is used. In general, it is worth noting from figure 8.10 that the lower limit of the experimental data is not significantly altered by the prestrain process.

For the LUCF warm prestress effect, figure 8.18 indicates an increase in $L_{r,5\%}$, in keeping with the experimental data, for all predictive methods used. The local approach produced conservative estimates in all cases, the incremental strain models improved the estimate slightly, as did introduction of a threshold stress. The 'best estimate', using the incremental model with threshold stress, resulted in conservatisms of 27% and 13% using σ_1 and σ_h. Of some concern, the model of Chell over estimated the fracture strength by around 20%.

For pre-compressed NCT specimens (figure 8.19) the elastic K_J method under estimates the $L_{r,5\%}$ load by 37% and incremental local approach methods over estimate it by 32%. The elastic superposition method, based on a weight function analysis, suggested no load carrying capacity for the specimens. It should be noted that the minimum experimental failure load (6.47kN) was considerably lower than the other observed loads and so may skew the value of $L_{r,5\%}$ for the data set. Hence, the 'true' value of $L_{r,5\%}$ may be higher than that estimated using methods such as equation 8.12.

For the NCT tests following tensile preload, figure 8.20 highlights the over estimation of the strengthening effect in all cases. The predictions closest to the $L_{r,5\%}$ load are those from the strain based local approach, based on σ_1 (3.7% over estimate). The greatest over estimate of fracture strength is that from the weight function K superposition method (37.9% over estimate).

The overall trends point to an increasing accuracy of assessment when local approach methods are employed, particulary in the AR state. The elastic methods based on superposition of stress intensity factor (or superposition of displacement in the WPS case) consistently over-estimate the effects of load history. If plasticity is not accounted for in the analyses it would be expected that the effect of residual stress would be over-estimated as relaxation due to deformation at high loads is not accounted for.

The strain nucleation method has showed an improved overall capability compared with the Beremin formulation although there is still considerable room for improvement in the prediction of load history effects. The fact that the fracture probabilities predicted Beremin model 'tail off' in figures 8.7 and 8.13 suggests a need to include strain effects to allow increasing probability of fracure even where local stress is not rising, as also suggested by [16].

The inclusion of a threshold stress on the overall variation of failure probability with load was not significant. There was, however, a greater effect on

results at lower loads and so use of non-zero threshold stress values may be beneficial in reducing conservatism in estimates of lower-bound safe loads for structures.

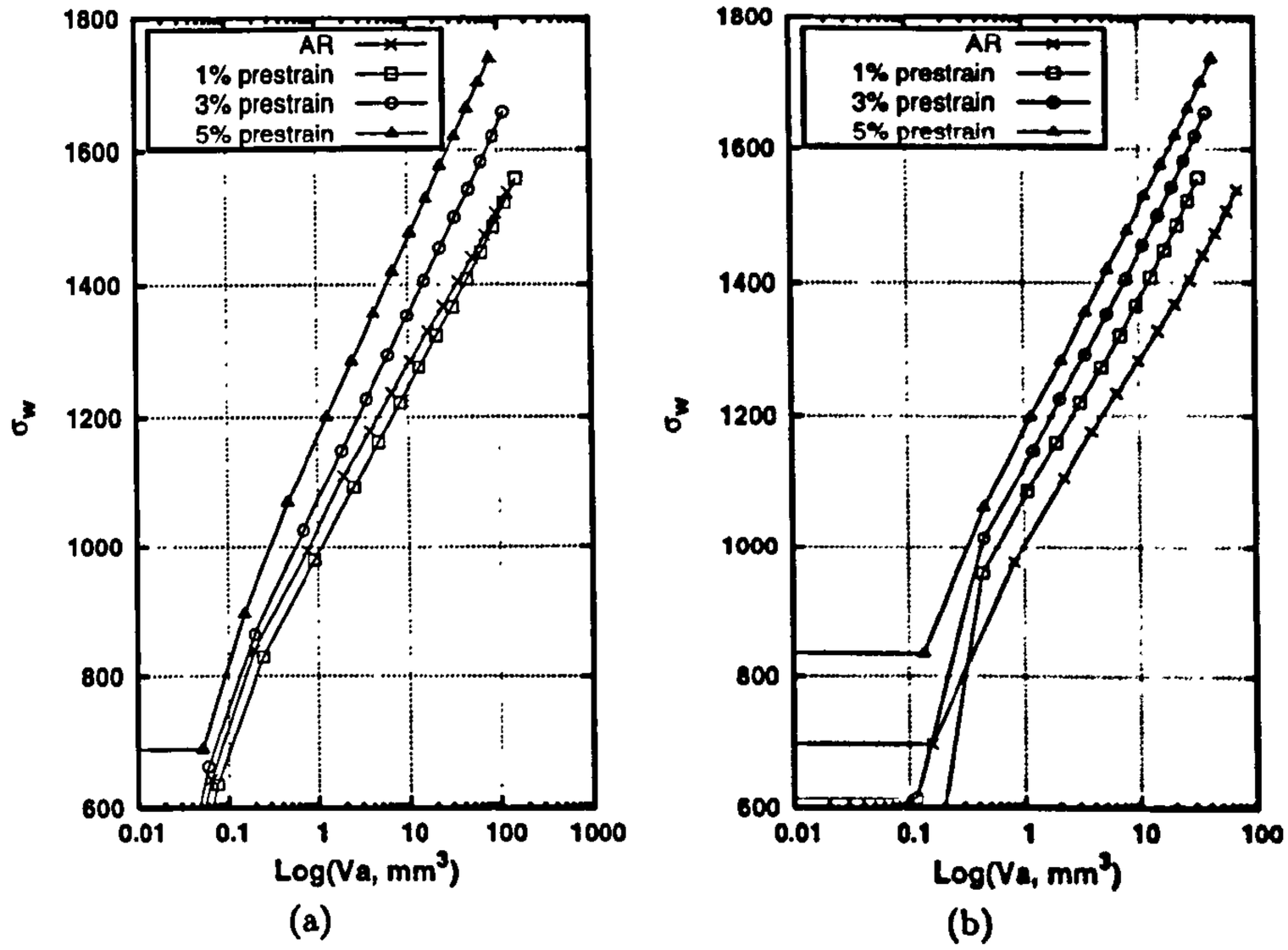

Figure 8.21: Variation of active volume size V_a with Weibull stress according to the incremental model with m=19. Based on maximum principal stress with (a) σ_{th}=0 and (b) σ_{th}=1200.

8.5 Conclusions

A number of models for fracture, based on the local approach as well as stress intensity factor K, have been used to predict brittle fracture across a range of geometries as well as following load history. Analysing the results of this work have produced the following conclusions:

1. Use of elastic stress intensity factor superposition methods provided reasonable estimates of the effects of load history, although the effects of residual stress were consistently over-estimated. This was attributed to the low temperature and high constraint conditions of the tests which inhibited plastic deformation when loading to eventual fracture.

2. Local approach methods were seen to produce excellent predictions of fracture across a range of geometries. Inclusion of strain to control defect nucleation improved the geometric independence of the models used.

3. Attempts to predict the effects of load history on fracture with the local approach correctly predicted increasing or decreasing fracture load following room temperature preload. In most cases, the resulting predictions were conservative, however the strength of the pre-tensioned NCT data was consistently over-predicted.

4. Using hydrostatic stress to describe microcrack propagation in the local approach had little effect on specimens without load history but consistently predicted increased strength following load history, compared to maximum principal stress.

5. In the context of the R6 assessments, the local approach was seen to improve accuracy compared to methods based on K and J, although this did result in non conservatism in the case of the precompressed NCT data.

6. Introduction of a local threshold stress for fracture did not profoundly effect the overall form of the fracture predictions but was seen to consistently improve predictions of lower bound fracture strength.

Chapter 9

Discussion

9.1 Effects of strain history

From the tests conducted in this thesis, it is clear that there is an influence of plastic strain history on fracture behaviour, separate from the effects of residual stress due to inhomogeneous deformation. The fracture tests conducted on CT specimens following uniform prestrain indicated a consistent drop in mean fracture toughness. As discussed in chapter 8, the strain hardening effect of deformation history results in a smaller crack tip plastic zone but higher peak stresses in the near-tip region.

Further to this, it was observed from neutron diffraction measurements made on prestrained specimens that even in the absence of macroscopic residual stress there is still a build-up of residual strain within individual grains. This is a result of inhomogeneous deformation between adjacent, differently aligned grains. Figure 5.23 clearly shows significant tensile residual strains on the [200] lattice plane, transverse to the direction of principal plastic strain. It was shown in [6] that fracture by quasi-cleavage occurs primarily on the [100] plane (equivalent in orientation to [200]), therefore any pre-existing tensile load on this plane is liable to increase the likelihood of fracture.

In terms of a change in overall fracture strength, it was seen that load history which produced tensile residual stresses reduced fracture loads, with compressive stress increasing the overall fracture load. In addition, there was a noticeable effect of load history on the scatter of the fracture data. Scatter was characterised using the Weibull modulus describing the variation of fracture probability with load. Based on variation of the load data Weibull moduli, the effect of tensile preloading was to reduce variation in fracture load.

Compressive preload (i.e. tensile residual stress) was seen to increase scatter. Both trends are in keeping with those of [49].

The effect of residual stress on the scatter in fracture load was discussed in chapter 6 such that, for cracked structures, tensile residual stress raises peak stresses above the minimum level required to promote fracture at lower applied loads. The final fracture event is therefore assumed to be controlled by the presence, or absence, of an existing defect in the region of peak stress. In the case of compressive residual stresses, the peak in stress around the crack tip is 'blunted', such that above a given applied load there is a sharper increase in the 'active' volume where stresses are high enough for fracture to occur. This is not borne out by the results of figure 9.1(b) where the active volume exceeding the threshold stress at failure does not show a clear dependency on preload type.

The change in scatter may be related to intragranular residual stresses. Tensile preloading, generally resulting in compressive residual stress, will produce compressive residual strain on the [100] plane in the direction of preloading. If subsequent loading to fracture is applied along the preload axis, it may be that this inhibits propagation of cracks at lower applied loads, effectively raising the lower bound fracture load and so reducing the overall level of scatter in fracture loads.

Similar effects may explain the variations noted in the prestrained CT data. Figure 8.10 showed that predictions based on macroscale stress and strain were relatively good at higher (3% and 5%) plastic strain but did not predict any significant influence of 1% prestrain. This may be related to figures 3.29 and 3.30 which showed a sharp effect of prestrain on diffraction peak width up to 1% plastic strain, with a much reduced effect of further deformation. This also corresponds to the portion of the stress/strain curve exhibiting discontinuous yielding (figure 5.6). It may be that in the absence of significant strain hardening, the grain scale effects of prestrain (which are not considered in terms of FE modelling) dominate the change in fracture behaviour after 1% prestrain. Once strain hardening effects became greater, the finite element modelling was able to capture the effects on the local stress/strain field and so predictions were improved.

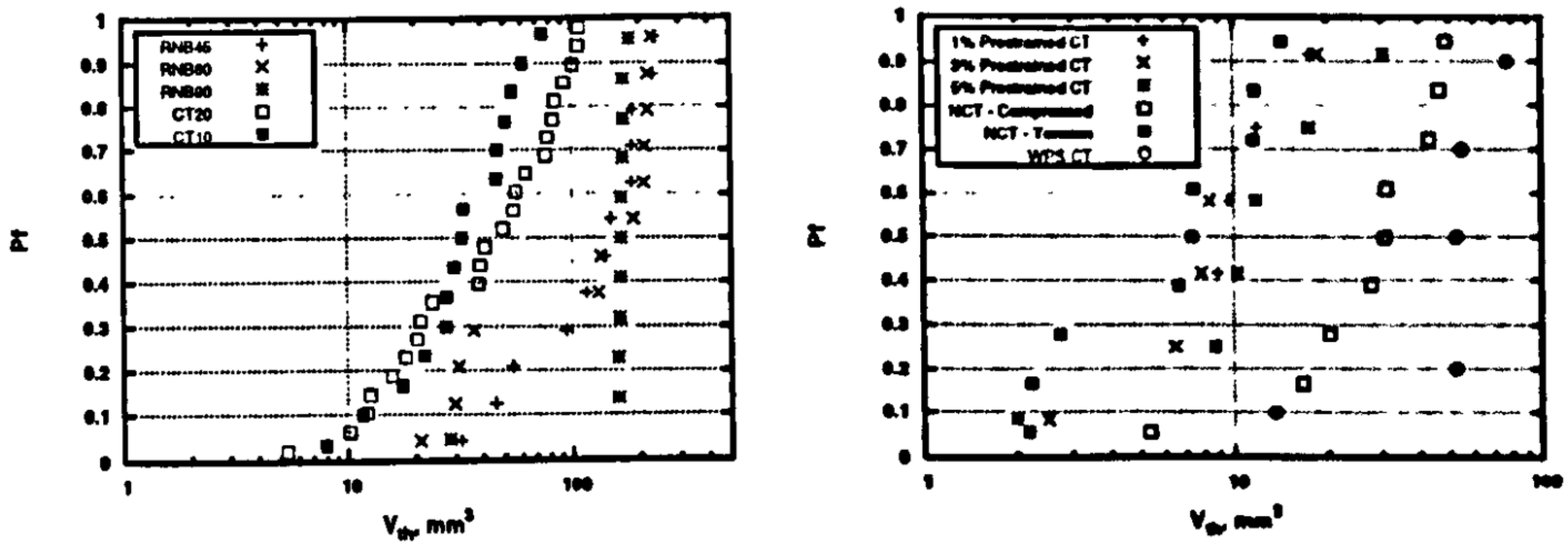

(a) (b)

Figure 9.1: Variation in the active fracture volume V_{th} at fracture with ranked fracture probability for tests a) in the as-received state b) with load history. The active volume is defined as that where yielding is occurring and where $\sigma_1 > 1200$ MPa.

9.2 Modelling and predicting fracture

Attempts to predict the influence of specimen geometry and load history, based on crack tip fracture parameters, produced mixed results. Excepting cases where cracks were introduced into a pre-existing residual stress field, allowing clear definition of 'initial state' strains, the modified J integral formulation of equation 2.24 proved unable to characterise the effect of load history on ensuing facture.

Methods based on elastic superposition of stress intensity factors correctly predicted increasing or decreasing fracture load following load history. The same was seen to be true in chapter 4 for the F_k parameter, describing the force on the crack tip plastic region. It was seen that superposition methods over-estimated the increase or decrease in fracture load following load history. This over prediction can be attributed to plastic deformation upon re-loading relaxing the residual stress field [108]. The fact that such over predictions were noted in the low temperature tests here, where plasticity was inhibited, suggests even more significant error may be introduced at higher temperature or in lower constraint specimens where yielding is more pronounced.

The primary difference between the J_m and F_k or K approaches is the dependency of the calculations on plastic strain history. The K and F_k methods, being primarily stress based, are affected by plasticity only in terms of any knock-on effect on the elastic stress/strain fields. As J_m is related to energy

of fracture, it is strongly affected by plasticity and the dissipative effects that accompany it. It is therefore apparent that a much more considered approach to the influence of accumulated plastic strain is needed in order to use J for cyclic loads. The overall nature of these findings would seem to confirm the primarily stress driven nature of cleavage fracture.

It was seen in the majority of cases studied that considering micro-defect nucleation as a continuing, strain controlled process improved the ability of local approach models to characterise the experimental behaviour.

The precise treatment of strain requires further investigation, specifically whether un-propagated defects remain 'active' in the fracture process or are blunted by further deformation. Neither assumption was seen to significantly effect predictions in chapter 4, excepting in cases where significant room temperature strain occurs prior to fracture. The incremental method of equation 4.8 (assuming blunting of defects with ensuing deformation) has the advantage of ensuring that Pf is an increasing function of time and was seen to avoid the drastic under prediction of strength following load history associated with a continuously increasing defect population.

It is worth noting that for all specimens with room temperature load history, it was assumed that the probability of fracture during preloading at 20°C was zero. In the case of the NCT and prestrained CT specimens, stresses during preloading did not exceed the threshold values (σ_1=1200 MPa σ_h=700 MPa). For the WPS CT tests, it would seem reasonable to assume there might be a finite (although small) chance of fracture by cleavage. A deeper issue is therefore the correct way to model the accumulation of fracture probability throughout the entire load history of the component. This is especially pertinent in cases where cyclic thermal and mechanical loading occurs - such as in many power generation applications. For proper life cycle assessments, it may be that determination of the appropriate model parameters at a range of temperatures is required.

The presence of microcracks in the fracture surface SEM images in chapter 5 suggests that, at the temperature studied, propagation of a microdefect to a grain scale crack is not the critical event for cleavage fracture. There was an amount of ductility prior to fracture as shown by the microvoids present on some of the fracture surfaces, and therefore fracture in this case should be regarded as quasi-cleavage, as also observed in [13]. Chapuliot [19] observed fatigue crack growth by cleavage at -253°C. This suggests that crack arrest,

such as at grain boundaries, must be accounted for even under very brittle conditions.

Crack arrest was considered in [19] in terms of minimum volume, where $\sigma_1 > \sigma_{th}$, required for cleavage cracks to propagate over neighbouring grain boundaries. It should be noted that a similar logic was employed in [83] where volume averaged stresses were used to account for grain boundary effects. In fact, a degree of volume averaging is unavoidable when using finite element methods to determine σ_w. Therefore, introducing a threshold due to a maximum defect size may partly serve to characterise arrest at grain boundaries when discrete numerical methods are used.

Figure 9.1 shows that lower values of the active volume V_{th} at failure were found following preloading than for the AR specimens. This is likely to be a result of strain hardening promoting higher peak stresses, although it does highlight the danger of attempting to determine any threshold value from limited experimental data.

The results of chapters 4 and 8 showed clear improvements in the ability of the local approach to predict load history when local facture probability was assumed to be a function of hydrostatic stress rather than maximum principal stress. The differentiation between results using σ_1 and σ_h was small for specimens in the as-received state, however following load history the conservatism of predictions was reduced when using σ_h. This effect was found to be beneficial in all cases, excepting the NCT specimens following tensile preload where the level of non-conservatism was increased (figure 8.12). As all methods over-predicted the fracture load for this data set, this is not surprising.

Although experimental results were favourable, it is important that the relative merits of using σ_1 or σ_h to describe fracture are set in a physical context. It was assumed by Beremin [104] that the nucleation of defects occurred following the onset of plastic deformation. Subsequent propagation of defects was then assumed to be controlled by σ_1. Defect propagation is a result of overcoming inter-atomic forces, which results from increasing atomic separation, i.e. strain. As cleavage crack propagation occurs primarily on the [100] and [110] lattice planes, it is the strain on these planes that is most likely to promote crack growth.

If grains or defects are properly aligned, relative to the direction of maximum principal stress, it can reasonably be assumed that the magnitude of σ_1 will control the cleavage process. If a grain or defect is not preferentially

aligned, the resolved shear stress on the material slip planes may reach sufficient levels for slip to occur, rather than separation within the lattice. As hydrostatic stress does not contribute to yielding behaviour and is the controlling parameter for material volumetric expansion, an increase in σ_h can be related to an increasing atomic separation regardless of grain or defect orientation.

If alignment of defects or microcracks is random, the effect of orientation is largely absorbed into the value of the material cleavage resistance σ_0 as a constant term. If microcrack or grain alignment is weighted towards a single direction, anisotropy and therefore the choice of characterising stress may become significant. The difference between the σ_1 and σ_h methods following load history can be interpreted in this way. The plastic deformation during preloading was primarily in one direction in the specimens considered here. This may have introduced preferential alignment such that anisotropy of the fracture response to σ_1 would occur upon reloading to failure.

9.3 Determining model parameters

When using experimental fracture data to calibrate local approach models, it was seen in chapter 4 that determining m from the linearisation method of section 4.5.1 is sensitive to the choice of data used. Consequentially, converged values were difficult to obtain when multiple data sets were used. The coefficient of determination between ranked and predicted fracture probabilities was found to be only weakly dependent on m for single specimen geometries. As such, chapters 4 and 7 suggest that maximising $R^2_{P_f}$ is not a reliable method of calibration in such cases. When data from high and low constraint specimen data were combined, $R^2_{P_f}$ displayed a strong sensitivity to m, allowing reliable determination of best fit values for m and σ_0.

When estimating fracture probability of experimental data using equation 4.12, it was seen in figures 7.9 and 7.10 that a maximum value of $R^2_{P_f}$ was more clearly defined when data were ranked separately by geometry. This can be attributed to the retaining of data in the fitting process. When data from multiple specimen types are mixed and ranked by other parameters such as Weibull stress, information about variability in fracture probability with load for each specimen type is discarded. By mixing data together in this way, a further degree of freedom is effectively added to the fitting process. This can

potentially hide underlying deficiencies in the model under investigation as seen in figure 7.7.

It was proposed in chapter 7 that predictions of the error introduced by the ranking equation may be used to analyse the quality of agreement between calibrated local approach models and the calibration data set. The results of chapters 7 and 8 suggested that using 90% confidence limits for the error introduced by equation 4.12 provided a reasonable indication of the ability of the calibrated models to describe fracture across varying geometries. This approach is attractive as it may provide a structures method for accepting or rejecting parameters determined from limited data sets.

It was however noted that the sensitivity of calibration data to variations in the finite element analyses should be considered, especially for data where Pf is a sharply increasing function of load, such as in the RNB data obtained in this work. It was suggested in such cases that a balance of error in fracture load and fracture probability should be used as a more pragmatic indicator of agreement between the model and the fracture data.

The majority of the issues associated with using local approach methods are related to the fact that parameters must be inferred from experimental fracture data. Finding values in this manner often results in unavoidable coupling between the values of the different parameters. Ideally, the values of m and σ_0 should be derived independently from their underlying physical meanings. For the case of m, this may be achievable from detailed examination of the material microstructure to determine the power relation best describing the distribution of defects. In undertaking such an investigation, questions are raised as to the nature of differing defects, for example carbide particles, manganese inclusions or twinned grains and how to assign them suitable defect sizes.

9.3.1 Bi-modality in fracture data

In the fracture data obtained it was apparent in some cases that there was a bi-modal nature to the probability distributions obtained. This was particularly notable in the CT20 data set where, for example, figure 8.5 shows a step increase in fracture load for a constant probability of approximately 0.4. Similar 'jumps' in fracture load were also apparent for the RNB60 data at $Pf \approx 0.3$ (figure 8.9) and to a lesser extent for the CT10 data at $Pf \approx 0.6$ (figure 8.7).

It is possible that this is a result of applying equation 4.12 to a limited data set, however it has also been suggested that this bi-modal behaviour may be a result of two competing defect populations [79] or the possibility that fracture may initiate in differing regions of the material microstructure [157]. As noted in [157], this may have particularly important implications when extrapolating to low fracture probabilities such as when determining limit loads for safety critical structures. This is especially true if the threshold conditions for fracture differ considerably between the two microstructures.

9.4 Implications for structural integrity assessment

The work conducted in this thesis has raised a number of issues regarding the determination of safe limit loads, such as in structural integrity assessments.

In determination of representative fracture toughness, chapter 3 suggested a maximum shift of 12.9 MPa.m$^{0.5}$ due to test specimen load history. The NCT specimen results in chapter 5 suggest shifts in mean toughness of -22.6 MPa.m$^{0.5}$ and +16.76 MPa.m$^{0.5}$ for specimens with pre-existing residual stresses. Perhaps most interestingly, the pre-compressed NCT data exhibited a minimum apparent toughness of 14.1 MPa.m$^{0.5}$ - below the commonly cited threshold of 20 MPa.m$^{0.5}$. It can therefore be concluded that the effects of residual stress in facture test specimens should be accounted for where appropriate. The potentially significant effects of residual stress were confirmed by the statistical analyses in chapter 6.

Where concern exists, it is suggested that the presence and magnitude of residual stresses be confirmed prior to fracture testing, for example by introducing cracks by wire EDM and measuring strain change during the cutting process. The crack compliance method may then be used to estimate the residual stress across the cracked region [158, 159].

The prestrained CT data highlighted that, even in the absence of significant residual stresses, plastic strain history can affect the mean measured toughness. In this case a reduction in mean measure toughness of 11-17% was recorded, compared to data in the AR condition. This is concerning as chapter 3 highlighted that experimental measurement of plastic strain is far from straightforward. Fortunately, the minimum K_I^{el} at fracture in the prestrained data was less than 5% below that measured in the AR state, suggesting that lower bound fracture behaviour is not significantly altered.

When using the R6 procedure, use of the incremental strain local approach formulation was generally shown to improve the overall accuracy of the assessments. The single exception was the pre-compressed NCT data where the K_J method produced the only conservative prediction. As the overall agreement with the data in figure 8.13 is very good, the non-conservatism of the 5% limit load prediction may be attributed to the limited data set producing an under-estimate for the true value of $L_{r,5\%}$.

It is worth noting that the statistical method used to determine the 5% failure load $L_{r,5\%}$ and the normalising toughness $K_{mat,5\%}$ may skew the results somewhat. In fact, the statistically determined value for $K_{mat,5\%}$ (51.08MPa.m$^{0.5}$) is above the minimum observed value at fracture (47.6MPa.m$^{0.5}$). In a practical assessment, a more extreme limiting value may be used to ensure safety, such as the toughness corresponding to 1% fracture probability. This would raise values of K_r by 30%, placing the local approach estimates for fracture load below the minimum observed values in all cases.

Chapter 10

Conclusions

The effect of load history on brittle cleavage fracture was investigated, primarily using A533B ferritic steel. A program of experimental testing was undertaken to probe the influences of specimen geometry, residual stress and accumulated plastic strain on material fracture behaviour.

Of particular interest was the influence of prior loading or strain history on fracture toughness, when measured using ex-service material. In addition, the ability of numerous fracture criteria to capture the effects of constraint change, residual stress and plastic deformation on fracture was explored.

The micro-mechanics of the fracture process, and the implications in terms of the local approach for fracture were investigated. Important issues in this section of the work were choice of stress measure, treatment of strain and reliable empirical determination of model constants.

At the outset of this thesis, chapter 1 defined a number of objectives. The work conducted has largely fulfilled these aims by:

- Demonstrating and quantifying the effects of residual stress on measured fracture toughness.

- Verifying the significance of the change in toughness, relative to the inherent scatter in fracture toughness data.

- Confirming the abilities and limitations of current models of cleavage fracture to predict the effects of load history on fracture behaviour.

In addition, based on the experimental data collected and the ensuing analyses, the following conclusions are drawn:

1. Removing fracture toughness specimens from components with significant weld residual stresses was shown to significantly reduce the magnitude of stress in the extracted coupon. The maximum shift in toughness due to these remnant stresses was estimated to be 12.9 MPa.m$^{0.5}$.

2. Experimental data from preloaded notched CT specimens showed shifts in mean measured toughness of -22.6 MPa.m$^{0.5}$ and +16.76 MPa.m$^{0.5}$. One such test failed at an applied elastic stress intensity factor of 14.14 MPa.m$^{0.5}$, below the commonly cited minimum value of 20 MPa.m$^{0.5}$. This highlights the potentially highly significant effect residual stresses may have on measured toughness and the need to account for such effects when determining material toughness from preloaded specimens.

3. Plastic strain history, even in the absence of residual stress, was shown to have an appreciable influence on measured toughness. Permanent uniform prestrains of 1-5% were seen to decrease the mean fracture load by up to 17%. This has implications for determining material K_{IC} where, if toughness is determined from specimens with plastic strain history, ensuing assessments of virgin material may be excessively conservative.

4. Attempts to measure existing plastic strain in fracture specimens resulted in limited success. Diffraction peak width and anisotropy of peak response were able to qualitatively but not quantitatively represent the level of plastic strain. Diffraction peak width displayed good independence from elastic deformation and it is concluded that more detailed measurements on single diffraction peaks - rather than using full spectrum time of flight measurements - may improve results.

5. A large number of fracture tests were undertaken on A533B ferritic steel. Fracture in all cases occurred at -150°C with crack propagation seen to occur primarily by cleavage mechanisms. However, in all cases studied, evidence of microvoid clusters and arrested microcracks was observed on the fracture surfaces. It is therefore concluded that the fracture mechanism was quasi-cleavage and the critical event for specimen failure was propagation of microcracks to a macroscopic scale, rather than initial propagation of a local defect.

6. Use of a modified, path independent J integral showed that reasonable prediction of load history could be obtained when prior load was

applied before crack insertion, allowing clear definition of an initial material state. Where non-proportional loading was applied to cracked specimens, ambiguity as to the proper treatment of accumulated plastic strain resulted in considerable under-prediction of fracture loads. It was also noted that the modelling assumptions for crack growth into existing stress fields had a strong influence on the level of plastic deformation at the final crack tip. This created significant variability in the values of J_m which could be obtained from a given uncracked body residual stress state.

7. Crack tip fracture parameters based primarily on elastic field quantities were able to correctly predict increasing or decreasing fracture load resulting from residual stress. Superposition methods, based on elastic stress intensity factor or displacement states, were seen to over-estimate the effects of prior loading. This was seen to result in considerable non-conservatism in some cases. The Eshelby force on the crack tip plastic zone, F_k, was able to predict residual stress effects on specimens preloaded in the cracked and un-cracked states, although the predictions of fracture were conservative.

8. The local approach was able to correctly predict the effect of load history on fracture behaviour in terms of an increase or decrease in fracture load. It was seen that consideration of the dependence of defect nucleation on plastic strain improved agreement with experimental data. Introducing a local threshold stress for fracture did not significantly alter predictions but was seen to reduce the conservatism of estimates of lower bound fracture load. It is suggested that, for general prediction of cleavage fracture following cyclic loading, the incremental strain model should be used.

9. Use of hydrostatic stress, rather than maximum principal stress, to describe defect propagation in the local approach did not significantly alter predictions of specimens in the as-received state but was seen to reduce over-conservatism of predictions following strain history.

10. It was shown that local approach parameters for a large data set (74 fracture tests) could be well approximated from a limited data set of high and low constraint data. Plane strain compact tension data and low

constraint notched bar data were shown to produce reliable estimates of m and σ_0, based on maximising the coefficient of determination between predicted and ranked experimental fracture probabilities.

11. Montecarlo simulations were used to estimate the error introduced by assigning fracture probabilities to experimental data. These analyses allowed confidence limits to be established for the 'true' fracture probability associated with values estimated from a ranking equation. Confidence limits were then used with some success to judge the ability of calibrated local approach models to characterise the calibration data set and thus determine their applicability to other specimen types.

12. Experimental results showed a consistent effect of preloading on scatter of fracture load data. In keeping with other published works, it was noted that tensile preload served to reduce scatter in fracture load, while compressive preload served to increase variability.

13. When local approach methods were used to estimate effective stress intensity factor values, estimates of failure load using the R6 structural integrity assessment code were seen to be improved, compared to methods based on elastic K_I^{el} or K_J. The nonconservatism resulting following some load cycles was attributed to the choice of normalising fracture toughness, based on a 5% failure probability. If a 1% value is chosen, the local approach results in conservative values for all load cycles studied.

Bibliography

[1] R. Von-Mises. Mechanik der festen korper im plastisch deformablen zustand. *Gottin. Nachr. Math. Phys*, 1:582–592, (1913).

[2] D.B. Bannerman and R.T Young. Some improvements resulting from studies of welded ship failures. *Welding Journal*, 25, (1946).

[3] A.A. Wells. The condition of fast fracture in aluminium alloys with particular reference to comet failures. Technical report, (1955).

[4] F.M. Burdekin. The role of fracture mechanics in the safety analysis of pressure vessels. *International Journal of Mechanical Sciences*, 24(4):197–208, (1981).

[5] G. Bartholome, M. Miksch, G. Neubrech, and G. Vasoukis. Fracture and safety analysis of nuclear pressure vessels. *Engineering Fracture Mechanics*, 4:431–446, (1973).

[6] A. Kumar, A.J. Wilson, and S.G. Roberts. Quasi-cleavage fracture planes in spherodized A533B steel. *Journal of Microscopy*, 227(3):248–253, (2007).

[7] C.J. McMahon and M. Cohen. Initiation of cleavage in polycrystalline iron. *Acta Metallurgica*, 13:591–604, (1965).

[8] J. Gurland. Observation on the fracture of cementite particles in a spherodised 1.05% steel deformed at room temperature. *Acta Metallurgica*, 20:735–741, (1972).

[9] T.C. Lindley, G. Oates, and C.E. Richards. A critical appraisal of carbide cracking mechanisms in ferrite/carbide aggregates. *Acta Metalluryica*, 18:1127–1135, (1970).

[10] S.R. Bordet, B Tanguy, and A.Pineau. Cleavage fracture of an RPV steel following warm pre-stressing: Micromechanical analysis and interpretation through a new model. *Fatigue & Fracture of Engineering Materials & Structures*, 29:799–816, (2006).

[11] J. Bošanský and T. Šmida. Deformation twins - probable inherent nuclei of cleavage fracture in ferritic steels. *Materials Science and Engineering A*, 323:198–205, (2001).

[12] Tibor Šmida and Jan Bošanský. Deformation twinning and its possible influence on the ductile brittle transition temperature of ferritic steels. *Materials Science and Engineering A*, 287:107–115, (2000).

[13] M. Coates, A. Kumar, and S.G. Roberts. Crack initiation in the brittle fracture of ferritic steels. *Fatigue & Fracture of Engineering Materials & Structures*, 29:661–671, (2006).

[14] S.G. Roberts A. Kumar and and A.J. Wilkinson. Low-temperature fracture mechanisms in a spherodised reactor pressure vessel steel. *International Journal of Fracture*, 144:121–129, (2007).

[15] C. Bouchet, B. Tanguy, J. Besson, A. Pineau, and S. Bugat. Transferability of cleavage fracture parameters between notched and cracked geometries. In *Fracture of Nano and Engineering Materials and Structures, ECF16*, Andropolous, Greece, (2006).

[16] J. Hohe, V. Friedmann, and D. Siegele. On the local conditions for cleavage initiation in ferritic steels. In *Fracture of Nano and Engineering Materials and Structures, ECF16*, Alexandroupolis, Greece, (2006). Springer.

[17] A. Pineau. Development of the local approach to fracture over the past 25 years: Theory and applications. *International Journal of Fracture*, (138):139–166, (2006).

[18] J.H. Chen. Physical models for cleavage fracture at various temperatures-bases for local approach to fracture of HSLA steel. *Materials Science and Engineering A*, 486:369–375, (2008).

[19] S. Chapuliot and V. Le Corre. A simplified expression of low cleavage probability calculation. *Engineering Fracture Mechanics*, 75:1488–1506, (2008).

[20] C.E. Inglis. Stresses in a plate due to the presence of cracks and sharp corners. *Transactions of the Institute of Naval Architects*, 55:219–241, (1913).

[21] A.A. Griffith. The phenomenon of rupture and flow in solids. *Philosophical Trans. A*, 221:163–198, (1920).

[22] T.L. Anderson. *Fracture Mechanics, Fundamentals and Applications.* CRC Press, 2nd edition, (1995).

[23] G.R. Irwin. Fracture dynamics. *Fracturing of Metals; American Society for Metals*, pages 147–166, (1948).

[24] G.R. Irwin. Onset of fast crack propagation in high strength steel and aluminium alloys. *Sagamore Research Conference Proceedings*, 2:289-305, (1956).

[25] E. Orowan. Fracture and strength of solids. *Reports on Progress in Physics*, 12:185, (1948).

[26] M.L Williams. On the stress distribution at the base of a stationary crack. *Journal of Applied Mechanics*, 24:109–114, (1957).

[27] ASTM. Standard test method for plane-strain fracture toughness of metallic materials. In *Annual book of ASTM standards*, page E399. ASTM, (1996).

[28] J.R Rice. A path independent integral and the approximate analysis of strain concentration by notches and cracks. *Journal of Applied Mechanics*, 35:379–386, (1968).

[29] J.D. Eshelby. *The Continuum Theory of Lattice Defects*, volume 3 of *Solid State Physics.* Academic Press, (1956).

[30] J.A. Begley and J.D. Landes. The J integral as a fracture criterion. In *National Symposium on Fracture Mechanics, Part II*, pages 1–20, (1972).

[31] J.D. Landes and J.A. Begley. The effect of specimen geometry on J_{IC}. In *National Symposium of Fracture Mechanics*, pages 24-39, (1972).

[32] J.W. Hutchinson. Singular behaviour at the end of a tensile crack in a hardening material. *Journal of the Mechanics and Physics of Solids*, 16:13–31, (1968).

[33] J.R Rice and G.F Rosengren. Plane strain deformation near a crack tip in a power law hardening material. *Journal of the Mechanics and Physics of Solids*, 16:1–12, (1968).

[34] F.Z Li, C.F. Shih, and A. Needleman. A comparison of methods for calculating energy release rates. *Engineering Fracture Mechanics*, 21(2):405–421, (1985).

[35] R.A. Ainsworth, B.K. Neale, and R.H. Price. Fracture behaviour in the presence of thermal strains. In *Proc. Int. Conference on Tolerance of Flaws in Pressurised Components*, pages 171–178, (1978).

[36] C.F. Shih, B. Moran, and T. Nakamura. Energy release rate along a three dimensional crack front in a thermally stressed body. *International Journal of Fracture*, 30:79–102, (1986).

[37] W.K. Wilson and I.W. Yu. The use of the J-integral in thermal stress crack problems. *International Journal of Fracture*, 15(4):377–387, (1979).

[38] Y. Lei, N.P. O'Dowd, and G.A. Webster. Fracture mechanics analysis of a crack in a residual stress field. *International Journal of Fracture*, 106:195–216, (2000).

[39] W.C. Carpenter, D.T. Read, and R.H. Dodds. Comparison of several path independent integrals including plasticity effects. *International Journal of Fracture*, 31:303–323, (1986).

[40] W.A. Meith and M.R. Hill. Domain-independent values of the J-integral for cracks in three dimensional residual stress bearing bodies. *Engineering Fracture Mechanics*, 69:1301–1314, (2002).

[41] K. Kishimoto, S. Aoki, and M. Sakata. On the path independent integral $\hat{J}$. *Engineering Fracture Mechanics*, 13:841–850, (1980).

[42] Y Lei. J-integral evaluation for cases involving non proportional stressing. *Engineering Fracture Mechanics*, 72:577–596, (2005).

[43] A. Mirzaee-Sisan, C.E. Truman, and D.J. Smith. Interaction of residual stress with mechanical loading in a ferritic steel. *Engineering Fracture Mechanics*, 74(17):2864–2880, (2006).

[44] S.J. Lewis, C.E. Truman, and D.J. Smith. A comparison of two- and three- dimensional fracture assessments in the presence of residual stress. *International Journal of Pressure Vessel Technology*, 131(2), (2009).

[45] J.D. Eshelby. The force on an elastic singularity. *Phil. Trans of the Royal Society, Mathematical and Physical Sciences*, 244(877):87–112, (1951).

[46] G.G. Chell, J.R. Haigh, and V. Vitek. A theory of warm prestressing: Experimental validation and the implications for elastic plastic failure criteria. *International Journal of Fracture*, 17(1):61–81, (1981).

[47] G.G. Chell and V. Vitek. The J-integral as a fracture criterion: Perhaps it doesn't mean what you thought it meant. *International Journal of Fracture*, 13:882–886, (1977).

[48] K. Wallin. The size effect in K_{IC} results. *Engineering Fracture Mechanics*, 22(1):149–163, (1985).

[49] D.J. Smith and J.D. Booker. Statistical analysis of the effects of prior load on fracture. *Engineering Fracture Mechanics*, 74(14):2148-2167, (2007).

[50] B.A. Bilby, G.E. Cardew, M.R. Goldthorpe, and I.C. Howard. A finite element investigation of the effects of specimen geometry on the fields of stress and strain at the tips of stationary cracks. In *Size Effects in Fracture*, pages 37–46. IMECHE, London, (1986).

[51] C. Betegon and J.W. Hancock. Two parameter characterisation of elastic-plastic crack tip fields. *Journal of Applied Mechanics*, 58:104-110, (1991).

[52] N.P. O'Dowd and C.F. Shih. Family of crack-tip fields characterised by a triaxiality parameter - 1. Structure of fields. *Journal of the Mechanics and Physics of Solids*, 39(8):989–1015, (1991).

[53] A.H. Sherry, D.G. Hooton, D.W. Beardsmore, and D.P.G. Lidbury. Material constraint parameters for the assessment of shallow defects in

structural components - part II: Constraint-based assessment of shallow defects. *Engineering Fracture Mechanics*, 72, (2005).

[54] N.P O'Dowd, Y. Lei, and E.P. Busso. Prediction of cleavage failure probabilities using the Weibull stress. *Engineering Fracture Mechanics*, 67:87–100, (2000).

[55] A.H. Sherry, M.A. Wilkes, D.W. Beardsmore, and D.P.G. Lidbury. Material constraint parameters for the assessment of shallow defects in structural components - part I: Parameter solutions. *Engineering Fracture Mechanics*, 72:2273–2395, (2005).

[56] G.C. Sih and B. Macdonald. Fracture mechanics applied to engineering problems - strain energy density fracture criterion. *Engineering Fracture Mechanics*, 6:361–386, (1974).

[57] G.C. Sih and E. Madenci. Fracture initiation under gross yielding: Strain energy density criterion. *Engineering Fracture Mechanics*, 18(3):667–677, (1983).

[58] C.L Chow and J. Xu. Mixed mode ductile fracture using the strain energy density criterion. *International Journal of Fracture*, 28:17–28, (1985).

[59] G. Labeas and Th. Kermanidis. Stress multiaxiality factor for crack growth prediction using the strain energy density theory. *Theoretical and Applied Fracture Mechanics*, 45:100–107, (2006).

[60] M. Alves and N. Jones. Influence of hydrostatic stress on failure of axisymmetric notched specimens. *Journal of the Mechanics and Physics of Solids*, 47:643–667, (1999).

[61] G. Matsoukas, B. Cotterell, and Y.-W. Mai. Crack opening displacement and hydrostatic stress. In *Advances in Fracture Research*, volume 2, pages 1543–1549, New Delhi, India, (1984).

[62] M. Shimura and S. Saito. The effects of hydrostatic tensile stress on fracture in some structural alloys. In *Advances in Fracture Research, ICF 6*, pages 1447–1455, New Delhi, India, (1983).

[63] A.S. Kao, H.A. Kuhn, O. Richmond, and W.A. Spitzig. Tensile fracture and fractographic analysis of 1045 spherodized steel under hydrostatic pressure. *Journal of Materials Research*, 5(1):83-91, (1990).

[64] J.P. Auger and D. Francois. Variation of fracture toughness of a 7075 aluminium alloy with hydrostatic pressure and relationship with tensile ductility. *International Journal of Fracture*, 13(4):431–441, (1977).

[65] P.T. Williams, B.R. Bass, and W.J. McAfee. Shallow flaws under biaxial loading conditions - part II: Applications of Weibull stress analysis of the cruciform bend specimen using a hydrostatic stress criterion. *Journal of Pressure Vessel Technology*, 123:25–31, (2001).

[66] B.R. Bass, W.J. McAfee, P.T. Williams, and W.E. Pennell. Fracture assessment of shallow-flaw cruciform beams tested under uniaxial and biaxial loading conditions. *Nuclear Engineering and Design*, 188:259-288, (1999).

[67] B.R. Bass, W.J. McAfee, P.T. Williams, and W.E. Pennell. Evaluation on constraint methodologies applied to a shallow flaw cruciform bend specimen tested under biaxial loading conditions. In *Proceedings of ASME PVP*, San Diego, (1998). ASME.

[68] D.P.G. Lidbury, A.H. Sherry, B.R. Bass, et al. Validation of constraint-based methodology in structural integrity of ferritic steels for nuclear reactor pressure vessels. *Fatigue & Fracture of Engineering Materials & Structures*, 29:829–849, (2006).

[69] J.R. Rice and D.M. Tracey. On the ductile enlargement of voids in triaxial stress fields. *Journal of the Mechanics and Physics of Solids*, 17:201–217, (1969).

[70] J.G Cowie and F.R. Tuler. The influence of second-phase dispersions on shear instability and fracture toughness of ultrahigh strength AISI 4340 steel. *Materials Science and Engineering A*, 141:23-37, (1990).

[71] R.H. Dodds, C.F. Shih, and T.L. Anderson. Continuum and micromechanics treatment of constraint in fracture. *International Journal of Fracture*, 64:101–133, (1993).

[72] S. Hadidi-Moud, A. Mirzaee-Sisan, C.E. Truman, and D.J. Smith. A local approach to cleavage fracture in ferritic steels following warm pre-stressing. *Fatigue & Fracture of Engineering Materials & Structures*, 27:931–942, (2004).

[73] W. Lefevre, G. Barbier, R. Masson, and G. Rousselier. A modified Beremin model to simulate the warm pre-stress effect. *Nuclear Engineering and Design*, (216):27–42, (2002).

[74] A. Mirzaee-Sisan. *The influence of prior thermal and mechanical load on fracture.* Ph.D thesis, University of Bristol, (2005).

[75] X. Gao, C. Ruggieri, and R.H. Dodds. Calibration of Weibull stress parameters using fracture toughness data. *International Journal of Fracture*, 92:175–200, (1998).

[76] K. Wallin. The scatter in K_{IC} results. *Engineering Fracture Mechanics*, 19(6):1085–1093, (1984).

[77] A Bakker and R.W.J. Koers. Prediction of cleavage fracture events in the brittle-ductile transition region of a ferritic steel, ESIS/EGF9. In *Defect assessment in components - Fundamentals and applications*, pages 613–632, (1991).

[78] L. Xia and C.F. Shih. Ductile crack growth - III. transition to cleavage fracture incorporating statistics. *Journal of the Mechanics and Physics of Solids*, 44(4):603–639, (1996).

[79] O.M.L. Yahya, F. Borit, R. Piques, and A. Pineau. Statistical modelling of intergranular brittle fracture in a low alloy steel. *Fatigue & Fracture of Engineering Materials & Structures*, 21:1485–1502, (1998).

[80] E. Kantidis, B. Marini, L. Allais, and A. Pineau. Validation of a statistical criterion for intergranular brittle fracture of a low alloy steel through uniaxial and biaxial (tension-torsion) tests. *International Journal of Fracture*, 66:273–294, (1993).

[81] E. Kantidis, B. Marini, and A. Pineau. A criterion for intergranular brittle fracture of a low alloy steel. *Fatigue & Fracture of Engineering Materials & Structures*, 17(6):619–633, (1994).

[82] M. Kroon and J. Faleskog. A probabilistic model for cleavage fracture with a length scale-influence of material parameters and constraint. *International Journal of Fracture*, 118:99–118, (2002).

[83] J. Faleskog, M. Kroon, and H. Oberg. A probabilistic model for cleavage fracture with a length scale - parameter estimation and predictions of stationary crack experiments. *Engineering Fracture Mechanics*, 71(1):57–59, (2004).

[84] R.O. Ritchie, J.F. Knott, and J.R. Rice. On the relationship between critical tensile stress and fracture toughness in mild steel. *Journal of the Mechanics and Physics of Solids*, 21:395–410, (1973).

[85] X. Gao, G. Zhang, and T.S. Srivatsan. Prediction of cleavage fracture in ferritic steels: a modified Weibull stress model. *Materials Science and Engineering A*, 394:210–219, (2004).

[86] J. Hohe, V. Friedmann, J. Wenck, and D. Siegele. Assessment of the role of micro defect nucleation in probabilistic modelling of cleavage fracture. *Engineering Fracture Mechanics*, 75:3306–3327, (2008).

[87] S.R. Bordet, A.D. Kartensen, D.M. Knowles, and C.S. Weisner. A new statistical local criterion for cleavage fracture in steel. part I: model presentation. *Engineering Fracture Mechanics*, 72:435–452, (2005).

[88] H. Stockl, R. Boschen, W. Schmitt, I. Varfolymeyev, and J.H. Chen. Quantification of the warm prestressing effect in a shape welded 10 MnMoNi 5-5 material. *Engineering Fracture Mechanics*, (67):119-137, (2000).

[89] D.J. Smith. The influence of prior loading on structural integrity. In R. Ritchie I. Milne and B.L. Karihaloo, editors, *Practical Failure Assessment Methods*, volume 7 of *Comprehensive Structural Integrity*. City, (2003).

[90] S. Sivaprasad, S. Tarafder, V.R. Ranganath, and K.K. Ray. Effect of prestrain on fracture toughness of HSLA steels. *Materials Science and Engineering*, A284:195–201, (2000).

[91] H. Zhu, G. Li, C. Li, and H. Kitagawa. Effects of prestrain on the fracture properties of pressure vessel steel. *International Journal of Fracture*, 52:291–299, (1992).

[92] K.F. Amouzouvi. A comparative fracture study of a slightly prestrained low alloy steel and a slightly prestrained austenitic stainless steel. *Materials Science and Engineering*, (78):65–70, (1986).

[93] C.G. Chipperfield. Detection and toughness characterisation of ductile crack initiation in 316 stainless steels. *International Journal of Fracture*, 12(6):873–886, (1976).

[94] N.J. Petch and R.W. Armstrong. Work-hardening in cleavage fracture toughness. *Acta Metallurgica*, 37(8):2279–2285, (1988).

[95] L. Banks-Sills and I. Dunye. A note on the effect of plastic strain on fracture toughness. *Engineering Fracture Mechanics*, 57(1):67–73, (1997).

[96] K.F. Amouzouvi and M.N. Bassim. Determination of fracture toughness from stretch zone width measurement in pre deformed AISI type 4340 steel. *Materials Science and Engineering*, (55):257–262, (1982).

[97] K.F. Amouzouvi and M.N. Bassim. Effect of the type of prior straining on the fracture toughness of AISI 4340 steel. *Materials Science and Engineering*, (60):1–5, (1983).

[98] P.R. Arora, M.R. Raghavan, and Y.V.R.K. Prasad. Effect of prestrain on fracture toughness of rolled mild steel with significant inclusion content. *Journal of Testing and Evaluation*, 16(3):298–304, (1988).

[99] J.Q. Clayton and J.F. Knott. Observations of fibrous fracture modes in a prestrained low-alloy steel. *Metal Science*, 10(2):63–71, (1976).

[100] N. Nabil Bassim and M.R. Bayoumi. The observation of dislocation structures during the fracture of prestrained AISI 4340 steel. *Materials Science and Engineering*, (81):317–324, (1986).

[101] J.D.G. Groom and J.F. Knott. Cleavage fracture in prestrained mild steel. *Metal Science*, 9:390–400, (1975).

[102] R. Sandstrom, G. Engberg, and Y. Bergstrom. Influence of prestrain and strain aging on cleavage fracture in C-Mn steel. *Metal Science*, 15:409–412, (1981).

[103] B.Z. Margolin, V.A. Shvetsova, and G.P. Karzov. Brittle fracture of nuclear pressure vessel steels - I. local criterion for cleavage fracture. *International Journal of Pressure Vessels and Piping*, 72:73–87, (1997).

[104] F.M. Beremin. A local criterion for cleavage fracture of a nuclear pressure vessel steel. *Metall. Trans. A*, 14A:2277–2287, (1983).

[105] P.A.S. Reed and J.F. Knott. Investigation of the role of residual stresses in the warm prestress (WPS) effect. part 1 - experimental. *Fatigue & Fracture of Engineering Materials & Structures*, 19(4):485–500, (1995).

[106] C. Ruggieri, X. Gao, and R.H. Dodds. Transferability of elastic-plastic fracture toughness using the Weibull stress approach: significance of parameter calibration. *Engineering Fracture Mechanics*, 67:101–117, (2000).

[107] Assessment of the integrity of structures containing defects. Technical Report R/H/R6, British Energy, Barnwood, (1999).

[108] R.A. Ainsworth, J.K. Sharples, and S.D. Smith. Effects of residual stresses on fracture behaviour - experimental results and assessment methods. *Journal of Strain Analysis*, 35(4):307–316, (2000).

[109] Z. Budrovic, H. Van Swygenhoven, P. Derlet, S. Van Petergem, and B. Schmitt. Plastic deformation with reversible peak broadening in nanocrystalline nickel. *Science*, 304:273–304, (2004).

[110] M. Kamaya, A. Wilkinson, and J. Titchmarsh. Measurement of plastic strain of polycrystalline material by electron backscatter diffraction. *Nuclear Engineering and Design*, 235:713–725, (2005).

[111] T.B. Brown, T.A. Dauda, C.E. Truman, D.J. Smith, D. Memhard, and W. Pfeiffer. Predictions and measurements of residual stresses in repair welds in plates. *International Journal of Pressure Vessels and Piping*, (83):809–818, (2006).

[112] P.J. Bouchard, L. Edwards, A.G. Anastasius, and R. Dennis. Development of a residual stress simulation benchmark for a single bead-on-plate weldment. In *Proceedings of ASME PVP*, Vancouver, Canada, (2006). ASME.

[113] ASTM. Standard test methods for tension testing of metallic materials. In *Annual book of ASTM standards*, page E8. ASTM, (1996).

[114] M.C. Smith and L. Edwards. The net residual stress measurement and modelling round robin on a single weld bead-on-plate specimen. *Int. Journal of Pressure Vessels and Piping*, 86.

[115] S.J. Lewis, H. Alizadeh, and C.Gill. Modelling and measurement of residual stresses in autogenously welded stainless steel plates: Part 1 - fabrication and modelling. (Under review).

[116] H. Alizadeh, S.J. Lewis, C. Gill, S. Hossain, D.J. Smith, and C.E. Truman. Measurement and prediction of the residual stress field in an autogenously welded stainless steel plate. In *Proceedings of ASME PVP*, Chicago, (2008).

[117] S. Hossain, C.E. Truman, D.J. Smith, and P.J. Bouchard. Measurement of residual stresses in a type 316H stainless steel offset repair in a pipe girth weld. *Journal of Pressure Vessel Technology*, 128:420–426, (2006).

[118] G.A. Webster and R.C. Wimpory. Non-destructive measurement of residual stress by neutron diffraction. *Journal of Materials processing technology*, 117:395–399, (2001).

[119] M.E. Fitzpatrick and A. Lodini. *Analysis of Residual Stress by Diffraction using Neutron and Synchrotron Radiation.* Taylor & Francis, New York, (2003).

[120] A.N. Ezelio, G.A. Webster, P.J. Webster, and X. Wang. Characterisation of elastic and plastic deformation in a nickel superalloy using pulsed neutrons. *Physica B*, 180:1044–1046, (1992).

[121] R.B. Rogge, P.R. Dawson, and D. Boyce. Neutron diffraction measurement of the evolution of strain for non-uniform plastic deformation. *Applied Physics*, A74:1725–1727, (2002).

[122] M.R. Daymond, M.A.M. Bourke, R.B. Von Dreele, B. Clausen, and T. Lorentzen. Use of Rietveld refinement for elastic macrostrain determination and for evaluation of plastic strain history from diffraction spectra. *Journal of Applied Physics*, 82(4):1554–1562, (1997).

[123] H.M. Rietveld. Line profiles of neutron powder-diffraction peaks for structure refinement. *Acta Cryst.*, 22:151–152, (1967).

[124] A.M Korunsky, M.R. Daymond, and K.E. James. The correlation between plastic strain and anisotropy strain in aluminium alloy polycrystals. *Materials Science and Engineering*, A334:41–48, (2002).

[125] W.G. Moffatt, G.W. Pearsall, and J. Wulff. *The Structure and Properties of Materials, Vol. 1, Structure.* John Wiley & Sons, New York, (1964).

[126] D.J. Smith, R.H. Leggatt, G.A. Webster, H.J. Macgillivray, P.J. Webster, and G. Mills. Neutron diffraction measurements of residual stress and plastic deformation in an aluminium alloy weld. *Journal of Strain Analysis*, 23(4):201–211, (1988).

[127] D.J. Smith and G.A. Webster. The measurement of prior plastic deformation in metallic alloys using the neutron diffraction technique. *Journal of Strain Analysis*, 32(1):37–46, (1997).

[128] P.J. Bouchard, D. George, J.R. Santisteban, et al. Measurement of the residual stresses in a stainless steel pipe girth weld containing long and short repairs. *International Journal of Pressure Vessels and Piping*, 82:299–310, (2005).

[129] R.A. Winholz and A.D. Krawitz. The effect of assuming principal directions in neutron diffraction measurement of stress tensors. *Materials Science and Engineering*, A205:257–258, (1996).

[130] A.H. Mahmoudi. *Influence of Residual Stresses on Fracture.* PhD thesis, University of Bristol, (2005).

[131] A. Mirzaee-Sisan, A. Mahmoudi, C.E. Truman, and D.J. Smith. Application of the local approach to predict load history effect in ferritic steels. In *Proceedings of ASME PVP*, Denver, Colorado, (2005). ASME.

[132] A.H. Mahmoudi, D. Stefanescu, S. Hossain, C.E. Truman, D.J. Smith, and P.J. Withers. Measurement and prediction of the residual stress field generated by side-punching. *Journal of Engineering Materials and Technology*, 128(3):451–459, (2006).

[133] *Abaqus/CAE v6.71.* Dassault Systèmes, (2008).

[134] A.H. Sherry, J. Qunita Da Fonseca, M.R. Goldthorpe, and K. Taylor. Measurement and modelling of residual stress effects on cracks. *Fatigue & Fracture of Engineering Materials & Structures*, 30:243–257, (2006).

[135] M.C. Smith. ENPOWER task 2.2: Design of a beam-type fracture specimen containing a residual stress field. Technical report, (2002).

[136] J.C.W. Davenport. *Mixed Mode Elastic-Plastic Fracture.* PhD thesis, University of Bristol, (1993).

[137] S. Carassou. *D'elenchement du clivage dans un acier faiblement allie: role de l'endommagement ductile localise autour des inclusions.* PhD thesis, Ecole des Mines de Paris, (1999).

[138] B. Bergman. On the estimation of the Weibull modulus. *Journal of Materials Science Letters*, 3:689–692, (1984).

[139] F. Minami, A. Bruckner-Foit, D. Munz, and B. Trolldenier. Estimation procedure for the Weibull parameters used in the local approach. *International Journal of Fracture*, 54:197–210, (1990).

[140] C.R. Mischke. Stochastic methods in mechanical design: Part 2: Fitting the Weibull distribution to the data. *Proc. 8th biannual conference on failure prevention and reliability, Montreal Canada*, pages 11–15, (1989).

[141] I.J. Davies. Best estimate of Weibull modulus obtained using linear least squares analysis: An improved empirical correction factor. *Journal of Mateials Science*, 39:1441–1444, (2004).

[142] J.A. Griggs and Y. Zhang. Determining the confidence intervals of Weibull parameters estimated using a more precise probability estimator. *Journal of Materials Science Letters*, 22:1771–1773, (2003).

[143] M. Tiryakioglu. On estimating Weibull modulus by moments and maximum likelihood methods. *Journal of Materials Science*, 43:793–798, (2007).

[144] J. Gong. Determining the confidence intervals for Weibull estimators. *Journal of Materials Science Letters*, 18:1405–1407, (1999).

[145] K. Hojo, I. Muroya, and A. Bruckner-Foit. Fracture toughness transition curve estimation from a notched round bar specimen using the

local approach method. *Nuclear Engineering and Design*, 174:247–258, (1997).

[146] X. Wu. *Weight Functions and Stress Intensity Factor Solutions.* Pergamon Press, (1991).

[147] Y. Wadier. Reconsidering the paradox of Rice for a linear strain hardening mateial. *International Journal of Fracture*, 127:125–132, (2004).

[148] K.S Lee, A.H. Sherry, and M.R. Goldthorpe. Residual stress and constraint effects on fracture in the transition temperature regime. In *Proceedings of ASME PVP*, Chicago, (2008).

[149] D.J. Smith, S. Hadidimoud, and H. Fowler. The effects of warm prestressing on cleavage fracture. Part 1: Evaluation of experiments. *Engineering Fracture Mechanics*, 71:2015–2032, (2004).

[150] D.J. Smith, S. Hadidimoud, and H. Fowler. The effects of warm prestressing on cleavage fracture. Part 2: Finite element analysis. *Engineering Fracture Mechanics*, 71:2033–2051, (2004).

[151] T. Lorentzen, T. Faurholdt, B. Clausen, and J Danckert. Characterisation of residual stresses generated during inhomogeneous plastic deformation. *Journal of Strain Analysis*, 33(3):243–252, (1998).

[152] E.C. Oliver, M.R. Daymond, and P.J. Withers. Interphase and intergranular stress generation in carbon steels. *Acta Materialia*, 52:1937–1951, (2004).

[153] G.E. Dieter. *Engineering design: a materials and processing approach.* McGraw-Hill, New York, 3rd edition, (2000).

[154] K. Wallin. Master curve analysis of the 'Euro' fracture toughness dataset. *Engineering Fracture Mechanics*, 69:451–481, (2002).

[155] X. Gao and R.H. Dodds. Constraint effects on the ductile-to-brittle transition temperature of ferritic steels: a Weibull stress model. *International Journal of Fracture*, 102:43–69, (2000).

[156] J.P. Petti and R.H. Dodds Jr. Coupling of the Weibull stress model and macroscale models to predict cleavage fracture. *Engineering Fracture Mechanics*, 71:2079–2103, (2004).

[157] J.F. Knott. Local approach concepts and the microstructure of steels. *Engineering Fracture Mechanics*, 75:3560–3569, (2008).

[158] M.B. Prime. Residual stress measurement by successive extension of a slot: The crack compliance method. *Applied Mechanics Review*, 52(2):75–96, (1999).

[159] M.B. Prime. Measuring residual stress and the resulting stress intensity factor in compact tension specimens. *Fatigue & Fracture of Engineering Materials & Structures*, 22(3):195–204, (1998).

	Partially welded specimens Position, (X,Y,Z)	**Fully welded specimens** Position, (X,Y,Z
Thermocouple 1	(-30,-12,0)	(-78,-12,0)
Thermocouple 2	(0,-12,0)	(0,-12,0)
Thermocouple 3	(30,-12,0)	(78,-12,0)
Thermocouple 4	(0,7,20)	(0,7,20)
Strain gauge	(0,0,20)	(0,0,20)

Table 3.1: Positions of thermocouples and strain gauges during welding.

	Arc time (s)	Current (A)	Voltage (V)	Travel rate (mm/s)	Heat input (kJ/mm)
Partially welded specimens	35	156	12.4	103	1.128
Fully welded specimens	100	156	12.4	108	1.075

Table 3.2: Weld parameters for fabrication of autogenously welded 316L steel plates.

Line description	**X**	**Y**	**Z**
LT, along weld line, top surface	-80 to 80	0	2
TT, scross weld line, top surface	0	-15 to 15	2
LB, along weld line, back surface	-80 to 80	0	18
TB, scross weld line, back surface	0	-15 to 15	18
DHD1, through thickness, weld centre	0	0	2 to 18
DHD2, through thickness, weld stop	-30	0	2 to 18
DHD3, through thickness, weld start	30	0	2 to 18

Table 3.3: Positions and labels of measurement lines.

20°C		-150°C	
σ_e, MPa	ϵ_e^{pl} %	σ_e, MPa	ϵ_e^{pl} %
475.77	0.00	736.2	0.00
460.59	0.15	719.4	0.07
463.78	0.29	706.7	0.15
468.78	0.48	704.8	0.21
468.51	0.67	704.1	0.48
470.93	0.97	700.9	0.82
482.36	1.17	695.5	1.30
490.47	1.36	700.9	1.48
498.74	1.55	710.6	1.78
507.79	1.77	722.4	2.17
515.27	1.99	741.9	2.81
527.04	2.24	761.1	3.35
536.60	2.49	800.1	4.63
544.42	2.74	841.5	6.23
561.41	3.23	877.7	8.17
576.50	3.72	916.9	10.21
589.79	4.23	938.4	12.21
601.15	4.72	968.1	14.23
611.24	5.20	975.5	16.29
620.40	5.70	960.8	18.56
628.74*	6.20*		
637.62*	6.64*		
647.56*	7.26*		
E=202 GPa		E=209 GPa	

* Extrapolated values

Table 3.4: Measured stress/strain response for A533B ferritic steel at 20°C and -150°C.

	σ_1		σ_h	
Model	m	σ_0	m	σ_0
Beremin	20.3	1839.9	14.3	1351.1
	(14.3 , 26.3)	(460.1 , 7357.1)	(10.1 , 18.5)	(360.2 , 5067.2)
Strain nucleated	16.5	1345.4	11.9	880.4
	(11.6 , 21.4)	(352.2 , 5139.5)	(8.4 , 15.4)	(251.8 , 3078.2)
Incremental strain	18.3	1384.7	12.9	907.1
	(12.9 , 23.8)	(356.7 , 5375.0)	(9.1 , 16.7)	(254.6 , 3232.5)

Table 4.1: Fitted parameters for local approach models, with 90% confidence limits, calibrated to A508 steel CT fracture data.

Model	σ_1		σ_h	
	m	σ_0	m	σ_0
Beremin	19.7	1836.2	14.0	1348.0
	(13.9 , 25.5)	(456.5 , 7385.2)	(9.9 , 18.1)	(359.8 , 5050.1)
Strain nucleated	14.7	1288.0	10.9	842.4
	(10.3 , 19.1)	(341.4 , 4858.3)	(7.7 , 14.1)	(244.9 , 2898.0)
Incremental strain	17	1352.8	12.0	879.6
	(11.9 , 22.0)	(351.0 , 5212.9)	(8.4 , 15.6)	(250.2 , 3092.8)

Table 4.2: Fitted parameters and 90% confidence limits for local approach models with threshold stress, calibrated to A508 steel CT fracture data.

Model	σ_1		σ_h	
	m	σ_0	m	σ_0
Beremin	12.8	1600.5	10.5	1180.6
	(10.7 , 14.8)	(785.0 , 3263.1)	(8.9 , 12.0)	(669.6 , 2081.8)
Strain nucleated	8.9	1018.8	5.9	598.2
	(- , -)	(670.8 , 2117.5)	(- , -)	(412.4 , 1088.6)
Incremental strain	11.7	1027.4	7.4	601.77
	(- , -)	(646.17 , 2606.4)	(- , -)	(402.3 , 1193.6)

Table 4.3: Fitted parameters and 90% confidence limits for local approach models, calibrated to A533B steel SENB fracture data.

Model	σ_1		σ_h	
	m	σ_0	m	σ_0
Beremin	9.8	1543.2	8.3	1151.5
	(8.2 , 11.4)	(789.9 , 3014.8)	(6.6 , 10.0)	(441.8 , 3001.5)
Strain nucleated	6.2	764.8	3.8	349.3
	(- , -)	(528.3 , 1384.8)	(- , -)	(253.6 , 561.2)
Incremental strain	9.3	879.71	6.0	478.88
	(- , -)	(572.32 , 1900.4)	(- , -)	(329.32 , 877.35)

Table 4.4: Fitted parameters and 90% confidence limits for local approach models with threshold stress, calibrated to A533B steel SENB fracture data.

Model	σ_1		σ_h	
	m	σ_0	m	σ_0
Beremin	49.2	1602.4	26.5	1153.5
	(- , -)	(831.01 , 22323)	(- , -)	(679.01 , 3830)
Strain nucleated	58	1489.8	35.8	1009.6
	(- , -)	(770.97 , 22047)	(- , -)	(569.11 , 4465.6)
Incremental strain	57	1451.9	29.4	961.32
	(- , -)	(744.39 , 29286)	(- , -)	(554.32 , 3617.1)

Table 4.5: Fitted parameters and 90% confidence limits for local approach models, calibrated to A508 steel RNB fracture data.

Model	m	σ_0	m	σ_0
Beremin	49	1602.6	26.4	1153.82
	(- , -)	(831.7 , 21912)	(- , -)	(679.41 , 3823.92)
Strain nucleated	57.8	1489.6	35.5	1008.91
	(- , -)	(771.25 , 21714)	(- , -)	(569.59 , 4411.28)
Incremental strain	57	1450.3	29.6	961.92
	(- , -)	(743.9 , 28765)	(- , -)	(554.09 , 3643.8)

Table 4.6: Fitted parameters and 90% confidence limits for local approach models with threshold stress, calibrated to A508 steel RNB fracture data.

Load level	D1 (mm)	D2 (mm)	σ_{eq} (MPa)
1	0.1	0.05	245.2
2	0.2	0.1	479.7
3	0.3	0.05	591.4

Table 4.7: Applied displacements to edge cracked plate for crack introduction modelling.

Specimen type	Preload?	Number of tests (Total/Used)	Temperature (° C)
CT20	N	30/24	-150
CT10	N	15/15	-150
RNB45	N	12/12	-150
RNB60	N	12/12	-150
RNB90	N	12/11	-150
NCT - Compression	Y	10/9	-150
NCT - Tension	Y	10/10	-150
CT20 - WPS	Y	5/5	-150
CT20 - 5% PS	Y	5/5	-150
CT20 - 3% PS	Y	5/5	-150
CT20 - 1% PS	Y	5/5	-150

Table 5.1: Summary of conducted fracture tests.

Specimen Label	Fracture load (kN)	K_I^{el} MPa$\sqrt{m}$	K_J MPa$\sqrt{m}$
CT20_1	42.53	91.60	102.06
CT20_2	26.97	58.08	61.37
CT20_3	30.53	65.75	70.09
CT20_4*	23.79	51.25	54.15
CT20_5*	46.55	100.26	113.24
CT20_6*	48.34	104.13	118.28
CT20_7*	43.94	94.64	105.96
CT20_8*	25.60	55.14	58.18
CT20_9	36.27	78.12	85.03
CT20_10*	31.69	68.27	73.05
CT20_11	28.72	61.85	65.59
CT20_12	38.91	83.80	92.13
CT20_13	25.83	55.63	58.70
CT20_14	35.82	77.16	83.84
CT20_15	43.12	92.88	103.70
CT20_16	44.36	95.55	107.14
CT20_17	43.36	93.39	104.36
CT20_18	39.15	84.34	92.81
CT20_19	29.70	63.97	68.02
CT20_20	46.09	99.28	111.97
CT20_21	42.30	91.11	101.42
CT20_22	27.19	58.57	61.90
CT20_23	45.44	97.87	110.14
CT20_24	46.20	99.51	112.27
CT20_25	35.69	76.88	83.50
CT20_26	37.90	81.63	89.40
CT20_27	30.78	66.30	70.74
CT20_28	22.10	47.60	50.58
CT20_29	31.69	68.26	73.04
CT20_30	40.17	86.53	95.59
Mean	36.36	78.31	85.94
Minium	22.10	47.60	50.58
Maximum	48.34	104.13	118.28

* *Specimens with 'pop in'.*

Table 5.2: Load and stress intensity factor at failure for CT20 specimens.

Specimen Label	Fracture load (kN)	K_I^{el} MPa$\sqrt{m}$	K_J MPa$\sqrt{m}$
CT10_1	19.81	85.58	106.76
CT10_2	17.43	75.31	89.94
CT10_3	21.01	90.75	115.10
CT10_4	23.62	102.04	135.74
CT10_5	20.35	87.89	110.46
CT10_6	26.26	113.43	167.77
CT10_7	18.56	80.19	98.04
CT10_8	20.89	90.25	114.28
CT10_9	29.19	126.11	234.48
CT10_10	19.85	85.75	107.03
CT10_11	25.03	108.12	150.64
CT10_12	24.38	105.32	143.28
CT10_13	15.61	67.45	76.67
CT10_14	14.17	61.20	66.62
CT10_15	23.56	101.77	135.16
Mean 21.32 92.08 123.46 Minimum 14.17 61.20 66.62 Maximum 29.19 126.11 234.48			

Table 5.3: Load and stress intensity factor at failure for CT10 specimens.

Specimen Label	Fracture load (kN)	K_I^{el} MPa$\sqrt{m}$	K_J MPa$\sqrt{m}$
CT20_11a	30.65	65.92	71.01
CT20_11b	30.60	65.80	70.87
CT20_11c	31.33	67.37	72.71
CT20_12a	36.72	78.97	86.47
CT20_12b	33.01	70.99	76.96
CT20_12c	21.10	45.38	47.61
Mean	30.57	65.74	70.94
Minium	21.10	45.38	47.61
Maximum	36.72	78.97	86.47

Table 5.4: Load and stress intensity factor at failure for CT20 specimens with 1% prestrain.

Specimen Label	Fracture load (kN)	K_I^{el} MPa$\sqrt{m}$	K_J MPa$\sqrt{m}$
CT20_31a	36.79	79.11	85.73
CT20_31b	29.91	64.31	68.75
CT20_31c	22.11	47.54	50.03
CT20_32a	28.01	60.23	64.15
CT20_32b	29.42	63.27	67.58
CT20_32c	36.19	77.82	84.24
Mean	30.40	65.38	70.08
Minium	22.11	47.54	50.03
Maximum	36.79	79.11	85.73

Table 5.5: Load and stress intensity factor at failure for CT20 specimens with 3% prestrain.

Specimen Label	Fracture load (kN)	K_I^{el} MPa$\sqrt{m}$	K_J MPa$\sqrt{m}$
CT20_51a	21.41	46.04	48.42
CT20_51b	30.56	65.72	70.16
CT20_51c	41.91	90.13	97.98
CT20_52a	31.81	68.40	73.17
CT20_52b	36.35	78.17	84.24
CT20_52c	32.92	70.78	75.86
Mean	32.49	69.87	74.97
Minium	21.41	46.04	48.42
Maximum	41.91	90.13	97.98

Table 5.6: Load and stress intensity factor at failure for CT20 specimens with 5% prestrain.

RNB45 specimens		RNB60 specimens		RNB90 specimens	
Label	F, kN	Label	F, kN	Label	F, kN
RNB45_1	69.06	RNB60_1	67.90	RNB90_1	68.87
RNB45_2	73.33	RNB60_2	60.11	RNB90_2	68.41
RNB45_3	65.82	RNB60_3	56.91	RNB90_3	69.01
RNB45_4	70.81	RNB60_4	70.05	RNB90_4	68.67
RNB45_5	61.80	RNB60_5	75.17	RNB90_5	75.17
RNB45_6	62.77	RNB60_6	59.82	RNB90_6	67.85
RNB45_7	74.06	RNB60_7	71.57	RNB90_7	59.82
RNB45_8	70.87	RNB60_8	71.87	RNB90_8	69.70
RNB45_9	59.82	RNB60_9	73.49	RNB90_9	69.69
RNB45_10	67.08	RNB60_10	67.78	RNB90_10	71.59
RNB45_11	70.76	RNB60_11	73.29	RNB90_11	69.47
RNB45_12	68.49	RNB60_12	61.18	RNB90_12	67.80
Min load	59.82		56.91		59.82
Max load	74.06		75.17		75.17
Mean load	67.89		67.43		68.84

Table 5.7: Fracture loads for round notched bar specimens.

	Preload		Fracture load	
Label	F_p	K_{Ip}^{el}	F_f	K_{If}^{el}
CT20_WPS_1	50.02	108.04	58.60	126.58
CT20_WPS_2	50.01	108.02	58.92	127.27
CT20_WPS_3	49.97	107.93	58.59	126.56
CT20_WPS_4	50.16	108.34	61.42	132.68
CT20_WPS_5	50.17	108.37	48.83	105.46
		Mean	57.27	123.71
		Min	48.83	105.46
		Max	61.42	132.68

Table 5.8: Load and stress intensity factor at failure for CT20 specimens with LUCF WPS load cycle.

Pre-compression			Pre-tension		
Label	F, kN	K_I^{el}	Label	F, kN	K_I^{el}
NCT_C1	16.99*	37.14*	NCT_T1	49.35	107.89
NCT_C2	27.00	59.02	NCT_T2	44.99	98.36
NCT_C3	24.87	54.36	NCT_T3	35.20	76.96
NCT_C4	33.73	73.74	NCT_T4	49.24	107.64
NCT_C5	26.70	58.36	NCT_T5	51.47	112.52
NCT_C6	6.47*	14.14*	NCT_T6	43.95	96.07
NCT_C7	36.75	80.35	NCT_T7	36.75	80.35
NCT_C8	19.77	43.23	NCT_T8	44.86	98.06
NCT_C9	-	-	NCT_T9	43.99	96.17
NCT_C10	36.75*	80.35*	NCT_T10	35.06	76.65
Mean	25.45	55.63		43.49	95.07
Min	6.47	14.14		35.06	76.65
Max	36.75	80.35		51.47	112.52

** value for first propagation of non-catastrophic crack growth*

Table 5.9: Load and stress intensity factor at failure for NCT with tensile and compressive preloading.

Specimen data	CT20	CT10	WPS CT20	NCT Comp.	NCT Ten.	CT20 1% prestrain	CT20 3% prestrain	CT20 5% prestrain
Fitted Weibull parameters								
R^2	0.971	0.983	0.743	0.924	0.937	0.845	0.93106	0.943
K_m	23.920	42.149	0.000	0.000	0.000	0.000	29.376	0.000
K_0	84.216	98.101	128.900	63.763	99.620	71.262	70.167	76.271
M	3.826	3.092	11.898	2.149	8.138	5.936	3.180	5.172
Estimated normal parameters								
μ	78.435	92.181	123.480	56.469	93.894	66.072	65.900	70.166
σ	15.737	17.592	12.466	27.808	13.474	12.699	12.512	15.320
T and F test results								
n	24	15	5	9	10	6	6	6
Means same?	-	N	N	Y	N	N	N	Y
Variances same?	-	Y	Y	N	Y	Y	Y	Y

Table 6.1: Results of statistical T and F testing of fracture data.

	σ_1				σ_h			
	R^2		MLE		R^2		MLE	
	RNB90 &CT20	All data	RNB90 &CT20	All data	RNB90 &CT20	All data	RNB90 &CT20	All data
m	11.8	12.2	17.9	17.6	7.3	7.7	12.2	12.4
+	13.2	13.7	-	-	8.2	8.8	-	-
-	10.5	10.6	-	-	6.5	6.6	-	-
σ_0	2107.5	2078.2	1923.1	1970.0	1832.5	1680.8	1487.5	1441.8
+	1413.3	1509.4	-	-	1280.2	1273.7	-	-
-	4142.2	3334.7	-	-	3223.3	2470.4	-	-

Table 7.1: Beremin model parameters and 90% confidence limits, from maximisation of the coefficient of determination R^2 and likelihood estimator.

	σ_1				σ_h			
	R^2		MLE		R^2		MLE	
	RNB90 &CT20	All data	RNB90 &CT20	All data	RNB90 &CT20	All data	RNB90 &CT20	All data
m	19.3	17.9	24.4	18.2	12.1	11.7	13.7	12.5
+	21.1	20.0	-	-	13.5	13.1	-	-
-	17.5	15.7	-	-	10.7	10.4	-	-
σ_0	1421.8	1404.6	1472.2	1430.0	940.2	935.7	963.0	954.5
+	1003.6	1065.2	-	-	703.3	746.6	-	-
-	2437.5	2061.5	-	-	1417.9	1253.0	-	-

Table 7.2: Incremental local approach model parameters and 90% confidence limits, from maximisation of the coefficient of determination R^2 and likelihood estimator.

	σ_1				σ_h			
	R^2		MLE		R^2		MLE	
	RNB90 &CT20	All data	RNB90 &CT20	All data	RNB90 &CT20	All data	RNB90 &CT20	All data
m	18.6	19.4	24.5	20.6	11.7	12.3	13.7	14.8
+	20.4	22.0	-	-	12.7	13.7	-	-
-	16.7	16.8	-	-	10.7	10.8	-	-
σ_0	1417.2	1429.1	1466.5	1487.3	936.1	952.2	957.1	1008.1
+	976.1	1063.0	-	-	686.5	743.7	-	-
-	2585.6	2179.6	-	-	1470.9	1323.2	-	-

Table 7.3: Incremental local approach model parameters, including threshold stress, and 90% confidence limits. Based on maximisation of the coefficient of determination R^2 and likelihood estimator.

	σ_1		σ_h	
	RNB90 &CT20	All data	RNB90 &CT20	All data
m	22.6	23.6	13.9	15.0
+	24.5	26.1	14.9	16.4
-	20.7	21.2	12.9	13.5
σ_0	1380.5	1387.4	891.0	893.8
+	1391.2	1406.7	892.0	917.9
-	1367.1	1361.7	887.0	875.4

Table 7.4: Non-Weibull incremental local approach model parameters, including threshold stress, and confidence limits. Based on maximisation of the coefficient of determination R^2.

Appendix A - Weibull formulation for the local approach

The failure probability of a small element of volume, ΔV is given by

$$\Delta Pf = f(\sigma, \epsilon)\Delta V \tag{7.1}$$

The probability of survival is then given by

$$\Delta Ps = 1 - \Delta Pf \tag{7.2}$$

Overall failure probability, for the entire component under consideration is therefore

$$Pf = 1 - \prod \Delta Ps = 1 - \exp\left(\sum \ln(1 - \Delta Pf)\right) \tag{7.3}$$

Taking Taylor series expansion of $\ln(1 - x)$

$$\ln(1 - x) = -\sum_{k=1}^{\infty} \frac{x^k}{k} \tag{7.4}$$

which, for small x, can be approximated to $\ln(1 - x) \approx -x$. This then leads to simplified expression of overall failure probability

$$Pf = 1 - \exp\left(-\sum \Delta Pf\right) \tag{7.5}$$

where in the terminology of the Beremin model $\sum \Delta Pf = (\sigma_w/\sigma_0)^m$.

When x is not small, i.e. where the failure probability of any individual element of volume becomes too high, this approximation is no longer accurate and therefore the Weibull model is no longer appropriate.

Appendix B - The Chell model for warm prestress

The predictive model for the effect of warm prestressing due the Chell [46] was outlined by Smith [150] for fracture following the LUCF load cycle. The J integral, about a contour around the yielding region, can be expressed as

$$J^e = \frac{K_{IC}^2}{E} = \sigma_Y \left[u(a) - u(x)\right] \tag{7.6}$$

Where $u(a)$ and $u(x)$ are displacements at the crack tip and across the yielding region ahead of the crack tip. Using the strip yielding model of Bilby and coworkers

$$u(x) = \frac{K_{IC}^2}{E\sigma_Y} f(x/R) \tag{7.7}$$

$$f(x/R) = \left[\zeta - \frac{x}{2R} \ln\left(\frac{1+\zeta}{1-\zeta}\right)\right] \tag{7.8}$$

where σ_Y is the yield stress and x is the distance ahead of the crack tip. The function ζ is

$$\zeta = \left(1 - \frac{x}{R}\right)^{1/2} \tag{7.9}$$

and R is the size of the plastic zone, equivalent to

$$R = \frac{\pi}{8} \frac{K_{IC}^2}{\sigma_Y^2} \tag{7.10}$$

The fracture stress intensity factor for the LUCF cycle, following a preload K_I, can be found from

$$\frac{K_{IC}^2}{\sigma_{Y2}} = \frac{K_{IC}^2}{\sigma_{Y1}} \left(1 - f(R_1/R_2)\right) - \frac{K_1^2}{2\sigma_{Y1}} \left(1 - f(R_3/R_2)\right) + \frac{K_f^2}{\sigma_{Y1} + \sigma_{Y2}} \tag{7.11}$$

Which must be solved numerically for K_f. The subscripts 1 and 2 refer to the proof load and fracture conditions with the ratio between yield region sizes given by

$$\frac{R_3}{R_2} = \left(\frac{K_f}{K_I}\right)^2 \left(\frac{2\sigma_{Y1}}{\sigma_{Y1} + \sigma_{Y2}}\right)^2 \tag{7.12}$$

$$\frac{R_3}{R_1} = \left(\frac{K_f}{K_I}\right)^2 \left(\frac{\sigma_{Y1}}{\sigma_{Y1} + \sigma_{Y2}}\right)^2 \tag{7.13}$$

Appendix C - Derivation of the Incremental strain local approach

As for the Beremin model, it is assumed that the distribution of defects in the material of interest can be described by a power law distribution. Following the method of section 2.4.1, it can be shown that the likelihood of the local principal stress exceeding that required to propagate a crack from a defect is,

$$P_{prop} = \left(\frac{\sigma_1}{\sigma_0}\right)^m \tag{7.14}$$

where P_{prop} is the probability of propagation in a given unit volume. Introducing a maximum defect size leads to,

$$P_{prop} = \frac{\sigma_1^m - \sigma_{th}^m}{\sigma_0^m} \tag{7.15}$$

where σ_{th} is the stress needed to propagate the largest viable defect.

The overall failure probability is a function of the number of defects and the likelihood of there propagation. It is assumed that the rate of defect nucleation is controlled by the equivalent plastic strain such that,

$$\delta N = C\delta\epsilon_e^{pl} \tag{7.16}$$

where N is the numebr of defects per unit volume and C is a constant. It is assumed here that if defects do not propagate upon their nucleation, they are blunted by subsequent plastic deformation. Therefore, the probability of nucleation and propagation over a strain increment is,

$$P_{np} = \left(\frac{\sigma_1}{\sigma_0}\right)^m \delta\epsilon_e^{pl} \tag{7.17}$$

where the constant C has been incorporated into the σ_0 term.

The fracture probability, for a general volume V_i over a strain increment is therefore determined.

$$Pf_i = \int_{Vi}\int \frac{\sigma_1^m - \sigma_{th}^m}{\sigma_0^m} d\epsilon_e^p dV \tag{7.18}$$

For a component, consisting of N stressed volumes, the overall probability of

failure may then be expressed,

$$Pf = \prod_{i}^{N} (1 - Pf_i) \approx 1 - \exp(\int \int \frac{\sigma_1^m - \sigma_{th}^m}{\sigma_0^m} d\epsilon_e^p dV) \tag{7.19}$$

which may also be expressed in the standard Beremin Weibull distribution form, defining Weibull stress as,

$$\sigma_w^m = \int_{Va} \left[\int (\sigma_1^m - \sigma_{th}^m)\, d\epsilon_e^p \right] dV. \tag{7.20}$$

To implement in a discrete form, the change in σ_w^m is calculated over a discrete strain increment $\Delta\epsilon_e^p$,

$$\Delta\sigma_w^m = \sum_{i=1}^{I} \left((\bar{\sigma}_1^{i,k})^m - \sigma_{th}^m \right) (\Delta\epsilon_e^p)^i v^i. \tag{7.21}$$

As it is assumed that defects not propagated upon nucleation are blunted by further plastic deformation, the accumulation of 'damage' in individual volume elements is not considered. Therefore, the probabilty of fracture occuring in a single volume element is not dependent on the history of that element, only the current stress and plastic strain increment. If this is so, the cumulative Weibull stress may then be calculated.

$$\sigma_w = \left(\sum \Delta\sigma_w^m \right)^{1/m} \tag{7.22}$$